



HAL
open science

Analysis of the data of the EDELWEISS-LT experiment searching for low-mass WIMP

Emeline Queguiner

► **To cite this version:**

Emeline Queguiner. Analysis of the data of the EDELWEISS-LT experiment searching for low-mass WIMP. *Cosmology and Extra-Galactic Astrophysics [astro-ph.CO]*. Université de Lyon, 2018. English. NNT : 2018LYSE1196 . tel-02025002

HAL Id: tel-02025002

<https://theses.hal.science/tel-02025002>

Submitted on 19 Feb 2019

HAL is a multi-disciplinary open access archive for the deposit and dissemination of scientific research documents, whether they are published or not. The documents may come from teaching and research institutions in France or abroad, or from public or private research centers.

L'archive ouverte pluridisciplinaire **HAL**, est destinée au dépôt et à la diffusion de documents scientifiques de niveau recherche, publiés ou non, émanant des établissements d'enseignement et de recherche français ou étrangers, des laboratoires publics ou privés.



N° d'ordre NNT : 2018LYSE1196

THÈSE DE DOCTORAT DE L'UNIVERSITÉ DE LYON
opérée au sein de
l'Université Claude Bernard Lyon 1

École Doctorale ED52 PHAST

Spécialité de doctorat : Physique des particules

Soutenue publiquement le 23/10/2018, par :
Emeline Queguiner

**Analysis of the data of the
EDELWEISS-LT experiment searching
for low-mass WIMP**

Devant le jury composé de :

Petricca Federica, Chercheure

Tonazzo Alessandra, Professeure des Universités

Davidson Sacha, Directeure de recherche

Salati Pierre, Professeur des Universités

Gascon Jules, Professeur des Universités

Rapporteure

Rapporteure

Examinatrice

Examineur

Directeur de thèse

Contents

Resume	ix
Résumé	xi
Remerciements	xiii
Introduction	1
1 Theoretical context	3
I Cosmological introduction	3
I.1 Cosmological notions	3
I.1.1 General relativity and metric	4
I.2 The thermal story of the Universe	5
I.2.1 Inflation	5
I.2.2 Radiation era	5
I.2.3 Matter era	6
I.2.4 Actual status	6
II Evidences for dark matter	6
II.1 At galactic scales	6
II.2 At galaxy cluster scales	7
II.3 Gravitational lensing	8
II.4 Cosmic Microwave Background (CMB)	8
II.5 Baryonic Acoustic Oscillations (BAO)	10
II.6 Big Bang Nucleosynthesis (BBN)	10
II.7 Combination	11

III	Dark matter properties	11
III.1	Structure formation constraints	12
III.2	Particle properties	13
III.2.1	Non-baryonic nature	13
III.2.2	Density in the Universe	13
III.2.3	No electric charge	13
III.2.4	No strong interaction with ordinary matter	14
III.2.5	Long lifetime	14
III.2.6	Cold dark matter	15
III.3	WIMP miracle	15
III.4	Dark matter candidates	16
III.4.1	Massive Astrophysical Compact Halo Objects (MACHOs)	16
III.4.2	Axions	17
III.4.3	WIMP	17
IV	Dark matter detection	18
IV.1	Production in a collider	18
IV.2	Indirect detection	19
IV.2.1	Antimatter	19
IV.2.2	γ -ray telescopes	20
IV.2.3	Neutrino telescopes	20
IV.3	Direct detection	21
IV.4	Complementarity	21
V	Direct detection	22
V.1	WIMP-matter interaction	22
V.1.1	Spin-independent cross-section	23
V.1.2	Spin-dependent cross-section	23
V.2	Theoretical recoil spectrum	23
V.3	Inclusion of Earth rotation	25
V.4	Inclusion of form factor	25
V.5	Final theoretical recoil spectrum	26
V.6	Shape of the recoil spectrum	26
V.6.1	Mass and velocity	26
V.6.2	Target nucleus and form factor	26
V.7	WIMP signature in detectors	27
V.8	State of art	28
V.9	Noble gases detectors	29
V.9.1	The XENON experiments	29

V.9.2	The DarkSide-50 experiment	30
V.9.3	Summary on noble gas experiment	31
V.10	Cryogenic detectors	31
V.10.1	The CRESST experiment	32
V.10.2	The SuperCDMS experiment	33
V.11	Others techniques	33
VI	Conclusion	34
2	The EDELWEISS experiment	37
I	Backgrounds and mitigation strategies	37
I.1	Muon backgrounds	38
I.2	Neutron background	39
I.3	Gamma background	41
I.4	Alpha background	43
I.5	Beta background	43
I.6	Radiopurity of materials	44
II	Cryogenic germanium detectors	47
II.1	Ge properties	47
II.2	Charge migration and ionization signals	47
II.3	Thermal sensors	48
III	Description of the cryostat, cold electronics and DAQ systems	49
III.1	Cryogenic installation	49
III.2	Cold electronics	50
III.2.1	Ionization channel readout	51
III.2.2	Heat channel readout	52
III.2.3	DAQ (Data AcQuisition system)	53
IV	EDELWEISS FID800 detectors	54
IV.1	FID design	54
IV.2	Evaporated electrodes	55
IV.3	Combined measurement: ionization and heat	56
V	Thermal modeling of FID800 bolometers	58
VI	Luke-Neganov effect in FID800 detectors	61
VI.1	Principle	61
VI.2	High-voltage optimization in FID800 detectors	63
VII	Conclusion	65
3	Data analysis and selection	67
I	High-voltage cryorun goals and detector set-up	67

II	Signal processing	70
II.1	Trigger	70
II.2	Pulse height determination	71
II.2.1	Pulse amplitude of ionization channels	71
II.2.2	Pulse amplitude of heat channels via optimal filtering	72
II.3	Energy calibration	73
II.3.1	Ionization channels	73
II.3.2	Heat channels	76
II.4	Heat energy baseline resolutions	77
II.5	Nuclear and electronic recoil regions	78
III	Data selection	79
III.1	Time period selection	79
III.2	Exposure calculation	81
III.3	Event cuts	82
III.4	Efficiency	84
III.5	Fiducial events selection	85
IV	Luke-Neganov effect in FID800 detectors	86
V	Conclusion	87
4	Study of the heat-only background in the EDELWEISS detectors	89
I	Heat-only event definition	89
II	Measured properties of heat-only events	91
II.1	Heat-only time distribution	92
II.2	Heat-only rate as a function of time	92
II.3	Heat-only count rate anomaly	93
III	Heat-only energy spectrum	97
III.1	Kolmogorov-Smirnov test	97
III.2	Study of heat-only spectra dependence	100
III.2.1	Voltage dependence of heat-only spectra	100
III.2.2	Detector dependence	103
III.2.3	Time dependence	103
III.3	Modelization of the heat-only background	103
III.3.1	Two-exponential spectrum model	103
III.3.2	Kernel Density Function principle	108
III.3.3	Conclusion: selection of the model	108
IV	Discussion about the possible origin of heat-only events	109
IV.1	Evaporation of ${}^4\text{He}$	109

IV.2	Stress in germanium induced by vibrations	111
IV.3	Stress induced from the contact between the Ge crystal and the Teflon [®] holders	111
IV.4	Stress in germanium induced by gluing	112
IV.5	Stress induced by surface treatment of FID	113
IV.6	Surface events in Al and in the amorphous layer of Ge	113
IV.7	Nuclear property of the glue at the NTD-absorber interface	115
IV.8	Properties of NTD	115
IV.9	Gold pads	116
IV.10	Heat pulses coming through the thermal link	117
IV.11	Electronic noise	117
V	Conclusion	119

5	WIMP search results with EDELWEISS-III detectors operated at high voltage bias	121
I	Characterization of the different EDELWEISS backgrounds	121
I.1	Compton background	122
I.1.1	Fiducial compton events	122
I.1.2	Surface compton events	123
I.1.3	Total compton rate	124
I.2	Cosmogenic background	124
I.2.1	Peaks background	124
I.2.2	Tritium background	127
I.3	Beta background	129
I.3.1	Spectral shape	129
I.3.2	Quenching factor of β -events	130
I.4	Lead background	131
I.5	Neutron background	133
I.6	Heat-only background	133
II	WIMP rate limit obtained from Poisson fluctuations within an optimized range	133
II.1	Methodology of WIMP limit calculations	134
II.1.1	Poisson method	134
II.1.2	Optimization of the counting interval	134
II.2	WIMP rate limits	136
II.2.1	Expected signal used	136
II.2.2	Optimization of the energy range	137
II.2.3	Limit associated to the first run at high voltage	137

II.2.4	Study of the exposure limitation on WIMP-nucleon cross-section for low-mass WIMP	138
III	Likelihood analysis	139
III.1	Modelization of the different types of events	140
III.1.1	Probability Density Functions	141
III.1.2	Generating fake experiments	142
III.2	Maximum likelihood function	143
III.3	Profile Likelihood	144
III.3.1	Experimental sensitivity	146
IV	Extraction of the exclusion limits	149
IV.1	Dataset of the FID803 detector in run309	149
IV.2	Dataset of the FID803 detector in run310	150
IV.3	Discussion	152
V	Conclusion	154
	Conclusion and outlook	155
	Appendix A	157
I	Expected signal	157
II	Compton background	157
III	Tritium background	158
IV	Cosmogenic peaks background	158
V	Beta background	159
VI	Lead background	159
VII	Neutron background	160
VIII	Heat-only background	160
	Bibliography	165

Many astrophysical and cosmological observations lead to postulate the existence of an unknown matter, called dark matter. Ordinary matter can explain only 5 % of the energy content of the Universe : the main components would be the dark energy (70 %) and dark matter (25 %). This latter is invisible and manifest itself only via its gravitational effects. Several particles, grouped under the generic term of WIMP (Weakly Interacting Massive Particles), could correspond to this theory and are actively searched. Many experiments have been developed for this purpose and are based on three strategies: the production of these particles with colliders, the observation of the particles produced by their annihilation in astrophysical objects or the direct detection of these particles via their interaction with the nucleus of the atoms constituent of a detector.

It is on this last method that the EDELWEISS experiment is based. It is a dark matter direct detection experiment dedicated to the search for WIMP with masses between 1 GeV and 1 TeV. Its primary purpose is to detect nuclear recoils induced by elastic scattering of dark matter particles in detectors. Since the expected event rates $< 10 /(\text{kg}\cdot\text{year})$ are several orders of magnitude lower than those induced by ambient radioactivity, a double measurement of ionization and heat is used to discriminate electron-induced recoils arising from β and γ interactions from WIMP-induced nuclear recoils. In addition, the experiment was placed underground to guard against cosmic radiation, inducing events in the detectors. These are germanium bolometers, called FID, cooled to cryogenic temperatures (18 mK) and operating at low field (1 V/cm). Since 2015, the new strategy of the experiment consists of focusing on WIMPs with mass below 10 GeV, an interesting research area where experiments using cryogenic detectors can exploit their ability to operate with experimental thresholds well below 1 keV. The operation of the experiment has been improved to achieve this goal.

The aim of this thesis is to analyze the data set recorded by EDELWEISS in 2015 and 2016. These used the FID detectors subjected to a greater electric field than previously to improve their sensitivity. It is expected that the limit on the spin-independent WIMP-nucleon cross-section extracted from these data will be greatly impacted by a dominant background, called heat-only events.

That is why they are studied in detail in this work. They are characterized by a rise in heat seen by thermal sensors without any ionization signal on the collecting electrodes. This study resulted in to highlight a model for these events that can be used in the WIMP search analyses. Following these results, a maximum likelihood analysis was constructed. This method of anal-

ysis makes it possible to statistically subtract the background noise from the experiment by exploiting the difference between the energy spectra of signal and backgrounds. In this way, limits on the spin-independent WIMP-nucleon cross-section are obtained. They will be compared to the results of other experiments.

Résumé

De nombreuses observations astrophysiques et cosmologiques tendent à prouver que la matière ordinaire (dite baryonique) ne constituerait qu'environ 5 % du contenu énergétique de l'Univers. Les principales composantes de celui-ci seraient l'énergie noire (à 70 %) ainsi que la matière noire (à 25 %). Cette dernière serait invisible et seuls ses effets gravitationnels traduiraient sa présence dans l'Univers. Plusieurs particules, regroupées sous le terme générique de WIMP (Weakly Interacting Massive Particles), pourraient correspondre à cette théorie et sont activement recherchées. Plusieurs dispositifs expérimentaux ont été développés dans ce but et s'appuient sur les stratégies suivantes : la production de ces particules au sein de collisionneurs, l'observation de particules produites via l'annihilation de WIMP ou encore la détection directe de ces particules via leur interaction avec le noyau des atomes constitutifs d'un détecteur. C'est sur cette dernière méthode que s'appuie l'expérience EDELWEISS.

Il s'agit d'une expérience de détection directe de matière noire dédiée à la recherche de WIMP de masse comprise entre 1 GeV et 1 TeV. Son but premier est de détecter les reculs nucléaires induits par la diffusion élastique de particule de matière noire dans les détecteurs. Les taux d'événements attendus $< 10 /(\text{kg}\cdot\text{an})$ étant de plusieurs ordres de grandeur inférieurs à ceux induits par la radioactivité ambiante, une double mesure de l'ionisation et de la chaleur est employée pour discriminer les reculs électroniques induits par les bruits de fonds β et γ des reculs nucléaires induits par les WIMPs. De plus, l'expérience a été placée en site souterrain pour se prémunir des rayonnements cosmiques, induisant des événements dans les détecteurs. Ceux utilisés par l'expérience sont des bolomètres en germanium, appelés FID, refroidis à des températures cryogéniques (18 mK) et opérant à bas champ (1 V/cm). Depuis 2015, la nouvelle stratégie de l'expérience consiste à se focaliser sur les WIMPs de masse inférieure à 10 GeV, zone de recherche privilégiée pour les expériences utilisant des détecteurs cryogéniques. Le fonctionnement de l'expérience a donc été amélioré afin d'atteindre cet objectif.

Le but de cette thèse consiste à analyser les campagnes de données de l'expérience, effectuées en 2015 et 2016. Celles-ci utilisaient les détecteurs FID soumis à un champ électrique plus important que précédemment afin d'améliorer leur sensibilité. La limite extraite à partir de ces données s'appuie sur la statistique de Poisson et a permis de mettre en évidence que le bruit de fond dominant de l'expérience à basse énergie impacte grandement les résultats.

C'est pourquoi une étude de ces événements, appelés heat-only, a été réalisée. Ceux-ci se caractérisent par une élévation de chaleur vue par les senseurs thermiques sans que les électrodes du détecteur ne mesurent d'ionisation en son sein. Une étude de ce bruit de fond a été réalisée

et a permis de mettre en évidence la possibilité de modéliser ces événements.

Suite à ces résultats, une analyse par maximum de vraisemblance a été construite. Cette méthode d'analyse permet de soustraire de manière statistique les bruits de fond de l'expérience grâce à leurs spectres en énergie différents de ceux attendus pour un signal de matière noire. De cette façon, une limite sur la section efficace des WIMP a été calculée en utilisant pour la première fois des détecteurs FID soumis à des champs électriques supérieurs aux valeurs utilisées jusqu'à présent.

Remerciements

Je remercie le LABEX Institut Lyonnais des Origines (ANR-10-LABX-0066) de l'Université de Lyon pour son soutien financier dans le cadre du programme "Investissements d'Avenir" (ANR-11-IDEX-0007) de l'Etat Français géré par l'Agence Nationale de la Recherche (ANR).

Un grand merci à l'ensemble des membres de mon jury, qui m'ont fait l'honneur de prendre de leur temps pour lire et évaluer mon travail ainsi que pour leur rapport favorable. Je remercie donc chaleureusement Federica Petricca et Alessandra Tonazzo pour avoir accepté d'être mes rapporteurs, pour leur lecture attentive du manuscrit et leurs rapports extrêmement bienveillants. Je suis également très reconnaissante envers Sacha Davidson et Pierre Salati et sincèrement touchée qu'ils fassent partie de ce jury.

Mes remerciements vont également à chacun des membres du groupe MANOIR qui m'ont aidé durant cette thèse. Chacun d'eux contribue chaque jour à cette ambiance conviviale et ce cadre de travail agréable que j'ai connu pendant ces trois années. Je remercie en premier lieu mon directeur de thèse, Jules Gascon, au contact duquel j'ai beaucoup appris. Les discussions autour de l'univers des séries, des films et des shokobons ont été des souvenirs marquants de cette thèse. Un grand merci à Corinne, cheffe vénérée, de m'avoir accueillie dans son bureau les six derniers mois de cette thèse. Je ne te remercierai jamais assez pour toute l'aide que tu m'as apportée pendant cette thèse mais également durant le master. Je sais bien que mon absence est supportable au contraire des tartes au citron... Il me faudra donc en ramener une de temps en temps. Maryvonne, je garderai un souvenir ému de tes gros dégueulasses¹ ainsi que tes patates au micro-onde. Merci pour ton aide, avec le CC notamment. Je remercie également Alex et Julien, pour leurs discussions animées sur les séries du moment; Véronique et Antoine, pour tous les déjeuners dans la salle de pause passés en votre compagnie et vos aides pour les nombreuses répétitions de mes présentations. Une pensée pour mes prédécesseurs, Quentin et Cécile, qui m'ont accueillie dans leur bureau en fin de thèse. Merci à Romain de ne PAS m'avoir aidé pour ROOT... Je suis sûre que tu es maintenant parfaitement conditionné à finir les phrases telles que : "ou alors ..." et "c'est fort aimable". Dimitri, je suis honorée de t'avoir montré le *Munchkin* et j'espère que tu continueras de jouer à *Blanc manger coco*. Tu as maintenant la charge (ingrate) de supporter Eva dans ton bureau... Eva, sois sage et nourris Jules (pour qu'il te préfère au chien). Accessoirement, je vous souhaite à tous les deux de passer vos thèses avec succès.

Je souhaite remercier tous ceux que j'ai pu croiser durant cette thèse. Un grand merci à Pierre

¹Comme promis, cette phrase n'est compréhensible que pour nous.

et Guillaume pour leurs après-midi/soirées jeux et de nous avoir donné l'adresse du Petit Poisson Rouge. Merci également aux doctorants de l'IPNL, croisés lors des gouters et autres événements. Merci à Anthony qui a été un binôme de TP inoubliable pendant le master, le meilleur binôme de l'Univers observable. Merci à Marine, 25 ans que l'on se connaît, pour être venu me voir soutenir. Je ne peux malheureusement pas citer tout le monde, mais je remercie tous mes amis de Tours et ailleurs ;)

En dernier lieu, je remercie toute ma famille. A ma tante qui a fait le déplacement Morlaix-Lyon pour assister à cette thèse (ce fut épique). Je n'oublie pas celles et ceux qui sont resté en Bretagne mais qui étaient là par la pensée. Merci à mes deux frérots d'être venu, j'ai vraiment apprécié de vous voir dans l'amphithéâtre pour cette soutenance. A Benji² également, tu as été d'un grand secours durant cette journée également, ainsi que pour les répétitions. Vous avez tous les trois passés avec succès l'épreuve de dormir sur mon inconfortable canapé. Merci également à mes parents d'avoir fait le déplacement, cette semaine lyonnaise a été riche en souvenirs. C'est grâce à vous que j'ai pu réaliser cette thèse, merci. Et félicitations pour vos noces de perle! Enfin, je remercie *ma valeur ajoutée, mon con-joint, ma pièce rapportée, etc* pour être patient quand je m'énerve, m'écouter quand j'ai besoin de parler, d'avoir subi cette thèse sans faiblir, de t'être énervé à ma place de temps en temps, ³... bref merci d'être là.

²Et oui, tu es dans ce paragraphe, tu fais parti de la famille ;)

³de manger tous les desserts que je fais... :p

Introduction

Many astrophysical and cosmological observations indicate that only 5% of the energetic content of the Universe is constituted of ordinary matter. The remaining part is constituted by the dark energy (at 69.2%) and dark matter (at 25.8%). The latter doesn't interact via electromagnetism and up to now only gravitationnal effects point to its presence. The Standard Model of particle doesn't offer any particle which can correspond with this type of matter. This is why a generic term, WIMP (Weakly Interacting Massive Particle), which regroups many candidates for dark matter, was created. To match with the observations, these particles have to be massive, weakly interact with ordinary matter and stable over the lifetime of the Universe. An intensive search is ongoing to detect them and three main strategies are proposed by different experiments: the production of these particles in a collider, the study of cosmic particle flux which can contain an excess of standard particles produced by the annihilation of dark matter particles, and the study of WIMP elastic scattering with a nucleus constituent of a detector. This last method is used by the EDELWEISS experiment.

The first chapter describes the astrophysical and cosmological observations that have led to postulate the existence of dark matter. The different experimental methods to detect it are presented and the direct detection strategy using by the EDELWEISS experiment is described. The recent results on the WIMP-nucleon cross-section as a function of its mass are presented to set the context in which this thesis has been made.

The second chapter describes the EDELWEISS experiment. The different sources of backgrounds and their interaction with matter are presented. A description of the set-up of the experiments and of its detectors is made. The measurement of the ionization and heat signals allows to discriminate electronic recoils (induced by β and γ) from the nuclear recoils expected from WIMP scattering inside the detector. Moreover, the detector design allows to reject surface events arising from β and ^{206}Pb recoils. However, the new goal of the collaboration to detect low-mass WIMP imposes to operate the detectors at high voltage bias, and thus lose this discrimination in favor of much improved experimental energy thresholds.

The third chapter describes the data analysis method for this new mode of operating the EDELWEISS detectors. Initially, the first run using this high-voltage mode was performed in order to test the Luke-Neganov effect on FID800 detectors. The different steps necessary for the analysis to obtain the final spectra are presented (quality cuts, trigger efficiency, ...) and a study of the improvement of the heat resolution of the detector is also described.

The fourth chapter is dedicated to the study of the main background of the EDELWEISS

experiment, called heat-only events. Those are characterized by a heat measurement on the thermal sensors, without any ionization signal measured on the electrodes of the detectors. At low energy, this background strongly impacts the data. The different hypotheses on their origin and the various tests and experiments done to verify them are described. Their behavior is also studied systematically, with the objective to provide a reliable model to be used in next analyses.

The fifth chapter describes the two analysis methods to extract a limit on the spin-independent WIMP-nucleon scattering cross-section from the first dataset using the Luke-Neganov effect. After determining the different backgrounds of the study using sidebands, the first statistical method is presented as well as the associated results. Then, a description of the maximum Likelihood analysis implemented in order to derive from the data a limit on the spin-independent WIMP-nucleon scattering cross-section as a function of the WIMP mass is made. This Likelihood method allows to take into account the known shape of the energy spectra of the different backgrounds as well as of the expected WIMP signal to extract the most stringent constraints. The results are then compared to those of other experiments, and the prospects for the EDELWEISS experiment are discussed.

CHAPTER 1

Theoretical context

Many observations point to the presence of missing matter at both galactic and cosmological scales. This unknown matter can't be ordinary matter¹, for the reason it interacts mainly by gravitationnal effect. This dark matter, which is one of the major challenges of this century in particle physics, has been postulated to be one exotic particle class called WIMP (Weakly Interacting Massive Particle). This chapter presents the observations leading to postulate the existence of dark matter. The different methods to detect it will be developed.

I Cosmological introduction

I.1 Cosmological notions

Modern-day cosmology has emerged soon after the publication of general relativity by Einstein in 1915 [1]. It is based on the works of Friedmann (1922) and Lemaitre (1927) works whereby the Universe could be dynamic, because the general relativity has no static solution. Hubble (1929) has corroborated this assumption with his work on the radial expansion of galaxies [2]. For different galaxies, he confronted the Doppler shift of emissions with estimated distances using the parallax method. In this way, the Hubble's law has been established. It describes the recession velocity v as a function of the distance from the observer to the galaxy r :

$$\vec{v} = H_0 \vec{r} \tag{1.1}$$

where the constant H_0 corresponds to the actual expansion rate of the Universe. Its value is $H_0 = 100h \text{ km.s}^{-1}.\text{Mpc}^{-1}$ with h the reduced measurement of the Hubble constant, corresponding to $h = 0.678 \pm 0.009$ [3], knowing that the direction of the observation has no influence on it. Eq.1.1 satisfies the first cosmological principle whereby the Universe is isotropic and homogeneous². In other words, the Hubble's law is valid in all points in space.

¹i.e baryonic matter

²This is the Mach's principle: there is no special place in the Universe.

I.1.1 General relativity and metric

Gravitation is the dominant interaction at the Universe scale, inducing a strong effect on cosmological structures. Einstein's equation of general relativity relates the scalar curvature R with its energy content³:

$$R_{\mu\nu} - \frac{1}{2}Rg_{\mu\nu} + \Lambda g_{\mu\nu} = 8\pi GT_{\mu\nu} \quad (1.2)$$

where $R_{\mu\nu}$ is the Ricci tensor and R its contraction, $g_{\mu\nu}$ is the metric tensor, $T_{\mu\nu}$ the energy-momentum tensor and G is the gravitational constant. Λ is the cosmological constant which could be assimilated to the vacuum energy. To apply this equation to cosmology, the metric characterizing the Universe geometry should be selected carefully. The most global metric which satisfies to the cosmological principle is the Robertson-Walker metric defined as:

$$ds^2 = dt^2 - a^2(t) \left[\frac{dr^2}{1 - kr^2} + r^2(d\theta^2 + \sin^2\theta d\phi^2) \right] \quad (1.3)$$

In Eq.1.3, the system of comoving coordinates (r, θ, ϕ) follows the Universe expansion. The variable $a(t) = \frac{R(t)}{R_0}$ is the Universe scale factor, with $R(t)$ the Universe radius and $R_0 = R(t_0)$ the value at the present date t_0 . The parameter k represents the space curvature and corresponds to 1, 0 or -1 for open, flat or closed space, respectively. It is used to depict the Universe expansion as a function of time for a defined scale factor. A diagonal energy-momentum tensor is set as a result of symmetry properties. The Universe may be assimilated to a perfect fluid with a density $\rho(t)$ and a pressure $p(t)$. Using Eq.1.2 and the metric in Eq.1.3, the evolution of this fluid density can be resolved by:

$$\left(\frac{\dot{a}}{a} \right)^2 = \frac{8\pi G\rho(t)}{3} = \frac{8\pi G}{3}(\rho_m + \rho_r + \rho_\Lambda - \rho_k) \quad (1.4)$$

where $\rho_m, \rho_r, \rho_\Lambda$ and ρ_k are energy densities associated to matter, radiation, cosmological constant and curvature, respectively. Using a critical density $\rho_c = 3H^2/8\pi G$ corresponding to a flat Universe i.e $k = 0$ (with H the Hubble factor describing the expansion rate of the Universe), Eq.1.4 can be rewritten such as:

$$\left(\frac{\dot{a}}{a} \right)^2 = H^2(\Omega_m + \Omega_r + \Omega_\Lambda - \Omega_k) = H^2(1 - \Omega_k) \quad (1.5)$$

with $\Omega_n = \frac{\rho_n}{\rho_c}$ for each energy density n and:

$$\Omega_{tot} = \Omega_m + \Omega_r + \Omega_\Lambda = 1 - \Omega_k \quad (1.6)$$

Thus Ω_{tot} is correlated to the Universe geometry thanks to the Ω_k curvature parameter. The study of the Universe combines the measurement of cosmological observables which have different contributions:

- The radiation density contains the relativistic contribution of neutrinos (ν) and photons (γ): $\Omega_r = \Omega_\nu + \Omega_\gamma$. It is negligible today.
- The matter density includes the non-relativistic contribution of the baryonic matter density Ω_b ⁴, and the non-baryonic contribution Ω_{CDM} (no coupling to photons): $\Omega_m = \Omega_b + \Omega_{CDM}$

³Considering the speed of light $c = 1$.

⁴Some part of this density may contribute to baryonic dark matter (MACHO), discussed later (section III.2.1).

Chapter 1: Theoretical context

- Ω_Λ corresponds to the dark energy density for a flat Universe.

For a flat Universe ($\Omega_{tot} = \Omega_m + \Omega_\Lambda = 1$, with $\Omega_k = 0$), a lower bound on the cold dark matter density can be posed as: $\Omega_{CDM} \geq 0.1$ [4].

I.2 The thermal story of the Universe

In the Universe, a temperature $T(t)$ can be defined as the inverse of the scale factor $a(t)$. During its expansion, the Universe cools down and the density of particles inside are diluted, thus modifying their reactions. At each step of the evolution, each species reaches their thermal equilibrium, eventually freezing their density once the temperature and density are no longer sufficient to sustain their reactions. The decoupling of the different particle species depends on the temperature:

$$\Gamma > H: \text{ coupled species, } \Gamma \sim H: \text{ freeze-out, } \Gamma < H: \text{ decoupling} \quad (1.7)$$

As an example, for neutrinos, the collision rate with the particles of the thermal bath is proportional to T^5 whereas $H \sim T^2$ ($H = \sqrt{\frac{8\pi}{3}G\rho} \propto \sqrt{T^4}$ because of $\rho \propto T^4$ at this time) [3]. The neutrino decoupling takes place when the collision rate is less than the expansion rate, for a temperature around 10^{10} K (i.e 1 MeV). The neutrino wavelength decreases as a result of the expansion, and today the cosmic neutrino background $C\nu B$ is expected to have a temperature of $T_\nu \sim 1.95$ K. The main steps of the Universe evolution in the Big Bang model are described as a function of time but also of the energy and the temperature.

I.2.1 Inflation

The Universe description begins at the Planck time (at $t < 10^{-43}$ seconds after the Big Bang and $T > 10^{32}$ K $\sim 10^{19}$ GeV). At this earliest time, the Universe is supposed to be a plasma of relativistic particles, infinitely dense, highly luminous and hot. All fundamental interactions (electromagnetism, strong, weak and gravitational interactions) were unified. The description of this era requires quantum corrections inside the general relativity that are currently missing. It is only after this era that the evolution of the Universe can be extrapolated from the present knowledge in particles physics, cosmology and relativity. The Universe goes through its first spontaneous symmetry breaking with the separation of gravity from the other interactions (electronuclear force) at a temperature $T > 10^{29}$ K $\sim 10^{16}$ GeV (for $t < 10^{-36}$ seconds), corresponding to the GUT epoch (Grand Unification Theory).

I.2.2 Radiation era

For $t < 10^{-32}$ seconds, an exponential expansion period begins. The strong interaction separated from the electroweak force, containing electromagnetism and weak forces ($T \sim 10^{28} - 10^{22}$ K $\sim 10^{15} - 10^9$ GeV). Exotic particles can still be produced. Some of the bosons like the W, Z and Higgs are continuously created and annihilated during this period. Then comes the quark epoch for $t \sim 10^{-12} - 10^{-6}$ s. The four interactions were decoupled. Quarks and their antiparticles are in a thermodynamic equilibrium until $t \sim 10^{-5}$ s ($T \sim 1$ GeV) when the Universe temperature decrease forces quark confinement. Baryons and mesons appeared at this time. Below $T \sim 10^{10}$ K (1 MeV), the interaction rate of leptons is less than the expansion rate and neutrinos have too weak interactions to stay in equilibrium as mentioned before. After that, the temperature drops below the mass of the electron, and the entropy in e^+e^- pair

production is transferred to photons. Then, the Universe is dominated by photons which are still in interaction with charged particles. The population of photons, neutrinos, antineutrinos, baryons, electrons and positrons are no longer in equilibrium. At $T \sim 10^9 - 10^7$ K $\sim 100 - 1$ keV, the first light elements are generated: deuterium and tritium at the beginning, then heavier nuclei such as helium and lithium. Because of the expansion, density and temperature are not sufficient to allow the creation of heavier atoms. So far, the Universe expansion, corresponding to $a(t) \propto t^{1/2}$, originated essentially from radiations. Then the expansion increases with $a(t) \propto t^{2/3}$ and the domination of matter begins.

I.2.3 Matter era

Up to now, the photoionization reaction $e + p \rightarrow H + \gamma$ obstructs the formation of hydrogen atoms. The generation of the first neutral atoms is allowed around 3700 K stabilizing the link between electrons and baryons. This process is called recombination (at $T \sim 4000$ K ~ 0.4 eV). The γ emission from the last scattering surface is shifted toward red, due to the Universe expansion. Observed overdensities are present since this moment. As a result of their own gravity, they grow up and the distance between these different density areas increases. Thus it remains fluctuations at small scales but, at large scales, homogeneity and isotropy are present. It is taken for granted that structures are formed by accretion. Galaxies have assembled into clusters that in turn assembled into superclusters, generating filament structures (see section III.1).

I.2.4 Actual status

According to [3], parameters for the Λ CDM⁵ model at 68% C.L. are thus:

- $H_0 = 67.81 \pm 0.92$ km.s⁻¹.Mpc⁻¹, leading to $h = 0.6781 \pm 0.0092$.
- Dark energy density: $\Omega_\Lambda = 0.692 \pm 0.012$.
- Matter density: $\Omega_m = 0.308 \pm 0.012$ with a baryonic and a dark matter components such as: $\Omega_b h^2 = (2.226 \pm 0.0023) \times 10^{-2}$ and $\Omega_{CDM} h^2 = 0.1186 \pm 0.0020$ (corresponding to $\Omega_b = 0.0484$ and $\Omega_{CDM} = 0.258$ values, respectively).

II Evidences for dark matter

II.1 At galactic scales

The evidence that relaunched the problem of dark matter in the 70's is the rotation velocity curves of spiral galaxies. By estimating the rotation's velocity of stars and gases inside a galaxy as a function of their distance to the galactic center using the Doppler shift of emission rays, Rubin [6], in 1970, brought to light a stability of the velocities at large scale, beyond the visible part of the galactic disk. It is explainable only by the existence of a large halo of missing matter surrounding the galaxy. For a spherical distribution of mass $M(r)$, the second law of Newton predicts that the rotational velocity of an object v , located at a distance r of the center, is

⁵The Λ CDM corresponds to the Big Bang model parametrization, in which the Universe contains both a cosmological constant Λ associated with dark energy and cold dark matter (CDM).

Chapter 1: Theoretical context

given by:

$$v(r) = \sqrt{\frac{GM(r)}{r}} \quad (1.8)$$

with G the gravitational constant. For radius r larger than the average radius of visible objects in the galaxy, the velocity is expected to decrease proportionally to $\frac{1}{\sqrt{r}}$, which is not observed, as shown in Fig.1.1. Instead, beyond the visible frontier of the galaxy, the velocity becomes almost constant. These results could not be explained by observable matter and it is why a presence of dark matter whose the mass increases with the radius was invoked. For dwarves

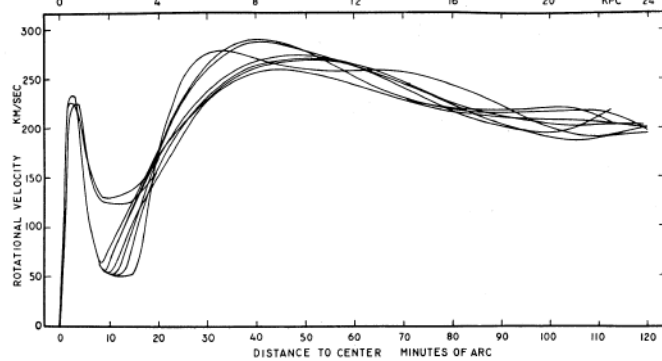


Figure 1.1 – Left: Andromeda’s galaxy (M31). Right: rotational curves measured by Rubin [6]. The velocity doesn’t decrease with the radius after exceeded the optical radius of the galaxy as it was expected. A missing mass could explain this phenomena.

spheroidal galaxies, the dark matter abundance is more impressive. Indeed, this type of galaxy is thinly luminous and lacking gases. Visible matter is less than one percent of the total mass of these objects and they should be dominated by dark matter [7].

II.2 At galaxy cluster scales

Galaxy clusters are a group of galaxies tugged around by each other’s gravity. The method used to determine their mass consists of measuring the velocity dispersion of galaxies in a cluster to estimate its total mass. This is the method used by Zwicky in 1933 [8] for the Coma cluster, applying the Viriel theorem, which links the total mass M of a spherical cluster (with a radius R), at equilibrium, with the velocity dispersion σ such as:

$$M = \frac{5R\sigma^2}{3G} \quad (1.9)$$

Knowing the average luminosity of galaxies and the number of them in the cluster, Zwicky calculated a mass-to-light ratio $M/L \simeq 500 M_{\odot}/L_{\odot}$ ⁶, namely around 100 times higher than inside a local stellar system. Even if the measured ratio was too high, these observations are considered as the first study leading to the dark matter assumption. Present-day measurements indicate that gases and galaxies constitute only 15% of the total mass of galaxy clusters [9].

⁶ $M_{\odot} = (1.98848 \pm 0.00009) \times 10^{30}$ kg corresponds to the solar mass and $L_{\odot} = 3.828 \times 10^{26}$ W the solar luminosity [4].

II.3 Gravitational lensing

Another evidence for dark matter existence is its gravitational effects on visible objects in the Universe. The study of gravitational lensing is made by analyzing the deflection of photons when they pass through the deformed space induced by a gravitational field. Indeed, photons don't have a linear trajectory if they pass near massive objects (stars, galaxies, dark matter, ...) along the line of sight of an observer based on Earth. The first study of it has been made in 1919 [10], when a solar eclipse in front of the Hyades star cluster induced a movement of its stars when they pass behind the Sun. Not only checking the General Relativity principles, gravitational lensing also confirm the existence of the dark matter. Its study, as shown in Fig.1.2, allowed to deduce:

- there is five times more dark matter than baryonic matter in the Universe;
- dark matter should interact normally, i.e in a same way as baryonic matter, via gravitational interaction;
- dark matter has very small weak and self-interaction cross-sections;
- dark matter is dynamically cold.

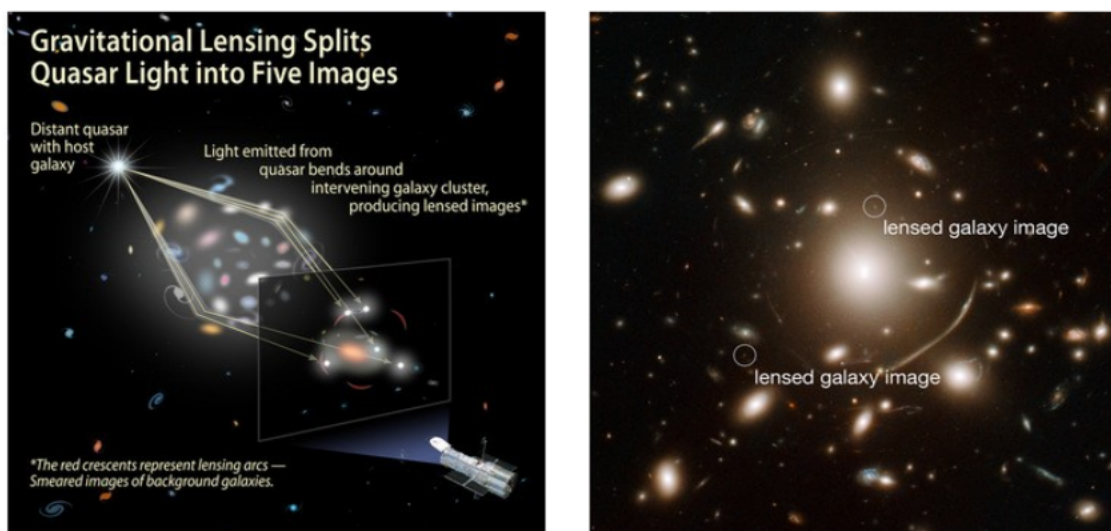


Figure 1.2 – Left: schematic of gravitational lensing, taken from [11]. The image of a quasar is splitted in five images due to gravitational lensing. Right: a galaxy image is deviated due to the gravity of the massive cluster of galaxies (Abell 383) in front of it.

II.4 Cosmic Microwave Background (CMB)

Photons forming the cosmic microwave background were emitted when matter and radiation separated. They contain information of the Universe state at the time of their last scattering. The photons observed today were emitted in the surface of a sphere centered around us and with a radius corresponding to the distance travelled by the photons decoupled from the plasma, 380000 years after the Big Bang. Before that, the photons were in equilibrium with the plasma, forming a black body radiation with a temperature of 3000 K. This corresponds today to a temperature $T = 2.725 \pm 0.001$ K as a result of the expansion of the Universe [12]. Density

Chapter 1: Theoretical context

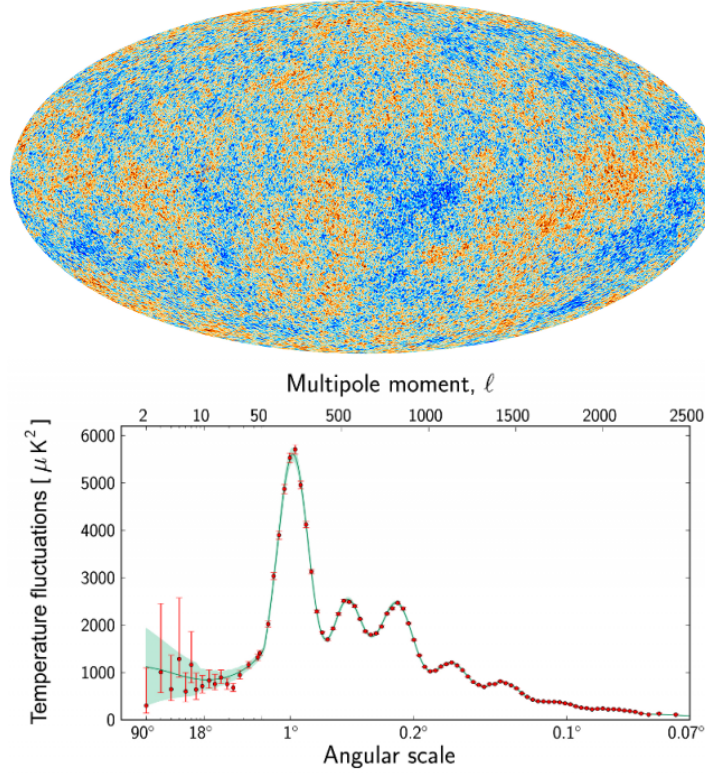


Figure 1.3 – Top: fluctuations of the CMB radiation measured by Planck [3]. The different colors represent relative fluctuations of temperature $\Delta T/T$. Bottom: the power spectrum measured by Planck, showing the fluctuations in temperature.

inhomogeneities of matter in the primordial plasma correspond to temperature anisotropies in the CMB spectrum as shown in Fig.1.3. Many experiments have been built to measure as precisely as possible these anisotropies of primordial origin, the most complete survey being that of Planck [3]. These perturbations come from oscillations produced by the balance between gravitation (which tends to deepen the gravitational potential wells) and the radiation pressure (which tends to smooth the density). The amplitude and frequency of these oscillations are very sensitive to the Universe content. The temperature fluctuations $\frac{\delta T}{T}$ are decomposed into a spherical harmonic basis and their correlations are given by:

$$\frac{\delta T}{T}(\theta, \phi) = \sum_l \sum_m |a_{l,m}|^2, \text{ and } C_l = \langle |a_{l,m}|^2 \rangle = \frac{1}{2l+1} \sum_m |a_{l,m}|^2 \quad (1.10)$$

where l is related to the angular scale and C_l is a function of l , giving information of the variance of temperature between two points separated by an angle corresponding to the considered multipole. The quantity $l(l+1)C_l/2\pi$ is shown in Fig.1.3 as a function of l . High l values are equivalent to small angular scales and vice versa. The peaks are called acoustics and correspond to hot zones separated by a characteristic angular distance. The exact shape of the spectrum depends on the different cosmological parameters. These are well constrained by the Planck measurements [3], via a maximum Likelihood fit with the theoretical spectrum of the Λ CDM model. Peak amplitudes depend on Ω_m and the amplitude ratio between the first peak and the one with the highest dipolar momentum l depends on Ω_b . In this way, the constraints of Planck measurements, as given in section I.2.4, are:

$$\Omega_k = 0.0008_{-0.0039}^{+0.0040}, \Omega_b h^2 = 0.02226 \pm 0.00023 \text{ and } \Omega_{CDM} h^2 = 0.1186 \pm 0.0020 \quad (1.11)$$

II.5 Baryonic Acoustic Oscillations (BAO)

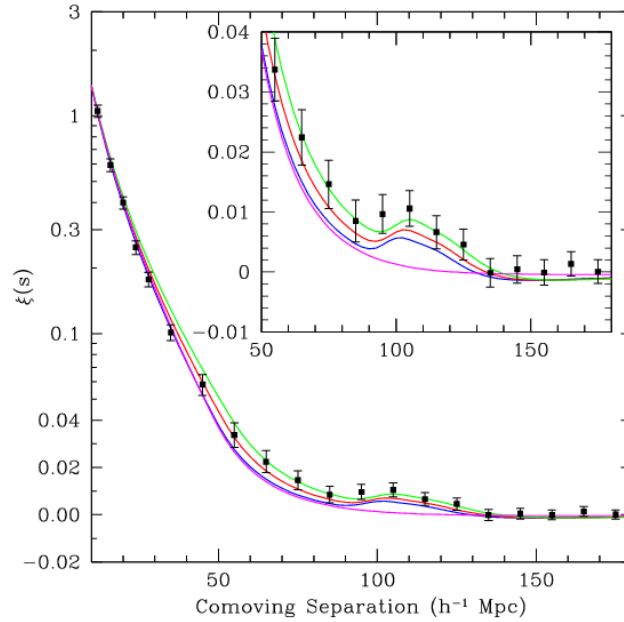


Figure 1.4 – Correlation function between two galaxies as a function of the comoving distance between them in the SDSS LRG galaxy sample, from [13]. The lines correspond to different dark matter density ($\Omega_m h^2 = 0.12$ in green, 0.13 in red and 0.14 in blue, all with $\Omega_b h^2 = 0.024$). The magenta line without a peak is the correlation function for $\Omega_b = 0$ i.e an Universe without baryons.

CMB fluctuations are due to density fluctuations in the primordial plasma [3]. Those oscillate under the influence of radiation pressure (which dilutes it) and gravitational attraction (which compress it). It generates pressure waves. This plasma vanished when the Universe was 380000 years old, creating a resonance at the multipole l value associated to the size of the acoustic horizon, i.e the comoving distance that an acoustic wave can travel between the Big Bang and recombination. With the Universe expansion, the actual radius of these waves increases whereas dark matter stays still at the center of the overdensity. For each overdensity region, a spike due to dark matter surrounded to a sphere corresponding to gas is observed. Throughout the Universe evolution, the matter trapped in these overdensities collapse under their own gravity, giving birth to galaxies. Today, the maximum l value corresponds to a distance of 500 million light years, and therefore there is a larger probability to find two galaxies at this distance relative to other distances. This was confirmed by the Sloan Digital Sky Survey in 2005 [14], as shown in Fig.1.4. The peak, observed in this figure, is called Baryon Acoustic Oscillation peak and helps to constrain cosmological parameters.

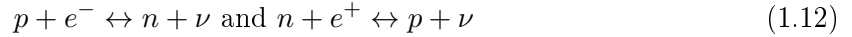
II.6 Big Bang Nucleosynthesis (BBN)

The Big Bang Nucleosynthesis describes the production of light nuclei in the first 20 minutes of the Universe [15]. It depends mainly on the neutron-proton and baryon-photon ratios.

The first ratio can be determined with Standard Model physics and the thermal history of the Universe, in the first seconds after the Big Bang. Neutrons and protons were in thermal

Chapter 1: Theoretical context

equilibrium via following reactions:

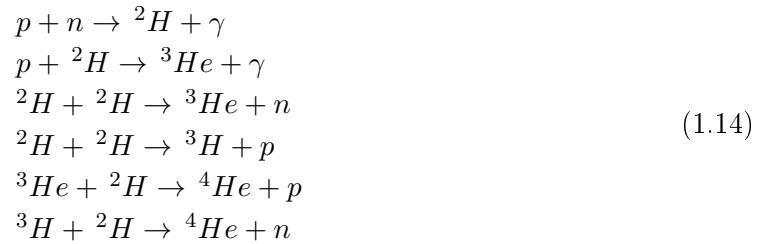


As long as the matter density was large enough, the density ratio between protons and neutrons was fixed by the temperature:

$$\frac{n}{p} \propto e^{-\frac{Q}{kT}} \quad (1.13)$$

where $Q = 1.293$ MeV is the mass difference between neutron and proton and k is the Boltzman constant. Reactions (1.12) occur until a critical temperature of $T = 0.7$ MeV, called freeze-out, when reactions are stopped, i.e the ratio is $n/p \approx 1/6$. Neutron decays reduce this ratio to $\approx 1/7$.

The initial neutron-proton ratio and the baryon-photon ratio then determine the abundance of light elements after the BBN. The main reactions were:



Despite their low probability, few productions of ${}^7\text{Li}$ and ${}^7\text{Be}$ might have occurred. Most fusion chains at this time finished with the ${}^4\text{He}$ nuclei, as a result of the non existence of a stable nuclei above helium. More the baryon-photon ratio is high, more the reaction to produce deuterium $p + n \leftrightarrow {}^2\text{H} + \gamma$ is efficient and eventually the transformation into ${}^4\text{He}$ can be made. This is why the deuterium is a strong probe to measure the baryon-photon ratio.

The abundance of these elements is shown in Fig.1.5. They can be expressed as a function of the photon density $\eta = n_A/n_\gamma$, which is a conservative quantity as a function of the time. It is common to use the ratio $\eta_{10} = 10^{10}n_A/n_\gamma$ because of the weakly value of η . The measurement of the different element abundances allows to constrain the η_{10} value and thus to deduce, knowing the photon density, that: $0.012 < \Omega_b h^2 < 0.025$ [16]. It corresponds to $\Omega_b \simeq 0.0457 - 0.0544$ (for $h = 0.678$ [3]). This $\Omega_b < \Omega_m$ value implies that there exists non-baryonic dark matter.

II.7 Combination

Each probe presented previously allows to constrain one or several cosmological parameters. Their combination allows to determine precisely the Universe content in energy and matter. In Fig.1.6, the different constraints introduced before are presented in the (Ω_m, ω) plane, where $\omega = \frac{p}{\rho}$ with p the pressure and ρ the energy density. The grey zone corresponds to the combination of results obtained by supernova studies (blue area), those obtained by BAO (green area) and those from CMB (red area). The CMB can constrain both Ω_m and Ω_Λ in the same proportion. In contrast the BAO results constrain more precisely Ω_m . The supernovae can constrain the sum $(\Omega_m + \Omega_\Lambda)$. All actual measurements [4] are resumed as: $\Omega_b h^2 = 0.02226 \pm 0.00023$, $\Omega_{CDM} h^2 = 0.1186 \pm 0.0020$ and $\Omega_\Lambda h^2 = 0.3182 \pm 0.055$.

III Dark matter properties

The difference between Ω_b and Ω_m values derived from the measurements presented in section II leads to postulate the presence of dark matter, with density $\Omega_{CDM} = \Omega_m - \Omega_b \simeq 0.258$.

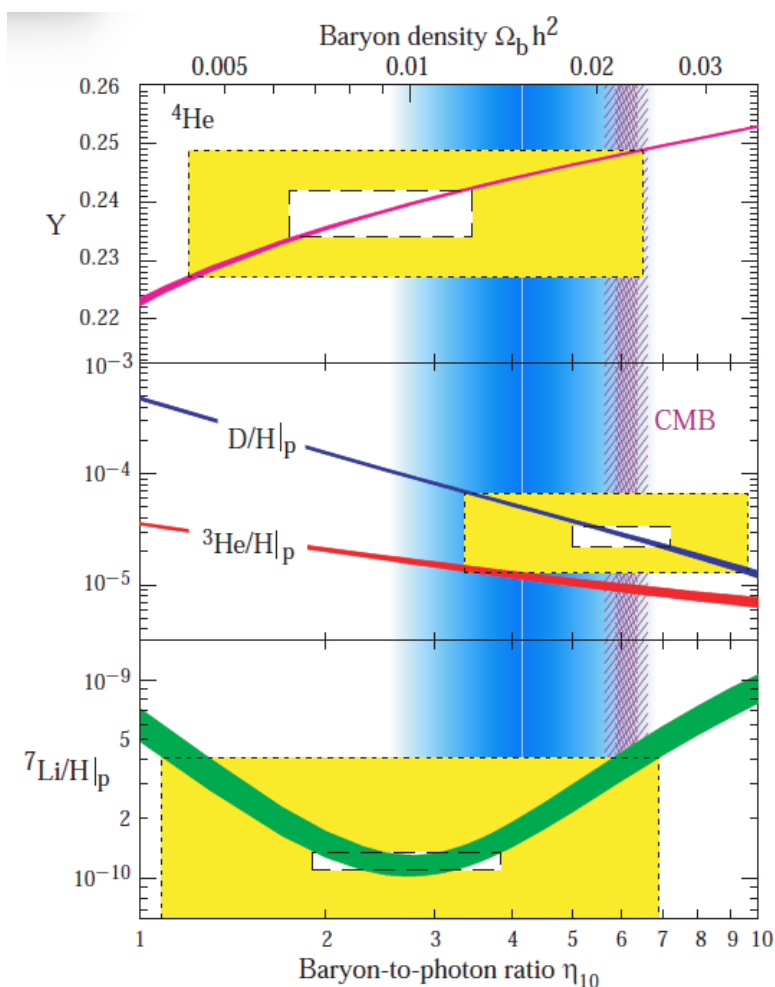


Figure 1.5 – Abundance of different nuclei as a function of baryon-photon ratio η_{10} as predicted by the Big Bang Nucleosynthesis theory. Boxes indicate the observed light element abundances (in white, 2σ statistical errors and in yellow $\pm 2\sigma$ statistical and systematic errors added). The vertical pink line corresponds to the CMB measurement of the cosmic baryon density $\Omega_b h^2$ [16].

From now on, χ is used as the symbol for dark matter particle.

III.1 Structure formation constraints

Two scenarii are possible to explain the evolution of the initial overdensities to the structures observed nowadays [18]. In the first scenario, called top-down, dark matter is relativistic, i.e hot, when structures are in formation. In this case, the radiation pressure erases the overdensities of matter at small scales. In the second scenario, called bottom-up, gases and stars create small structures that only after merge into larger structures. The study of structure formation favours this bottom-up scenario, leading to a Cold Dark Matter, ie in the case of thermally produced particles, to non-relativistic and therefore massive candidates [19].

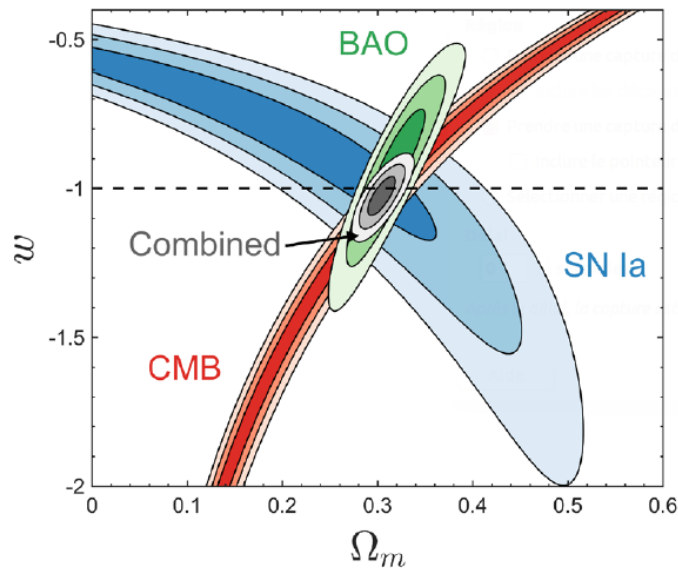


Figure 1.6 – Constraints on cosmological parameters using SNIa (in blue), BAO (in green) and CMB (in red) observations. It is expressed as a function of the matter density Ω_m and the equation of state parameter w . Contours correspond to 68.3 % C.L., 95.4 % C.L. and 99.7 % C.L. of the analysis with the assumption of a flat Universe [17].

III.2 Particle properties

III.2.1 Non-baryonic nature

The cosmological observations presented in section II show that around 85 % of massive matter in the Universe is non-baryonic. Dark matter thus cannot be composed to ordinary matter, like protons and neutrons. Known particles can not explain the different evidences described in section II. Massive astrophysical objects, compact and lightless⁷, like black holes or brown dwarves have been postulated. They have been searched for a while with experiments like EROS or MACHO [20] without explaining the dark matter density. It means that a particle postulated from beyond the Standard Model is required.

III.2.2 Density in the Universe

A valid dark matter particle should have a cosmological abundance of $\Omega_{CDM} \simeq 0.258$. A dark matter model is considered to be satisfactory if it offers a producing mechanism which can reproduce this density. This constraint is important to discriminate possible candidates.

III.2.3 No electric charge

Dark matter is, by definition, not sensitive to electromagnetic interaction, i.e it does not radiate or absorb it. Consequently, its existence as charged particles is strongly improbable. Particles similar to massive hydrogen atoms have been postulated [21] but observations like the stability of neutral interstellar gases [22] or the absence of this type of element in Earth's atmosphere [23] reject this hypothesis. Nevertheless, it has to be noted that some researchs evoke dark

⁷They are called MACHOs (Massive Astrophysical Compact Halo Objects).

matter particles with an infinitesimal charge, inferior to one [24], which could not participate in the BAO at the recombination era.

III.2.4 No strong interaction with ordinary matter

Strong constraints exist on the interaction between dark matter and nucleons. It is expressed as a spin independent cross-section with nucleon, written $\sigma_{\chi N}$. Astrophysical observations like galactic disk stability constrain high values of $\sigma_{\chi N}$: high frequency of interaction between baryonic disk of galaxies and dark matter leads to their destruction. Consequently, for the Milky Way galaxy: $\sigma_{\chi N} < 5 \times 10^{-24} (m_{\chi}/\text{GeV}) \text{ cm}^2$ with m_{χ} the dark matter particle mass. Weak cross-sections are probed by underground direct detection experiments, which aim to measure nuclear recoils generated by elastic scattering of dark matter particles on nuclear target. They will be discussed later in section IV.3.

Galaxy clusters in dissociative fusion, like the Bullet cluster, show no collisional behavior for dark matter. In contrast to hot gases, dark matter is not stopped during the collision, and is separated from the ordinary matter as shown in Fig.1.7. This constrains strongly self-interacting $\sigma_{\chi\chi}$ cross-sections. The combination of gravitational lensing and X-ray emission studies with theoretical model and numerical simulations of the Bullet cluster allows to established a limit on the dark matter cross-section $\sigma_{\chi\chi}$ (in [25], the constraint corresponds to $\sigma/m < 1.25 \text{ cm}^2 \cdot \text{g}^{-1}$).



Figure 1.7 – The Bullet cluster, observed by NASA [26]. This cluster was formed after the collision of two large clusters of galaxies. Most of the matter in the clusters (blue) is clearly separated from the normal matter (pink), giving direct evidence that nearly all of the matter in the clusters is dark. The distribution of hot gas is inferred from X-ray measurements. The blue regions provided from studies of gravitational lensing, which deforms the shape of galaxies behind the cluster.

III.2.5 Long lifetime

Dark matter must be stable at the scale of the age of the Universe in order to fit with the observations. Searching particles of the Standard Model like photons or electrons derived from dark matter annihilation allows to strongly constrain its lifetime. While the dark matter does not emit electromagnetic rays, an upper limit on its decay can be calculated by study the

Chapter 1: Theoretical context

collision of astrophysical objects. Actual constraints are around $\tau_\chi > 10^9 \text{ Gyr}$ [27]. They are nevertheless model dependent.

III.2.6 Cold dark matter

The freeze-out starts when the interaction rate of the dark matter particles with the plasma becomes inferior to the expansion rate of the Universe. The overdensities of the primordial plasma and the accumulation of matter around them by gravitation allow to initiate the training process of large structures of the Universe. After decoupling, dark matter spreads until gravitational collapse of overdensities, i.e until the beginning of the training process, after the recombination. The distance traveled by dark matter particles is called free streaming, and defines a characteristic scale fall short of the vanishing of fluctuations (damping effect [28]). Only surviving fluctuations can collapse and form structures, showing the influence of kinetic properties of dark matter on the training process of the Universe.

Dark matter candidates can be ordered in three groups, as a function of their decoupling with primordial plasma.

The first class is the hot dark matter, ultra-relativistic after the decoupling. Free streaming length is important, and density perturbations smaller than super-galaxy cluster scales (mass equivalent to $M \approx 10^{15} M_\odot$) vanished [29]. The training process which follows is a top-down one: first super clusters form themselves, then galaxies and cluster are created by fragmentation. This scheme is nevertheless contradicted by observations, which indicate galaxies are the first to be formed [29] (see section III.1).

On the contrary, cold dark matter is non relativist after the decoupling and its free streaming length is negligible. Perturbations survive until small scales ($M \approx 10^{-6} M_\odot$ [30]). In this scenario, the training process which follows is bottom-up: the highest structures are formed by successive accretions of smaller objects. Numerical simulations realized in the context of cold dark matter, like Millenium simulation [31], are in excellent agreement with galaxy distribution measurements obtained by SDSS [14] or 2dFGRS [32]. This is why the cold dark matter model is considered as the dominant paradigm in this domain.

Finally, the last class corresponds to warm dark matter, characterized by a free streaming length in the range of smaller galaxies (mass equivalent to $M \approx 10^9 M_\odot$ [28]). The training process at large scales is similar to the cold dark matter one, and only the behavior at galactic scale is different. This model can resolve some difficulties of cold dark matter at small scales but is strongly constrained by many cosmological observables.

To conclude, the different astrophysical and cosmological observables encourage the dark matter description in the form of a non-baryonic particle, cold and stable, insensitive to strong interaction and electromagnetism. These observations are the origin of the cosmological model of the Universe Λ CDM.

III.3 WIMP miracle

The WIMP (Weakly Interacting Massive Particle) is a dark matter particle that is massive, neutral, stable, weakly interactive, and therefore non relativistic. In the earlier Universe, dark matter particles annihilate with their antiparticles to other particle-antiparticle pairs: $\chi + \bar{\chi} \rightarrow p + \bar{p}$. Progressively, WIMP do not find their antiparticles as the Universe expands, and their population undergoes a chemical freeze-out. Their comoving density remains constant and

becomes a relic from this period. This can be described by the Boltzmann equation:

$$\frac{dn_\chi}{dt} + 3Hn_\chi = - \langle \sigma v \rangle (n_\chi^2 - (n_\chi^{eq})^2) \quad (1.15)$$

where n_χ is the WIMP density, H is the Hubble constant, $\langle \sigma v \rangle$ the WIMP annihilation cross-section averaged over all WIMP velocities, and n_χ^{eq} is the WIMP density at thermal equilibrium. At a temperature $T^3 \propto n_\chi^{eq}$, the density of photons is equivalent to the density of WIMP. The term $3Hn_\chi$ becomes dominant and the freeze-out occurs during the exponential decreasing of the comoving density. In Fig.1.8, the density of WIMP evolution is drawn as a

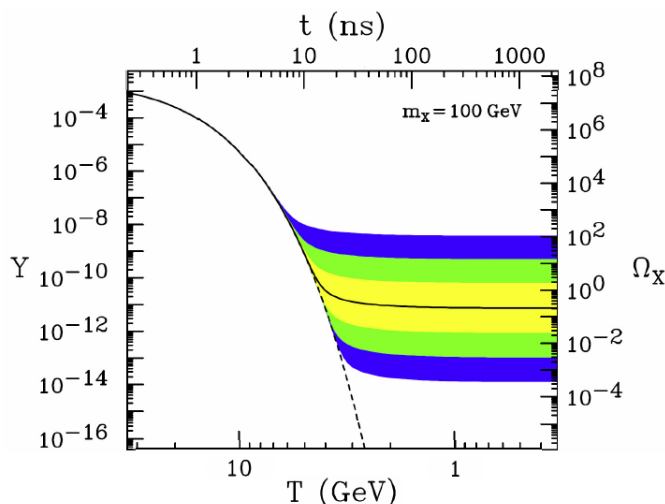


Figure 1.8 – Comoving density as a function of the temperature and resulting thermal relic density for a WIMP mass of $100 \text{ GeV}/c^2$. The annihilation cross-section corresponding to the correct relic density is the solid contour and the shaded zone are for cross-sections which differ by 10 , 10^2 and 10^3 from this value. The density of particle that remains in the thermal equilibrium is the dashed curve [33].

function of the Universe temperature T . The WIMP freeze-out is around $T \sim m_\chi/20$. Varying the annihilation cross-section has a strong effect on the temperature of the freeze-out. The relic dark matter density can be determined knowing that $n_\chi \langle \sigma v \rangle = H$ at the freeze-out condition [33]:

$$\Omega_\chi h^2 \simeq \frac{3 \times 10^{-27} \text{ cm}^3 \cdot \text{s}^{-1}}{\langle \sigma v \rangle} \quad (1.16)$$

This relation is not dependent of the WIMP mass. With a weak interaction cross-section around 10^{-38} cm^2 , the annihilation cross-section is $\langle \sigma v \rangle \sim 10^{-26} \text{ cm}^3 \cdot \text{s}^{-1}$. The resulting value of $\Omega_\chi h^2$ is ~ 0.1 , corresponding to the dark matter relic density in the Universe $\Omega_{CDM} h^2 = 0.1186$ [3]. The fact that particle physics considerations alone can give the correct order of magnitude for WIMP mass density is referred as the WIMP miracle and is a strong motivation to look for these particles.

III.4 Dark matter candidates

III.4.1 Massive Astrophysical Compact Halo Objects (MACHOs)

Massive objects in the Universe, emitting no light could be dark matter (MACHOs). They are sufficiently massive to have a gravitational effect around them. Some objects are envisaged:

Chapter 1: Theoretical context

black holes, white dwarves, neutron stars, hydrogen gas clouds. As mentioned previously (section III.2.1), dedicated experiments try to measure the number of these objects to determine if it could be enough to explain dark matter evidences. It is the case for EROS [20] and MACHO [34]. EROS concluded that the contribution of MACHOs to the mass of the galactic halo can not exceed 8 % while MACHO has put an upper limit of 40 %. Thus, it consolidates the need for non-baryonic dark matter.

III.4.2 Axions

To resolve the Strong CP problem of the Standard Model, the axion particle has been postulated [35]. Indeed, the lagrangian describing strong interaction has a term which violates the CP symmetry (charge parity). Such violation should produce measurable effects, like electric dipolar moment of the neutron ($d_e \sim 10^{-16} e \text{ cm}^2$), where e is the elementary charge. But actual experimental constraints impose $d_e < 2.9 \times 10^{-6} e \text{ cm}^2$. Introducing a new global symmetry in the Standard Model, which spontaneously breaks, allows to cancel the problematic term in the lagrangian. A broken symmetry implies a new particle, in this case the axion. It weakly interacts and should be light. With astrophysical constraints, the axion mass is restricted to be less than $m_a < 10 \text{ meV}$. In the case of a non-thermal production in the Universe, axions could be warm dark matter.

III.4.3 WIMP

They are main candidates of dark matter. Different theories predict a mass between $1 \text{ GeV}/c^2$ and $1 \text{ TeV}/c^2$ [4]. They couple to ordinary particles via weak interaction. Many particles are called WIMP as it is a generic term. The two main WIMP kind investigated are the following:

Neutralino

In the supersymmetry (SUSY) theory, each particle of the Standard Model (SM) is associated to a super-particle. Each fermion is coupled to a SUSY boson, and inversely, each SM boson is coupled to a SUSY fermion. This theory resolves the gauge hierarchy problem and allows to unify interactions at the Planck scale. The supermassive particle should ideally have identical mass that its SM partner but as no superparticle has been observed, this symmetry must be broken and SUSY particles be heavier. These new particles are searched at the LHC, at CERN. The simplest extension of this theory is the MSSM (Minimal Supersymmetric Standard Model), where most partners have similar masses, and which contains a second neutral scalar Higgs boson in addition. The non observation of proton decay indicates that a new quantum number, the R-parity, prevents the SUSY particle decay in SM particles. The lightest supersymmetric particle (LSP) is thus stable. Usually, the neutralino is this LSP, a mixing of SUSY partners of gauge boson and Higgs bosons. Moreover, the neutralino can interact only via weak interaction which makes it a serious WIMP candidate. The MSSM doesn't predict precisely its mass because of the high number of free parameters but this mass is constrained to be below $\sim 10 \text{ TeV}/c^2$ by theory and above $10 \text{ GeV}/c^2$ by experimental searches, in particular at LHC [36] (see section IV.1). In other extensions of SUSY, more freedom is allowed to SUSY particle masses and more Higgs doublets are allowed, relaxing these bounds.

Kaluza-Klein boson

In the extra-dimension theories, there are one or several spatial dimensions. The Universal Extra Dimension UED presents one additional dimension with a compacted size R . In this case, quantum fields of SM particles propagate in this extra dimension, with an impulsion of

$p^2 \sim 1/R^2$. Each SM particle has an infinity of partners, called Kaluza-Klein particles, and each is associated to a mass:

$$m^2 = \frac{n^2}{R^2} + m_0^2 \quad (1.17)$$

with n the mode number (i.e the number of extra-dimensions) and m_0 the SM particle mass. Partners have the same spin that SM particles. A discrete symmetry, called Kaluza-Klein parity, stabilizes the lightest Kaluza-Klein particle, called LKP. Its mass depends on the unknown compactification radius R and must be between 600 GeV and 1.4 TeV. The LHC searches for this type of particles have resulted in bounds: $1.25 \text{ TeV} \leq R^{-1} \leq 1.5 \text{ TeV}$ [37].

IV Dark matter detection

The cosmological observations at different scales lead to conclude on the existence of dark matter (DM). The challenge remains to detect the WIMP as a dark matter particle. For this, three methods can be used, as shown in Fig.1.9. Note that these processes can depend on the

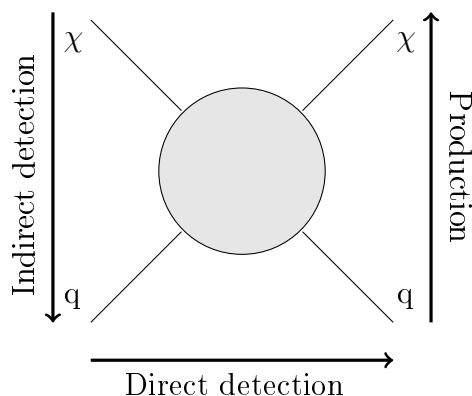


Figure 1.9 – Different processes for the detection of WIMP. The symbol χ represents a dark matter candidate and the symbol q a SM particle. The circle corresponds to the interaction between these particles. From left to right, direct detection uses the scattering of WIMP on SM particles. From top to bottom, the annihilation of dark matter particles is used in indirect detection. From bottom to top, the production of dark matter particles is searched in colliders.

WIMP spin. In this way, results are often presented in two forms: one is spin-dependent and the second is spin-independent, depending on the nature of the interaction.

IV.1 Production in a collider

In colliders, like the LHC, proton-proton collisions can produce dark matter particles in addition to other SM particles (quarks, photons, ...). Two of the LHC experiments, ATLAS and CMS, try to constrain Standard Model parameters and study new physics. The main searches of supersymmetry involve the measurement of missing energy and momentum associated to the escape of the LSP like neutralinos. The observations are compared to the different theories. In the context of effective theories [38], it is possible to reduce the model dependence to a minima, allowing to compare the LHC results to other detection method results. Thus, for spin-dependent interaction, ATLAS and CMS have strong constraints on DM-nucleon cross-sections for m_χ between 1 GeV and 1 TeV [39]. For spin-independent cross-sections, it is for

Chapter 1: Theoretical context

low-mass WIMP (6-10 GeV) that they are more competitive than direct detection experiments. It has to be noted that identify a missing energy do not allow to necessarily confirm the existence of a dark matter particle. Although the LHC can discover new invisible particles, it cannot prove that they are stable at cosmological scale. It can just consolidate the presence of a neutral and stable particle that might have even decayed outside the detector. As shown in Fig.1.10, results can be expressed in the space parameter (m_χ, σ_{SI}) to be compared with direct detection experiments like LUX (in green), Panda-X (in purple) and CDMSlite (in blue). Note that such results are strongly model dependent.

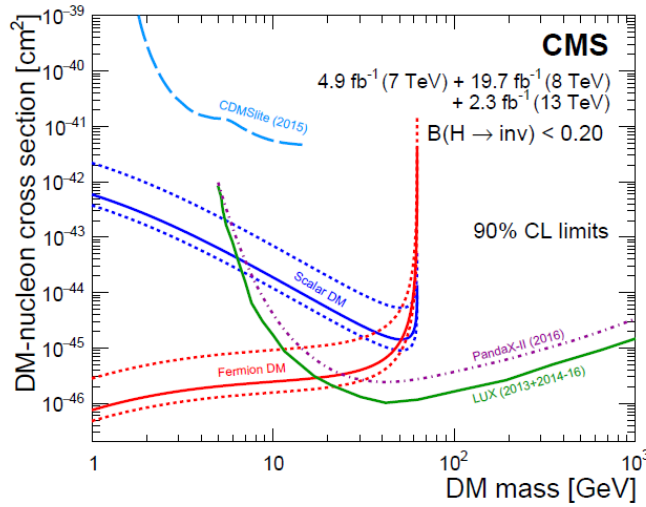


Figure 1.10 – Limits on the spin-independent WIMP-nucleon cross-section in Higgs-portal models, assuming a scalar or vector dark matter particle. Dashed lines correspond to exclusion limit at 90% C.L. associated to different values for nuclear form factor F (see section V.4). Figure taken from [40].

IV.2 Indirect detection

This method consists to observe the radiations of Standard Model (SM) particles produced by the decay or annihilation of dark matter, or their secondary effects. The flux of these radiations are proportional to both the annihilation rate and the square of the dark matter density. These searches focus on regions where the dark matter density is more important, like in the galactic halo, the center of the Sun and regions with a strong gravity. Three main radiations can be interesting: neutrinos (IV.2.3), γ -rays (IV.2.2) and antimatter (IV.2.1). An excess flux with respect to predictions from Standard Model physics processes could correspond to dark matter annihilation.

IV.2.1 Antimatter

Experiments like AMS [41] measure the excess of antimatter (positrons, antiprotons, antideuteron) with respect to theoretical expectations. Indeed, dark matter annihilation can

produce antimatter cosmic-rays as positrons, antiprotons and antideuteron. By studying the positron spectra, the experiment AMS-02 has identified an excess that could be attributed to a dark matter particle with a mass around $1 \text{ TeV}/c^2$ [41] (Fig.1.11). But it could be also explained by an astrophysical object such as a pulsar [42].

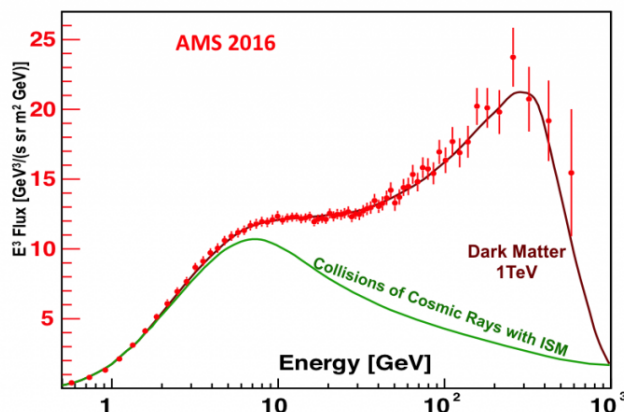


Figure 1.11 – The current AMS positron flux measurement compared with theoretical models [43]. The spectrum (dot red) increases as expected (model in green for the rate expected from cosmic-rays collisions). The points follow the dark matter prediction for a mass of $1 \text{ TeV}/c^2$ (red line). An alternative explanation for this result is that this rise and drop off may come from new astrophysical phenomena such as pulsars.

IV.2.2 γ -ray telescopes

Photons can be produced by dark matter annihilations: $\chi\chi \rightarrow \gamma\gamma$. Earth-based γ -ray telescopes like H.E.S.S. [44] detect the Cerenkov radiation from the electromagnetic cascade induced by the photons in the atmosphere, in the energy range from few tens of GeV/c^2 to tens of TeV/c^2 . With a network of telescopes, the photon direction can be measured accurately. In this way, the experiment can focus on a region of the Universe with a theoretical high density of dark matter. Also spatial experiments, like Fermi-LAT [45], measure the gamma flux in the E_γ range from 20 MeV to more than 300 GeV. The expected experimental signal for a dark matter particle will be a ray in the energy spectrum, directly correlated to the DM mass in the case of a primary reaction. In the case of secondary effects, it is expected to have a continuum in this energy spectrum.

The strongest constraints are obtained by observing dwarf spheroidal galaxies which have a theoretical high dark matter density and therefore reduced backgrounds. A comparison between the two collaboration results is shown in Fig.1.12 (left). Note that results are dependent of the chosen dark matter halo (in this case, an Einasto profile [46]).

IV.2.3 Neutrino telescopes

A dark matter particle passing through a massive astrophysical object can be trapped there by gravitational effect. These trapped WIMP can annihilate themselves by: $\chi\bar{\chi} \rightarrow \nu\bar{\nu}$ and the neutrinos can escape the astrophysical object. ANTARES [47] and IceCube [48] experiments study neutrinos providing from high density DM regions (i.e from the Sun) by charged current interaction ($\nu_\mu + A \rightarrow \mu + X$) inside the detection medium. The Cerenkov light allows to identify the produced muon. The emission gives the direction of the particle and allows to discriminate

Chapter 1: Theoretical context

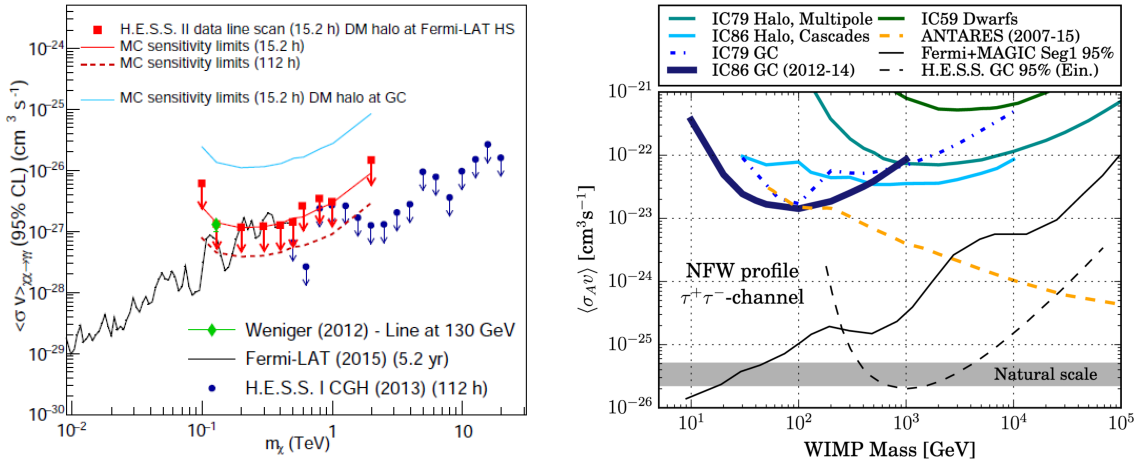


Figure 1.12 – Left: dark matter annihilation cross-section $\langle \sigma v \rangle$ limits at 95% C.L. (red points) between 100 GeV and 2 TeV, using an Einasto profile as DM halo model. By considering the DM halo at the galactic center, the extracted limit becomes the blue line. Blue and black points are results from H.E.S.S.-I and Fermi-LAT. Figure taken from [46]. Right: annihilation cross-section as a function of the WIMP mass, using a NFW profile dark matter halo. Limits of IceCUBE are drawn and compared with previous limits of the experiment, ANTARES results, γ -ray searches from the dwarf galaxy Segue 1 by FermiLAT+MAGIC and limit obtained from the galactic center by H.E.S.S. Figure taken from [46].

atmospheric neutrinos from those coming from the Sun. The dark matter density trapping in the Sun is correlated to its interactions with hydrogen atoms. Fig.1.12 (right) shows the results of the IceCUBE experiment as well as those of the ANTARES collaboration. A comparison with some γ -ray searches is also shown.

The indirect detection allows to determine properties of dark matter, as its velocity, mass, density, annihilation cross-section, but it depends strongly on the density profile of dark matter inside a galaxy.

IV.3 Direct detection

The third method to search for dark matter is the direct detection. As the solar system moves inside the dark matter galactic halo of the Milky Way, this induces a wind of DM particles on Earth, with a flux of 10^5 particles/cm². Detecting elastic scattering of these particles on nuclei of a detector based on Earth is difficult, due to their weak coupling with ordinary matter. This type of detection is dependent on the DM velocity distribution, its local density and its coupling with matter. The direct detection methods will be discussed in section V.

IV.4 Complementarity

The three detection technics presented here are complementary since they give different informations about dark matter particles.

- Searches at colliders can study DM properties such as its neutrality, spin or mass. They are sensitive to different models of DM particles. Contrarily to the other approaches, they are not able to determine if the particle is either stable or long-lived, due to the timescales relevant to the detectors (~ 100 ns).
- Indirect detection is dependent of the dark matter interactions with all SM particles. This approach can determine the dark matter density in galaxies, its annihilation cross-section and also the DM particle mass. Understanding the astrophysical backgrounds is an important issue.
- Direct detection is sensitive to the particle mass and scattering cross-sections with protons and neutrons. This approach requires a careful control of low-energy backgrounds.

Using these different approaches allow to constrain the characteristics of the dark matter.

V Direct detection

This section describes in more details direct detection methods. The elastic scattering of a dark matter particle with a nucleon is observed as the production of a recoil of a nucleus⁸ inside a detector. The WIMP-nucleon cross-section being weak, the event rate is very low and the procedures to detect it have to be adapted accordingly. The operation of WIMP detectors in an underground laboratory using all the typical precautions of rare event searches (material selection, shielding) is required to protect itself from cosmic-rays muons. Indeed, they can induce neutrons in the background, which have the same signature as WIMP (a nuclear recoil) in detectors. Furthermore, the background mainly consists of electronic recoils from photons (γ -ray radiation) or electrons (β radiation). Any successful method allowing to discriminate between these two types of recoil energy depositions automatically reduces the background significantly. Finally, a long exposure is useful in regard to the weak expected interaction rate.

V.1 WIMP-matter interaction

WIMP are non-relativistic, they have elastic scattering with ordinary matter. The energy spectrum associated to the nuclear recoil based on [49] is:

$$\frac{dR}{dE_R} = \frac{\rho_0}{2m_\chi m_r^2} (\sigma_0^{SI} F_{SI}^2(E_R) + \sigma_0^{SD} F_{SD}^2(E_R)) \int_{v_{min}} \frac{f(v)}{v} d^3v \quad (1.18)$$

where ρ_0 is the local dark matter density, m_χ is the WIMP mass, $m_r = m_\chi m_N / (m_N + m_\chi)$ is the reduced mass of the WIMP-nucleon system, m_N is the target nucleus mass, σ_0^{SI} is the scalar interaction term (independent of the spin), σ_0^{SD} is the axial interaction term (dependent of the spin), $v_{min} = \sqrt{2E_R / m_\chi r}$ is the minimum velocity of a WIMP to generate a nuclear recoil of energy E_R and $F_{SI,SD}$ is the relevant form factors as described in [49]. In the velocity formula, $r = 4m_r / (m_N + m_\chi)$.

⁸It is called a nuclear recoil.

Chapter 1: Theoretical context

V.1.1 Spin-independent cross-section

The spin-independent cross-section of a WIMP to a nucleus A_ZX derives from the scalar and vector couplings between WIMP and quarks. It is given by [50]:

$$\sigma_{\chi-A}^{SI} = \frac{4\mu_A^2}{\pi} (Zf_p + (A-Z)f_n)^2 \quad (1.19)$$

where μ_A is the reduced WIMP-nucleus mass and f_p (f_n) is the effective coupling of scalar interaction on a proton (a neutron). If the diffusion is dominant on quark, $f_p \approx f_n$, which gives:

$$\sigma_{\chi-A}^{SI} = \frac{4\mu_A^2}{\pi} (Af_n)^2 \quad (1.20)$$

The cross-section is proportional to A^2 from the coherent properties of the scattering, favoring heavy target nuclei in direct detection. To compare experiments using different nuclei, it is common to use the WIMP-nucleon cross-section $\sigma_{\chi-n}^{SI}$ corresponding to the case $A = 1$ and $\mu_A = \mu_n$. This leads to:

$$\sigma_{\chi-A}^{SI} = \frac{\mu_A^2}{\mu_n^2} A^2 \sigma_{\chi-n}^{SI} \quad (1.21)$$

with $\sigma_{\chi-n}^{SI} = \frac{4\mu_n^2}{\pi} f_n^2$.

V.1.2 Spin-dependent cross-section

The spin-dependent cross-section $\sigma_{\chi-A}^{SD}$ derives from axial-vector coupling. It is given by [50]:

$$\sigma_{\chi-A}^{SD} = \frac{32}{\pi} G_F^2 \mu_A^2 \frac{J+1}{J} (a_p \langle S_p \rangle + a_n \langle S_n \rangle)^2 \quad (1.22)$$

where a_p and a_n are the effective couplings of axial interactions on a proton and a neutron respectively, G_F is the Fermi constant, $\langle S_{p,n} \rangle$ is the average value of neutron or proton spin in the nucleus and J is the total angular momentum of the target nucleus. There is no dependence on A apart from μ_A in Eq.1.22. There is a strong dependence on the nucleus spin and its origin (neutron or proton). Hence, only target nucleus with an odd number of protons and neutrons have sufficient sensitivity to this interaction. For example, Ge, Xe, Ar and Si⁹ have an even number of protons so they are sensitive to the spin-dependent interaction on neutrons. Isotopes with odd neutron numbers are sensitive to spin-dependent interaction on protons. This is why experiments often quote their spin-dependent results separately for $\sigma_{\chi-p}^{SD}$ and $\sigma_{\chi-n}^{SD}$.

V.2 Theoretical recoil spectrum

Direct detection experiments measure a number of WIMP-scattering events per mass unit and time unit. This rate also depends on the experimental threshold on the recoil energy. The formulation of this rate is described in details by Lewin and Smith [49]. A simplified description is presented here. Using the energy and momentum conservation, the recoil energy of the nucleus is:

$$E_R = \frac{1}{2} r E_i (1 - \cos(\theta^*)) = r E_i \cos^2(\theta_R) \quad (1.23)$$

⁹Used by EDELWEISS or CDMS [51], XENON [52], DarkSide [53] and CRESST [54] experiments, respectively.

Chapter 1: Theoretical context

with $r = 4 \frac{m_\chi m_A}{(m_\chi + m_A)^2}$ (with m_A the target nucleus mass), θ_R (resp. θ^*) the scattering angle in the laboratory (resp. mass center) reference frame. For a given initial WIMP kinetic energy $E_i = m_\chi v^2/2$, the possible recoil energies are $E_R \in [0, rE_i]$ corresponding to the cases $\cos(\theta^*) \in [-1, 1]$. The recoil energy is uniformly distributed along the $\cos(\theta^*)$ range with a probability density $P(E_R) = 1/(rE_i)$. Different E_i values can give the same recoil energy E_R . The smallest initial energy E_i corresponds to the case where the WIMP is back-scattered ($\theta^* = \pi$), thus the minimum initial energy is $E_{i,min} = E_R/r$, corresponding to a velocity $v_{min} = \sqrt{(2E_R)/(m_\chi r)}$. The maximum initial energy E_i yielding a recoil E_R has no limitation linked to the kinematic of the interaction. However, WIMP with velocities beyond the v_{esc} value needed to escape the galactic halo have a very low probability to be detected. This defines a maximum initial energy $E_{i,max} = \frac{1}{2}m_\chi v_{esc}^2$. The recoil energy spectrum is obtained with all these possible E_i values resulting to E_R , weighted by the probability $P(E_R)$:

$$\frac{dR}{dE_R} = \int_{E_{i,min}}^{E_{i,max}} P(E_R) dR(E_i) = \int_{E_{i,min}}^{E_{i,max}} \frac{1}{rE_i} dR(E_i) \quad (1.24)$$

The differential scattering rate per volume unit and mass unit for a WIMP with a velocity v and a cross-section σ is given by:

$$dR = \frac{N_0}{A} \sigma v dn(v) \quad (1.25)$$

with N_0 the Avogadro number, A the atomic mass of the target nucleus and n the number of WIMP per volume unit with velocity v . Here it is assumed that the WIMP velocities in the galactic halo follow a maxwellien distribution:

$$f(\vec{v} + \vec{v}_{Earth}) = \frac{e^{(-\vec{v} + \vec{v}_{Earth})^2/v_0^2}}{k} \quad (1.26)$$

with $v_0 = 220 \pm 20$ km/s the local circular velocity, \vec{v}_{Earth} the Earth velocity with respect to galaxy and k a normalisation factor defined such as:

$$k = \int e^{-\frac{(\vec{v} + \vec{v}_{Earth})^2}{v_0^2}} d^3\vec{v} = 4\pi \int_0^{v_{esc}} e^{-\frac{(\vec{v} + \vec{v}_{Earth})^2}{v_0^2}} v^2 dv \quad (1.27)$$

The WIMP velocity relative to the Sun is the sum of their velocity relative to the galaxy \vec{v}_G and the Earth velocity: $\vec{v} = \vec{v}_G + \vec{v}_{Earth}$. The density of WIMP with a relative velocity to Earth between \vec{v} and $\vec{v} + d^3\vec{v}$ is given by:

$$d^3N = \frac{n_0}{k} e^{-\frac{(\vec{v} + \vec{v}_{Earth})^2}{v_0^2}} d^3\vec{v} \quad (1.28)$$

with n_0 the WIMP density in the galaxy ($n_0 = \rho_0/m_\chi$ where $\rho_0 = 0.3$ GeV/c²/cm³ [3]). Eq.1.25 can be reformulated as:

$$dR = \frac{N_0}{A} n_0 f(\vec{v} + \vec{v}_{Earth}) \sigma v d^3\vec{v} \quad (1.29)$$

If the Earth velocity is neglected ($v_{Earth} = 0$) and the escape velocity is set to infinity ($v_{esc} = \infty$), $k = k_0 = (\pi v_0^2)^{\frac{3}{2}}$, thus the WIMP event rate R_0 is:

$$R_0 = \frac{N_0}{A} \sigma n_0 \int_0^\infty v \frac{e^{-\frac{v^2}{v_0^2}}}{k} d^3\vec{v} = \frac{N_0}{A} \sigma n_0 \frac{2v_0}{\sqrt{\pi}} \quad (1.30)$$

Using Eq.1.24 and 1.30, the theoretical spectrum can then be expressed as:

$$\frac{dR}{dE_R} = \frac{R_0}{E_0 r} \frac{k_0}{k} \frac{1}{2\pi v_0^2} \int_{v_{min}}^{v_{max}} \frac{1}{v} e^{-\frac{(\vec{v} + \vec{v}_{Earth})^2}{v_0^2}} d^3\vec{v} \quad (1.31)$$

Chapter 1: Theoretical context

with $E_0 = m_\chi v_0^2/2$ the most probable WIMP incident energy. In this case, for $v_{Earth} = 0$ and $v_{esc} = \infty$, the value of k is:

$$k_1 = k_0 \left(\operatorname{erf}\left(\frac{v_{esc}}{v_0}\right) - \frac{2}{\sqrt{\pi}} \frac{v_{esc}}{v_0} e^{-\frac{v_{esc}^2}{v_0^2}} \right) \quad (1.32)$$

where $\operatorname{erf}(x)$ is the error function such as:

$$\operatorname{erf}(x) = \frac{2}{\sqrt{\pi}} \int_0^x \exp(-t^2) dt \quad (1.33)$$

The more general expression for $v_{Earth} = 0$ and $v_{esc} < \infty$ is [55]:

$$\frac{dR}{dE_R} = \frac{k_0}{k_1} \left\{ \frac{\sqrt{\pi}}{4} \left[\operatorname{erf}\left(\frac{v_{min}(E_R) + v_{Earth}}{v_0}\right) \operatorname{erf}\left(\frac{v_{min}(E_R) - v_{Earth}}{v_0}\right) \right] - \frac{R_0}{r E_0} e^{-\frac{v_{esc}^2}{v_0^2}} \right\} \quad (1.34)$$

V.3 Inclusion of Earth rotation

The Earth velocity relative to the galaxy is not constant and varies as a function of seasons as:

$$v_{Earth} = 232 + 15 \cos\left(2\pi\left(\frac{t - 152.5}{365.25}\right)\right) \text{ km.s}^{-1} \quad (1.35)$$

with t the time in days since the first of January. The expected modulation of v_{Earth} is 6%. The corresponding annual modulation of the v_{Earth} depends on the energy threshold and may vary from $\pm 3\%$ to $\pm 7\%$ [56].

V.4 Inclusion of form factor

So far, the interaction between the WIMP and all A nucleons of a nucleus has been considered as fully coherent. However, this coherence is lost when wavelength \hbar/q associated to the transferred momentum \vec{q} (where $q = \sqrt{2M_N E_R}$) becomes comparable to the nuclear radius ($r_N \approx A^{\frac{1}{3}}$ fm), i.e when:

$$E_R > \frac{2 \times 10^4}{A^{\frac{5}{3}}} \text{ keV} \quad (1.36)$$

This is around 100 keV in recoil energy for $A \sim 100$. At these energies, the form factor $F(q)$ must be taken into account. The cross-section for $q = 0$ must be corrected by the nuclear form factor:

$$\sigma_{\chi-A}(q) = \sigma_{\chi-A}(0) \times F^2(q) \quad (1.37)$$

For spin-independent interactions, the form factor corresponds to the Fourier transform of the matter distribution in the nucleus $\rho(r)$:

$$F(\vec{q}) = \int \rho(r) e^{i\vec{q}\cdot\vec{r}} d^3\vec{r} \quad (1.38)$$

For the spin-dependent interaction, $\rho(r)$ must be replaced by the spin distribution inside the nucleus. Considering an uniform density distribution and a spherical symmetry with a radius r_N , the form factor for spin-independent interaction can be rewritten as:

$$F(q) = \frac{3[\sin(qr_N) - qr_N \cos(qr_N)]}{(qr_N)^3} \times \exp\left(-\frac{(qs)^2}{2}\right) \quad (1.39)$$

where the s factor takes into account some smoothing of the edge of the nucleus. In the paper of Lewin and Smith [49], $s = 0.9$ fm and r_n is such as:

$$r_n^2 \approx (1.23A^{\frac{1}{3}} - 0.6\text{fm})^2 + \frac{7}{3}(0.52\pi\text{fm})^2 - 5s^2 \quad (1.40)$$

In a simplified spin-dependent model, an incident WIMP interacts with only one nucleon of the nucleus. The situation is more complicated and only a first approximation is applied:

$$F(q) = \frac{\sin(qr_n)}{qr_n} \quad (1.41)$$

V.5 Final theoretical recoil spectrum

The final spectrum is:

$$\frac{dR}{dE_R}(E_R)|_q = \frac{dR}{dE_R}|_{(0)} \times F^2(q) \quad (1.42)$$

with $F^2(q)$ and $\frac{dR}{dE_R}|_{(0)}$ defined in Eq.1.39 and 1.34. The R_0 event rate as defined in Eq.1.30 depends on the WIMP cross-section $\sigma_{\chi-A}^{SI}$ (see Eq.1.21). The velocity distribution is calculated from [55] using as parameters:

- $v_{Earth} = 232$ km.s⁻¹,
- $v_0 = 220$ km.s⁻¹, as the local WIMP density,
- $v_{esc} = 544$ km.s⁻¹,
- $\rho_0 = 0.3$ GeV/c²/cm³ used as the WIMP density.

The effect of annual modulation is neglected at this point.

V.6 Shape of the recoil spectrum

V.6.1 Mass and velocity

Several parameters have a strong impact on the predicted recoil spectrum. The most obvious impact is the WIMP mass. It modifies the shape of the spectrum as well as the expected event rate. As shown in Fig.1.13 (left), the spectrum for a light WIMP is steeper than for heavier WIMP, while the area spectrum doesn't change. On the contrary, the escape velocity has an influence on it, as shown in Fig.1.13 (right). Indeed, the smaller the velocity v_{esc} the less the area is important. Also the shape of the spectrum changes near the maximum recoil energy value.

V.6.2 Target nucleus and form factor

As it was described in subsection V.1.2, the target nucleus is an important choice for a direct detection experiment. As shown in Fig.1.14, different nuclei give different recoil energy spectra. For example, the xenon spectrum is steeper compared to the germanium spectrum.

Chapter 1: Theoretical context

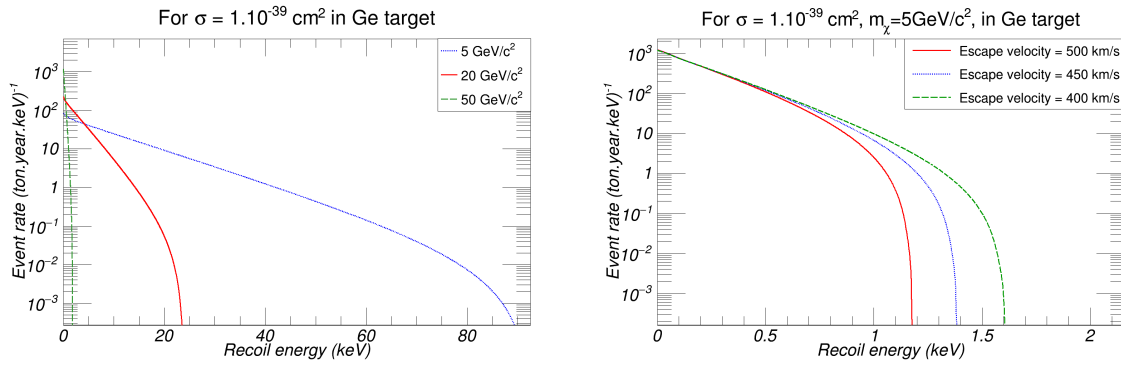


Figure 1.13 – Left: final recoil spectrum for different WIMP masses with the same escape velocity ($v_{esc} = 544 \text{ km/s}$) for Ge nucleus target. Right: final recoil spectrum for a WIMP of $5 \text{ GeV}/c^2$ and different escape velocity values for Ge nucleus target.

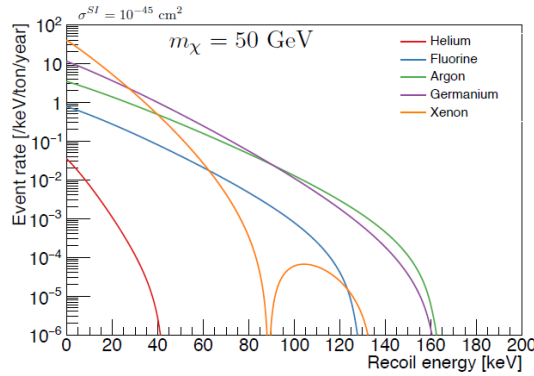


Figure 1.14 – Final recoil spectrum for a WIMP mass of $20 \text{ GeV}/c^2$ with different target nuclei, taken from [57].

V.7 WIMP signature in detectors

Not only the small recoil energies and interaction rates make difficult to detect WIMP dark matter, one also needs to take into account the abundant background from radioactive isotopes in the environment and in the detector itself. Composed mainly from daughter nuclei of the ^{238}U and ^{232}Th chains and from ^{40}K , it produces α -, β -, and γ -rays, as well as neutrons via (α ,n) reactions and spontaneous fissions of uranium. Cosmic-rays also lead to background, the most dangerous being muon-induced neutrons, since the neutral WIMP will, similar to neutrons, only interact with the nucleus (nuclear recoils), while all other backgrounds interact electromagnetically with the atomic electrons (electronic recoils). Taking into account all these conditions, an ideal detector for the direct detection of WIMP should feature:

- A large target mass of an isotope with a high mass number A . Since WIMP direct detection means a rare event search with total rates constrained by experiments to be roughly below 1 event per kg of detector mass and per year, one would need target masses generally far above the kilogram scale in order to gain a sufficient statistic in a reasonable lifetime of the experiment.
- A low energy threshold. Since the WIMP signal is expected to originate from elastic scattering, a featureless, quasi exponentially decreasing energy spectrum will result. The relevant recoil energy region will be typically in the keV range. Therefore, the lower the

energy threshold, the larger will be the size of the signal that will be detected.

- An ultra-low radioactive background since experiments are searching for rare events.
- A discrimination between electronic and nuclear recoils to differentiate background signals from WIMP signal.

In order to reduce the cosmic-ray induced background, dark matter detectors have to be installed in deep-underground laboratories (in tunnels or mines) where the overburden completely eliminates the hadronic component of the cosmic rays, and reduces the muon flux by 5 to 7 orders of magnitude. Most experiments exploit either the phonon, charge or light signal, or a combination of some of those.

To discriminate the WIMP signals from the backgrounds, the detector design is optimized on the basis of the following considerations:

- WIMP interacts with a nucleus. Thus, backgrounds inducing an electronic recoil can be rejected (like β and γ interactions) if they can be identified.
- The mean free path is different for neutrons, β and γ in comparison with WIMP. The ability to reject surface events can reduce significantly the α - and β -backgrounds.
- Due to their low cross-section, WIMP have a weak probability to produce coincidences in detectors. Because of that, an interaction producing nuclear recoils in multiple detectors will be allocated to a neutron.
- Moreover, most experiments are equipped with a muon veto, able to tagged any interaction, induced by an incident muon in the veto, in coincidence with a recoil energy deposit in the detector.
- The WIMP rate is modulated as a function of the date because of the rotation of the Earth around the Sun. Based on the phase and the amplitude of the modulation, it can be possible to discriminate dark matter particles from background. Nevertheless, it is necessary to have important statistics for this.
- The spectral shape of WIMP interactions can be clearly different to other shapes from different backgrounds. In this case, a subtraction of these different backgrounds allows to determine the presence of a dark matter particle, if reliable spectral shapes are available.
- The WIMP-nucleon cross-section is proportional to $(\mu_A^2/\mu_n^2)A^2$, whereas the cross-section for neutron scattering is proportional to $A^{\frac{2}{3}}$. Thus it is possible to use target nuclei with different A values to check the dependence of the observed rate with A .

V.8 State of art

Many direct detection experiments exist and allow to strongly constrain the spin-independent WIMP cross-section. Different technologies, illustrated in Fig.1.15, are used to allow a discrimination between electronic and nuclear recoils. As shown in Fig.1.16 (left and right), direct detection can be divided in two regions in the space parameter of (m_χ, σ_{SI}) . The most common detection methods used for these searches are presented in this subsection.

Chapter 1: Theoretical context

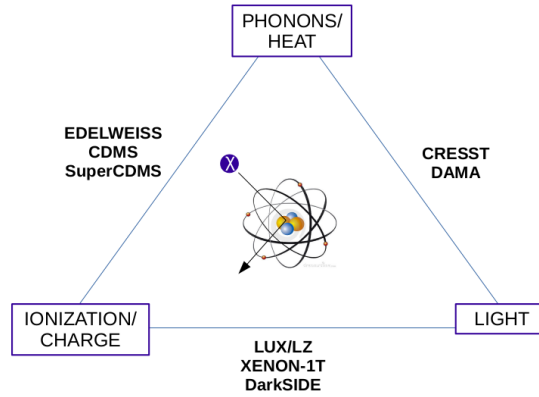


Figure 1.15 – Scheme of the different possible signals that can be measured when a dark matter particle interact in a detector. Direct detection often uses two of these technologies as detection method.

V.9 Noble gases detectors

The most sensitive experiments to high WIMP masses use noble gases absorbers inside Time Projection Chambers (TPC), operated in dual-phase (liquid/gas)¹⁰. LUX [60], XENON-1T [52] and PandaX-II [61] are the main experiments using this technology with liquid xenon (LXe with $Z = 54$ and $A = 131.29$). Also liquid argon (LAr with $Z = 18$ and $A = 40.0$, used by DarkSide [62]) and liquid neon (LNe) can be used for direct detection detectors.

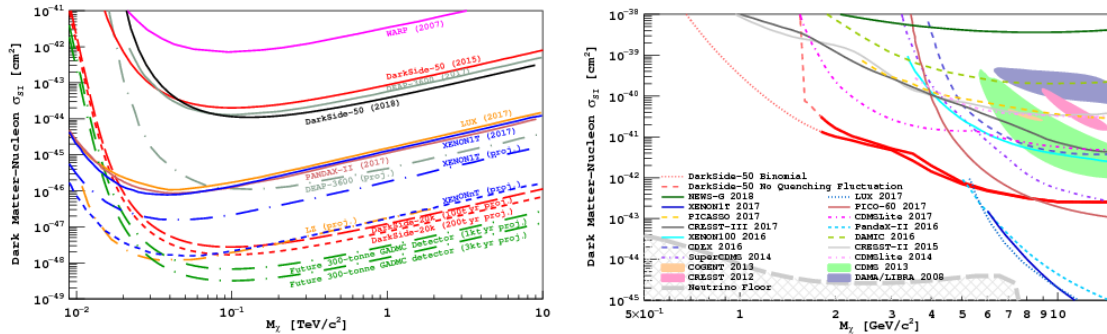


Figure 1.16 – Left: Spin-independent DM-nucleon cross-section 90% C.L. exclusion limits from the analysis detailed in [62], compared with selected results and projections. Right: 90% upper limits on spin-independent DM-nucleon cross-sections from DarkSide-50 in the range above $1.8 \text{ GeV}/c^2$. Figure taken from [53].

V.9.1 The XENON experiments

Located in the Gran Sasso National Laboratory (LNGS) in Italy (3800 m w.e.), the XENON experiments (XENON10, XENON100, XENON1T) use dual-phase (liquid/gaz) xenon TPC. XENON1T [52] is the largest TPC to date containing 3.2 tons of ultra-pure LXe, with 2 tons

¹⁰Note that several experiments use single phase (liquid) detectors, such as XMASS and DEAP/CLEAN [58] [59]

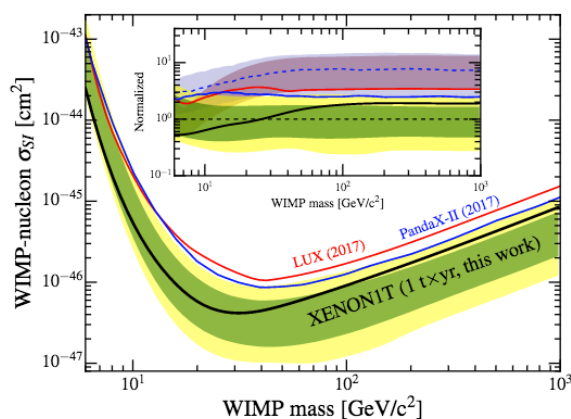


Figure 1.17 – Results of the Xenon-1T collaboration. Limits on WIMP-nucleon cross-section as a function of the WIMP mass are plotted, originating from different experimental results. Taken from [52].

used as the target material in the active volume, viewed by top and bottom arrays of photomultiplier tubes (PMT). A particle incident on the LXe target deposits energy that produces a prompt scintillation signal (S1) and ionization electrons. The active volume is defined by a cathode and a grounded gate electrode separated by 97 cm to provide a drift field for the electrons. These electrons are extracted into gaseous xenon (GXe) where they produce proportional scintillation light (S2) via electroluminescence through a ≥ 10 keV/cm multiplication field. The S2/S1 ratio allows for discrimination between nuclear recoils (NR) from WIMP or neutrons, and electronic recoils (ER) from β or γ -rays. The time delay between S1 and S2 and the localization of the S2 pattern in the top PMT array indicate the vertical and horizontal position of the interaction respectively. The detector is surrounded by an active water Cherenkov muon veto system. Using 278.8 days of data collected with the XENON1T experiment, resulting in a 1.0 ton.yr exposure, the collaboration excludes new parameter space for the WIMP-nucleon spin-independent elastic scattering cross-section for WIMP masses above 6 GeV/ c^2 , with a minimum of 4.1×10^{-47} cm 2 at 30 GeV/ c^2 and 90% C.L. [52]. As shown in Fig.1.17, this is the best world result for the high WIMP mass region.

V.9.2 The DarkSide-50 experiment

The DarkSide-50 experiment [62] located in LNGS, uses a LAr TPC with an active mass of (46.4 ± 0.7) kg of low-radioactivity argon from underground sources (UAr), deployed in a liquid-scintillator neutron and gamma-ray veto (LSV) and water Cherenkov veto (WCV) for shielding and muon detection. The DarkSide-50 DM detector is a two-phase (liquid and gas) LAr TPC, which is a cylindrical volume containing UAr viewed by top and bottom arrays of PMT. Interactions in the active volume result in electronic or nuclear recoil events which produce, as for XENON experiments described in V.9.1, two scintillation signals: the primary one (S1) and the secondary one (S2) by gas proportional scintillation, leading to the event vertex reconstruction in the (x,y,z) plane. The TPC PSD parameter f_{90} , defined as the fraction of S1 light detected in the first 90 ns of a pulse, allows very strong pulse shape discrimination between nuclear and electronic recoil. Using a blind analysis of their 532.4 live-days dataset, no events were observed in their defined DM search region, an upper limit on the spin-independent scattering cross-section at 1.14×10^{-44} cm 2 was set for 100 GeV/ c^2 DM particles [62], as shown in Fig.1.16 (left).

Chapter 1: Theoretical context

The DarkSide collaboration recently published a low-mass search with the DarkSide-50 experiment [53] in the mass range below $20 \text{ GeV}/c^2$, using the same target of low-radioactivity argon. Their analysis is based on the ionization signal, for which the DarkSide-50 TPC is fully efficient at 0.1 keV equivalent-electron¹¹ (keV_{ee}). The observed rate in the detector at 0.5 keV_{ee} is about $1.5 \text{ events}/\text{keV}_{ee} \cdot \text{kg} \cdot \text{day}$ and is almost entirely accounted for by known background sources. They obtain a 90% C.L. exclusion limit above $1.8 \text{ GeV}/c^2$, for the spin-independent cross-section of dark matter WIMP on nucleons, extending the exclusion region for dark matter below previous limits in the range $1.8\text{-}6 \text{ GeV}/c^2$ (see Fig.1.16 right).

V.9.3 Summary on noble gas experiment

The better performance of xenon at large masses are explained by a high exposure, a higher WIMP-nucleon interaction cross-section (the spin-independent cross-section σ_{SI} depends on the atomic number A : $\sigma_{SI} \propto A^2$), the absence of Xe radioisotopes of small period¹² in natural Xe and the presence of an odd number of neutrons with non-zero nuclear spin, which makes the detector also sensitive to a spin-dependent interaction. A large difference between the decay times of the two scintillation lights S_1 and S_2 implies a better electronic recoil discrimination. However, LAr TPC have powerful pulse shape discrimination (PSD) in the scintillation channel that allows the separation between the nuclear (NR) and electronic (ER) recoils. That is the reason why their projected limits, as shown in Fig.1.16 (left, green curves), have the best sensitivity.

V.10 Cryogenic detectors

In solid detectors, phonon excitations of the crystal originate from the conversion of the energy from the incident particle inducing vibration of the crystal lattice. The typical energy scale to produce phonons in this way is around few meV, lower than the energy of the quanta of charge or light. If, in addition, the scintillation or charge is recorded, the energy dependence of the signal ionization yield can be used to discriminate between electronic (γ , β , ...) and nuclear (neutron, WIMP) recoils. Phonons induced by an incident particle can be thermal and athermal. The first are related to the thermal equilibrium of the crystal after an energy deposit and can be measured by the temperature rise. The second describe a fraction of the initially produced phonons which are out of equilibrium and show a larger mean free path in the crystal. Bolometers are generally equipped with thermal sensors as NTD (Neutron Transmutation Doped germanium) or TES (Transition Edge Sensor). For NTD, their resistance decreases with the temperature rise, whereas for TES they operate at temperature near their phase transition between the conducting and the superconducting states. In general, TES are most sensitive to athermal phonon than NTD. Most of bolometer experiments uses in addition to the measurement of the phonons, the scintillation or charge measurement to allow a particle discrimination. In contrast to the phonon signal which is not quenched (i.e linear with deposited energy), ionization signal (i.e charge) vary as a function of the deposited energy. For detectors applying an electric field to collect induced charges, the drifted electron/hole pairs dissipate an additional energy in the crystal producing phonons (called the Luke-Neganov effect [63], [64]). By using it, the phonon signal can be optimized. The energy threshold can be enhanced by taking into account this effect in the estimation of the recoil energy by applying a high voltage bias. It will be discussed in chapter 2 while the EDELWEISS experiment has made the choice to use it to improve the energy threshold of its detectors. Note however that using this effect can induce the loss of the discrimination between electronic and nuclear recoils (i.e no

¹¹See chapter 2.

¹² $T(^{124}\text{Xe})=1.1 \times 10^{17} \text{ yr}$ and $T(^{136}\text{Xe})=2.36 \times 10^{21} \text{ yr}$.

possibility to discriminate a γ from a WIMP for example). Cryogenic detectors can reach low energy thresholds much easier than dual-phase experiments for which the energy threshold is intrinsically limited by the quanta of light. Hence, they are optimized to search WIMP down to masses of a few GeV/c^2 .

V.10.1 The CRESST experiment

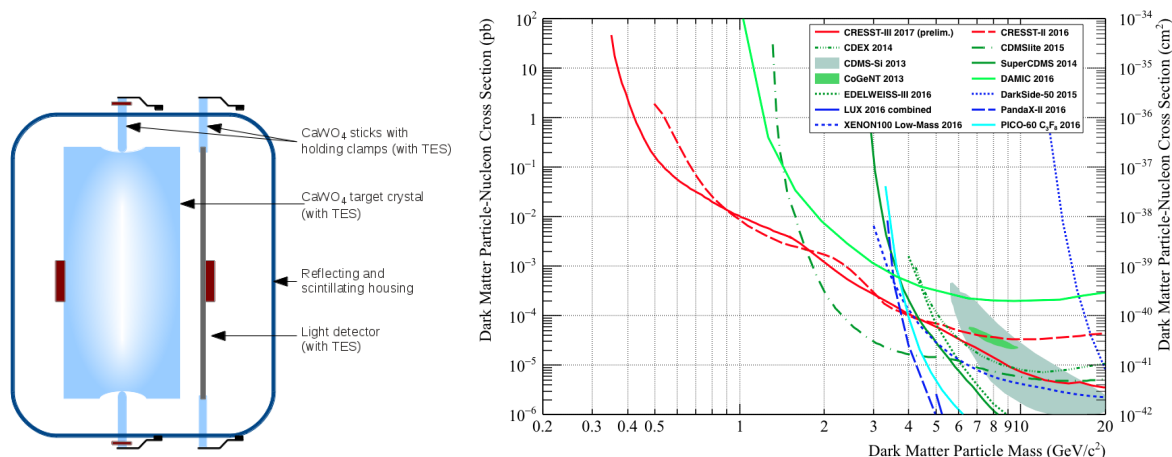


Figure 1.18 – Left: schematic view of the detector design for CRESST-III modules. Right: parameter spaces for elastic spin-independent dark matter-nucleon scattering. The first result on low-mass dark matter search from CRESST-III Phase 1 (solid red) is compared with the limit from CRESST-II Phase 2 (dashed red). For comparison, exclusion limits (90% C.L.) of other dark matter experiments are shown and the favoured parameter spaces reported by CDMS-Si and CoGeNT are drawn as shaded regions. Both figures taken from [54].

The target used by the CRESST experiment consists of scintillating CaWO₄ crystals operated as cryogenic calorimeters at mK temperatures (phonon detectors). Most of the energy deposited in a crystal by a particle interaction induces a heat signal, yielding a precise energy measurement. A small fraction of the deposited energy is emitted as scintillation light that is measured by a secondary independent cryogenic calorimeter (light detector). This double heat-scintillation measurement allows for particle identification. A phonon detector and the corresponding light detector form a detector module. Both, phonon and light detectors are read out via tungsten transition edge sensors (TES). Each detector is equipped with a heater to stabilize the temperature at the operating point and to inject pulses which are needed for the energy calibration. The experiment is based in the LNGS. For CRESST-III phase [54], the CaWO₄ target crystals have been scaled down in mass from ~ 300 g to 24 g and the thermometer design has been optimized to achieve a threshold of less than 100 eV. A schematic view of the detector layout is presented in Fig.1.18 (left).

Since 2015, the CRESST experiment is leading the field of direct dark matter search for dark matter masses below $1.7 \text{ GeV}/c^2$, extending the reach of direct searches to the sub- GeV/c^2 mass region. The first results on low-mass dark matter obtained with the Phase 1 of CRESST-III are shown in Fig.1.18 (right). It corresponds to an exposure of 2.39 kg.day with a conservative analysis threshold set at 100 eV. It confirms that a low energy threshold is a crucial requirement for direct dark matter searches aiming to achieve sensitivity to dark matter particles with masses

Chapter 1: Theoretical context

in the $1 \text{ GeV}/c^2$ range and extends the reach of the experiment down to $350 \text{ MeV}/c^2$, reaffirming its leading sensitivity for light dark matter [54].

V.10.2 The SuperCDMS experiment

The SuperCDMS Soudan experiment [65] uses the Cryogenic Dark Matter Search (CDMS II) low-background apparatus, which consists of a cryostat surrounded by a passive shield made of polyethylene and lead, and an outer muon veto situated beneath an overburden of 2090 meters water-equivalent. The cryostat and internal cold hardware provide an additional 3 cm of copper shielding. Interleaved Z-sensitive Ionization- and Phonon-mediated (iZIP) detectors of 0.6 kg each are used. Each detector consists of a 76-mm diameter, 25-mm thick, cylindrical, high-purity germanium substrate, with interleaved ionization electrodes ($\pm 2 \text{ V}$) and grounded phonon electrodes on both of the crystal faces. The ionization measurement is made by drifting the electron/hole pairs to electrodes on the crystal surface in a weak electric field ($\sim 0.5 \text{ V/cm}$). The phonon measurement is realized by athermal phonon sensors: athermal phonons propagating in the crystal interact with superconducting Al electrodes at the crystal surface, breaking Cooper pairs to form quasiparticles in the Al electrodes. Diffusion of these quasiparticles to a tungsten Transition Edge Sensor (TES) increases the temperature and resistance of the TES, which is operated in the transition region between the superconducting and normal states. The double heat-ionization measurement allows to discriminate between electronic and nuclear recoils, as explained in chapter 2 for the EDELWEISS experiment.

Last results from SuperCDMS at Soudan of a search for dark matter scatters off atomic nuclei using 15 interleaved iZIP detectors [65] use datasets taken from March 2012 through July 2014, yielding a total exposure of 1690 kg.days. A single candidate event has been observed, consistent with expected backgrounds. This analysis sets an upper limit on the spin-independent WIMP-nucleon cross-section of $1.4 \times 10^{-44} \text{ cm}^2$ at $46 \text{ GeV}/c^2$ [65], as shown in Fig.1.19 (left), which is the strongest limits for WIMP-germanium-nucleus interactions for masses $> 12 \text{ GeV}/c^2$.

During its operation at the Soudan Underground Laboratory, SuperCDMS germanium detectors were run in the CDMSlite mode to gather data sets with sensitivity specifically for WIMP with masses $< 10 \text{ GeV}/c^2$. In this mode, a higher detector voltage bias was applied to amplify the phonon signals produced by drifting charges. A search for WIMP masses down to $1.5 \text{ GeV}/c^2$ has been realized by achieving analysis thresholds as low as 56 eV_{ee} . The CDMSlite Run2 90% C.L. upper limit on the DM-nucleon cross-section, which is the best result in germanium detector for this WIMP mass range, is presented in Fig. 1.19 (right).

V.11 Others techniques

Bubble chambers were often used in the last decades in accelerator experiments until new technologies as gaseous detectors provided a better performance. In the last years, the technology of using superheated liquids has been revived in the context of dark matter searches as example by PICO experiment [66]. This type of experiment can be separated into bubble chambers and droplet detectors. Both technologies use refrigerant targets operated in a superheated state mildly below its boiling point. Interactions of particles with the target can be observed by the induced process of bubble formation. A phase transition of the medium is necessary to create a bubble in the detector. Moreover, the created bubble must be sufficiently large, requiring a minimum energy deposition per unit of volume. This process can be described by the hot spike model [67]. An event is then photographed with CCD cameras, and the position of the bubble can be determined with few mm resolution. This allows to define an innermost volume for the analysis, featuring lower background. After the formation of each bubble, the medium

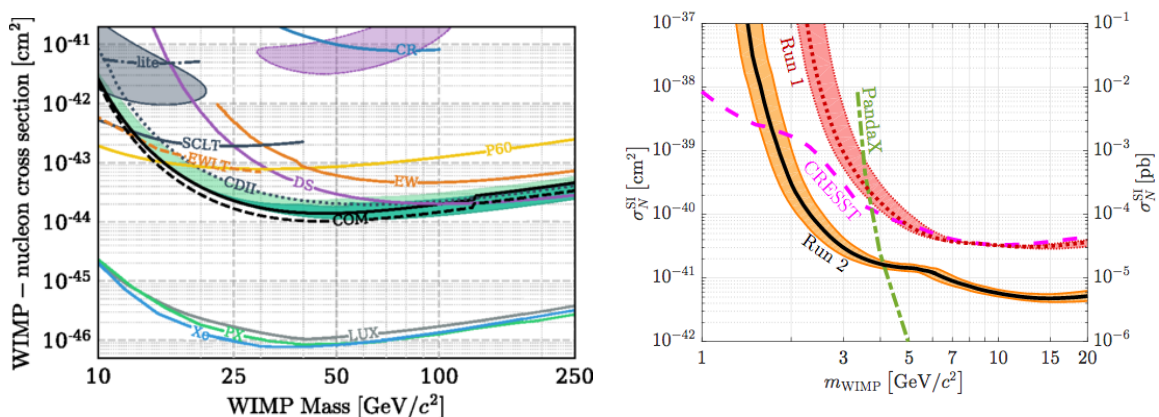


Figure 1.19 – Left: the 90% C.L. upper limit on the DM-nucleon cross-section (solid black) based on the single observed event in SuperCDMS dataset. The range of the pre-unblinding 68% (95%) most likely expected upper limits are shown as dark green (light green) bands. Closed contours shown are CDMS II Si (solid gray, 90% C.L.) and DAMA/LIBRA (dotted purple, 90% C.L.). Also 90% C.L. exclusion limits from other experiments are shown in the figure, taken from [65]. Right: Spin-independent WIMP-nucleon cross-section 90% upper limits from CDMSlite Run 1 (red dotted curve with red uncertainty band) and Run 2 (black solid curve with orange uncertainty band) compared to the other (more recent) most sensitive results in this mass region: CRESST-II (magenta dashed curve), which is more sensitive than CDMSlite Run 2 for $m_\chi < 1.7 \text{ GeV}/c^2$, and PandaX-II (green dot-dashed curve) which is more sensitive than CDMSlite Run 2 for $m_\chi \geq 4 \text{ GeV}/c^2$. The Run 1 uncertainty band gives the conservative bounding values due to the systematic uncertainty in the nuclear-recoil energy scale. The Run 2 band additionally accounts for the uncertainty on the analysis efficiency and gives the 95% uncertainty on the limit. Figure taken from [51].

has to be reseted by a compression of the liquid phase followed by a decompression to a value below the vapour pressure. In contrast to bubble chambers, droplet detectors make use of a water-based cross linked polymer to trap the bubbles resulting in a shorter dead time of the detector [68]. For example, PICO experiment uses droplets of $200 \mu\text{m}$ diameter dispersed in a polymerized water saturated acrylamide. For a pressure of 1.013 bar, the boiling temperature is $T_b = -1.7 \text{ }^\circ\text{C}$. At ambient temperature and pressure, it is in a metastable superheated state. When a particle crosses the liquid, a heat spike is created and triggers a phase transition if the energy deposition is higher than a critical energy (around keV). Background discrimination is possible by using acoustic parameter (for α -background), multiple events (for neutrons) and the mean free path parameter.

VI Conclusion

The different evidences described in this chapter allow to converge to the presence of dark matter, with a contribution of $\Omega_{CDM} = 0.258$. Its nature remains unknown but constraints can be assumed in regard to its relic density and the structure formation. In this way, a generic class of particles has been postulated, the WIMP, which is the main candidate as dark matter particle.

Three different technics used for dark matter detection allow to constrain its presence in different

Chapter 1: Theoretical context

parameter spaces. The complementarity of these different methods is important to explore the whole region of parameters. Furthermore, only an accordance between several detection results would prove the dark matter discovery. This is why it is so important that many experiments using different technologies search for dark matter.

WIMP have to be distributed in a halo surrounding the galaxy to be detected by direct detection experiments. Different methods allow to survey the entire range of WIMP mass, i.e $m_\chi \in [1; 10000] \text{ GeV}/c^2$. Indeed, the dual-phase experiments are concentrated to high WIMP mass region, as a result of their increase of exposure. On the contrary, due to their ability to reduce energy threshold, experiments using cryogenic detectors are more competitive at low WIMP mass.

Chapter 1: The EDELWEISS experiment

The EDELWEISS experiment

The EDELWEISS (Experience pour DEtecter Les Wimps En Site Souterrain) experiment is a direct detection experiment dedicated to dark matter search. The collaboration is composed of seven laboratories from three countries: KIT (Karlsruhe, Germany), CSNSM, CEA, C2N, Néel, IPNL (Orsay, Saclay, Marcoussis, Grenoble and Lyon in France) and JINR (Dubna, Russia). The experimental set-up is located in the underground laboratory of Modane (*LSM: Laboratoire Souterrain de Modane*), in the Frejus tunnel at the french-italian border since 1994. The experiment target is made of germanium crystals operating at ~ 18 mK. The main properties of this material is to be semiconductor which is often used for physics search. At cryogenic temperatures, a heat signal can be measured and an ionization signal is read via electrodes on the crystal. The simultaneous measurement of heat and ionization signals is the key to the event-by-event discrimination in order to differentiate electronic from nuclear recoils.

This chapter describes the experimental set-up and its functioning. First, the different backgrounds and shieldings will be described. Then the operating principle of cryogenic detectors based on the measurement of two signals will be presented as well as the associated electronic and DAQ systems. The FID800 detectors of the experiment and the associated thermal model will be detailed. Finally, the upgrade of EDELWEISS-III to achieve low energy thresholds will be exposed.

I Backgrounds and mitigation strategies

The performance of rare event search experiments are strongly correlated to their environmental backgrounds. An adequate experimental set-up is the key for an efficient background reduction. Indeed, direct detection experiments are based on the measurement of the nuclear recoil energy induced by a WIMP scattering off on a detector nucleus. Nevertheless surface experiments are exposed to overwhelming backgrounds of different origins: cosmic-rays, natural and artificial radioactivity. These radiations interact in detectors via different types of particles: μ , neutron, γ , etc. Depending on the nature of these particles, the shielding strategy will be different.

The first step for a rare event search experiment is to operate deep underground to avoid cosmic-rays. As mentioned previously, the EDELWEISS experiment is located in the LSM,

Chapter 2: The EDELWEISS experiment

under 1700 m of rock (equivalent to 4800 m w.e). The overall structure is inside a clean room and is made of two sliding parts on rails in order to open them and give access to the cryostat, as shown in Fig.2.1. The natural radioactivity, as γ -rays and neutron from the environment, is mitigated using adequate shieldings. For the materials in the very close vicinity of the detectors, drastic material selection is mandatory.

I.1 Muon backgrounds

Cosmic-ray interactions with nuclei of the Earth's atmosphere produce a shower of particles including muons μ . The interaction of these particles with a proton ($\mu^- + p \rightarrow n + \nu_\mu$) can generate an important background in the experiment. At sea level, the muon flux is approximately $1 \mu/\text{cm}^2/\text{min}$ ($\sim 1.5 \times 10^6 \mu/\text{m}^2/\text{day}$) [4]. To drastically reduce the μ -background component by several orders of magnitude, direct detection experiments are located in underground laboratory. In the LSM, the muon flux Φ_μ has been measured [69]:

$$\Phi_\mu = (5.4 \pm 0.2_{-0.9}^{+0.5}) \mu/\text{m}^2/\text{day} \quad (2.1)$$

Although the μ -flux is very low, its mean energy arriving at LSM is very high, greater than $E_\mu \approx \mathcal{O}(TeV)$. At these high energies, the momentum exchanged in an electromagnetic interaction of a muon with a nucleus is sufficient to expel several neutrons from the nucleus: $\mu^- + (Z, A) \rightarrow \mu^- + (Z, A') + xn + \dots$. This process is particularly important in high-Z materials like lead used to shield the experiment from the radiogenic γ -background from the walls of the lab. This μ -background has a high event-multiplicity probability (i.e a scattering of the particle in more than one detector) and can thus be rejected. Cosmic- μ induced neutrons have a typical energy of many MeV but can be as large as many GeV and can disturb an analysis.

In order to tag these high-energy muons and thus reject neutrons (in an offline analysis), the EDELWEISS experiment is equipped with an external muon veto, as illustrated in green in Fig.2.1. The total area of this muon veto is around 100 m^2 allowing a geometrical muon flux coverage of 98%. It is composed of 46 plastic scintillator modules with different lengths: 2 m, 3.15 m, 3.75 m or 4 m. 44 of them are viewed from both sides by 2 PMT. The scintillator modules allow to identify coincidences with detector. The rate of muon events in the detector mimicking a WIMP signal due to the 2% geometrical uncovered area or to the untriggered events has been evaluated for an exposure of 3000 kg.d in [70]:

$$N_{WIMP-like}^\mu < 0.06 \text{ events/day (at 90\% C.L.)} \quad (2.2)$$

For run308 cool-down period¹ which lasted between July 2014 and April 2015, the muon veto efficiency $\epsilon_{\mu-veto}$ was estimated to:

$$\epsilon_{\mu-veto} \geq 93\% \text{ (at 90\% C.L.)} \quad (2.3)$$

In [70], the muon flux, spectrum and angular distributions at LSM have been propagated through the EDELWEISS simulation code based on Geant4 and gives the expected rate of WIMP-like events due to muon-induced neutrons:

$$\Gamma^{\mu-n} = 0.008_{-0.004}^{+0.005} \text{ events/(kg.day)} \quad (2.4)$$

corresponding to a muon-induced neutron background of:

$$N^{\mu-n} = 0.6_{-0.6}^{+0.7} \text{ events for 3000 kg.day} \quad (2.5)$$

From these results, the EDELWEISS collaboration concluded that the unexpected observed nuclear recoil rate of run308 [71] could not be explained by the μ -induced neutron rate in the experimental set-up.

¹A cryorun is a cool-down period of the experiment with run number equal to 308 here.

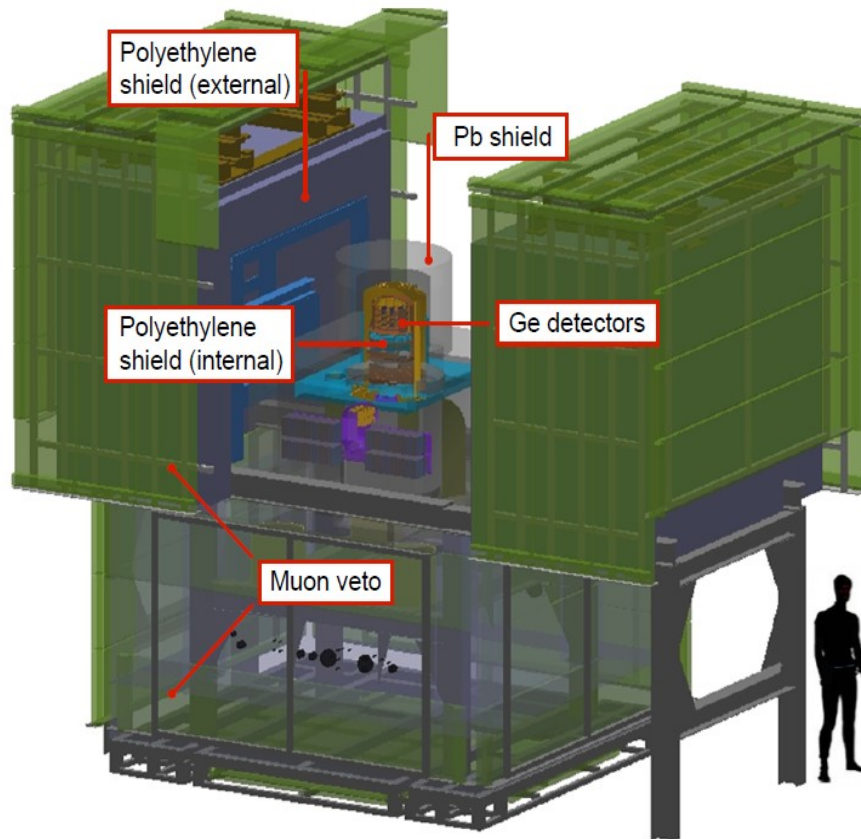


Figure 2.1 – Scheme of the EDELWEISS set-up. The muon veto (in green) is the outermost shell of the EDELWEISS shielding. PE (in violet) and lead (in gray) shields are installed between the muon veto and the cryostat (in orange).

I.2 Neutron background

Neutrons originate mainly from natural radioactivity of the laboratory rock walls. Neutron background has to be drastically controlled because the nuclear recoils induced by neutrons scattering off on a nucleus can mimic the WIMP signature (see section V.7).

The natural decay chains of ^{238}U and ^{232}Th (shown in Fig.2.2), present in the rock and more or less in all materials, produce radiogenic neutrons by (α, n) reactions with an average energy of 3.5 MeV. In addition, the spontaneous fission of the isotope ^{238}U produces neutrons with an average energy of 2 MeV [72]. The presence of a 50 cm polyethylene (PE) shield surrounding all the experiment reduces the neutron background from the rock by three to five orders of magnitude [73]. In addition, materials inside the polyethylene shielding have been selected for their extremely low contamination levels with radioactive ^{238}U and ^{232}Th isotopes (see section I.6).

Neutrons have a penetration length ranging from cm to m. Because of their neutral electric charge, they interact with the atomic nucleus. Their energy loss is mainly due to elastic scattering and occasionally to inelastic scattering. In the former case, the neutron is absorbed by the nucleus which decays by emitting a second neutron to return to its fundamental state. Neutrons with a kinetic energy between 1 and 10 MeV are the most significant for the EDELWEISS experiment. Indeed, their elastic scattering on Ge nuclei cause nuclear recoils with

Chapter 2: The EDELWEISS experiment

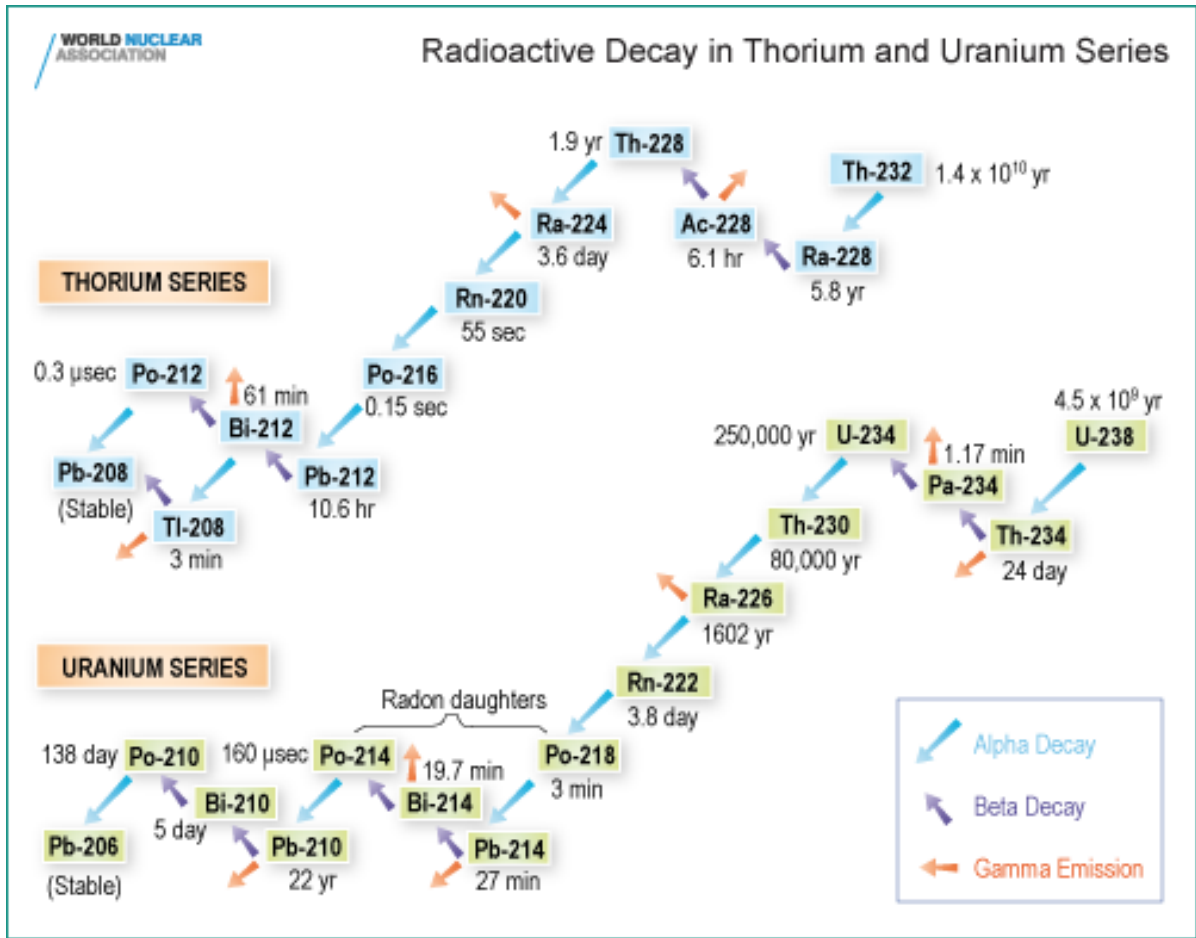


Figure 2.2 – ²³⁸U and ²³²Th radioactive chains, taken from [74]. The successive decays give α, β and γ particles.

energies between 0 and 200 keV, the same energy range as expected for a WIMP scattering (see section V.7). In an elastic scattering, a fraction of the kinetic energy E_k of the neutron is transmitted to the nucleus of mass m_A . The nucleus structure remains identical but the incident neutron is deviated: $n + {}^A X \rightarrow n + {}^A X$. The induced recoil energy E_R is:

$$E_R = 2 \frac{m_n m_A}{(m_n + m_A)^2} E_k (1 - \cos(\theta^*)) \quad (2.6)$$

where m_n is the neutron mass and θ^* is the scattering angle in the center of mass. Thus, for natural germanium ($\langle A \rangle = 73$), the maximum transferred energy is approximately $E_R^{max} \simeq \frac{4E_k}{A}$.

If the neutron energy is larger than 3 MeV, the cross-section of inelastic and elastic processes are equivalent. For the first mechanism, the absorption of the neutron n creates an intermediate nucleus, which decays by emitting another neutron n' . The nucleus radiates a photon γ to return to its ground state:

$$n + {}^A X^* \rightarrow {}^{A+1} X^* \rightarrow {}^A X^* + n' \rightarrow {}^A X + n' + \gamma \quad (2.7)$$

The neutron n' has a kinetic energy reduced by the amount given to both the γ and the recoil of the nucleus.

Chapter 2: The EDELWEISS experiment

From the run308 onwards, corresponding to the EDELWEISS-III upgrades, polyethylene has been added to the set-up inside the lead cryostat at 1 K stage and outside the cryostat above warm electronics, as shown in Fig.2.3. The addition of this PE was motivated by the high radioactivity level of the electronic components and cabling [75].

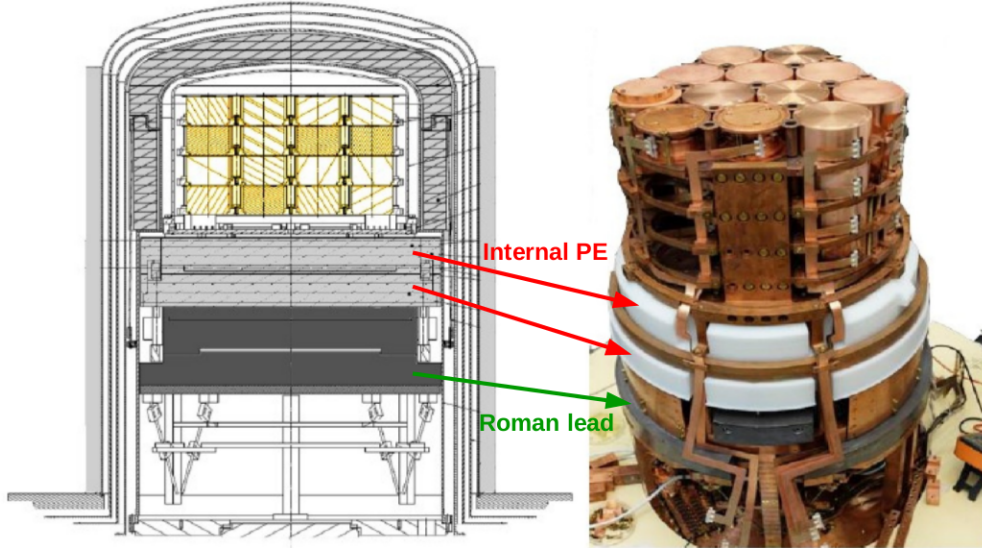


Figure 2.3 – Scheme of the upperpart of the cryostat and arrangement of detectors inside it. There is 12 towers, each tower can host up to 4 detectors. Internal polyethylene is visible in white (red arrows) in the right figure as well as the internal roman lead below PE (green arrow).

I.3 Gamma background

In addition to the natural radioactivity of the rocks (^{238}U , ^{40}K and ^{232}Th), γ -rays can also originate from artificial radioactivity (^{137}Cs) or cosmogenic activation (^{60}Co). Indeed the EDELWEISS experiment is particularly concerned by the cosmogenic activation of Ge crystals inducing an internal γ -background [76].

Photons in the keV to MeV range can interact with matter by three different processes: compton scattering, photoelectric effect and pair production as shown in Fig.2.4.

Below 150 keV, the dominant process is photoelectric effect, i.e the photon is absorbed by an atom. An electron, called photoelectron, is ejected with an energy $E_e = E_\gamma - E_L$ where E_L is the electron binding energy and E_γ is the photon energy. The created hole in the atom electronic configuration leads to a reorganization of the electrons with a X-ray emission. In turn, this X-ray can cause the ejection of another electron by photoelectric effect, called Auger electron.

The photoelectric cross-section $\sigma_{\text{photoelectric}}$ can be approximated by:

$$\sigma_{\text{photoelectric}} \propto \frac{Z^5}{E_\gamma^n} \quad (2.8)$$

where Z is the atomic number. For a photon energy E_γ less than 0.5 MeV, n is almost 3 and for $E_\gamma \sim 2$ MeV, $n \sim 1$.

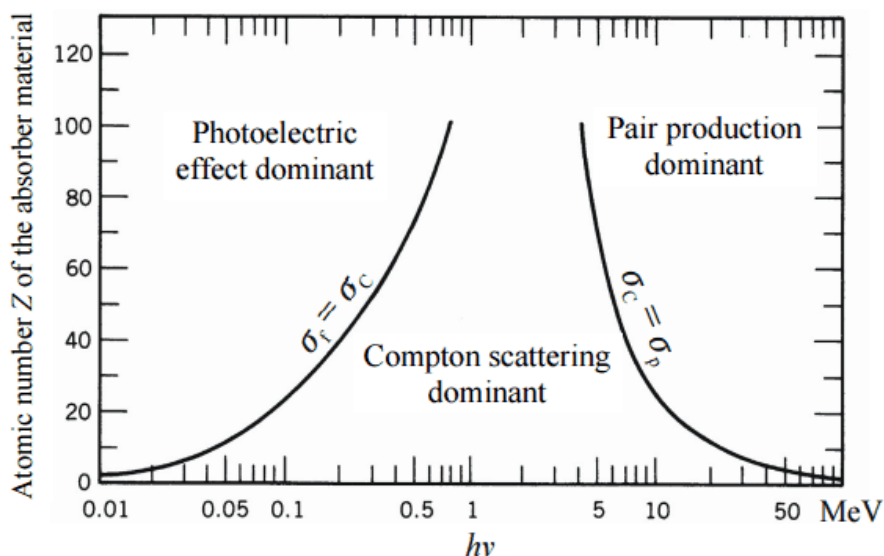


Figure 2.4 – Dominant processes for γ -ray interactions [77]. For germanium ($Z = 32$), the photoelectric effect is dominant below 150 keV. In the energy range between 150 keV and 10 MeV the Compton scattering dominates and beyond the pair creation prevails.

For an energy between 150 keV and 10 MeV, the dominant process is Compton scattering. It consists of the interaction between an incident γ and an electron leading to an electronic recoil. In this case, the incident photon is deviated with respect to its trajectory with an angle θ . An energy transfer between the γ and the electron takes place and is expressed as a function of the deviation angle θ according to:

$$E'_\gamma = \frac{E_\gamma}{1 + \frac{E_\gamma}{m_e c^2} (1 - \cos \theta)} \quad (2.9)$$

where E'_γ is the scattered photon energy, m_e is the electron mass and E_γ is the energy of the incident photon. In the case of $\theta = \pi$, the energy transfer is maximal. The probability of this mechanism increases with the atomic number Z . The mean free path for this type of interaction is between 0.6 cm and 5 cm in the considered energy range.

For an energy of the incident γ more than twice the mass energy of the electron at rest (i.e. 2×511 keV), electron pair production is possible. A γ is then converted into an electron-positron pair in the electromagnetic field of the nucleus. In the process, a fraction of the gamma ray momentum is transferred to the atom. The remaining momentum is shared between the electron and the positron. The produced positron can interact with another electron (10-100 ps time scale below 10 MeV), leading to the creation of a pair of γ emitted in opposite directions with energies of 511 keV. For the germanium, the probability of this interaction is very weak in the energy range considered in this work. For the γ -rays from natural radioactivity ($E_\gamma < 2614$ keV), this process is negligible.

The sum of the interaction probability of the three processes (τ , σ and κ) is the coefficient of linear absorption μ :

$$\mu = \tau_{\text{photoelectric}} + \sigma_{\text{Compton}} + \kappa_{\text{pair}} \quad (2.10)$$

The number of transmitted photons I through length x of matter with respect to the number

Chapter 2: The EDELWEISS experiment

of initial photons I_0 is:

$$\frac{I}{I_0} = e^{-\mu x} \quad (2.11)$$

From prevent against γ -rays, there is an additional 20 cm thick lead shield inside the PE shield. The innermost 2 cm of lead comes from a wreck of an ancient Roman galley ($\sim IV^e$ AD) and shields X-rays and bremsstrahlung photons from outside. The radioactivity of this lead is considerably low compared to normal lead as the ^{210}Pb decay period is 22.3 y. Moreover, inside the cryostat, 14 cm thick archeological lead plate, cooled-down at 1 K, separates the detection area from the dilution unit and the cold cabling, as illustrated in Fig.2.3.

I.4 Alpha background

As mentioned in the previous section, the ^{238}U and ^{232}Th natural radioactive chains decay emitting different particles among which α -particles (Fig.2.2). In the ^{238}U chain, it is worth to notice that the ^{222}Rn is a gas with a lifetime of 3.8 days. It decays rapidly into ^{210}Pb , a γ and β emitter, which has a much longer lifetime (~ 23 years). It constitutes an important background component and will be discussed later in chapter 5.

For α -particles above 1 MeV, the energy loss corresponds to the interaction with electrons of the target atom. Because of its mass, the α energy loss per unit length is small and its trajectory is almost linear. Typically, an α -particle of 5 MeV will travel 20 μm in germanium.

For energies below 1 MeV, the number of collisions between the α -particles and the target atoms becomes more important. The linear energy loss $-dE/dx$ is given by the Bethe-Bloch formula:

$$-\frac{dE}{dx} = \frac{4\pi n Z^2}{m_0 v^2} \left(\frac{e^2}{4\pi\epsilon_0} \right)^2 \left[\ln\left(\frac{2m_0 v^2}{I} \right) \right] \quad (2.12)$$

where E is the energy of the charged particle, x is the path length, Z the charge number of the target nucleus, m_0 the electron mass at rest, v the charged particle velocity, e the elementary charge, ϵ_0 the vacuum permittivity and I the average ionization potential. The electronic density n is:

$$n = \frac{N_A Z \rho}{A} \quad (2.13)$$

where N_A is the Avogadro number ($6.022 \times 10^{23} \text{ mol}^{-1}$), ρ is the matter density and A is the mass number of target atoms. The ionization constant I includes global properties of atoms (energy levels, cross-section). The most recent measurement for Ge [78] is:

$$\frac{I}{Z} = 9.76 + 58.8 Z^{-1.19} \text{ eV if } Z \geq 13 \quad (2.14)$$

The charged α -particle will be not deviated after interactions with electrons. Moreover, the transferred energy is less than $4m_0/M_\alpha$ of the α kinetic energy E_α (with M_α the α mass). Nevertheless, the electromagnetic interaction has a long range and the number of electrons in a crystal is important, inducing a high frequency of these interactions. The α -particle mean free path is around 20 μm and thus its interaction takes place near the detector surface, as shown in Fig.2.5.

I.5 Beta background

As described previously, the ^{222}Rn decay induces surface events due to α , β and lower energy γ interactions. The produced β -events can interact via the Bremsstrahlung radiation. It is an

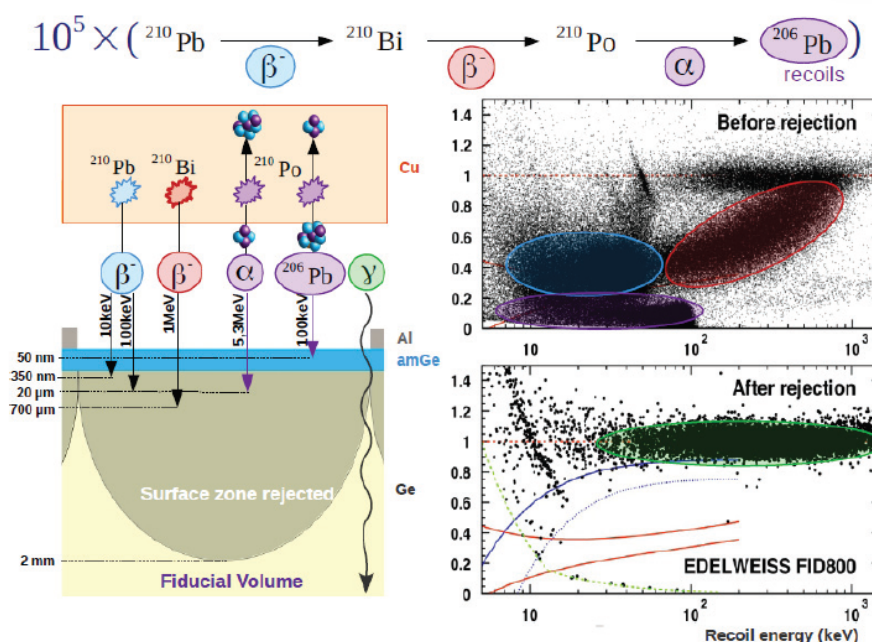


Figure 2.5 – Left: penetration length for different particle types in EDELWEISS germanium detector. Right: ionization yield as a function of recoil energy observed in two EDELWEISS detectors. The red band corresponds to the area where are expected nuclear recoil at 90% C.L. The blue lines correspond to the electronic recoil band at 90% (full) and 99.98% C.L. (dashed), taken from [75]. The green dashed line corresponds to the 2 keV ionization threshold cut. The different populations are indicated with the same color code used in the left figure.

electromagnetic radiation emitted by a charged particle when it decelerates. The probability of this process is proportional to EZ^2 so, it is important only at high energy ($E > 800/Z$ MeV). In EDELWEISS, it represents only few percents of the energy loss by incident electrons. The dominant interaction is ionization by impact and atomic excitations. The collision of two electrons induces an important energy transfer. Energy loss by inelastic collision stays predominant while electron energy is above a few eV and sufficient to release an electron from its atom. The released electron goes in the conduction band (creating a hole in the valence band) and can itself ionize other atoms if its energy is high enough. The Bethe formula allows to describe the linear energy loss for this process:

$$\frac{-dE}{dx} = \frac{2\pi e^4 N Z}{m v^2} \ln \left(\frac{m v^2 E}{I^2} \right) \quad (2.15)$$

where e is the elementary charge, m is the electron mass at rest and v is the velocity of the incident electron. N is the number of atoms per volume unit, Z is the atomic mass and I is the average ionization energy. This formula is valid in the non relativistic case. The energy loss increases with decreasing kinetic energy of the incident electron. At high energy, a relativistic correction must be applied.

I.6 Radiopurity of materials

As mentioned previously, the EDELWEISS experiment is installed in a clean room. It is a 10000 class room which means that there is less than 10000 particles of size 0.5 μm or larger

Chapter 2: The EDELWEISS experiment

per cubic foot of air. The ventilation system and the air conditioning can renew two times the entire volume of air in the laboratory every hour. The ^{222}Rn concentration in the laboratory is around 10-15 Bq/m³ [79]. Therefore, the volume between the cryostat surface and the external shielding is flushed using air coming from a facility that reduces this concentration to less than 20 mBq/m³.

In order to maintain this class level and reach the extremely low required background, all materials entering the room are radio-assayed and selected with respect to their radiopurity. The radiopurity of materials used in the experiment and modeled in Geant4 are listed in table 2.1 [75].

Chapter 2: The EDELWEISS experiment

Component	Mass (kg)	²³⁸ U chain		²³² Th chain ²³² Th	⁴⁰ K	⁶⁰ Co	¹³⁷ Cs
		²¹⁰ Pb	²³⁸ U				
Mill-Max conn.							
Brass pins	7.39 g	$(1.1 \pm 0.1) \times 10^4$	<62	<20	675±221	<36	<47
Brass sockets	9.41 g	$(2.6 \pm 0.4) \times 10^4$	<62	<20	<2645	<129	<132
CuBe press-fit cont.	1.63 g		$(1.2 \pm 0.2) \times 10^4$	980±196			
PTFE Delrin	0.040	<26	<16	1.5±1	<43	<2.3	<2.0
Kapton® connectors	0.094	<187	14±7	67±31	150±98		
PTFE contacts	0.061		10±5	20±7		5±3	3±2
Brass FID casing	0.40 g	524 ±102	<16	<15	<75		<4.0
Cu Kapton® cables	0.51	549±111	8±6	15±10	66±26	3±2	2.6±1.5
Brass screws	2.0 g	620 ±254		3.5±0.9	<19	<3.0	<6.4×10 ⁻³
Cu (NOSV)	295		<0.39	<32×10 ⁻³	<0.15	$(35\pm9) \times 10^{-3}$	<35×10 ⁻³
Cu (CuC2)	328		<10×10 ⁻³	$(24\pm12) \times 10^{-3}$	<0.50	$(42\pm16) \times 10^{-3}$	<0.06
PE internal	151	<3.0	0.65±0.08	0.30±0.07	<1.0	<0.06	<2.0
Axon cables ^a	3.5	138±53	4±3	5±2	177±22	<5.0	<39
Other connectors	0.43	$(6.0\pm0.5) \times 10^3$	$(2.6\pm0.4) \times 10^3$	450±44	<571	<36	
Cryostat structure	1236		<1.0				
PCB FET boxes	0.55	$(1.4\pm0.3) \times 10^4$	$(7.5\pm0.2) \times 10^3$	$(10.1\pm0.1) \times 10^3$	$(11.5\pm0.6) \times 10^3$		
PCB FID boxes	10.4		<1660	<1215			
Al FID boxes	27.8	88±36	4±3	<2.0	65±34	5±3	2.0±1.3
Axon cables ^b	6.32		182±70	13.0±2.5	1.1 ^{+0.2} _{-0.1}		
Electrodes/Al	<0.03 g			1.4 ± 0.2			
Mild steel structure	8600		<1.0	<1.0			
Lead shield	39000		<1.0	<1.0			
Polyethylene shield	40000		<12	<0.4	16 ± 2	<3.0	
Rock			$(10\pm3) \times 10^3$	$(10.0\pm0.8) \times 10^3$	$(230\pm30) \times 10^3$		
Concrete			$(23\pm3) \times 10^3$	$(5.7\pm0.8) \times 10^3$	$(77\pm13) \times 10^3$		

Table 2.1 – Radioactive contaminations in materials for the EDELWEISS set-up and shieldings [75]. All measurements have been made by gamma-ray spectrometry, except for ²³⁸U and ²³²Th in lead and mild steel which have been measured by mass spectrometry. In polyethylene, ²³⁸U and ²³²Th have been measured by neutron activation. The radioactivity quoted for the dilution unit is based on measurement of individual components. Abbreviations are used when needed: "conn." for connectors, "cont." for contacts. Also, ^acables for connecting 100 K and 1 K volumes; ^bcables for connecting 300 K and 100 K volumes.

II Cryogenic germanium detectors

The EDELWEISS detectors are germanium semiconductor crystals operating at temperatures around ~ 18 mK in order to measure the small heat signal induced by an incident particle. These very low temperatures are produced within a $^3\text{He}/^4\text{He}$ dilution refrigerator, described in section III.1. A dark matter particle interacting in a cryogenic detector induces a temperature increase of the order of $0.1 \mu\text{K}$. This section is dedicated to the properties of the germanium and the ionization and heat measurement principles.

II.1 Ge properties

In 1963, Tavendale and Ewan have postulated that germanium semiconductor detectors could be a judicious choice in particle physics searches [80]. The advantage of germanium relative to silicon is higher Z value and density, making it more appropriate to detect γ -rays. When an incident electron pass through the Ge detector, it creates electron/hole pairs with an average energy $\epsilon_\gamma=3$ eV/pair [81]. The pair drift in the electric field applied on detectors, and generate a charge signal on the electrodes. The high number of charge carriers with an energy close to ϵ_γ ensures a very good energy resolution.

The properties of semiconductors are limited by the impurities present in the material. Ge has a valence of 4, while impurities have valence of 3 (for acceptor) or 5 (for donor). Impurities tend to reduce the energy necessary to create electron/hole pairs and thus induce additional noise. The Ge crystal with acceptor impurities is called p-type and the same with donor impurities is called n-type.

Within a polarized electrode made as a p-n junction, no current passes through when there is no ionizing radiation (this is called reverse biasing or using non-injecting or blocking electrodes). In this way, few charge carriers remain in the depletion layer, resembling a pure semiconductor. By biasing the detector with a sufficient voltage bias, a large enough depleted volume can be created, sensitive to ionizing radiation especially X-rays and γ -rays. The performance of the detector is correlated to the depletion depth, which is inversely proportional to impurity concentration in the detector material. With higher purity Ge detectors, the impurity concentration of 10^{10} atoms.cm $^{-3}$ is achieved instead of 10^{13} atoms.cm $^{-3}$. In this way, the material has a higher resistivity. The major characteristics of the HPGe detector compared to Si are high atomic number, low impurity concentration (large depletion depth), low ionizing energy required to produce an electron/hole pair, high conductivity, compact size, and high resolution. However the small gap energy requires the detector to be cooled-down to at least 77 K.

II.2 Charge migration and ionization signals

The charge carriers induced by an incident particle in a germanium crystal drift under the influence of the electric field. A study of this migration in EDELWEISS detectors has been made in [82], taking into account the crystallographic structure of the Ge crystal. Fig.2.6 shows the electron/hole pair drifting simulation for a γ -ray interaction of 348 keV in the fiducial zone of a FID200² detector with four ionization electrodes. The polarization for this simulation is (± 2 V, ± 0.75 V). The development of the signal on the electrodes as a function of time is also shown. One can note the large spatial spread in the drift of electrons.

²A 200 g germanium crystal with interleaved electrodes. The FID design will be discussed in section IV.1.

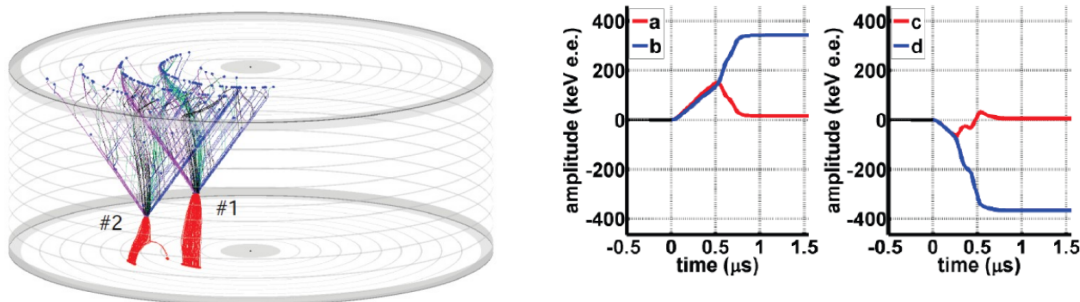


Figure 2.6 – Simulation of the charge drift and induced signals on ionization electrodes of a Ge detector of 200 g (taken from [82]). Left: electron tracks in blue and hole tracks in red for a bulk interaction of a 348 keV γ -ray. Right: amplitude and time dependence of induced signals on fiducial electrodes (in blue) and on veto electrodes (in red).

II.3 Thermal sensors

In the EDELWEISS experiment, phonons generated by an interaction in a crystal induce a temperature rise measured by two NTD (Neutron Transmuted Doped) sensors, as described in section IV.1. These thermal sensors are Ge crystals doped using an intense neutron irradiation. This process introduces impurities with a homogeneous distribution inside the crystal. For the EDELWEISS experiment, the NTD were produced with two different geometries: $4 \times 4 \times 0.45 \text{ mm}^3$ and $3 \times 5 \times 1 \text{ mm}^3$. Their resistance R as a function of the conducting electron temperature T_e follows the Efros and Shklovskii law [83]:

$$R(T_e) = R_0 \cdot e^{\sqrt{\frac{T_0}{T_e}}} \quad (2.16)$$

where R_0 and T_0 are characteristic parameters of the NTD and are strongly correlated to the impurity concentration. These parameters for FID824 detector are listed in table 2.2 as an example.

The R_0 and T_0 parameters of each NTD are determined in the following way. The NTD is biased with a low current I_{NTD} (0.022 nA) and the R value is measured for different cryostat temperatures (usually called bath temperature). The R_0 and T_0 are fitted parameters according to Eq.2.16. Fig.2.7 illustrates this procedure for the two NTD types.

	R_0 (Ω)	T_0 (K)	V_{NTD} (mm^3)
NTD A	0.370 ± 0.022	5.368 ± 0.041	7.2×10^{-3}
NTD B	0.301 ± 0.047	7.172 ± 0.123	15×10^{-3}

Table 2.2 – Example of R_0 and T_0 parameters for the two NTD of FID824 detector. V_{NTD} is the associated volume.

When a particule interacts in the crystal, the deposited energy ΔE induces a temperature rise ΔT such as:

$$\Delta T = \frac{\Delta E}{C} \quad (2.17)$$

where C is the heat capacity of the absorber (given by the Debye law: $C \simeq T^3$). If the energy is deposited in the crystal, the rise of temperature is measured by an increase of the NTD voltage bias, allowing the measurement of a heat signal.

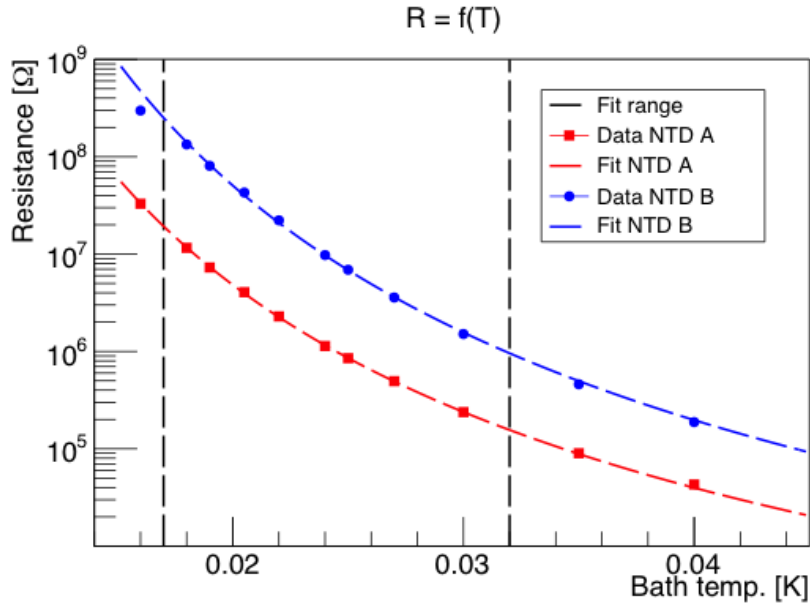


Figure 2.7 – Measurement of the NTD resistance as a function of temperature for NTD A (in red) and NTD B (in blue) for a FID800 detector [84], as described in section II.3.

III Description of the cryostat, cold electronics and DAQ systems

To achieve cryogenic temperatures, a $^3\text{He}/^4\text{He}$ dilution refrigerator is used. This section describes the cryogenic installation and its handling principle. The cold electronics used by the EDELWEISS experiment to read out detector signals will be also presented as well as its acquisition system.

III.1 Cryogenic installation

In the EDELWEISS-III set-up, the cryostat has an inverted geometry, i.e the thermal screens are above the detectors in order to make them more accessible (as shown in Fig.2.8). The cryostat volume of 50 L allows to contain 36×800 g-detectors. The detectors are mounted on four copper plates in an arrangement which was optimized for maximum self-shielding. They are organized in 12 towers. Each detector is installed with Teflon[®] clamps in a copper casing to shield against infra-red radiation. The refrigerator operates with different temperature stages, each obtained with different techniques. Each stage corresponds to a copper screen (10 mK, 4 K, 40 K, 100 K and 300 K). The 40 and 100 K stages are obtained by the Gifford McMahon (GM) machines located outside shieldings and linked to the screen via a caloduc. Each copper screen is separated by vacuum and is thermally decoupled to prevent black body radiation of the external screens to reach the detectors. The stage at 4 K reaches this temperature thanks to the ^4He bath whereas the temperature stage at 1 K is obtained by pumping the gas ^4He .

When the temperature is below 0.86 K, the $^3\text{He}/^4\text{He}$ mix is separated into two different phases: the first one is concentrated in ^3He and the second one is rich in ^4He (diluted in ^3He). The concentrated phase can be composed to almost 100% of ^3He whereas the diluted phase contains at least 6.4% of ^3He . Below 0.5 K, the superfluid ^4He of the diluted phase is in fundamental state with a negligible entropy. For that reason, ^4He behaves as a vacuum. The mixing

Chapter 2: The EDELWEISS experiment

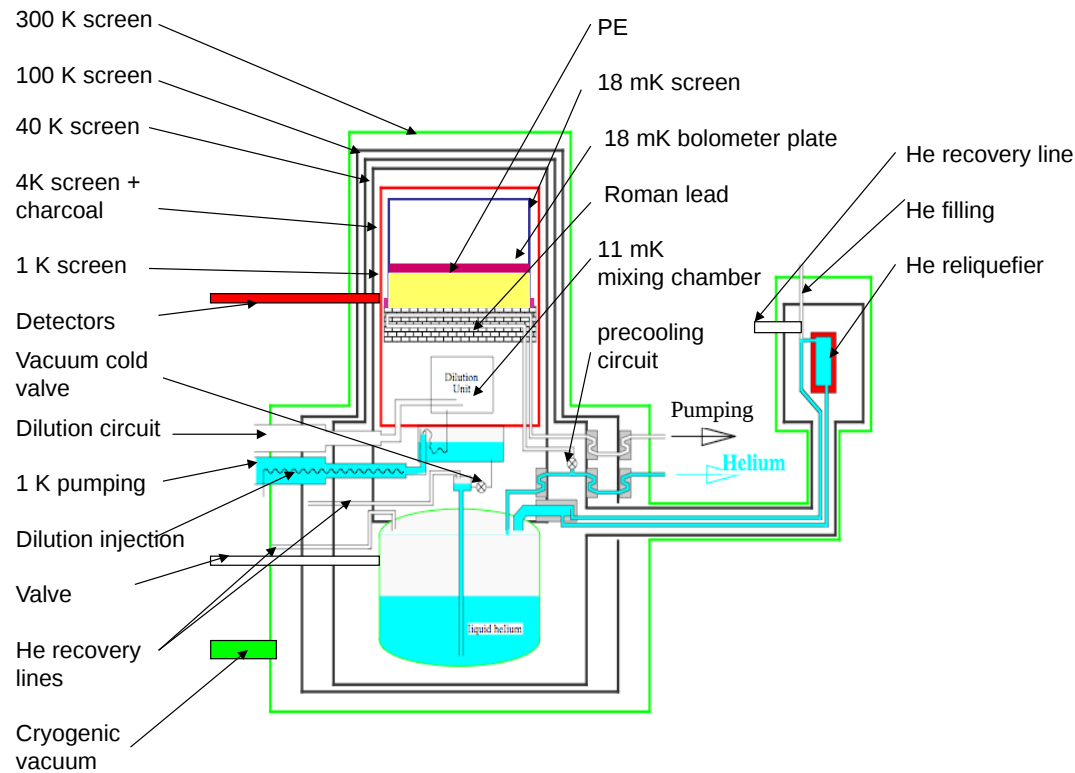


Figure 2.8 – Scheme of the EDELWEISS cryostat. The different screens corresponding to the 18 mK, 1 K, 40 K, 100 K and 300 K stage are represented.

chamber contains the two gaseous/liquid phases (diluted at the top and concentrated at the bottom). The pressure difference between the two vapors implies that the main gas extracted by pumping is composed of ^3He at 96%. The forced extraction of ^3He will result in ^3He passing from the concentrated phase to the diluted one to restore the equilibrium. This operation requires energy which is collected in the form of latent heat close to the interface. This process induces a cooling effect, allowing to reach very low temperatures. The pumped ^3He suffers a Joule-Thomson relaxation and passes through a heat exchanger that cools it down before its reinjection in the condensed phase. It operates in a closed cycle. The passage of the ^3He atoms into the dilute phase is possible even at the lowest temperatures, inducing a large cooling power, but the minimal reached temperature is limited by the heat exchange efficiency. The dilution unit is maintained at 11 mK.

With this procedure, the detector plate is regulated at 18 mK for an optimal running of the detectors. At these temperatures, a dedicated electronics is required for the data acquisition.

III.2 Cold electronics

Conventional amplifiers cannot be operated at temperature below 100 K, or dissipate too much heat. Therefore, the first electronic amplification stage is at 100 K with Field Effect Transistor (FET). In this way, the cable length from the detectors can be reduced to ~ 100 cm and thus, parasitic capacities associated. The detectors are connected to the FET via coaxial cables.

Chapter 2: The EDELWEISS experiment

This set-up allows to reduce the cross-talk between adjacent channels to a few percent, to keep the stray capacitances to 40 pF/m, and to control the sensitivity to microphonics as well as the electromagnetic noise and the power dissipation. The cold JFET (Johnson FET) are in copper boxes, screwed on the 100 K plate. Each FET-box contains 2 heat and 4 ionization channels and the elements shown in Fig.2.9. The FET have the function of an impedance converter. The remaining electronics (post-amplification, antialiasing filtering and digitization, DAC to bias the detectors) are installed in a module at room temperature, called bolometer-box (abbreviated as BB), which is directly fixed onto the 300 K screen of the cryostat. All input/output of this module are transmitted via optical fibers. A BB controls the cold electronics and relays, the voltage bias applied on the detector electrodes, resets the ionization Digital Analog Converter (DAC), and generates the modulation pattern for the heat channels. A BB can digitize up to 4 ionization and 1 heat channels of a detector, which means that two BB are required for the readout of a detector with two thermal sensors. The signals are amplified and digitized at a rate of 100 kHz and stored in ADU (Arbitrary Digital Units). The synchronization between channels is done with a common sampling clock allowing to easily identify and subtract common noise pattern due to electronic interferences.

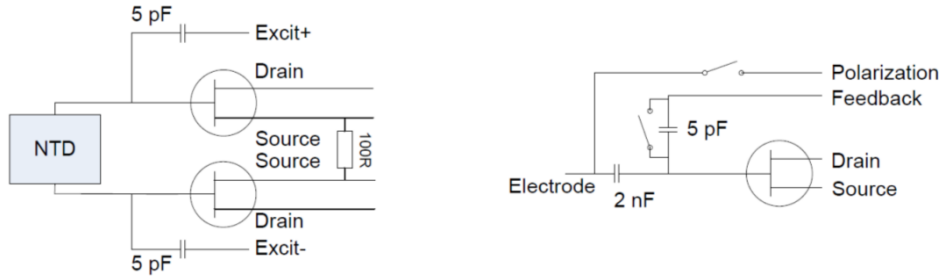


Figure 2.9 – Cold electronic readout for heat (left) and for ionization (right).

III.2.1 Ionization channel readout

In order to generate an electric field inside the detector, detectors are covered by biased electrodes. The electron/hole pairs produced by an incident particle drift through the detector toward the corresponding electrode to collect them. In most applications, these charges are integrated on the feedback capacitance of a charge amplifier. EDELWEISS-III uses instead a voltage amplifier to directly measure the voltage bias on the electrodes. This avoids the use of resistors in the amplification scheme, thus eliminating their contribution to noise. This is possible because of the low event rate and very cold environment able to reduce leakage currents below 0.1 fA. The reset of the FET input and the voltage bias of the electrode are done via mechanical relays as shown in Fig.2.9. The biasing of the detectors is achieved periodically (1/5400 Hz) with a maintenance procedure which consists in relay changeover and the biasing of detectors via DAQ. Between two maintenance procedures, detectors stay floating. As a consequence, the response of the system to a charge deposit is modeled by a Heaviside function, centered on the start time of the event. An ionization energy baseline resolution FWHM of 500 eV is achieved by integrating the signal on a large time range (1 s). The ionization resolution is limited by the current noise of the FET, introducing a 1/f noise below 1 kHz. As all electrodes are read out, the common noise can be measured at the digitizing rate of 100 kHz, and subtracted to all channels. By applying this correction, the peak structures due to the correlated microphonic shown in Fig.2.10 can be substantially reduced.

Chapter 2: The EDELWEISS experiment

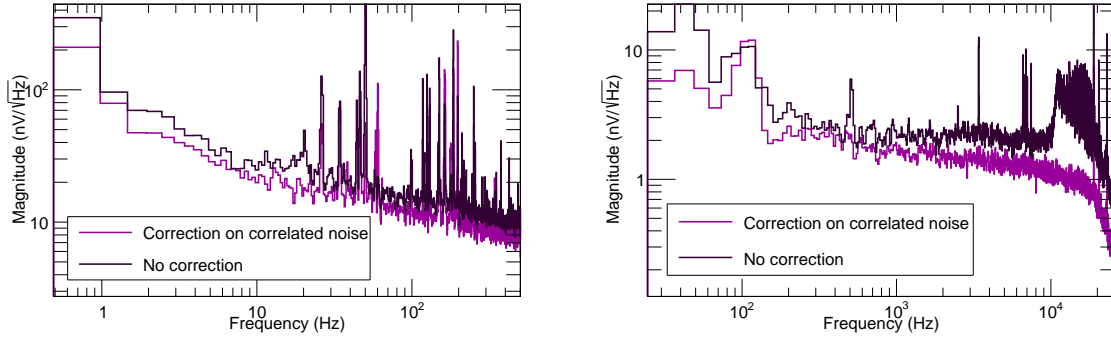


Figure 2.10 – Average noise amplitude (in nV/\sqrt{Hz}) as a function of frequency of the ionization channel for an EDELWEISS detector. The black histogram corresponds to the noise before the correlated noise correction and the purple histogram to the noise after the correction. Left: frequencies below 500 Hz. Right: high frequency part.

III.2.2 Heat channel readout

The heat signal is measured with NTD sensors, as described in section II.3. Typically resistance values at 18 mK are a few $M\Omega$ for a current bias of a few nA corresponding to a sensitivity of ~ 50 nV/keV for EDELWEISS detectors. As shown in section II.2.2 of chapter 3, heat signals typically present a rise time of ~ 10 ms and two decay time constants of ~ 10 and ~ 100 ms respectively. Fig.2.11 shows the noise plateau of the readout electronics at 1-3 nV/\sqrt{Hz} rms. The level of this white noise is due, in roughly equal parts, to the FET noise and the Johnson noise of the NTD resistance. Together with the signal response, shown also in Fig.2.11, these lead to a heat energy resolution baseline of 300 eV.

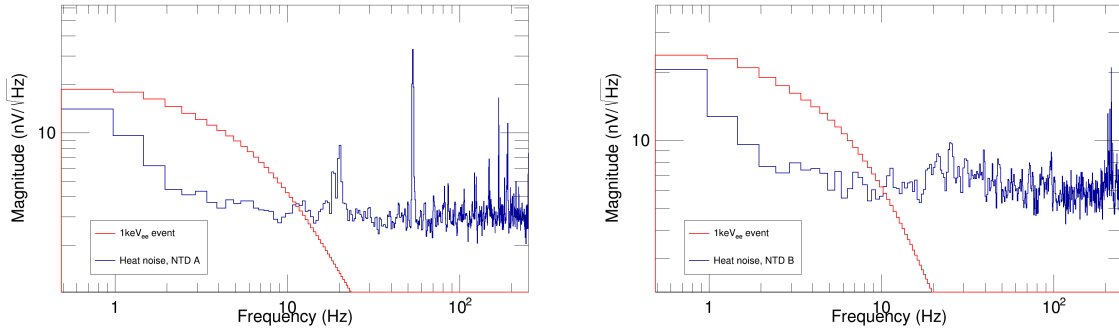


Figure 2.11 – Noise amplitude (in nV/\sqrt{Hz}) of a heat channel for an EDELWEISS detector with two heat sensors: NTD A (left) and NTD B (right). The red histograms correspond to 1 keV_{ee} (equivalent-electron) heat energy event spectra.

To obtain this resolution of 300 eV, the $1/f$ noise must be kept to a minimum. To reject the common-mode noise giving rise to a large $1/f$ noise, the EDELWEISS NTD readout adopts a square modulation method. Instead of biasing the NTD with a fixed current, a square excitation is injected at a frequency of 500 Hz. The resistance value during one cycle is derived from the difference in voltage bias between the negative and positive current portions of the cycle. This differential measurement is very efficient at removing common noise. However, thermal noise is not rejected, and in the presence of strong vibrations the $1/f$ noise degrades the energy resolution well above the 300 eV that could be obtained if it were only for the noise plateau.

Chapter 2: The EDELWEISS experiment

The noise spectra in Fig.2.11 show relatively good $1/f$ noise conditions, with a noise amplitude of $10 \text{ nV}/\sqrt{\text{Hz}}$ at 1 Hz.

To characterize the impact of the electronics on the noise of the heat channels, a thermal model will be detailed in section V and applied for EDELWEISS FID800 detectors (presented in section IV.1).

III.2.3 DAQ (Data Acquisition system)

The DAQ controls the bolometer boxes and thus the voltage bias applied on the thermal sensors and electrodes. The digitized data flow produced by the bolometer boxes is also managed by the DAQ. It performs triggering to select and store data on disk.

The user interface program used for data taking and to manage the EDELWEISS DAQ hardware configuration is called SAMBA, as illustrated in Fig.2.12. Input/output between the DAQ and SAMBA is transmitted via ethernet, allowing it to run in parallel on several computers. Data flow is distributed over multiple MAC computers, each controlling up to twelve detectors. The datasets recorded by each computer and the muon veto system are synchronized using the unique $10 \mu\text{s}$ time stamp distributed by the DAQ system.

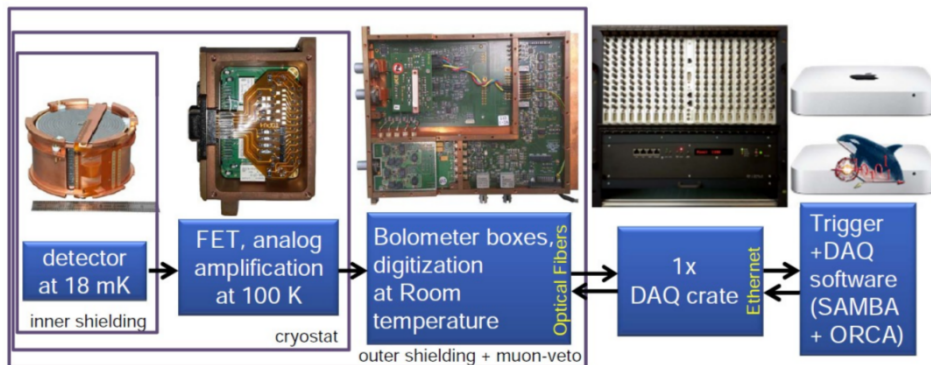


Figure 2.12 – Scheme of the acquisition system, taken from [75]. An analog amplification connected to BB allows to read out detectors. BB are linked to the DAQ crate by optical fibers. Then the user interface program SAMBA reads data.

The SAMBA program is highly flexible. The three MAC computers used for data taking are operated independently. This program allows to manage:

- the list of detectors to be readout,
- their corresponding bolometer boxes and associated DAQ crate channels,
- the voltage bias values for the electrodes,
- the frequency and amplitude of the heat excitations,
- the software-controlled gains of the digitizers.

SAMBA controls also the trigger, i.e the conditions under which fixed length time interval of the data streams are stored to disk, forming what defines an event. Triggered event is an event for which one or the two filtered heat channel signals are above a threshold value. The filter is a first order high-pass filter combined with a convolution function with a reference pulse.

Chapter 2: The EDELWEISS experiment

The cut frequency of each filter is optimized individually on each channel. In a WIMP search run, the value of the trigger threshold is continuously adapted by SAMBA to keep the trigger rate on each channel to 0.05 Hz. To do so, SAMBA counts the number of events recorded every minute and every 10 minutes. If there are less than 3 events/minute, the trigger level is decreased by 15 %. If there are more than 30 events/minute, the trigger level is increased by a fixed amount. The trigger level values are stored continuously so that its level can be monitored for each event.

SAMBA performs the demodulation of the NTD data when a channel exceeds a threshold value, a time tag is registered in order to be compared with other channels to look for coincidences. The data stored on disk are 2.048 second long for heat channels traces, sampled at 0.5 kHz and centered on the time of the trigger. For the ionization channel, the recorded traces have 40.96 ms for the raw 100 kHz ionization data. As the best signal-to-noise ratio for the ionization channel is obtained at low frequency, 2.048 s long ionization samples are also stored for each event. These long samples are down sampled to 1 kHz by averaging 100 kHz samples by group of 100. To study noise, trigger and coincidences, data of neighboring detectors are also saved. Each event is stored with values indicating the bit pattern of the triggered channels, the level of the trigger threshold for each channel, and the amplitude of each channel in the same units as the threshold.

The data stored on disk for each trigger are the heat channels in a ± 1.024 s window around the trigger time. For the ionization channels, the acquisition window is (-30.72 ms, +10.24 ms) because their risetime and decay time are around 100 ns.

IV EDELWEISS FID800 detectors

IV.1 FID design

EDELWEISS-III uses Fully Inter-Digitized (FID) detectors which are high purity Ge cylindrical crystals with an average mass of 850 g. Operating at 18 mK, their size is 4 cm in height and 7 cm in diameter. Equipped with Al electrodes and thermal sensors, they can measure both heat and ionization signals arising from particle interactions. This allows to discriminate electron recoils from nuclear recoils on an event-by-event basis. Each FID equipped crystal is surrounded by a low radioactivity copper casing to shield against infrared radiation, held by Teflon[®] clamps. A gold pad evaporated directly onto the crystal (with typically 20 gold wires of 25 μm diameter each) establishes a thermal connection to the detector casing (acting as a thermal bath) and allows to return detectors to the equilibrium temperature. As mentioned previously, heat measurements are performed by two NTD Ge sensors [85], glued on the center of the top and bottom electrodes. The specificity of using two thermal sensors allows to discriminate NTD events, i.e events measured by only one NTD. A thermal model has been performed to study the heat measurement of the FID800 detectors (see section V).

Charge signals are measured with two sets of evaporated electrodes described in details in next section. To avoid surface leakage current, a passivation treatment is made with a 60 to 80 nm amorphous layer of hydrogenated Ge deposited only under the electrodes, the surface between them being left unprocessed. While the detector is well insulated against leakage current via its readout electronics, another type of leakage can prevent its operation as a bolometer. A leakage current of the order of 1 pA between adjacent electrodes results in a Joule heating of approximately 1 MeV/s, incompatible with the detection of events in the keV range. The leakage between electrodes can occur because of charges accumulated in traps close to the surfaces. This is one of the reasons why, every 48 h, the electrodes are all grounded and the detector exposed to two very strong ^{60}Co γ -ray sources during one hour, to neutralize the

Chapter 2: The EDELWEISS experiment

accumulated space charges. The leakage can also occur because of surface defects, or, when a very large field is applied to trap charges displaced by the field. A solution to leakage currents due to surface defects is to apply a preventive post-processing XeF_2 pulsed dry etching of the detector surface after evaporating the electrodes. The chemical reaction is:



with removable gaseous products. Etched detectors still show leakage currents, but only for much higher voltage bias difference between adjacent electrodes, as described hereafter.

IV.2 Evaporated electrodes

FID800 bolometers are equipped with interleaved electrodes, whose a detailed description is illustrated in Fig.2.13. The biasing scheme is based on the co-planar grid technique for event localization [86]. The Al electrodes are 200 nm thick and are evaporated on both flat and

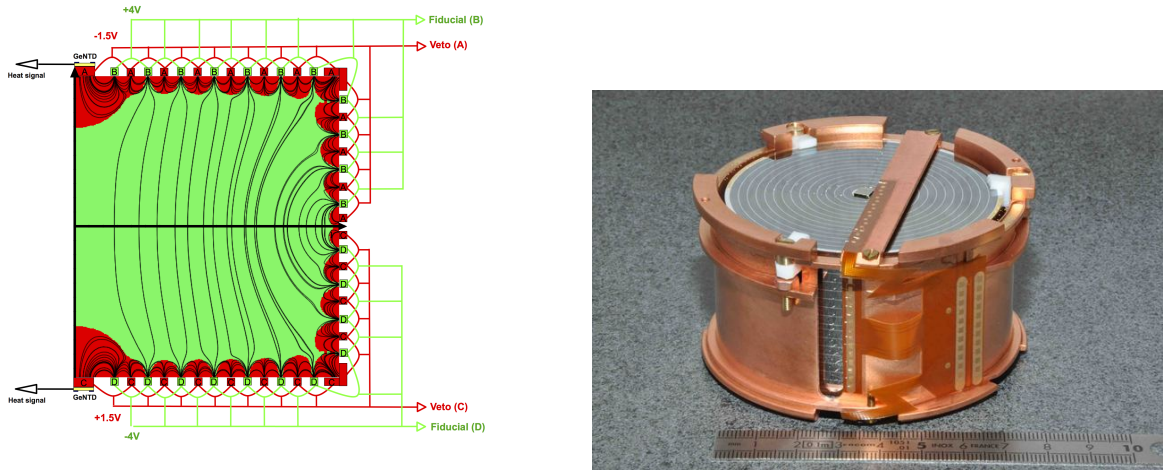


Figure 2.13 – Left: scheme of the electric field induced by the voltage biasing of the Al electrodes shown on the surface of the bolometer. The so-called fiducial electrodes (B/D) are at ± 4 V whereas the veto electrodes (A/C) are at ∓ 1.5 V. Events occurring near the surface of the detector (red zone) have their energy collected by a veto and a fiducial electrodes (A and B or C and D). For an event occurring in the fiducial volume of the detector (the green zone), only fiducial electrodes on each planar surface (B and D) collect the induced charge signal. Right: photo of a FID800 detector.

cylindrical surfaces, in the form of annular concentric rings $150 \mu\text{m}$ wide with a 2 mm pitch. The concentric electrodes are connected electrically such that all odd-numbered rings are connected to each other as well as all even-numbered rings. Voltage biasing thus requires four different voltage biases to measure the charge signal, with two sets of electrodes on both faces of the detectors. This full coverage of the FID detectors with interleaved electrodes allows to fully map the volume of the EDELWEISS detectors. Indeed, a higher electric field operates along both flat and cylindrical surfaces allowing to efficiently discriminate bulk and surface events. For example, events taking place near the border between the surface and bulk region exhibit charge sharing between more than two measurement channels and are also tagged and eventually rejected by adapted selection cuts. In the EDELWEISS-III phase, electrodes are alternately polarized at ± 4 V and ∓ 1.5 V on one face and with opposite signs on the other face, as illustrated in Fig.2.13.

Chapter 2: The EDELWEISS experiment

This corresponds to a voltage bias range high enough to provide sufficient electric field inside the crystal for charge drift [87], but low enough in order not to spoil the electronic recoil rejection by an excessive Luke-Neganov effect (see section VI). With this method, the rejection factor for interactions associated to radon-daughter induced α/β radioactivity is better than 4×10^{-5} .

The number of electron/hole pairs is determined by $N = \frac{E_R}{\epsilon}$ with E_R the recoil energy defined in section IV.3 and ϵ the average energy for the creation of one electron/hole pair. The value of ϵ depends on the recoil nature (electronic or nuclear). For an electronic recoil, $\epsilon_\gamma = 3$ eV and, for a nuclear recoil ϵ_n is a function of the energy and is approximately 12 eV [81]. Hence, a nuclear recoil produces less electron/hole pairs than an electronic recoil of the same energy. The ionization energy is measured in keV_{ee}, which means equivalent-electron, using calibrations of the signal with known γ -ray sources.

The EDELWEISS detectors can operate in two modes:

- FID mode, where a voltage bias less than 10 V is applied between opposite electrodes (fiducial electrodes),
- planar mode, where a higher voltage bias is applied across the two opposite face electrodes (for example, A/B are at +50 V and C/D at -50 V for a 100 V voltage bias) corresponding to the HV mode described in section VI.

IV.3 Combined measurement: ionization and heat

The combined measurement of ionization and heat energy allows to determine the recoil energy E_R induced by an incident particle, independently of its nature, as well as its ionization yield (or quenching factor) Q on an event-by-event basis. The ionization energy E_{ion} and the heat energy E_{heat} are expressed as a function of the recoil energy [81]:

$$E_{ion}^i = Q^i E_R \text{ and } E_{heat}^i = E_R \frac{(1 + Q^i \frac{V}{\epsilon_\gamma})}{1 + \frac{V}{\epsilon_\gamma}} \quad (2.19)$$

where i corresponds to the nature of the recoil and V is the voltage bias. Inverting these equations leads to the recoil energy:

$$E_R = E_{heat} \left(1 + \frac{V}{\epsilon_\gamma} \right) - E_{ion} \frac{V}{\epsilon_\gamma} \quad (2.20)$$

and the quenching factor:

$$Q = \frac{E_{ion}}{E_R} = \frac{E_{ion}}{E_{heat}(1 + \frac{V}{\epsilon_\gamma}) - E_{ion} \frac{V}{\epsilon_\gamma}} \quad (2.21)$$

Note that the Luke-Neganov effect³ contribution has to be subtracted to the heat energy to obtain the recoil energy as:

$$E_{heat,total} = E_R + E_{Luke} \quad (2.22)$$

The quenching factor as a function of the recoil energy is illustrated in Fig.2.14. Events induced by an electronic interaction have a quenching value of 1 by construction, whereas a nuclear recoil band is parametrized as $\langle Q^n(E_R) \rangle = 0.16 E_R^{0.18}$ [81]. The other events outside the gaussian

³An elevation of temperature induced by the charge drifting in the crystal. It will be explained in section VI.

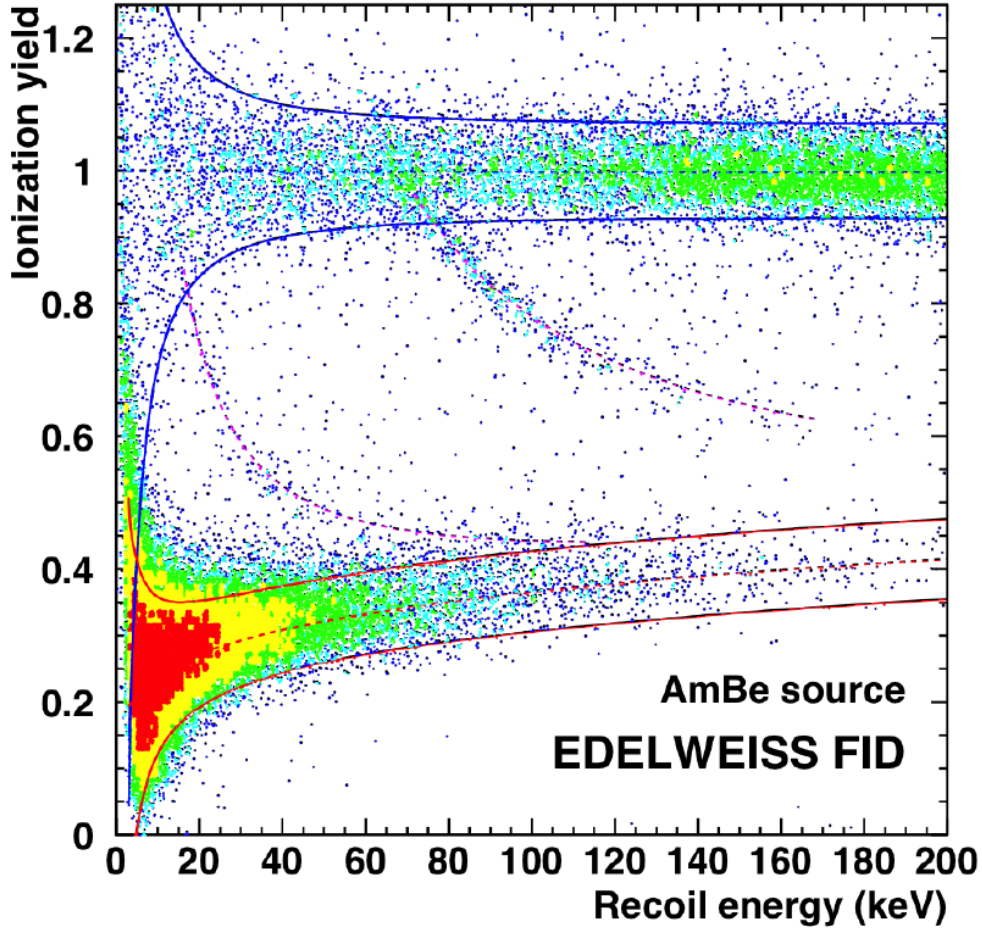


Figure 2.14 – Ionization yield as a function of the recoil energy for a FID800 detector from a neutron calibration using an AmBe source. The two red (blue) lines delimit the 90% C.L. nuclear (electronic) recoil band and the purple dashed lines correspond to inelastic scattering of neutrons on the first (13.28 keV) or the third (68.75 keV) excited state of ^{73}Ge .

repartitions around $Q = 1$ and $Q = 0.16E_R^{0.18}$ are inelastic recoils and surface events suffering an incomplete charge collection. To define the electronic and nuclear recoil bands with a chosen confidence level, it is necessary to calculate the quenching resolution. By imposing that heat σ_{heat} and ionization σ_{ion} resolutions are decorrelated, it is possible to write:

$$\sigma_{Q^i}^2 = \left(\frac{\delta Q^i}{\delta E_{heat}} \right) \sigma_{heat}^2 + \left(\frac{\delta Q^i}{\delta E_{ion}} \right) \sigma_{ion}^2 + C^2 \quad (2.23)$$

where the C^2 term describes the intrinsic width of the nuclear band, due to straggling in the nuclear energy loss with $C = 0.035$ [81]. The standard deviation is obtained with Eq.2.21 and Eq.2.23:

$$\sigma_{Q^i}(E_R) = \frac{1}{E_R} \sqrt{\left[\left(1 + \langle Q^j \rangle \frac{V}{3} \right) \sigma_{ion}(E_R) \right]^2 + \left[\left(1 + \frac{V}{3} \right) \langle Q^j \rangle \sigma_{heat}(E_R) \right]^2 + C^2} \quad (2.24)$$

Chapter 2: The EDELWEISS experiment

In this way, the different bands are described by:

$$(\langle Q^j(E_R) \rangle - \kappa \times \sigma_{Q^j}(E_R)) < Q(E_R) < (\langle Q^j(E_R) \rangle + \kappa \times \sigma_{Q^j}(E_R)) \quad (2.25)$$

with κ the chosen confidence level in number of sigma. The electronic recoil zone is similarly defined as $\pm \kappa \sigma_{Q^\gamma}$, where:

$$\sigma_{Q^\gamma}(E_R) = \frac{(1 + \frac{V}{3})}{E_R} \sqrt{\sigma_{ion}^2(E_R) + \sigma_{heat}^2(E_R)} \quad (2.26)$$

using $Q^\gamma = 1$. For the nuclear recoil zone, the straggling and multiple scattering cause an enlargement because of the dependence in the recoil energy of the quenching. The scattering corresponds to the statistical fluctuations originating from the number of collisions required to the Ge nucleus recoil to be stopped. With these contributions, the standard deviation associated to the nuclear recoil zone becomes:

$$\sigma_{Q^n}(E_R) = \frac{1}{E_R} \sqrt{\left[\left(1 + \langle Q^n \rangle \frac{V}{3} \right) \sigma_{ion}(E_R) \right]^2 + \left[\left(1 + \frac{V}{3} \right) \langle Q^n \rangle \sigma_{heat}(E_R) \right]^2 + C^2} \quad (2.27)$$

The quenching factor for nuclear recoils is described by the Lindhard model [88]. It calculates the energy loss of ions in matter and gives a prediction for Q values. This effect has been studied as a function of the recoil energy for germanium absorbers in [89]. In these studies, the detectors are calibrated with a gamma source and then exposed to a neutron source. The parametrization $Q^n(E_R) = 0.16E_R^{0.18}$ has been checked to be satisfactory.

The heat and ionization resolutions depend on the intrinsic characteristics of the detector but also on the readout electronics and cryogenic system.

V Thermal modeling of FID800 bolometers

A dedicated study of the heat signals in the EDELWEISS detectors has been made in order to determine the sensitivity of the FID800 detectors [84]. The model considers seven independent elements. The FID800 is composed of a high purity germanium crystal and one NTD on each planar surface. Gold wires between copper casing and the crystal thermally link the absorber to the cryostat. The schematic of the 7 elements of the system associated to FID800 detector is shown in Fig.2.15. These elements are:

- the absorber, i.e the Ge crystal (in green), with no electron in its conductance band, approximated by one block with a heat capacity C_{ab} and a temperature T_{ab} .
- The cryostat (in gray), at a fixed temperature T_{CRYO} .
- Two NTD A and B, polarized at currents $I_{p,A}$ and $I_{p,B}$. Electron and phonon populations inside the NTD are decoupled and are modeled by two distinct blocks (in pink for NTD A and violet for NTD B), in communication with each other by a thermal link G_{ep} . NTD are linked to the absorber via a glue spot with a conductance of G_{ap} . Each NTD electron system has a temperature $T_{e,i}$ and a heat capacity $C_{e,i}$, with $i = A, B$ the considered NTD. This is similar for phonon systems ($T_{p,i}$ and $C_{p,i}$).
- a hypothetical parasitic heat capacity (in yellow) linked to the absorber, with T_x and C_x , has been added in order to fully explain the data as detailed in [84].

Chapter 2: The EDELWEISS experiment

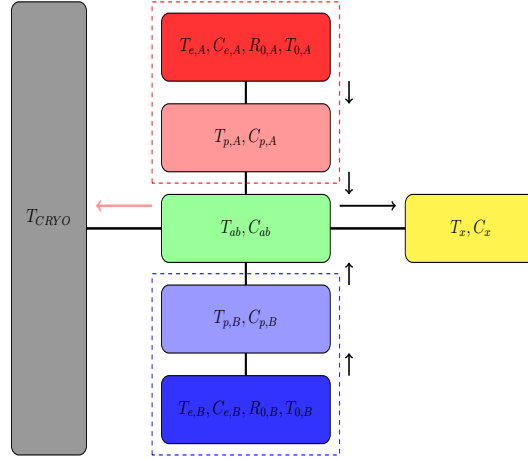


Figure 2.15 – Schematic of a FID800 detector. The gray block represents the temperature of the cryostat. Each NTD is represented by dashed block and have an electron bath and a phonon bath. The absorber bath is represented in green. Each element has a characteristic temperature T as well as a heat capacity C . A seventh element (in yellow) with a heat parasitic capacitance C_x has been required to fit correctly data.

All these blocks are connected to each other via thermal links characterized by different conductances G . The absorber is also connected to the bath corresponding to the cryostat which is kept at a fixed temperature T_{CRYO} . The heat capacitances of the glue spots, the wirebonds and the gold pads (for the thermal leak) are considered to be negligible. The polarizations of NTD induce a Joule power $P_{J,i} = I_{p,i}^2 R_i(T_{e,i})$ (with i the considered NTD), which dissipates through all blocks of the system up to the cryostat. The power dissipation between the phonon bath and the electron bath depends on decoupling phenomenon inside NTD. Experimentally, this power dissipation is modeled as:

$$P_{ep,i} = V_{s,i} g_{ep,i} (T_{e,i}^{n_i} - T_{p,i}^{n_i}) \quad (2.28)$$

with $V_{s,i}$ the NTD volumes, $g_{ep,i}$ the electron-phonon coupling constants and n_i a power that depends on NTD characteristics. Due to ballistic exchanges between electrons and phonons, the exponent should be superior to one (on contrary of a diffusive system). The equilibrium of the electron bath is described by:

$$C_{e,i} \frac{dT_{e,i}}{dt} = P_{J,i} - P_{ep,i} = I_{p,i}^2 R_i(T_{e,i}) - V_{s,i} g_{ep,i} (T_{e,i}^{n_i} - T_{p,i}^{n_i}) \quad (2.29)$$

For the phonon bath, the exchanges between electrons and phonons in the NTD and between phonons and the absorber must be taken into account. A power $P_{ep,i}$ comes from the electron bath and a power $P_{ap,i} = G_{ap,i}(T_{p,i} - T_a)$ dissipated toward the absorber. As this thermal transfer is diffusive ($P \propto \Delta T$, i.e no coupling between the phonon bath and the absorber), the equation describing the process is:

$$C_{p,i} \frac{dT_{p,i}}{dt} = P_{ep,i} + P_{ap,i} = V_{s,i} g_{ep,i} (T_{e,i}^{n_i} - T_{p,i}^{n_i}) - G_{ap,i} (T_{p,i} - T_a) \quad (2.30)$$

The parasitic heat capacity C_x linked to the absorber bath can be described by:

$$C_x \frac{dT_x}{dt} = G_{ax} (T_a - T_x) \quad (2.31)$$

Chapter 2: The EDELWEISS experiment

The equation for the absorber bath considers the sum of the different powers coming from NTD as well as the parasitic heat capacity. A non-diffusive process toward the cryostat is added with $P_{ab} = S_{Au}g_k(T_a^{n_k} - T_{CRYO}^{n_k})$, coming from the decoupling between absorber and thermal bath of the cryostat. S_{Au} is the surface of the gold pad of the thermal link, and g_k is its Kapitza conductance by surface units. All this leads to:

$$\begin{aligned} C_a \frac{dT_a}{dt} &= P_{ap,1} + P_{ap,1} + P_{ab} \\ &= G_{ap,1}(T_{p,1} - T_a) + G_{ap,2}(T_{p,2} - T_a) - S_{Au}g_k(T_a^{n_k} - T_{CRYO}^{n_k}) - G_{ax}(T_a - T_x) \end{aligned} \quad (2.32)$$

A system of 6 equations is built, with different free parameters to be determined. By considering small variations near an equilibrium state for all bath temperatures, these can be determined by imposing $\frac{dT}{dt} = 0$ such as:

- for electron baths:

$$\overline{T_{e,i}} = \left(\frac{I_{p,i}^2 R_i(T_{e,i})}{V_{s,i} g_{ep,i}} - \overline{T_{p,i}^{n_i}} \right)^{\frac{1}{n_i}} \quad (2.33)$$

- for phonon baths:

$$\overline{T_{p,i}} = \frac{I_{p,i}^2 R_i(T_{e,i})}{G_{ap,i}} + \overline{T_a} \quad (2.34)$$

- for the absorber bath:

$$\overline{T_a} = \left(\frac{I_{p,1}^2 R_1(T_{e,1}) + I_{p,2}^2 R_2(T_{e,2})}{S_{Au}g_k} + \overline{T_{CRYO}^{n_k}} \right)^{\frac{1}{n_k}} \quad (2.35)$$

The coupling between these different temperatures and their non linearity imposes to use numerical resolution method (fixed point iteration). Considering the steady state ($\frac{dT}{dt} = 0$), the parameters n_i and $g_{ep,i}$ can be determined with the following equations:

$$I_{p,i}^2 R_i(T_{e,i}) = V_{s,i} g_{ep,i} (T_{e,i}^{n_i} - T_{p,i}^{n_i}) \quad (2.36)$$

$$V_{s,i} g_{ep,i} (T_{e,i}^{n_i} - T_{p,i}^{n_i}) = G_{ap,i} (T_{p,i} - T_a) \quad (2.37)$$

$$G_{ap,1}(T_{p,1} - T_a) + G_{ap,2}(T_{p,2} - T_a) - S_{Au}g_k(T_a^{n_k} - T_{CRYO}^{n_k}) - T_{CRYO}^{n_k} - G_{ax}(T_a - T_x) = 0 \quad (2.38)$$

Fig.2.16 shows the determination of the n_i parameter by voltage biasing a NTD and keeping the other one fixed at low current bias. One rewrites equations 2.29 to 2.32 in the following form:

$$\frac{d\delta T}{dt} = -M\delta T + F(t - t_0) \quad (2.39)$$

where $F(t - t_0)$ represents any kind of external perturbation power in the system, including physical events with energy sharing among the different baths, and M is a (6,6) matrix describing the thermal couplings between the seven elements:

$$M = \begin{pmatrix} \frac{G_{epA}^e}{C_{eA}} - \alpha_A \frac{I_{pA}^2 \overline{R}_A}{C_{eA} \overline{T}_{eA}} & -\frac{G_{epA}^p}{C_{eA}} & 0 & 0 & 0 & 0 \\ -\frac{G_{epA}^e}{C_{pA}} & -\frac{G_{epA}^p + G_{apA}}{C_{pA}} & -\frac{G_{apA}}{C_{pA}} & 0 & 0 & 0 \\ 0 & -\frac{G_{apA}}{C_a} & \frac{G_{apA} + G_{apB} + G_{ab} + G_{ak}}{C_a} & -\frac{G_{apB}}{C_a} & 0 & -\frac{G_{ak}}{C_a} \\ 0 & 0 & -\frac{G_{apB}}{C_{pB}} & -\frac{G_{epB}^p + G_{apA}}{C_{pB}} & -\frac{G_{epB}^e}{C_{pB}} & 0 \\ 0 & 0 & 0 & -\frac{G_{epB}^e}{C_{eB}} & \frac{G_{epB}^e}{C_{eB}} - \alpha_A \frac{I_{pB}^2 \overline{R}_B}{C_{eB} \overline{T}_{eB}} & 0 \\ 0 & 0 & -\frac{G_{ak}}{C_k} & 0 & 0 & \frac{G_{ak}}{C_k} \end{pmatrix}$$

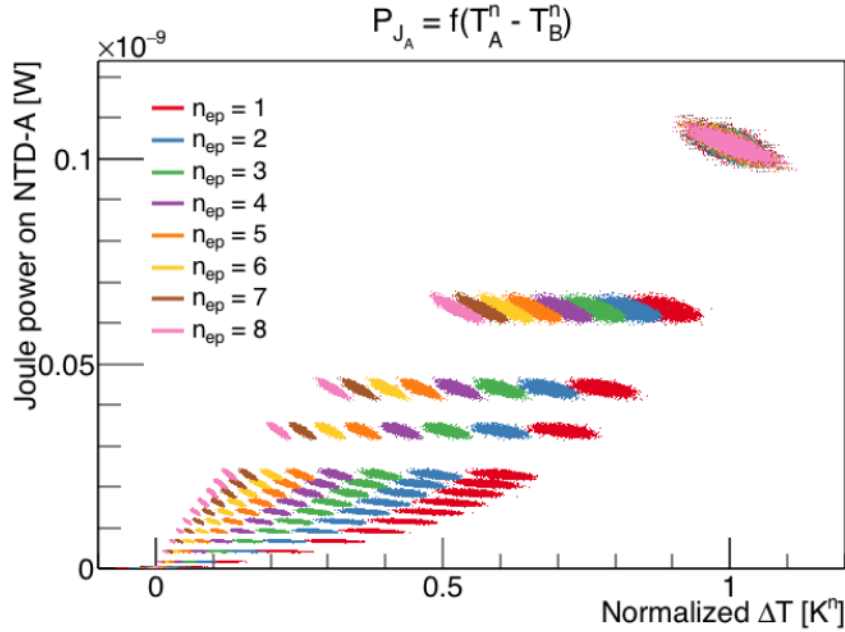


Figure 2.16 – Normalized temperature difference between NTD A and NTD B as a function of Joule power for different values of $n_{ep}(n_i)$.

The degeneracy between the absorber and the NTD events can be broken cross-checking the two NTD signals as illustrated in Fig.2.17. For an event occurring in one NTD, there is no signal in the other one (Fig.2.17 left), while an event occurring in the absorber is seen with more or less the same amplitude in both NTD (Fig.2.17 right). The thermal model describes successfully the pulses observed for events occurring either in the absorber or in one of the two NTD, with a set of parameters [84] as shown in Fig.2.17: C_{eA} , C_{pA} , C_a , C_{eB} , C_{pB} , C_k , G_{ak} and the rise time of pulses.

The characterization on the FID800 detectors allowed to help the R&D group in Lyon, focusing on heat resolution improvement to reach an energy resolution of 100 eV necessary to probe low-mass WIMP. Another important improvement needed to probe low-mass WIMP is the low threshold as nuclear recoils will be below 1 keV. This can be achieved by taking into account the Luke-Neganov effect, described in next section.

VI Luke-Neganov effect in FID800 detectors

VI.1 Principle

As the charges drift under the influence of the applied electric field, an additional heat is dissipated in the crystal in the form of phonons. This mechanism, called Luke-Neganov effect [63], is similar to the Joule effect in metals and resistances. As electrons constantly dissipate their energy to the phonons, the electric force must provide an equivalent work. The heat provided to the phonons is thus equal to the work qV provided by the electric field with $q = e$ the elementary charge. For an electron/hole pair created at a coordinate \vec{r}_i and drifting to the cathode \vec{r}_h and the anode \vec{r}_e , the applied work is:

$$W = e \int \vec{E} d\vec{r} - e \int \vec{E} d\vec{r} = -e \int \frac{\delta V}{\delta \vec{r}} + e \int \frac{\delta V}{\delta \vec{r}} = e(V(\vec{r}_e) - V(\vec{r}_h)) \quad (2.40)$$

Chapter 2: The EDELWEISS experiment

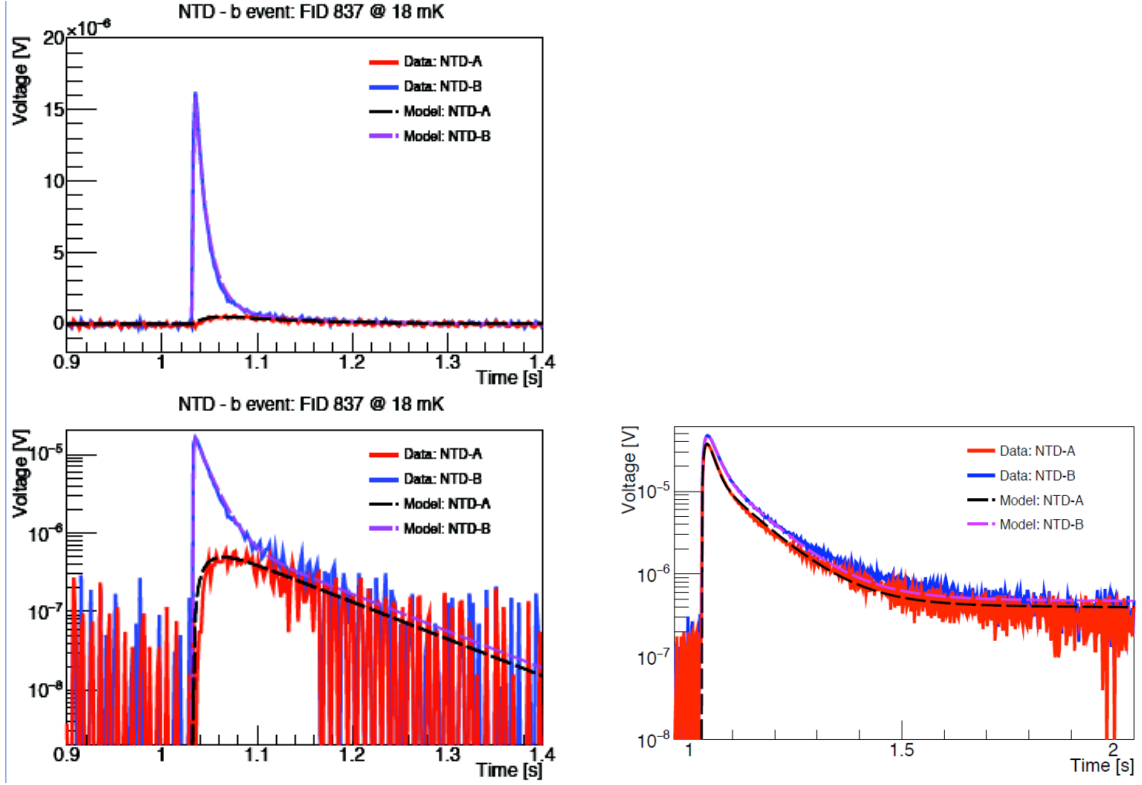


Figure 2.17 – Left: signal measured for an event occurring in one NTD (NTD B) with no signal in the other (NTD A). Top: linear scale. Bottom: log scale. Right: signal measured for an event occurring in the absorber and seen with nearly the same amplitude in both NTD. For all plots: in red, pulse recorded in the NTD A, in blue pulse recorded in the NTD B. Thermal model description of the response of each NTD are in black and magenta. In the two cases, the data and the model are in good agreement.

where e is the elementary charge. The total work depends on the number of charges collected N and the potential difference between electrodes V (voltage bias). The heat energy provided by the Luke-Neganov effect E_{Luke} is thus:

$$E_{Luke} = N^j V = \frac{E_R}{\epsilon^j} V \quad (2.41)$$

where j corresponds to the recoil type. Thus, the total heat energy measured by the heat channels $E_{heat,total}$ is the recoil energy E_R to which is added the Luke-Neganov effect:

$$E_{heat,total}^\gamma = E_R + \frac{E_R V}{\epsilon_\gamma} = E_R \left(1 + \frac{V}{\epsilon_\gamma} \right) \text{ for an electronic recoil} \quad (2.42)$$

$$E_{heat,total}^n = E_R + \frac{E_R V}{\epsilon_n} = E_R \left(1 + \frac{V}{\epsilon_n} \right) = E_R \left(1 + Q^n \frac{V}{\epsilon_\gamma} \right) \text{ for a nuclear recoil} \quad (2.43)$$

where $Q^j = \epsilon^\gamma / \epsilon^n$ is the quenching factor defined in section IV.3. The potential V applied to surface and fiducial events differs, creating different Luke-Neganov effects. In the FID mode described in section IV.2, $V = 8$ V for fiducial events and 5.5 V for surface events. In practice, the heat signal is calibrated for one type of particle (γ) selecting fiducial events. The heat

Chapter 2: The EDELWEISS experiment

energy is thus normalized in keV_{ee} with:

$$E_{heat}^i = \frac{E_{heat,total}^i}{1 + \frac{V}{\epsilon_\gamma}} = E_R \frac{(1 + Q^i \frac{V}{\epsilon_\gamma})}{1 + \frac{V_{fid}}{\epsilon_\gamma}} \quad (2.44)$$

where $V_{fid} = V = 8 \text{ V}$ for a fiducial event, and $V = 5.5 \text{ V}$ for a surface event in FID mode and $V = V_{fid}$ in planar mode.

VI.2 High-voltage optimization in FID800 detectors

The discrimination derives from the difference of the heat-ionization ratio as a function of the type of the recoil. This ratio depends on the voltage bias V because of the Luke-Neganov effect as:

$$r = \frac{E_R(1 + \frac{V}{\epsilon_\gamma})}{\frac{E_R}{\epsilon_\gamma}} \times \frac{\frac{E_R}{\epsilon_n}}{E_R(1 + \frac{V}{\epsilon_n})} = \frac{\epsilon_\gamma + V}{\epsilon_n + V} \quad (2.45)$$

This ratio evolves as: $r \xrightarrow[V \rightarrow \infty]{} 1$. In other words, the discrimination power decreases as the voltage bias increases, as shown in Fig.2.18. The electronic and nuclear recoil bands, shown on the (E_{ion}, E_{heat}) plane, overlap at 100 V.

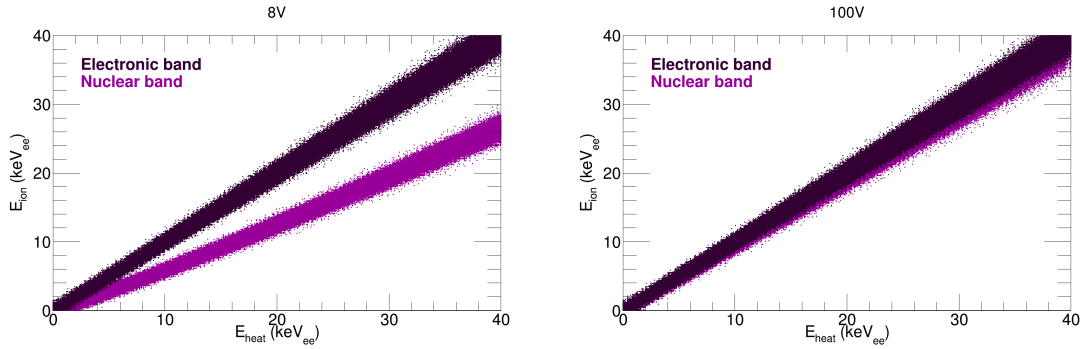


Figure 2.18 – Left: MC simulation of electronic recoil events (in dark purple) and nuclear recoil events (in light purple) for a detector operating at 8 V voltage bias in the (E_{ion}, E_{heat}) plane. Right: MC simulation of electronic recoil events (in dark purple) and nuclear recoil events (in light purple) for a detector operating at 100 V voltage bias. An overlapping occurs when detectors are at high voltage, thus the discrimination power between electronic and nuclear recoils is lost.

At large voltage bias V , the Luke-Neganov effect is the main component of the heat measurement and gives a measurement of the ionization. Furthermore, applying very high voltage on FID800 detectors implies operating in planar mode. In this way, there is no possible rejection of surface events, i.e a detailed analysis has to take into account a higher number of surface events than with the FID mode. However, the heat energy resolution is in keV_{ee} , and the corresponding trigger threshold is greatly improved by a factor $\frac{1}{(1+\frac{V}{\epsilon_\gamma})}$. This strategy of favoring low threshold with respect to discrimination by applying a high voltage bias on the electrodes has been first pioneered by the CDMSlite experiment [90] and proven to be the optimal strategy in EDELWEISS detectors for WIMP masses below $10 \text{ GeV}/c^2$ [91]. In Fig.2.19, the heat measurement spectra for different voltage biases of the FID803 detector is shown. It corresponds to data obtained with a ^{133}Ba source calibration. The expected 356 keV γ -ray of the source

Chapter 2: The EDELWEISS experiment

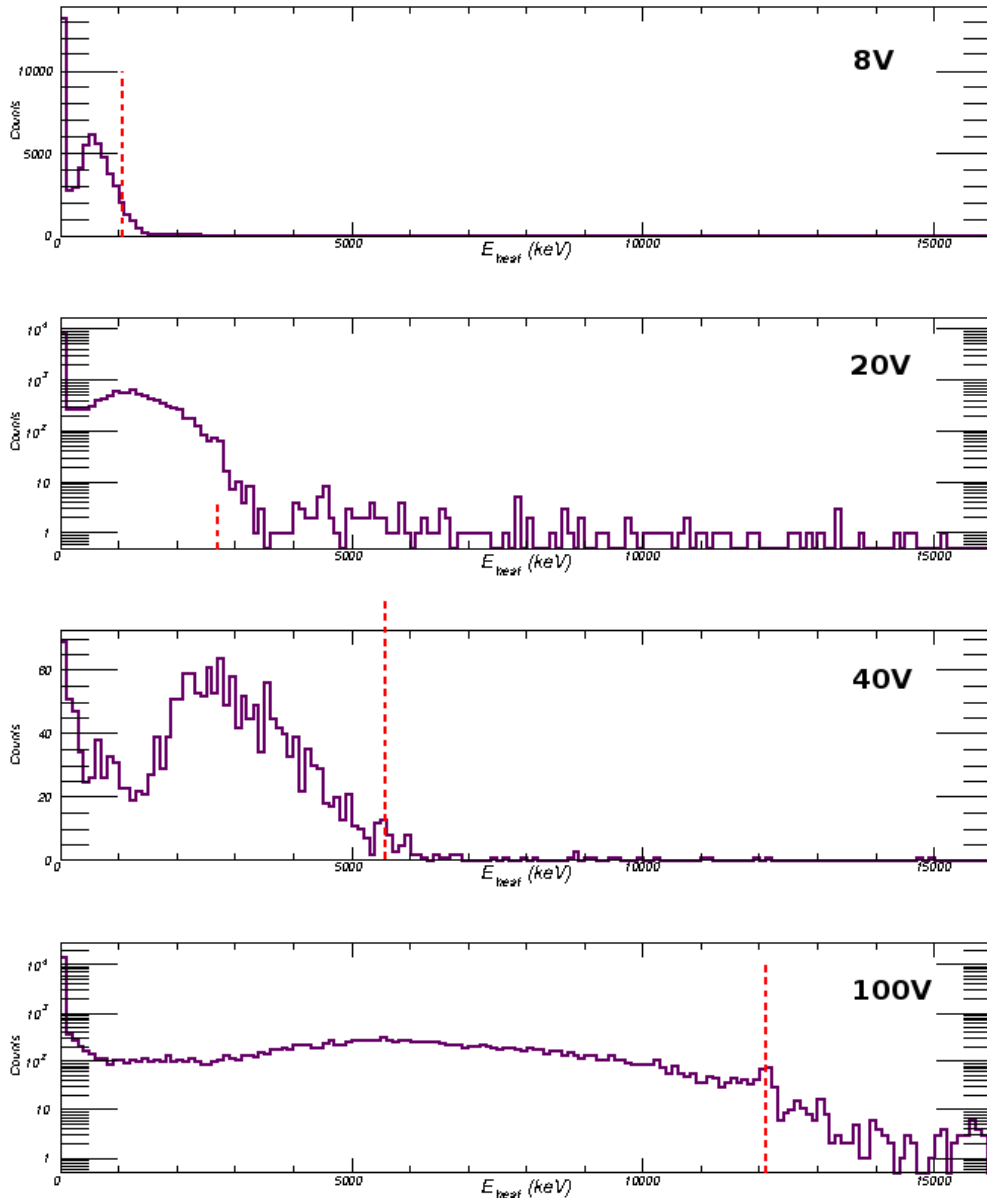


Figure 2.19 – Total heat measurement spectra (in keV) for different voltage biases of FID803 detector during a calibration run with a ^{133}Ba source. The red dashed lines correspond to the 356 keV γ -ray of the source. Top to bottom: data at 8 V, 20 V, 40 V and 100 V. At 100 V, the heat energy is increased by a factor 35 with respect to 0 V.

is the red dashed line. Its position varies with a factor $(1 + V)/3$ as expected. The average threshold obtained at these voltage biases has been reported in table 2.3.

Although the bolometer boxes allow $[+70; -70]$ V polarizations on the electrodes, cables have been tested only up to 100 V. Hence the highest voltage bias for a FID detector has been limited to 100 V for the future analyses.

Chapter 2: The EDELWEISS experiment

Voltage bias (V)	8	20	40	100
Threshold (keV_{ee})	2.59	1.24	0.57	0.21

Table 2.3 – Evolution of the average threshold as a function of the voltage bias applied on FID803 detector during run309.

VII Conclusion

The EDELWEISS experiment has developed a set-up dedicated to rare-event searches. The location of the experiment, the different shieldings and the choice of materials inside the cryostat ensure a low background rate. The detector design makes possible a discrimination between electronic and nuclear recoils. Nevertheless, detecting very low-mass WIMP implies low thresholds that can only be obtained by operating the detectors at high voltage bias. This method leads to a lower discrimination power but allows to considerably reduce the threshold. In the next chapter, the analysis method of a dataset exploiting this improvement is described in details.

Chapter 2: Data analysis method

Data analysis and selection

This chapter describes the data analysis of the first runs of the EDELWEISS experiment with FID800 detectors at high voltage bias. The first dataset (run309) corresponds to data taken between July and December 2015. The second one (run310) corresponds to data taken between March and August 2016. In this chapter, these datasets will be described as well as the signal processing and data calibration, followed by the definition of data selection.

I High-voltage cryorun goals and detector set-up

Following the results of EDELWEISS-III [92], the conclusion of the collaboration was to focus on low-mass WIMP searches and to fully exploit the low threshold capabilities of cryogenic germanium detectors. Detailed projection calculations based on realistic improvements of the detector have shown [91] that EDELWEISS detectors operating at higher voltage bias can be competitive in the WIMP mass range from 1 to 10 GeV/c², even with a modest exposure in an underground facility. In this work, two cryoruns were considered. The first one is called run309 and its goals were to test for the first time the performance of a standard EDELWEISS FID800 detector [75] operating at a voltage bias as high as 100 V, and to extract a WIMP-nucleon cross-section limit from these test data. The second one is the run310, whose goal was to increase the exposure of detectors operating at high voltage bias to publish the first EDELWEISS limit dedicated to low-mass WIMP using high-voltage conditions.

For run309, 24 detectors were installed in 6 towers hosting 4 bolometers each in the cryostat as shown in Fig.3.1. For run310, 15 FID800 detectors were installed in the 6 towers as shown in Fig.3.2. The detectors are readout by two MAC computers labelled s1 and s2 (distinguished by different colors in Fig.3.1 and Fig.3.2).

The temperature of the plates holding the detectors was regulated at 20 mK for run309 and 19 mK for run310. The high-voltage tests were done with the detectors performing the best phonon resolutions σ_{ph} (in keV). The tested detectors are listed in table 3.1. The maximum and optimum voltage biases as well as the respective resolutions are also reported. The maximum voltage bias is defined as the maximum value reached before the leakage current increases to values that permanently warm up the detector. In run309, only one detector (FID803) reached

Chapter 3: Data analysis method

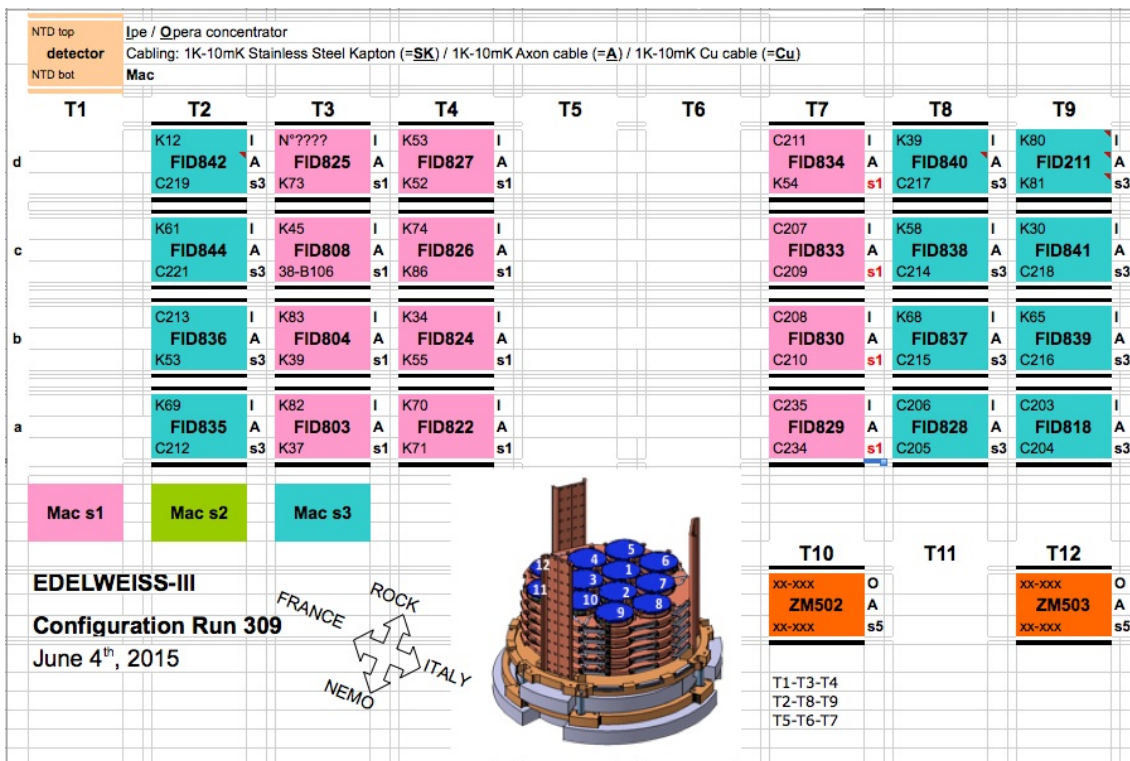


Figure 3.1 – Configuration of the 24 detectors in run309, composed of 6 towers of 4 detectors each. The different colors indicate the MAC computer used for the readout. The position of the towers and their orientation are also represented.

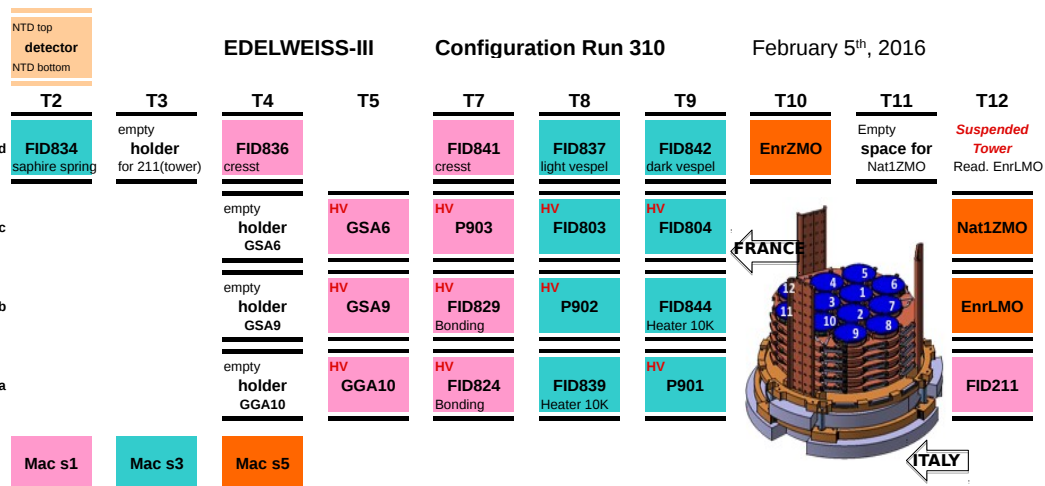


Figure 3.2 – Configuration of the detectors in EDELWEISS-III run310. Of the 15 detectors installed in the cryostat, only four are dedicated to the low-mass WIMP analysis. The different colors indicate the MAC computer used for the readout. The position of the towers and their orientation are also represented.

Chapter 3: Data analysis method

a voltage bias higher than 50 V. The FID804 detector reached a higher voltage than other FID800 detectors but its resolution was strongly deteriorated. Hence, it was decided to apply it a lower voltage bias (20 V) to preserve a reasonable heat resolution σ_{heat} (in keV_{ee}). In the same way, the detector with the best heat resolution in the previous cryorun (FID824) was ramped once at a voltage bias of 34 V but because of its degraded heat resolution, a voltage bias of 20 V was finally used. In run310, an asymmetry of the electrode bias allowed to increase the voltage up to 42 V and 60 V for the FID824 and FID829 detectors respectively.

FID detector	V_{max} (V)	σ_{heat} (FWHM) at 8 V (keV_{ee})	$V_{optimal}$ (V)	σ_{heat} (FWHM) at $V_{optimal}$ (keV_{ee})
803	110	0.73	100	0.074
804	140	0.81	20	0.63
824	34	0.42	20	0.19
829	52	0.56	45	0.11
834	48	1.53	20	1.55
836	36	0.71	36	0.2
837	26	0.46	20	1.27
839	30	0.62	20	1.06
841	38	0.49	20	0.50
844	26	0.63	20	0.39

Table 3.1 – Summary of high-voltage tests for FID800 detectors in run309. The V_{max} maximum voltage bias and the $V_{optimal}$ optimal voltage bias for each detector are listed together with the associated heat energy resolutions (FWHM).

The data taking for run309 lasted six months, as shown in Fig.3.3 (left). The first part (~ 150 days) was devoted to a full characterization of the detector when operated at a voltage bias of 8 V. Before the end of the cryorun, two weeks were dedicated to high-voltage tests. Only FID803 detector was able to reach 100 V without a deterioration of its heat resolution. The results presented in this chapter are mainly based on this detector. The run310 lasted five months, as shown in Fig.3.3 (right) with the goal of accumulating high-voltage dataset exposure. More than one month of high-voltage WIMP search data was collected.

Each cryorun is divided in 22-hours periods (on average) alternating with regeneration periods of the detectors. The regeneration procedure consists on applying a zero bias on detectors while at the same time the detectors are exposed to two strong ^{60}Co sources. This forces the neutralization of the space charges accumulated while detectors are biased [93]. After this, ramping the bias up to 100 V can take almost one hour. During the six months of run309 (five months for run310), 96 days (resp. 55 days) were dedicated to physics (with no calibration source). Periodic calibrations with two ^{133}Ba γ -ray sources were performed, accumulating 22 days of data taking. Most of the run309 data were recorded at 8 V voltage bias to characterize the detectors and in particular to study heat-only events, as described in chapter 4.

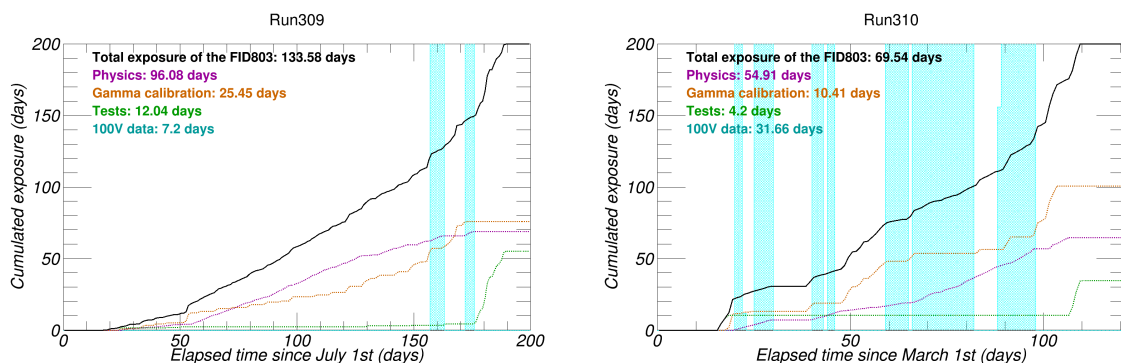


Figure 3.3 – Exposure of the data taking corresponding to run309 (left) and run310 (right) for FID803 detector. Calibration runs with a barium source exposure correspond to the orange curves. The magenta curves show the WIMP search data. The green curves correspond to runs dedicated to R&D purposes. The cyan zones indicate time periods with high voltage bias for FID803 detector.

II Signal processing

In this section, the method used to extract pulse height information is described. The first step is to determine the trigger level, defined as the minimal amplitude to be considered as a signal. The second step consists in calculating the amplitude of the signal. For the heat channels, an optimal filtering procedure is used. The calibration and the baseline resolution extraction are the last steps of the signal processing.

II.1 Trigger

In the context of low-mass WIMP searches, understanding the behavior of the detection threshold is essential. In EDELWEISS-III, the trigger is performed on the heat channels because of their better resolutions relative to the ones of the ionization channels. Moreover, a nuclear recoil induces a reduced ionization signal relative to the heat signal. Fig.3.4 shows the trigger level behavior (in keV) as a function of time in run309 (left) and run310 (right). The threshold is fixed when it is a calibration run.

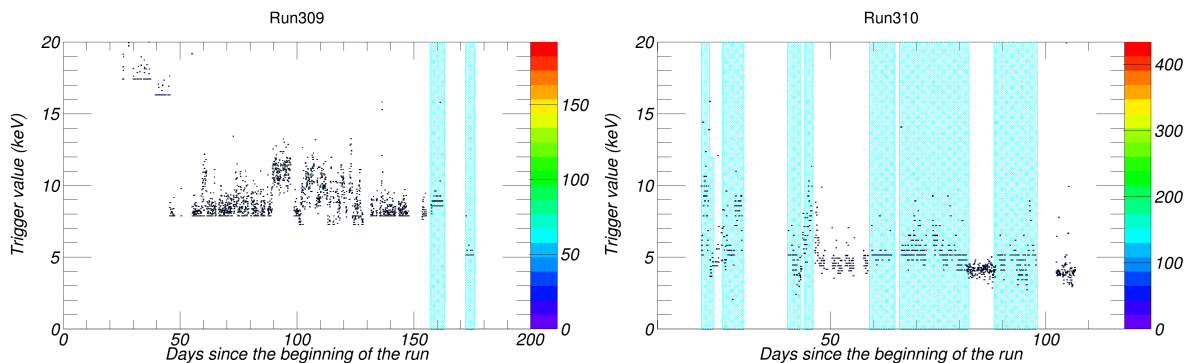


Figure 3.4 – Online trigger threshold as a function of the time of the cryorun, for run309 (left) and run310 (right). The cyan zones indicate time periods with high voltage bias for FID803 detector.

Chapter 3: Data analysis method

The online trigger algorithm works in the following way. The trigger identifies moments when the convolution product of the filtered data with a reference pulse template (see section III.2.1) exceeds a certain threshold value. This value is revised every minute in such a way that it increases or decreases depending on the heat baseline resolution fluctuations. This ensures a relative constant event rate of 50 mHz. In this way, the threshold is kept at the lowest value compatible with the varying signal-to-noise conditions.

For each triggered event, the data from all channels are stored on disk. For ionization measurement, they are saved in two forms. The first one is the slow ionization, corresponding to the down-sampling of the ionization trace at 1 kHz. It corresponds to a temporal window of 2.048 s centered around the start time of the event. This sampling operates as a low-pass filter and has a negligible effect on resolution as the highest signal-to-noise ratio is in the low frequency part of the signal. The demodulated trace of 1024 points has an effective sampling of 500 Hz, centered around the start time of the event reconstructed by SAMBA. It induces a temporal window of 2.048 s. The second form of stored data has a sampling of 100 kHz (fast ionization), which corresponds to a temporal window of 40.96 ms. It is used to determine more accurately the start time of the event. An example of an ionization trace event recorded on electrode B is shown in Fig.3.5 (right). For the heat measurement, traces are stored with a sampling frequency of 500 Hz.

The raw data of nearest neighbors of the detector which has triggered are also recorded, allowing coincidence studies between close detectors. This is important to calculate the trigger efficiency of a detector (see section III.4). Then an offline analysis allows to extract an event with a deposited energy below the defined threshold. It also constitutes an important source of random noise events to monitor continuously the varying noise conditions of the detector. Moreover, it allows to determine the baseline resolution, and evaluate the noise power spectral density as an input for the optimal filter analysis described in section II.2.2.

II.2 Pulse height determination

II.2.1 Pulse amplitude of ionization channels

The amplitude of the ionization pulses is determined in the following way. First, the data are compressed from 1 kHz to 500 Hz to remove the pattern due to heat excitation, as shown in Fig.3.5. A slope and a baseline level are fitted to the first half of the 2.048 s sample and a

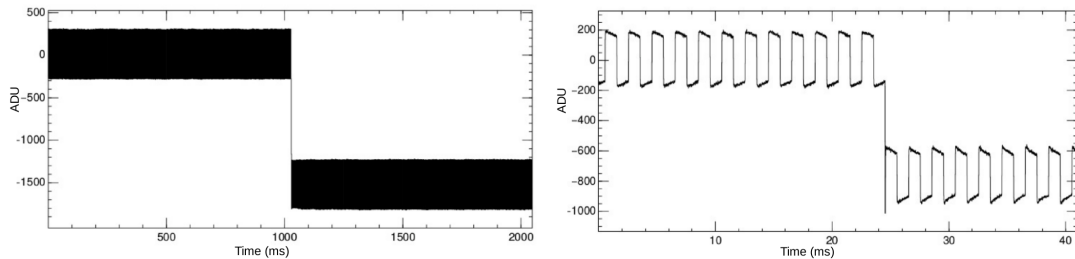


Figure 3.5 – Left: event measured by the electrode B, sampled at 1 kHz (so-called slow ionization). Right: same event measured by the electrode B, sampled at 100 kHz (fast ionization). The square-wave pattern visible on the 100 kHz ionization trace is induced by a cross-talk with the heat modulation. It is removed by subtracting the average pattern determined from the first half of the trace.

correction is applied to the signal. A first order numerical Butterworth filter is applied to the

Chapter 3: Data analysis method

data with a cut at 2 Hz. A template T_i (a Heaviside function filtered at 2 Hz) is used to determine the pulse amplitude A using the following unnormalized χ^2 :

$$\chi^2 = \sum_{i=1}^N (A \times T_i - D_i)^2 \quad (3.1)$$

where D_i is the reconstructed pulse for the sample i and N is the number of samples. The template T_i is centered in the time window at a fixed time t_0 common to all channels for the considered event. A first estimate of $t_0(\text{heat})$ comes from the heat channel data, filtered and convoluted in the same way as for the online trigger. The signal with the highest amplitude within ± 5 ms centered around the estimated online trigger value fixes the t_0 . This acts as a consistency check between the online and offline processing. Only the $t_0(\text{heat})$ value from the heat channel with the largest amplitude is considered. The convolution products of the slow ionization channels for the corresponding detector are then inspected in a ± 3 ms time window around $t_0(\text{heat})$ to find the second value $t_0(\text{slow})$. This narrow search window, smaller than the heat pulse rise time, ensures that the amplitude resolution is not degraded too much when there is no ionization pulse associated with the heat pulse. The convolution products of the fast ionization channels are also inspected in the same time interval. This gives a third value of $t_0(\text{fast})$ which has a resolution as good as $5 \mu\text{s}$ for high amplitude pulses. This $t_0(\text{fast})$ value is selected only if the significance of the fast pulse amplitude is more than 5σ . Otherwise, the previous estimates are kept, either $t_0(\text{heat})$ or $t_0(\text{slow})$ depending on the analysis.

The frequency structure of the noise for the ionization signal being nearly white, it is not necessary to introduce an optimal filter procedure, since it doesn't improve significantly the resolution. In contrast, the optimal filtering is needed for the heat channels, as shown hereafter.

II.2.2 Pulse amplitude of heat channels via optimal filtering

The heat channel data are 1024 point traces, corresponding to a time window of 2.048 s centered at the start time of the event reconstructed by SAMBA, i.e the trigger time (as shown in Fig.3.6). Heat channels are filtered with a highpass Butterworth filter and then convoluted by a template, defined at the beginning of the cryorun with a sample of selected 356 keV events from calibration runs with a ^{133}Ba source.

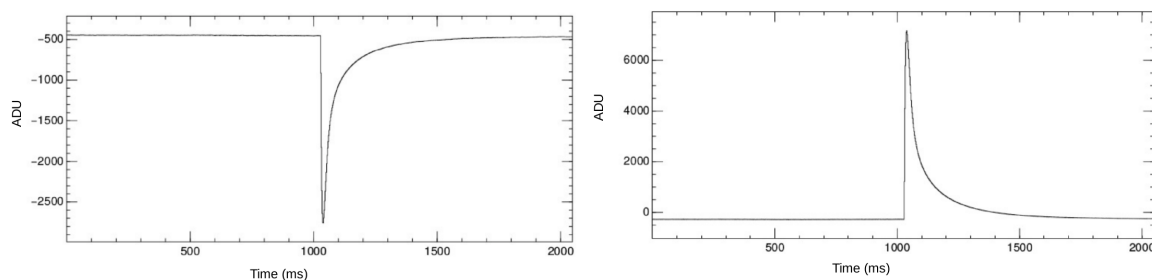


Figure 3.6 – Left: event measured by the NTD A. Right: same event measured by the NTD B. In both plots, the x-axis is in milliseconds and the y-axis in ADC units. The orientation of the pulse depends on the polarization sign imposed by the user.

An optimal filtering has been implemented for the offline processing of the heat signal. This procedure consists in estimating the frequency range for which the signal-to-noise ratio is the most efficient to calculate the amplitude of an event.

Chapter 3: Data analysis method

For each heat channel, it is expected that a measured event has a pulse shape defined as a function of the time t_i [84] as:

$$T_i = A \times \left(e^{-\frac{t_i}{\tau_1}} + f \cdot e^{-\frac{t_i}{\tau_2}} \right) \times \left(1 - e^{-\frac{t_i}{\tau_3}} \right) \quad (3.2)$$

where A is the pulse amplitude in ADU; τ_1 , τ_2 and τ_3 are the characteristic time constants of the signal and f an amplitude parameter. As data samples D_i are correlated ($i = 0, \dots, N$, with N the number of samples) in the time domain, there is no estimation of the noise included in the χ^2 , defined as:

$$\chi^2 = \sum_{i=1}^N (A \times T_i - D_i)^2 \quad (3.3)$$

and, as a consequence, the reconstruction of the pulse amplitude A is not optimal. In contrast, in the frequency domain, the noise at each frequency can be considered as uncorrelated. Hence, amplitudes can be determined more accurately. A discrete Fourier transform is applied on the time signal D_k as:

$$\tilde{D}_j = \sum_{k=0}^{N-1} D_k \exp\left(i \frac{-2\pi jk}{N}\right) \quad (3.4)$$

with \tilde{D}_j its Fourier transform. The normalized power spectral density for a given frequency f_j is:

$$PSD(f_j) = \frac{2|\tilde{D}_j|^2}{f_s N} \quad (3.5)$$

where f_s is the sampling frequency and j is the index in the frequency range. The optimal filtering consists in the evaluation of the pulse amplitude A by evaluating the χ^2 in the frequency domain:

$$\chi^2(A) = \sum_{j=1}^N \left[\frac{\tilde{D}_j - A\tilde{T}_j}{\tilde{\sigma}_j} \right]^2 \quad (3.6)$$

where \tilde{D}_j and \tilde{T}_j are the Fourier components at frequency f_j of the signal and the pulse templates respectively. $\tilde{\sigma}_j$ is the PSD of a template of noise data associated to the event dataset¹. A simulation of an event in both domains, time and frequency, and the respective reconstructed signals are shown in Fig.3.7. It allows to determine more accurately the heat pulses, this is why it is applied on the heat channels.

II.3 Energy calibration

The energy calibration is performed with a ^{133}Ba source. This γ -ray source produces energetic electronic recoils at 356.0 keV and 383.9 keV near the end-point of the spectrum. Detectors are periodically exposed to this source to accumulate calibration data and check their stability over time.

II.3.1 Ionization channels

For a given charge collection state, the gain of the ionization signals is stable over run. On the other hand, heat gains suffer some variations with temperature and the NTD voltage biases. Therefore the heat signals calibration is synchronized on the ionization, which is the

¹obtained with several noise events, see section III.2.3.

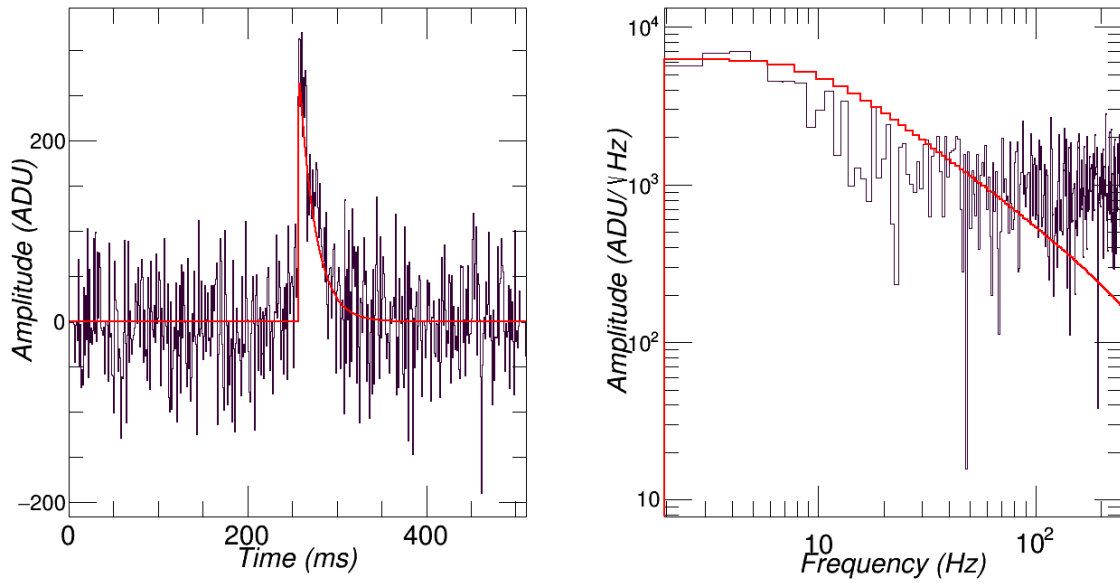


Figure 3.7 – Simulation of a recorded event and its template (in red) scaled with the amplitude resulting from the optimal filter (left) and their corresponding Fourier transforms (right).

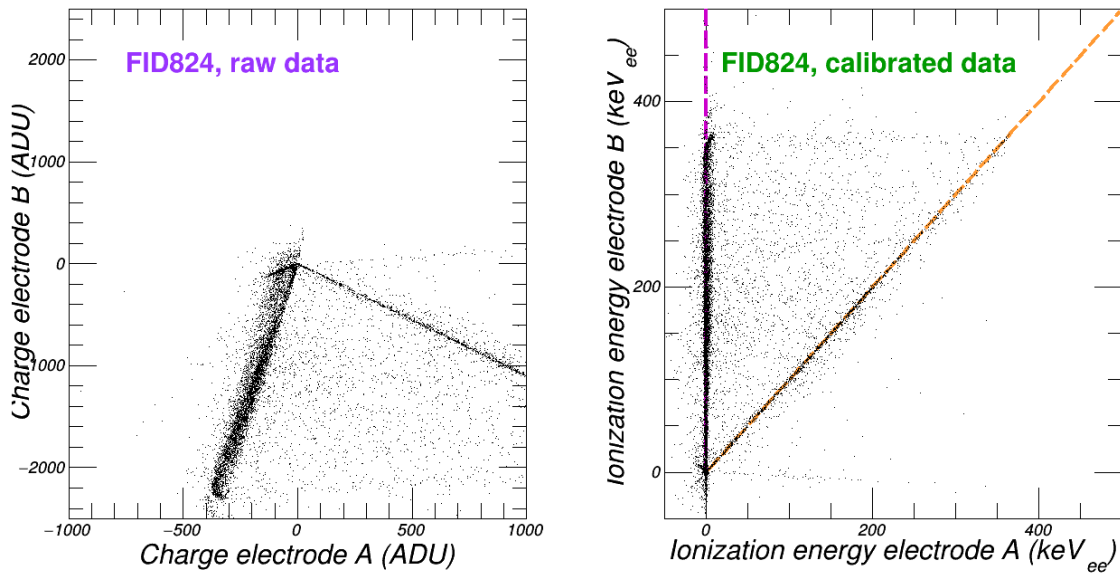


Figure 3.8 – Cross-talk correction on FID824 detector. Ionization measured by the electrode A as a function of the ionization measured by the electrode B before (left) and after (right) cross-talk correction and energy calibration. Fiducial events should be placed along the magenta dashed line.

first one to be processed. The first step consists in the correction of the cross-talks between the different electrode signals. This cross-talk is the result of electromagnetic interferences between

Chapter 3: Data analysis method

neighboring signal lines, and more importantly, of the mutual capacitance between adjacent electrodes. A charge collected on an electrode also induces proportional signals on the others. This cross-talk varies linearly from few percents to 30% in the case of interleaved electrodes and is constant over time. This cross-talk is visible on electrodes where no signal is expected. As shown in Fig.3.8 (left), the fiducial event population is off y -axis. The corrected amplitude A'_i for one channel i is:

$$A'_i = A_i + \sum_{i \neq j} \eta_i^j \times A_j \quad (3.7)$$

where η_i^j is the cross-talk coefficient of the channel j on the channel i , i.e the signal fraction induced on i by the charge collected on j . It is determined in such a way that there is a null amplitude for electrodes where no signal is expected for either surface or fiducial events. There is no symmetry between η_i^j and η_j^i , and therefore 12 coefficients have to be determined as there are four ionization channels. Fig.3.8 shows the effect of the correction on raw data of FID824 detector, during run308. On the right plot the energy calibration procedure as described hereafter has been also applied.

Once cross-talks are determined, the 356 keV ^{133}Ba peak for fiducial or surface events is used to determine the gain g_i for the four channels, in keV per ADU units (see section III.2). The gaussian fit to determine the position of the 356.0 keV in the spectrum is illustrated in Fig.3.9. In detectors that are partially shielded from the ^{133}Ba sources by other detectors, this peak can be difficult to identify, in particular for veto electrodes and for electrodes collecting electrons instead of holes, as these are more affected by charge trapping effects [94]. Consequently, the energy measured by these less effective electrodes is calibrated using the ratio of the two fiducial electrode signals. The calibration converts ADU into energy-equivalent-electron (keV $_{ee}$) and is only valid for electron interactions in the bulk. For fields below 1 V/cm, charge trapping [94] affects gains and cross-talks by a few percent.

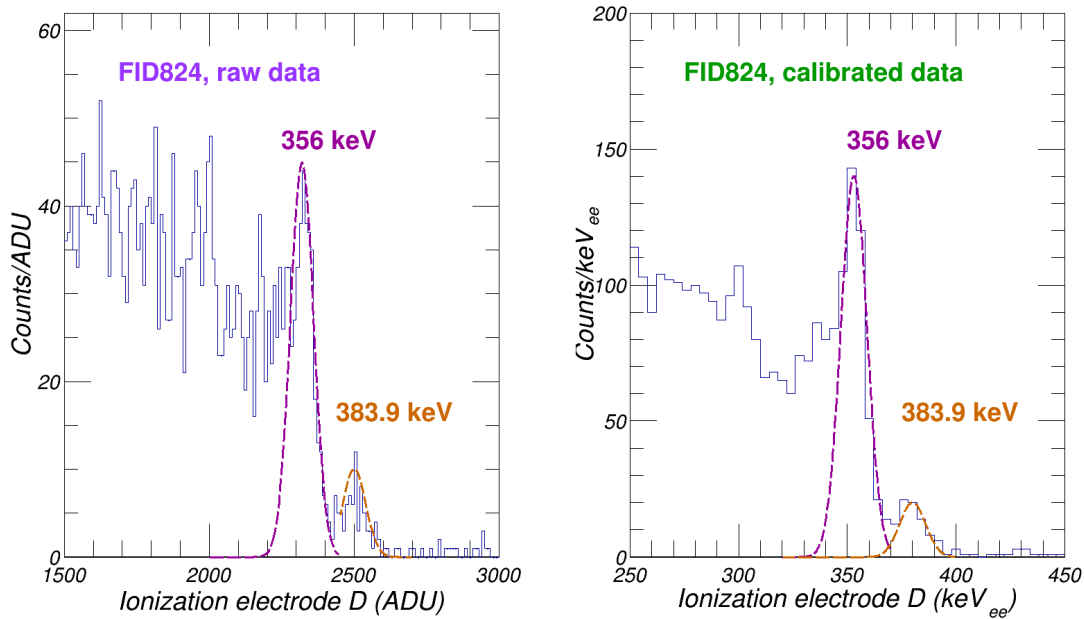


Figure 3.9 – Ionization spectrum for fiducial electrode D in ADU (left) and in keV $_{ee}$ (right). The 356 keV peak is fitted with a gaussian function to estimate the gain in keV $_{ee}$ /ADU.

For the following analysis, the total ionization energy E_{ion} has to be defined as:

$$E_{ion} = \frac{E_{i,A} + E_{i,B} + E_{i,C} + E_{i,D}}{2} \quad (3.8)$$

It corresponds to the total ionization measurement of the four electrodes (A , B , C and D).

II.3.2 Heat channels

Two steps are necessary to calibrate the heat channel amplitudes A_{heat} . The first step consists of a calibration of the heat/ionization ratio. It is studied in a sample of fiducial events in the [100;500] keV interval. The heat amplitude is thus calibrated in terms of fiducial electronic recoils (keV_{ee}) as:

$$E_{heat,i}^L = \alpha \times A_{heat,i} \quad (3.9)$$

where $A_{heat,i}$ is the amplitude of the heat signal in ADU, α is the linear gain and $E_{heat,i}^L$ is the linear heat energy in keV_{ee} measured by the NTD i ($i = A$ ou B). By construction, the heat energy is equal to the ionization energy (modulo resolution effects) for these fiducial events as shown in Fig.3.10.

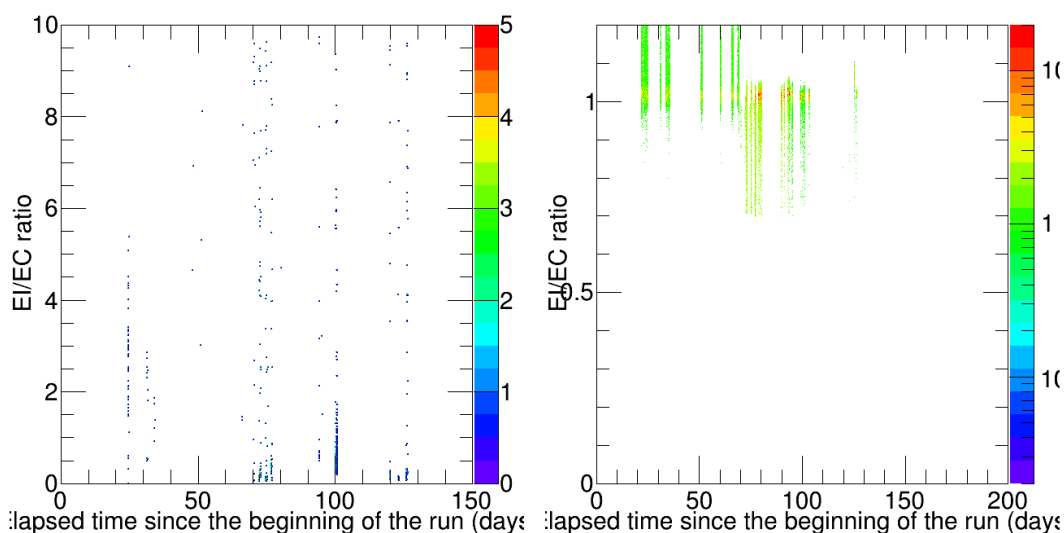


Figure 3.10 – Evolution of the ratio between ionization energy and heat energy as a function of the time of the run before (left) and after (right) the calibration of the heat channels. The ratio is centered around 1 after the calibration procedure.

The second step is the correction for the non-linearity in energy due to the dependence of the heat sensor i sensitivity on temperature. To correct this effect, an empirical fit is applied on the observed heat/ionization ratio as a function of heat. The correction function for fiducial γ -events is:

$$f(Z_i) = \beta_1 - \beta_2 \times (Z_i - \beta_3) \times \frac{(1 - \beta_5 \times (Z_i - \beta_3))}{(1 + \exp(\frac{\beta_3 - Z_i}{\beta_4}))} \quad (3.10)$$

where β_j are the fit parameters and $Z_i = \ln(E_{heat,i}^L \times (1 + \frac{V}{3}))$. The corrected heat energy becomes:

$$E_{heat,i} = \frac{E_{heat,i}^L}{f(Z_i)} \quad (3.11)$$

Chapter 3: Data analysis method

with the heat energy expressed in keV_{ee} . The correction is shown in Fig.3.11 for NTD A. The step at $E_{heat,A} \sim 7$ is due to a difference in statistics between the 8 V and 100 V voltage bias datasets, as well as tiny variations in the relative calibration of these two datasets.

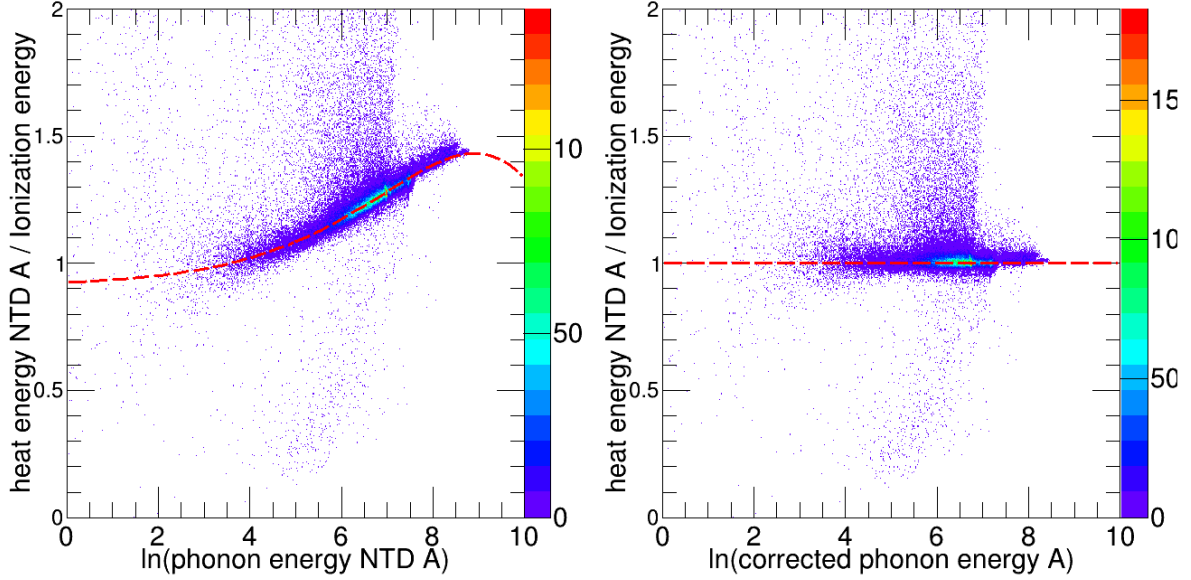


Figure 3.11 – Non-linearity correction for the NTD A of FID803 detector. Ratio of the heat energy measured by the NTD A to the ionization energy as a function of the non-corrected $\ln(E_{heat,A}^L \times (1 + \frac{V}{3}))$ value before the non-linearity correction (left) and as a function of $\ln(E_{heat,A} \times (1 + \frac{V}{3}))$ after the correction (right) for data recorded with a ^{133}Ba source, fitted with the function in Eq.3.10 (in red).

The combined heat energy E_{heat} is defined as:

$$E_{heat} = \psi E_{heat,A} + \rho E_{heat,B} \quad (3.12)$$

where ψ and ρ are the weighting factors that optimize the resolution for E_{heat} . To distinguish the heat energy E_{heat} in keV_{ee} for fiducial events from the total heat energy, a different variable is used by convention for the latter, E_{phonon} in true keV. For fiducial events, the two are related by:

$$E_{heat}(\text{keV}_{ee}) = \frac{E_{phonon}(\text{keV})}{1 + \frac{V}{3}} \quad (3.13)$$

The same convention is used for individual heat energy of $i = A$ for NTD A or $i = B$ for NTD B, with:

$$E_{heat,i}(\text{keV}_{ee}) = \frac{E_{phonon,i}(\text{keV})}{1 + \frac{V}{3}} \quad (3.14)$$

II.4 Heat energy baseline resolutions

The precision on the ionization and heat measurements E_{ion} and E_{heat} at low energy is quantified by their baseline energy resolutions, i.e the spread in the measured fitted amplitudes of noise samples, fixing the time of the pulse at an arbitrary position. These amplitudes are

distributed as a gaussian centered at zero and with a standard deviation (rms) value related to the noise associated to the sensor and its readout electronics. The resolutions are determined hourly for each detector. By convention, resolutions are often expressed as the FWHM (Full Width at Half Maximum) value corresponding to 2.35 times the rms of the gaussian. Some typical average heat energy resolution (FWHM) values are listed in table 3.2. The best heat energy baseline resolution reached by a FID800 detector is for FID803 detector, operated at 100 V voltage bias and is equal to 74 eV_{ee}.

FID detector	$V_{optimal}$ (V)	σ_{heat} (FWHM) at 8 V (keV _{ee})	σ_{heat} (FWHM) at $V_{optimal}$ (keV _{ee})
803	100	0.86	0.074
824	20	0.29	0.19
829	45	0.65	0.11

Table 3.2 – Heat energy baseline resolutions (FWHM) for detectors used in high-voltage runs (at $V_{optimal}$ voltage bias) during run309.

II.5 Nuclear and electronic recoil regions

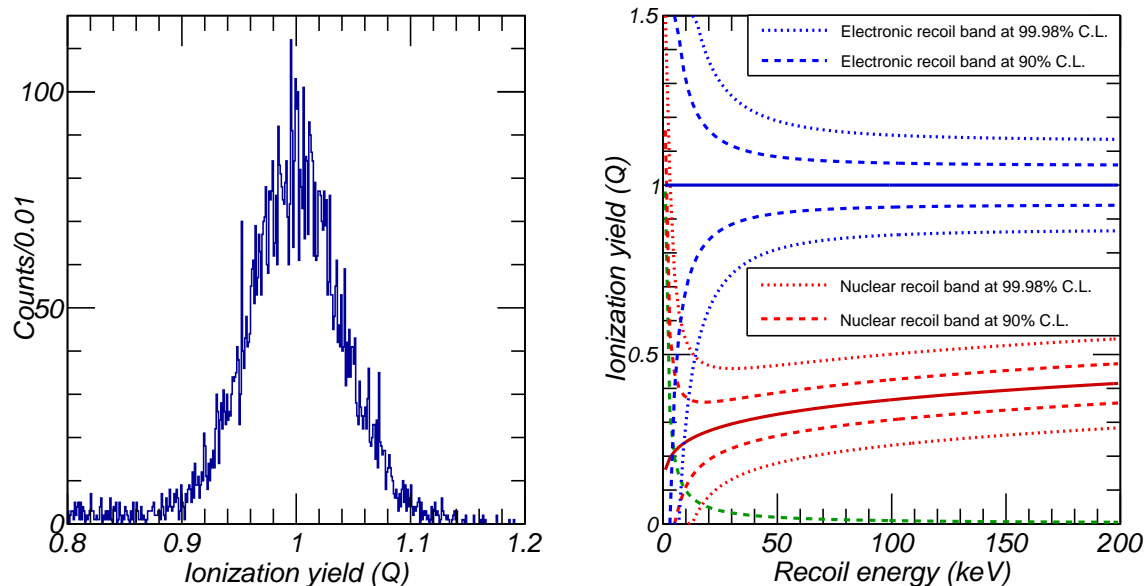


Figure 3.12 – Left: distribution of the ionization yield Q (quenching factor) for a calibration run with ^{133}Ba γ -ray source. By definition, the γ -distribution is centered at 1. Right: ionization yield Q as a function of the recoil energy. Electronic recoil bands (blue) and nuclear recoil bands (red) are calculated for 90% C.L. (dashed line) and 99.9% C.L. (point line). The analysis threshold depending on the ionization resolution is in green.

Parametrization of the dependence in energy of the nuclear and electronic recoil bands, defined in chapter 2, are made using heat $\sigma_{heat}(E_{heat})$ and ionization $\sigma_{ion}(E_{ion})$ energy resolution values

Chapter 3: Data analysis method

from the baseline and the 356 keV barium peak:

$$\sigma_{ion,heat}(E_{ion,heat}) = \sqrt{\sigma_{ion,heat}^2(0) + \alpha_{ion,heat}^2 E_{ion,heat}^2} \quad (3.15)$$

with:

$$\alpha_{ion,heat} = \frac{\sqrt{\sigma_{ion,heat}^2(356) - \sigma_{ion,heat}^2(0)}}{356} \quad (3.16)$$

where $\sigma_{ion,heat}$ is the ionization or heat resolution (FWHM) in keV_{ee}. The parametrization of the quenching factor dispersion σ_Q is valid if heat and ionization fluctuations are not correlated. Nevertheless charge trapping leads to simultaneous degradation of both resolutions [94]. As suggested in [94], the definition of the nuclear and electronic recoil bands requires the introduction of effective resolutions at 356 keV weaker than measured. The effective resolution is defined considering 90% of fiducial γ of the electronic recoil band. The determination of the two recoil bands are illustrated in Fig.3.12 (right) as well as the quenching factor distribution for a calibration run with ¹³³Ba source (left).

III Data selection

Calibrated amplitudes are stored in ROOT format files [95]. The data are stored according to detector and run-type (WIMP search, γ -calibration, tests...). A hundred of variables are also stored for each event such as the event time, the calibrated energies, the online threshold, etc. The list of some variables used in this work is in tables 3.3 (for run information) and 3.4 (for event variables). In the definition of the variables, the electrodes are identified by a letter $i = A, B, C$ and D (B and D corresponding to the fiducial electrodes, A and C to top and bottom veto electrodes). The abbreviations EC_A and EC_B correspond to the top and bottom heat channels, respectively. Combination of variables are also stored, such as the total ionization energy E_{ion} or the combined heat energy E_{heat} . The sensor resolutions are stored (FWHM) hourly, as well as the VVET veto voltage bias applied on veto electrodes. The V voltage bias applied on detectors is called VOLT in table 3.3. The information about coincidences between detectors used as a tag to identify multiple scatters is the variable MULT. The goodness of fit in the time domain is estimated by a χ^2 -like estimator which lacks proper normalization for the ionization channels. Normalization is performed dividing this value by the hourly average χ_i^2 for noise events. In this way, the time dependence vanishes. For optimal filter applied on heat channels, the χ_i^2 value is properly normalized and hence has no time dependence. For convenience, the values stored are the log of the determined χ^2 (i.e XOC_{*i*} or RCI_{*i*} as shown in table 3.4). The selection cuts used in the analyses are based on these variables.

Two different types of variables are used in this analysis: run and event variables. The first type describes the average behavior of events taken in a time period of up to one hour (≤ 1 hour) and the second type describes properties of one event. The exposure, i.e a time during which selected data was recorded, is defined with cuts on run variables. A selection on event variables results in an energy-dependent efficiency.

III.1 Time period selection

The procedure for data quality selection is described using FID803 detector as an example. The main goal of these cuts is to achieve a high sensitivity for low-mass WIMP down to ~ 3 GeV/ c^2 minimizing the exposure loss. The first selection consists to remove all time periods with heat

Chapter 3: Data analysis method

Variable used in text	Symbol used in labels	Definition
$\sigma_{ion,i}$	$FWHM_i$	FWHM ionization resolution of electrode $i = A, B, C, D$
σ_{ion}	FWI	FWHM ionization resolution of E_{ion}
σ_{dif}	$FWHM_{dif}$	FWHM ionization resolution of E_{dif}
$\sigma_{heat,i}$	OWC_i	FWHM heat resolution of NTD $i = A, B$
σ_{heat}	FWC	FWHM heat resolution associated to E_{heat}
V	VOLT	voltage bias applied on detectors
VVET	VVET	voltage bias applied on veto electrodes

Table 3.3 – Summary of some run variables and symbols (as used to determine the exposure).

Variables used in text	Symbol used in labels	Definition
$E_{i,j}$	EI_j	Ionization energy for the electrode j in keV_{ee}
E_{ion}	EI	Total ionization energy in keV_{ee}
E_{dif}	EDIFF	Difference between the two B and D fiducial electrodes in FID mode
$E_{heat,i}$	EC_i	Heat energy for the NTD i in keV_{ee}
E_{heat}	EC	Combined heat energy in keV_{ee}
E_R	ER	Recoil energy in keV
$Q(E_R)$	Q	Quenching factor EI/ER
	CHI_i	Logarithm of the pseudo χ^2 associated to the fit applied on electrode i
	RCl_i	Average logarithm of the hourly χ^2 for electrode i
	XOC_i	χ^2 associated to the optimal filter applied on NTD i
Th_i	Th_i	online threshold value per NTD from SAMBA at the time of the event for heat channel i
E_{online}	Th	online threshold value from SAMBA at the time of the event was recorded (smallest value between the two individual Th_i)
$E_{offline}$	OTh	offline analysis threshold value at the time of the event was recorded
MULT	MULT	number of coincidences between detectors

Table 3.4 – Summary of some event variables and symbols used in the analysis.

Chapter 3: Data analysis method

channel resolutions $OWC_i > 5 \text{ keV}_{ee}$, as well as time periods with $OWC_i = 0$ corresponding to a failure of the processing algorithm:

$$0 < OWC_i < 5 \text{ keV}_{ee} \quad (3.17)$$

Time periods with saturated ionization are removed as well. A time period is rejected if it contains a 10 minute interval during which the ionization baseline was saturated for more than 10% of the events. The saturation is defined as:

$$- 20000 \text{ ADU} < \text{baseline} < 20000 \text{ ADU} \quad (3.18)$$

This removes time periods when the slope due to leakage current is too large.

As illustrated in Fig.3.13, time periods with both major problems with the thermal sensors and incorrect conditions of noise reconstruction can be rejected. This time selection cuts reduce the livetime for FID803 detector by 3%, as illustrated in Fig.3.13.

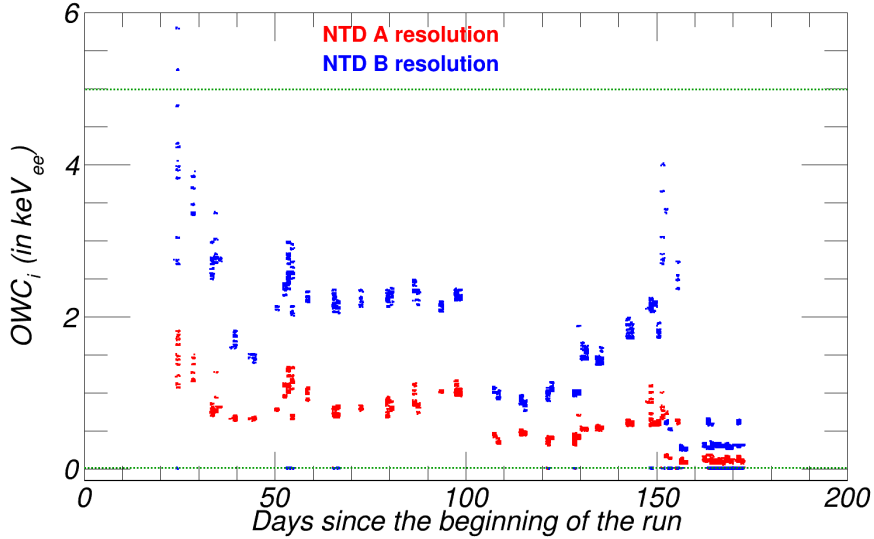


Figure 3.13 – Heat energy resolutions (FWHM) in keV_{ee} (NTD A in red, NTD B in blue) as a function of the time of the cryorun. The time selection quality cut of Eq.3.17 and Eq.3.18 removes 3% of the time, corresponding mostly to events above and below the interval between the two horizontal green dashed lines.

III.2 Exposure calculation

As explained in chapter 1, a WIMP-nucleon cross-section limit depends on the time exposure with good data collection, expressed in units of $\text{kg}\cdot\text{days}$. Data quality over time is performed defining successive cuts. The cumulated exposure is calculated in the following way. The cuts on the ionization channel saturation as well as heat channel resolutions are applied. A histogram with a binning Δt is filled with the event start time. If Δt is such that the average number of events after all cuts per bin is well above 1, the exposure will be then $N\Delta t$, where N is the number of bins with at least one event. This procedure automatically takes into account all intervals Δt where the data exist and can be used. However, a given period of length Δt with some observed events might contain some fraction of time when the data acquisition is not

active (for example, when the end of a run doesn't coincide with the upper limit of Δt). The bias in the exposure calculation can be controlled repeating the calculation with a reduced value of Δt . The calculated exposure as a function of Δt is shown in Fig.3.14. This value decreases slowly between $\Delta t = [10, 100]$ minutes and drops dramatically below 10 minutes. The chosen Δt is the intercept of the linear behavior between 10 and 100 minutes with the y-axis.

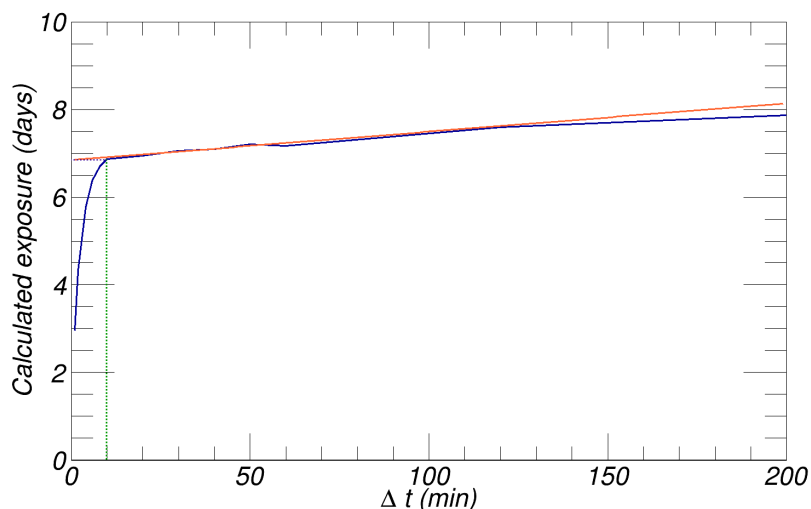


Figure 3.14 – Determination of the time range Δt for the calculation of the exposure. The chosen Δt is the intercept of the linear behavior between 10 and 100 minutes with the y-axis, drawn in dark blue dashed lines. It is this time range that is used in the following analysis.

Moreover, a dead time correction is applied to take into account regular interruptions of the DAQ for time periods less than 5 minutes, such as maintenance procedures to regularly reset the DAC used to ground the gate of the FET. This procedure lasts 3 minutes. It is achieved periodically (5400 seconds) and consists in a relay switch. The dead time calculation also takes into account pile-up effect: events recorded less than 600 ms after a previous event are rejected. The total dead time is 2.5%.

III.3 Event cuts

Pathological events are characterized by a deviation of the normalized χ^2 (pile-up events, DAQ resets,...). To reject these events, the distribution of the log of the normalized χ^2 for noise events is plotted (Fig.3.15 left) and fitted by a gaussian. The quality cut is defined at 2.58σ of this gaussian. The efficiency of this cut for triggered events is 94%. As shown in Fig.3.15 right, the energy dependence of these χ^2 for the ionization channels is negligible in particular in the low energy region (a WIMP of 5 GeV/ c^2 has a maximum recoil energy of 3 keV).

With the same procedure applied to the heat channel i (for NTD A or NTD B), the χ^2 value exhibits some energy dependence. The energy-dependent quality cut is defined in this case as:

$$\chi_i^2 < 2.58 \times \sigma_i + \alpha_i \times E_{phonon,i} \quad (3.19)$$

where σ_i is the standard deviation of the χ_i^2 distribution. α_i is defined to match with the energy dependence of the χ^2 and $E_{phonon,i}$ is the phonon energy (in keV) as defined in Eq.3.14. It is determined by fitting the χ^2 distribution with a gaussian function for different energy ranges

Chapter 3: Data analysis method

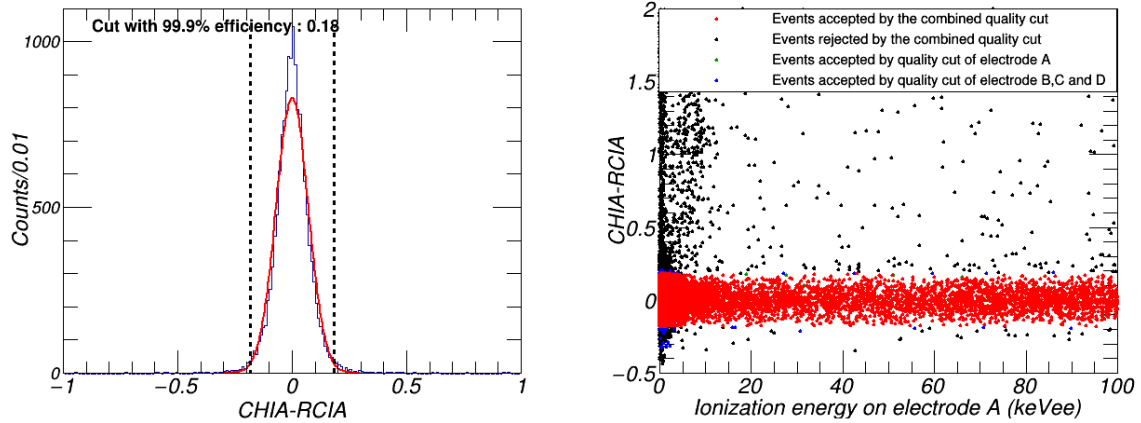


Figure 3.15 – Left: distribution of the log of the normalized χ^2 and its gaussian fit, for electrode A of FID803 detector for noise events. Right: effect of the selection on the χ^2 for the same electrode A for triggered data. In black, events rejected by the $\ln(\chi^2_A)$ cut. In blue, events rejected only by the other ionization channel cuts. In green, events rejected only by the cut of this channel. In red, events accepted by the four ionization channel quality cuts. In this energy range, no dependence in energy of the $\ln(\chi^2)$ (for each channel) is noticed.

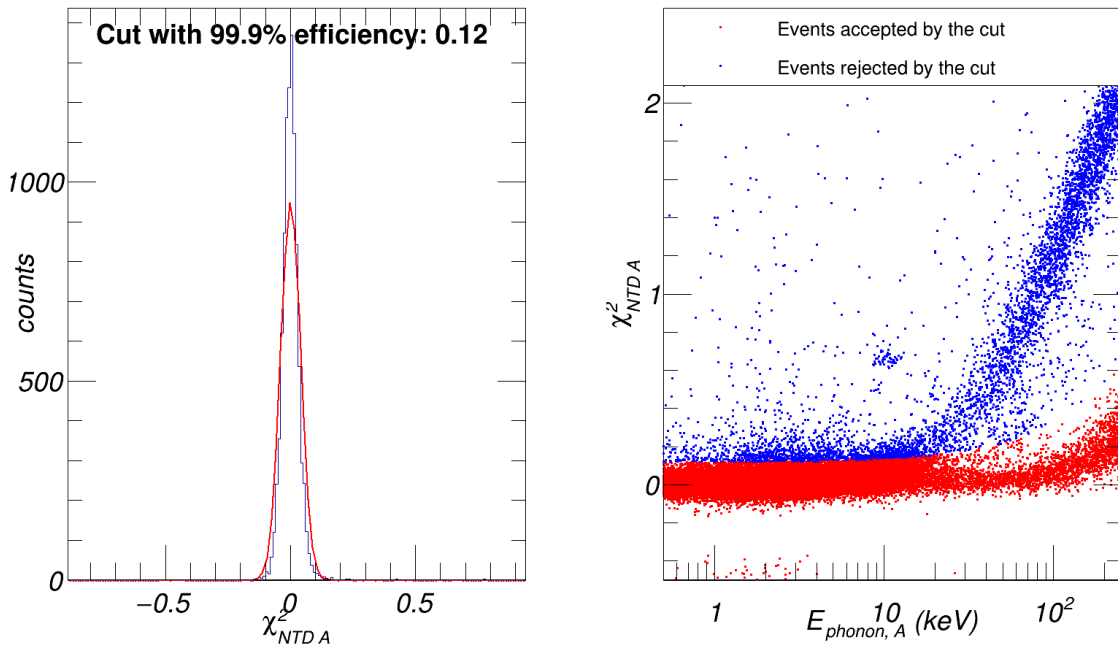


Figure 3.16 – Left: χ^2 distribution for the NTD A of FID803 detector for noise events. The distribution is fitted by a gaussian function allowing to determine the corresponding quality cut. Right: effect of the selection on the χ^2 of the NTD A as a function of the heat energy of the NTD A (in red, events accepted by the quality cut and in blue events rejected).

and by fitting the obtained means with a linear function. The resulting selection is shown in Fig.3.16.

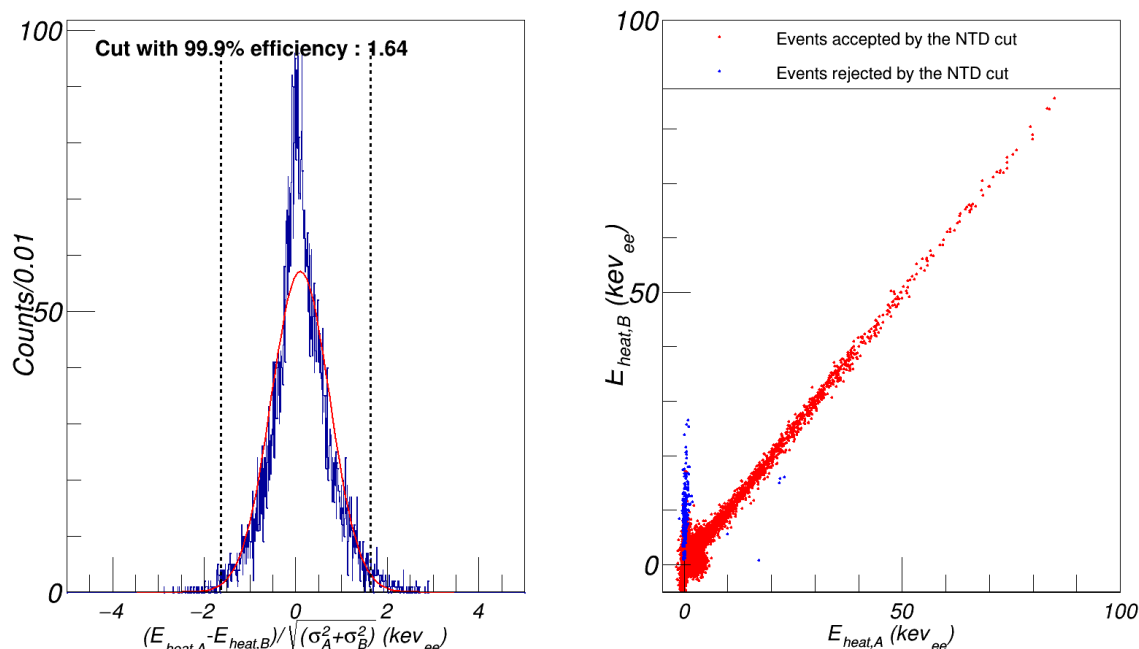


Figure 3.17 – Left: $\frac{E_{heat,A} - E_{heat,B}}{\sqrt{\sigma_{heat,A}^2 + \sigma_{heat,B}^2}}$ distribution (blue) for FID803 detector for noise events with its gaussian fit (red). Right: heat energy measured by the NTD A as a function of heat energy measured by the NTD B, for events rejected (blue) and accepted (red) after application of the cut from Eq.3.20.

The number of so-called NTD events² is reduced by an additional cut based on the difference between the two measured heat energies $|E_{heat,A} - E_{heat,B}|$. This cut takes into account the different resolutions of the two heat channels $\sigma_{heat,A}$ and $\sigma_{heat,B}$ as:

$$\frac{E_{heat,A} - E_{heat,B}}{\sqrt{\sigma_{heat,A}^2 + \sigma_{heat,B}^2}} \leq \lambda \quad (3.20)$$

where λ is taken as 2.58 standard deviations from a gaussian fit on the distribution of the quantity on the left hand side of Eq.3.20 (see Fig.3.17). The cut keeps 99.9% of the events when the detector hasn't triggered and 98.9% of triggered events.

III.4 Efficiency

The WIMP-nucleon cross-section limit for low-mass WIMP is strongly dependent on the trigger algorithm efficiency ϵ_{th} . Two different methods are used to determine this dependence.

The first method is based on coincidences between neighboring detectors. For two neighbors i and j , the energy dependence of the trigger efficiency for the detector i can be determined from the ratio of two heat energy spectra. The first spectrum S_j corresponds to the heat energy

²Events recorded by only one NTD, see chapter 2.

Chapter 3: Data analysis method

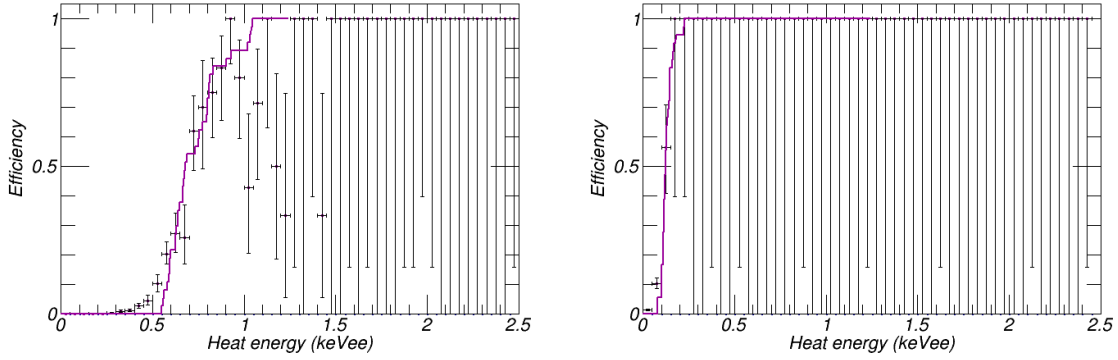


Figure 3.18 – Comparison of the two methods allowing to determine the trigger efficiency of FID803 detector at 8 V (left) and 100 V (right) voltage bias. The blue dots represent the first method considering the neighbor detector coincidence study. The magenta curve represents the analytical method considering the trigger value hour by hour.

recorded in i with the only requirement that the detector j has triggered. The second spectrum S_{ij} corresponds to the heat energy recorded in i when both i and j detectors have triggered. The ratio S_{ij}/S_j , shown as points with errors bars in Fig.3.18, measures the energy-dependent trigger efficiency $\epsilon_{th}(E_{heat})$. This method is a direct measurement of $\epsilon_{th}(E_{heat})$ based on data, but it suffers from limited statistics. However these values can be used to verify the calculated $\epsilon_{th}(E_{heat})$ values based on the knowledge of the Th threshold value used by the trigger algorithm for each event.

This second method giving $\epsilon_{th}(E_{heat})$ is based on the cumulative of the distribution of the Th values for all selected events. In order to compare these cumulatives with the direct measurement based on the first method, one more effect has to be taken into account. The energy estimator E_{online} used in the online trigger algorithm is slightly different from the offline determination $E_{offline}$ (corresponding to E_{heat}). For each event, the energy estimators used by the trigger algorithm have been stored. The sigma of the $(E_{offline} - E_{online})$ gaussian distribution, $\sigma_{offline-online}$, indicates how much the cumulative of the distribution of the threshold value E_{online} needs to be smeared in order to be compared to the first measurement S_{ij}/S_j :

$$\epsilon_{th}(E_{heat}) = \frac{1}{2} \left(\operatorname{erf} \left(\frac{E_{offline} - E_{online}}{\sqrt{2}\sigma_{offline-online}} \right) + 1 \right) \quad (3.21)$$

The comparison between the two methods is shown in Fig.3.18. The good agreement confirms that the calculation from the second method can be used reliably.

III.5 Fiducial events selection

In high-voltage mode, the FID800 detector is set in a planar mode, i.e top electrodes A and B (bottom electrodes C and D respectively) are at the same voltage bias. In this mode, the entire volume of the detector is fiducial. Nevertheless, a selection of fiducial events will be needed for specific studies of data samples recorded in the FID mode to select or reject surface events due to β , ^{206}Pb recoils and surface γ (see chapter 5). It requires an energy on the veto electrodes A and C lower than the energy measured by the fiducial electrodes B and D:

$$\operatorname{abs}(E_{ion,A}) < \sigma_{ion,A} + E_{ion} \times 20/356 \quad (3.22)$$

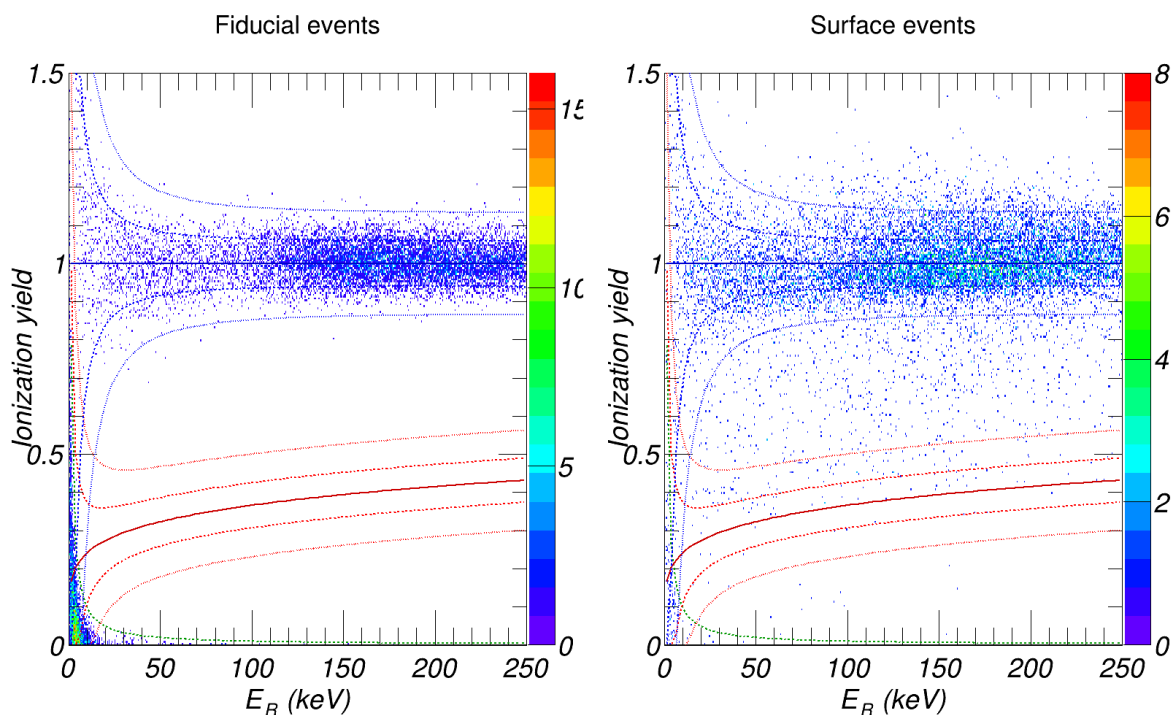


Figure 3.19 – Left: ionization yield Q as a function of the recoil energy E_R (in keV) for fiducial events in calibration runs. All events are distributed in the electronic recoil band (in blue) or are heat-only events (under the green dashed line). Right: ionization yield Q as a function of the recoil energy E_R (in keV) for surface events in calibration runs. Events distributed mostly around $Q = 1$ are surface γ , events below correspond to other surface events.

$$\text{abs}(E_{ion,C}) < \sigma_{ion,C} + E_{ion} \times 20/356 \quad (3.23)$$

where E_{ion} is the total energy measured by the four electrodes (Eq.3.8). Furthermore, it requires to control the difference between the signals measured by the two fiducial electrodes $E_{dif} = \frac{E_{ion,B} - E_{ion,D}}{2}$:

$$\text{abs}(E_{dif}) < \sigma_{dif} + E_{ion} \times 20/356 \quad (3.24)$$

The effect of this selection on data recorded in the FID mode by FID803 detector when exposed to a ^{133}Ba γ -ray source is shown in Fig.3.19.

IV Luke-Neganov effect in FID800 detectors

As the run309 is the first one in the EDELWEISS experiment using FID800 detectors in high-voltage mode, the impact of the Luke-Neganov effect on the energy resolution has been carefully studied. The phonon energy resolution σ_{phonon} (in keV) is associated to the phonon energy E_{phonon} as defined in Eq. 3.13 as a function of E_{heat} . The average σ_{phonon} value (FWHM) as a function of the applied voltage bias V has been extracted and reported in Fig.3.20 for three FID800 detectors. As shown on the figure, for dominant electronic noise, the σ_{phonon} value does not depend on the voltage bias. Small fluctuations are mainly due to variations of noise conditions over time period. Indeed, the operation of the detector at 100 V was decided in a period where the observed noise was relatively stable, while other voltage bias points are based

Chapter 3: Data analysis method

on datasets that include more noisy time periods. For FID824 detector, the voltage bias at 35 V was difficult to reproduce, leading to a noise degradation or an increase of temperature due to leakage currents, while the bias at 30 V was more easily reproducible (see middle plot). The increase in resolution at 20 V for FID803 detector (left plot) is due to the same reasons.

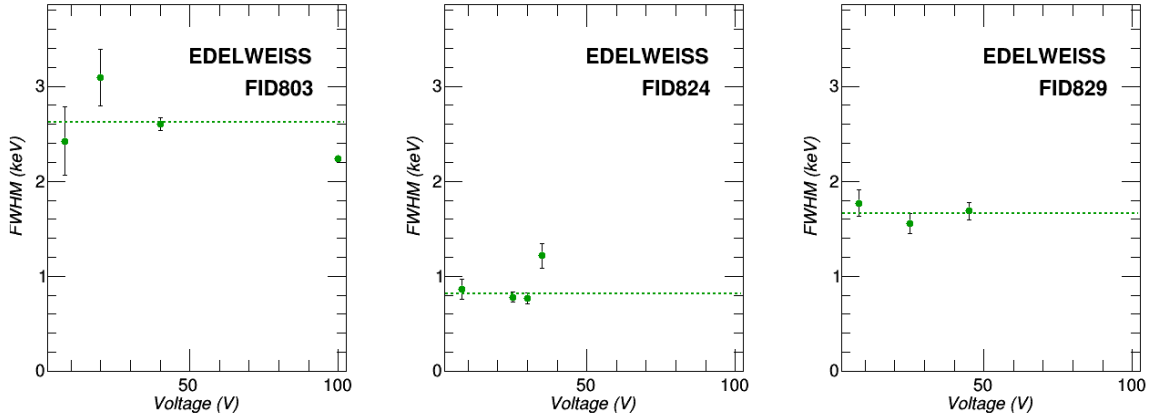


Figure 3.20 – Phonon resolution σ_{phonon} in keV as a function of the applied voltage bias V for FID803 (left), FID824 (middle) and FID829 (right) detectors. It was expected that the phonon resolution (in keV) is constant as a function of the voltage bias, as it is observed. The dashed line in each plot represents the fit of a constant resolution value as a guideline.

The consequence of a constant noise with respect to the σ_{phonon} resolution in keV is that the normalized heat resolution σ_{heat} in keV_{ee} decreases as a function of the voltage bias. The normalization being equal to $(1 + \frac{V}{3})$, it is expected that the σ_{heat} heat resolution is reduced by this factor. This behavior is confirmed in Fig.3.21 within the small fluctuations described above. The Luke-Neganov effect is observed, as long as the voltage bias applied on the detector does not exceed the V_{optimal} value (corresponding to the voltage bias from which the noise increases).

By biasing the FID800 detectors in high-voltage mode, the threshold value is strongly reduced. The search of WIMP with masses below 6 GeV/c² is thus accessible. The analysis methods to extract the spin-independent WIMP-nucleon cross-section from the data using this high-voltage mode will be described in chapter 5.

V Conclusion

In this chapter, the main steps of a standard analysis of the FID800 detectors at low and high voltage biases were described. Moreover, the study of the first runs using the Luke-Neganov effect to improve the threshold has been presented. These results are very promising. Nevertheless, the experiment performance is limited by a background strongly impacting the recoil energy spectrum at low energy, due to the so-called heat-only events. The next chapter of this work is dedicated to the study of this background. It will be demonstrated that a fully knowledge of heat-only events will be essential for the future analyses.

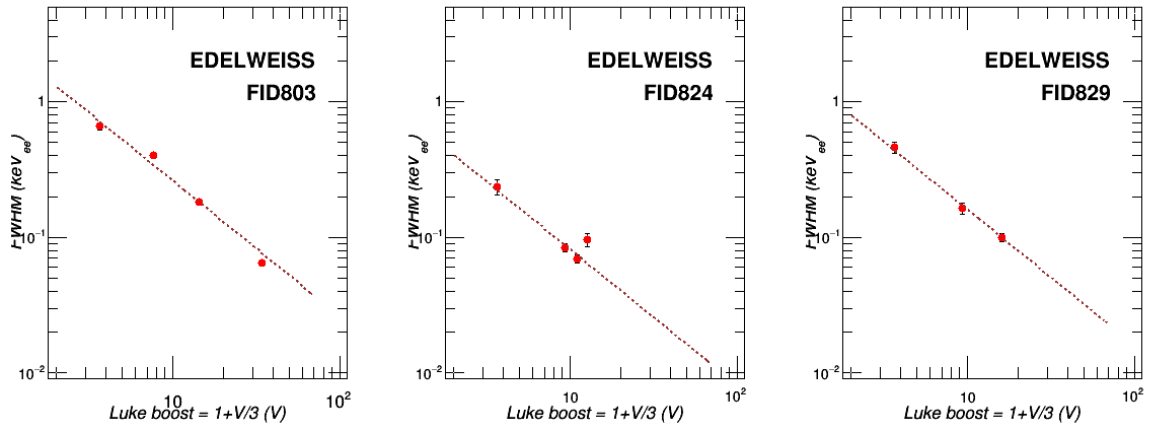


Figure 3.21 – Heat resolution σ_{heat} expressed in keV_{ee} as a function of the applied voltage $(1 + \frac{V}{3})$ for FID803 (left), FID824 (middle) and FID829 (right) detectors. As expected, the heat resolution σ_{heat} normalized by the Luke-Neganov boost $(1+V/3)$ with respect to σ_{phonon} decreases as the voltage bias increases. The dashed line in each plot is the fit of a linear function on the data, as a guideline.

Study of the heat-only background in the EDELWEISS detectors

The low-mass WIMP limit deduced from the 2014 data [92] was strongly impacted by a background of unknown origin called Heat-Only events (HO). The determination of the origin of this background is an important issue for the EDELWEISS experiment. A complete characterization of these HO events would permit to subtract their contribution or at least take them into account in order to obtain the best possible limit on WIMP-nucleon cross-section. In that context, a dedicated analysis has been performed and is presented in this chapter.

This type of events is not seen in experiments similar to EDELWEISS, as CDMS for example. In the CRESST experiment, an unknown type of events had appeared in their sapphire crystals [96]. Their origin was attributed to fracture events in sapphire due to the very tight clamping of detectors. They were removed by replacing the tight clamps by springs.

In this chapter, the description of this background is made and the different properties of these events are described. Their energy spectra are characterized as a function of different experimental conditions using a Kolmogorov-Smirnov test. A model able to characterize the HO events is built and will be used in chapter 5, for the calculation of the WIMP-nucleon cross-section limit. Finally, hypotheses concerning their origin are detailed. This study is based on all the data available since 2014 (on all detectors in the cryostat throughout the cool-down periods named run308 to run311).

I Heat-only event definition

Heat-only events are characterized by a normalized heat energy E_{heat} (in keV_{ee}) recorded simultaneously by the two NTD A and B, with resolution $\sigma_{heat,A}$ and $\sigma_{heat,B}$ respectively, and no ionization energy detected by electrodes:

$$|E_{heat,A} - E_{heat,B}| < \lambda \sqrt{\sigma_{heat,A}^2 + \sigma_{heat,B}^2} \quad (4.1)$$

$$E_{ion} < 2.58\sigma_{ion} \text{ i.e } Q \simeq 0 \quad (4.2)$$

where E_{ion} is the ionization energy measured by all electrodes of a detector, σ_{ion} is the resolution on this quantity and λ is a factor defined in Eq.3.20. The distribution of E_{phonon} (Eq.3.13) is

Chapter 4: Heat-only event characterization

shown in Fig.4.1 (top, right) for HO events of FID824 detector during run308. The shape of the heat pulses of these events is undistinguishable from those from γ -ray calibrations, i.e the heat χ^2 cuts described in chapter 3 don't reject this kind of events. Moreover no interaction is measured in coincidence with another detector.

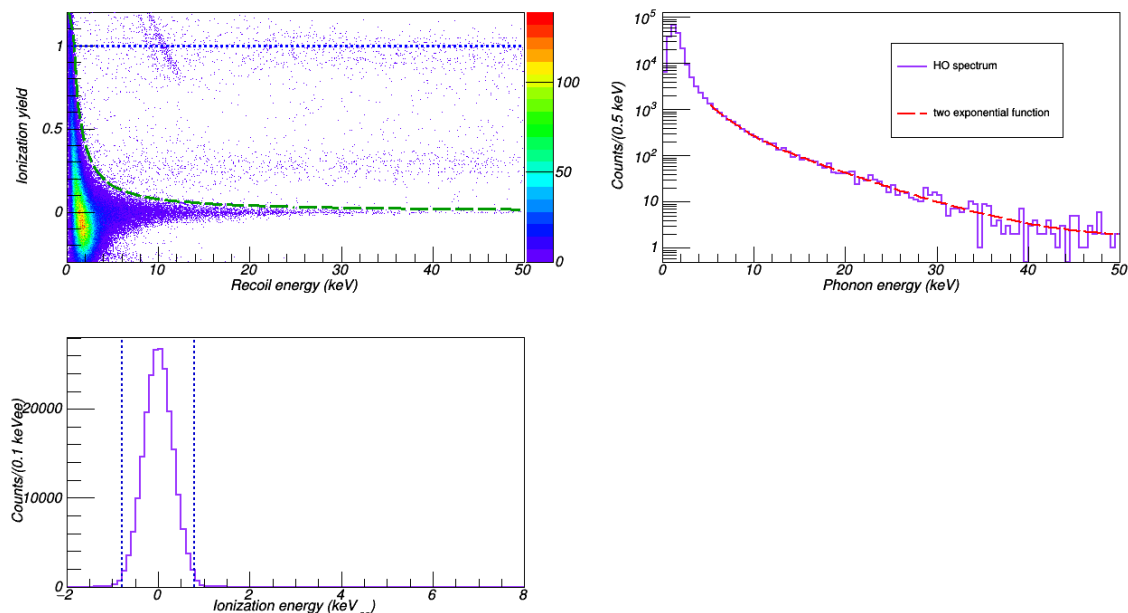


Figure 4.1 – Top, left: ionization yield as a function of the recoil energy (in keV) for FID824 detector in run308 (at 8 V). The blue dashed line corresponds to the center of the electronic recoil band. The green dashed line corresponds to the ionization threshold at $E_{ion} = 2.58\sigma_{ion}$ (99.9%). Heat-only events are distributed below this line (near $Q = 0$). Top, right: phonon energy distribution for heat-only events, in keV, fitted by a double exponential function (red dashed line). Bottom: ionization energy distribution for heat-only events in keV_{ee} . The dashed lines correspond to the value of the ionization cut at $\pm 2.58\sigma_{ion}$.

The phonon energy spectrum of HO events is well described by two exponential decays as illustrated in Fig.4.1 (top, right). This HO spectrum spreads up to 100 keV. The associated ionization energy distribution (Fig.4.1, bottom) follows a gaussian centered in zero with sigma corresponding to the resolution σ_{ion} as described in Eq.4.2. The importance of this background is illustrated in Fig.4.1 (top, left), showing the ionization yield Q as a function of the recoil energy for FID824 detector in run308, with a 8 V voltage bias and no calibration source. No fiducial cut is applied. Events centered around the blue line ($Q = 1$) are electronic recoils from γ -rays. Surface β -events have a Q value between 0.3 and 0.4. Heat-only events are below the green dashed line corresponding to 99.9% acceptance ($E_{ion} = 2.58\sigma_{ion}$). As shown in this plot, the big challenge of this study is to differentiate heat-only events from the population with low Q value at very low energy, which corresponds to events that have been triggered because of an upward fluctuation of the noise in the heat channels. To exclude a contribution of this noise distribution from the selected population of heat-only events, an analysis threshold must be set on E_{phonon} . To estimate its possible impact on the analysis, a procedure with three different minimum phonon energy values, $E_{phonon}^{min} = 5, 10$ and 15 keV, is repeated¹. The maximum

¹it is needed since one compares detectors with different threshold energy values.

Chapter 4: Heat-only event characterization

phonon energy is fixed at $E_{\text{phonon}}^{\text{max}} = 100$ keV (corresponding to ~ 3 keV $_{ee}$ for a Luke-Neganov boost of 100 V). It corresponds to the maximum recoil energy expected for a WIMP with mass below 6 GeV/ c^2 .

To study this background, it is essential to fix a set of cuts which will be applied in the same way to all data, even for different cryogenic run configurations. Consequently, the same quality cuts as defined in chapter 3 have been used:

- ionization channels χ^2 cut,
- heat channels χ^2 cut,
- heat resolutions cuts (Eq.3.17).
- NTD events cuts (Eq.3.20).

II Measured properties of heat-only events

Heat-only events are not removed by the χ^2 cut on the ionization channels allowing to determine that they have a pulse shape comparable with the pulse template (see chapter 3). Moreover, heat-only events survive after application of the χ^2 cut on the heat channels, as illustrated in Fig.4.2 (left). The right plot shows that they are not NTD events and can not be subtracted with the associated cut (no event belong x- or y-axis, as explained in chapter 3). Finally, single

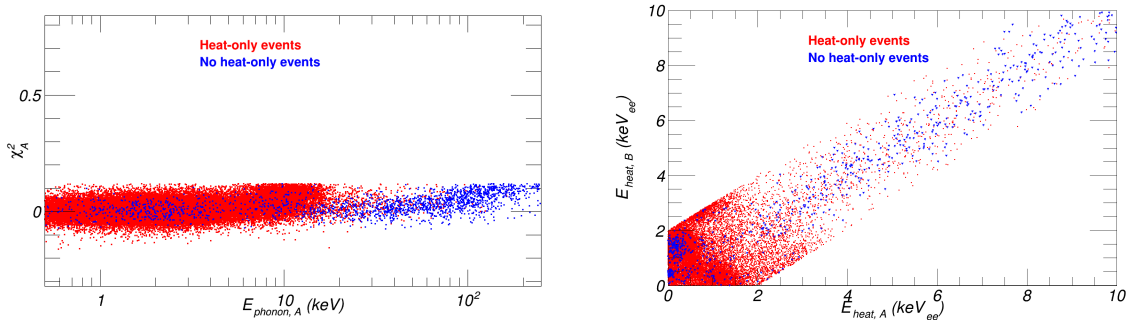


Figure 4.2 – Left: χ^2 cut on the heat channel for NTD A as a function of its measured phonon energy. Right: heat energy measured by the NTD B as a function of the one measured by the NTD A. The red points are heat-only events and blue points are not heat-only events. All these events are accepted by the different selection cuts listed in the text.

event selection, i.e no coincidence with another detector, doesn't reject HO background.

The phonon energy spectrum shown in Fig.4.1 has been modeled to be a double exponential function in previous analyses [92, 91]. Moreover, all heat-only energy spectra extracted for different detectors, runs or voltage bias seem to have the same behavior. And the ionization energy has to be, by definition, a gaussian centered at zero with a sigma value corresponding to the ionization resolution of the detector.

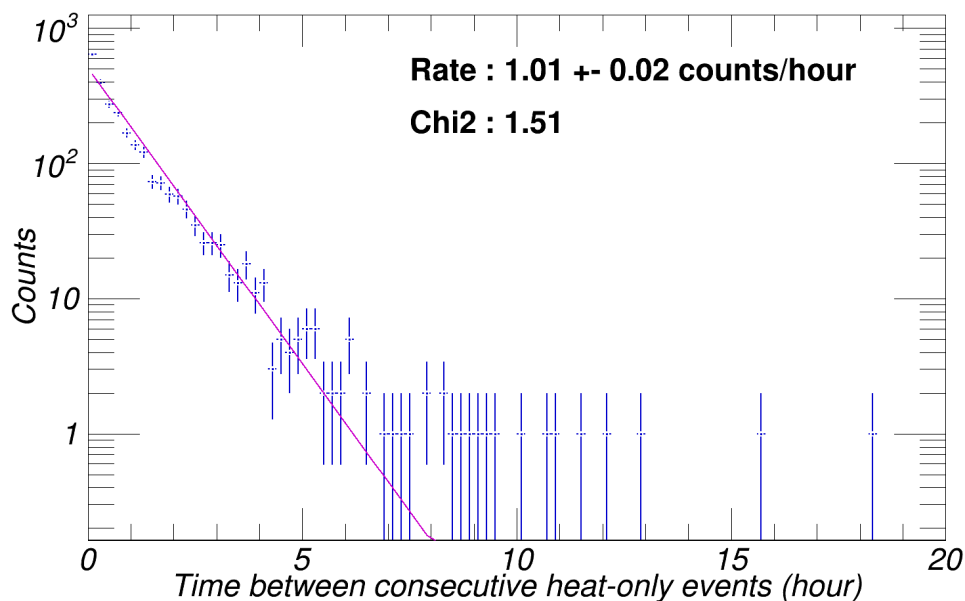


Figure 4.3 – Distribution of the time between consecutive heat-only events for FID824 detector. Data are limited to the end of the run308 ($d = [120, 300]$ days) to avoid the clear fluctuation of heat-only count rate observed before that and restrict the analysis to a period when the rate is approximately constant (see section II.2). The fit with an exponential function is shown as a magenta line.

II.1 Heat-only time distribution

If HO events occur randomly (i.e with no correlation) with an almost constant rate, the distribution of the time difference Δt between two consecutive events should be an exponential with a slope equal to the rate λ :

$$\frac{N(t)}{\Delta t} = R.e^{-\lambda t} \quad (4.3)$$

where $N(t)$ is the number of events. This law was tested on heat-only events in the period from day $d = 120$ to $d = 300$ in run308, where the HO rates appear to be constant. The result is shown in Fig.4.3 in which the distribution is described by Eq.4.3. There is no correlation between the arrival time of each heat-only event.

II.2 Heat-only rate as a function of time

The rate of heat-only is not constant over time, as shown in Fig.4.4 (bottom), which presents the heat-only count rate of FID824 detector during the time period between start of run308 and end of run310. The choice of the time interval is thus important in order to avoid bias in the measurement of the heat-only event rate. In this figure, the heat-only rate is represented with a day binning. It is therefore important to measure the exposure on a daily basis, including all the time period cuts defined in chapter 3. This calculation is made in the following way. An histogram with the number of events passing all period and quality cuts and having an energy superior to the energy threshold value $E_{\text{phonon}}^{\text{min}}$ is built, using a hourly binning. Each bin with at least one count is considered as a live hour. The exposure in time per day is defined as the number of live hours within day corrected by the dead time (see chapter 3). The choice of

Chapter 4: Heat-only event characterization

$\Delta t = 1$ h induces an overestimate of at most 3.5% of the exposure as shown in Fig.3.14. This is acceptable compared to the statistical uncertainties coming from the daily heat-only event rate (Fig.4.4, bottom). The heat-only rate is then simply the measured number of HO events in one day multiplied by the corresponding exposure.

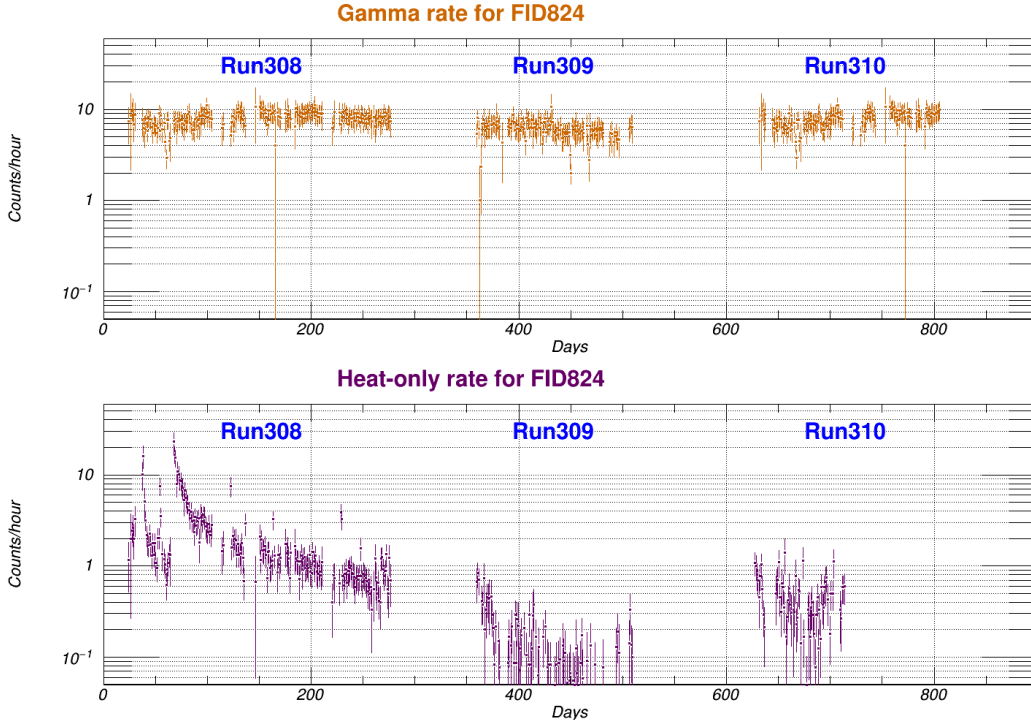


Figure 4.4 – Top: gamma count rate for FID824 detector between start of run308 and end of run310. It is expected that the gamma background is almost constant over time. Bottom: heat-only count rate of FID824 detector in the same time interval, for heat-only events with phonon energy above $E_{\text{phonon}}^{\text{min}} = 5$ keV. An unexpected variation is observed around the day 65 (run308).

Fig.4.4 (top) shows that the procedure, when applied to the calculation of the γ -ray rate, reproduces reasonably well the expected constant γ -ray rate as a function of time. The small variation from one cryorun to another is compatible with the changes in the run set-up. While the gamma count rate is constant, important variations on heat-only event rate are observed. This behavior is generally observed at the beginning of a cryorun with a constant decrease over time.

Nevertheless, anormal high heat-only event rates can happen during a cryorun, for example around the 65th days of run308 as shown in Fig.4.5 for two different detectors, or in run311 (see Fig.4.6). Fig.4.5 illustrates that the same trends are observed in all detectors when comparing the heat-only rates over time for FID824 and FID26 detectors in run308. The investigation on the possible causes for the sudden increase at day $d = 65$ in run308 will be described in next section.

II.3 Heat-only count rate anomaly

As explained previously, a strong variation of the heat-only count rate has been observed in all detectors, 65 days after starting run308. In this section, the behavior of all detectors is studied

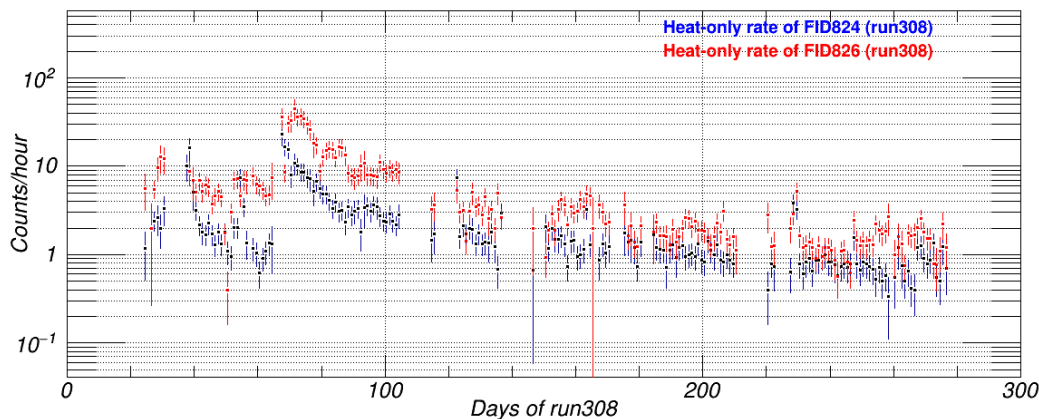


Figure 4.5 – Heat-only count rate during run308 for FID824 (in blue) and FID826 (in red) detectors, for heat-only events with phonon energy above $E_{\text{phonon}}^{\text{min}} = 5 \text{ keV}$. A sudden variation of these distributions occurs at day 65 with no clear explanation.

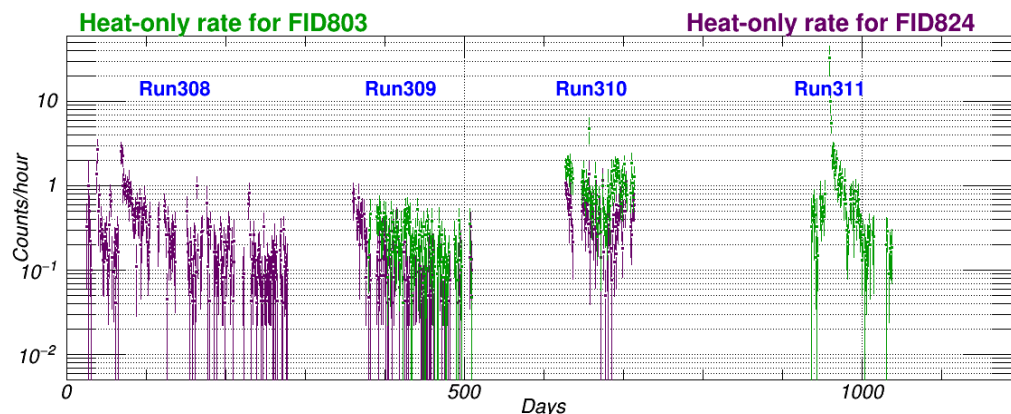


Figure 4.6 – Heat-only count rate for the whole studied data taking period for FID803 detector (which is in the cryostat since 2015, i.e. run309) in green and FID824 detector in magenta, for heat-only events with phonon energy above $E_{\text{phonon}}^{\text{min}} = 15 \text{ keV}$. This higher phonon energy threshold is needed for detector comparison if FID803 is present. A sudden variation has also been observed during run311, without explanation about its origin so far.

with respect to this particular moment. For each detector, a model of two exponentials is used to fit the heat-only count rate:

$$f(t) = A_1 \cdot e^{\frac{-(t-t_0)}{\tau_1}} + A_2 \cdot e^{\frac{-(t-t_0)}{\tau_2}} \quad (4.4)$$

where t_0 is equal to 65 days in run308, the A_i parameters are the amplitudes of the two exponentials (in count/hour) and the τ_i parameters are the decay time constants (in days). An example of a fit is shown in Fig.4.7, for FID824 detector. The fit parameters of some of the 24 detectors installed in the cryostat are reported in Fig.4.8. The τ_1 and τ_2 time constants are similar for all detectors (two right panels of Fig.4.8). The dashed lines are the average value of all time constants. The amplitude parameters A_1 and A_2 are shown on the two left panels in Fig.4.8. In contrast with time constants, the amplitudes vary from a detector to another.

Chapter 4: Heat-only event characterization

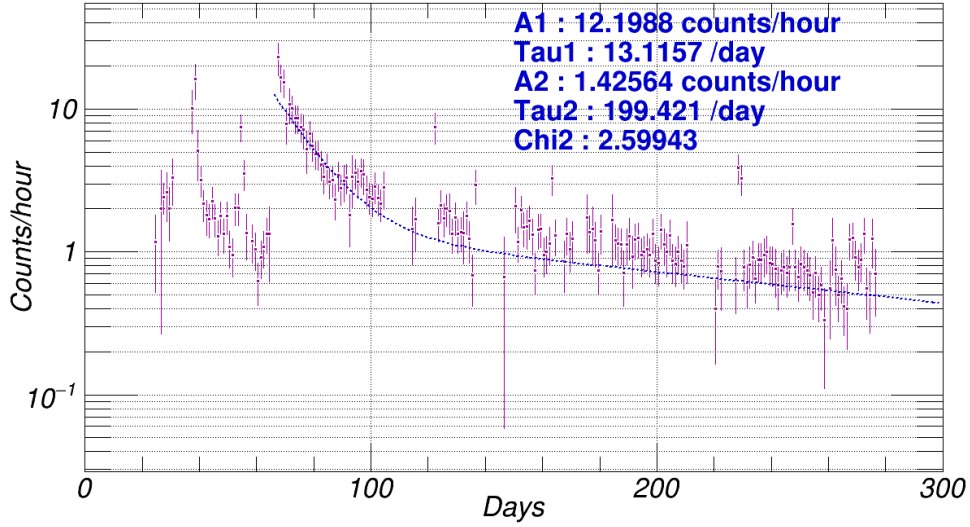


Figure 4.7 – Heat-only count rate for FID824 detector during run308, for events above $E_{\text{phonon}}^{\text{min}} = 5$ keV. A fit with two exponentials (in dashed blue) is applied to determine the amplitudes and time constants.

Nevertheless, for all detectors, the anomaly is seen in the same way, as illustrated in Fig.4.9 showing the ratio A_1/A_2 which is constant in average. Fig.4.10 summarizes these results

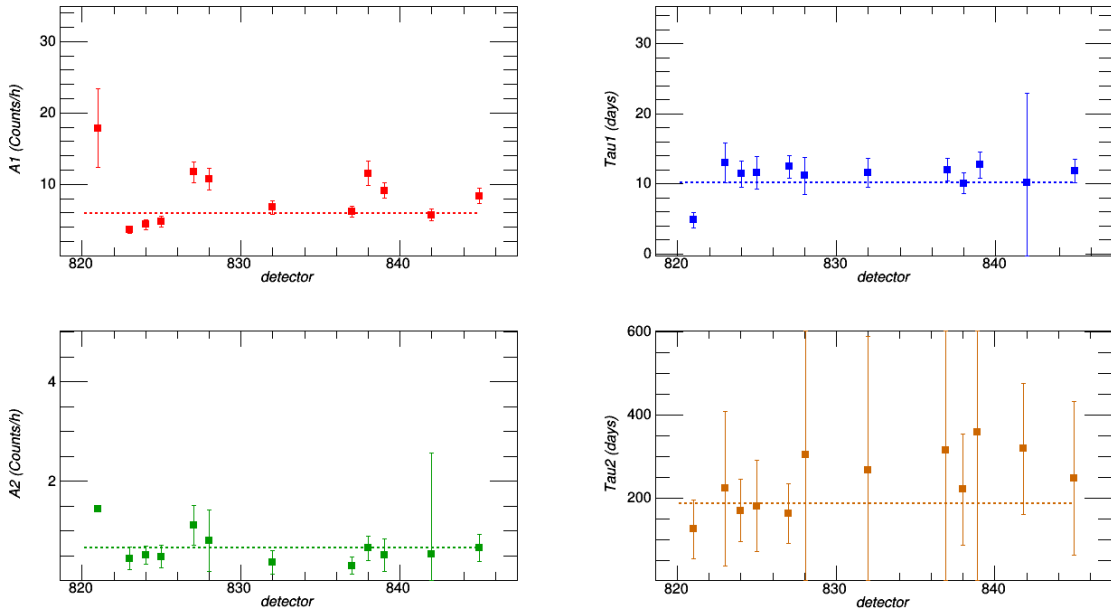


Figure 4.8 – Parameters of the fit $f(t) = A_1 \cdot e^{-\frac{(t-t_0)}{\tau_1}} + A_2 \cdot e^{-\frac{(t-t_0)}{\tau_2}}$ applied on all heat-only count rates for run308 detectors, for $E_{\text{phonon}}^{\text{min}} = 10$ keV. The two left plots correspond to the fitted amplitudes A_i whereas the right plots show the time constants τ_i . Dashed lines are the average values of respective parameters.

where the A_i amplitudes parameters (left) are strongly correlated and τ_i time constants (right)

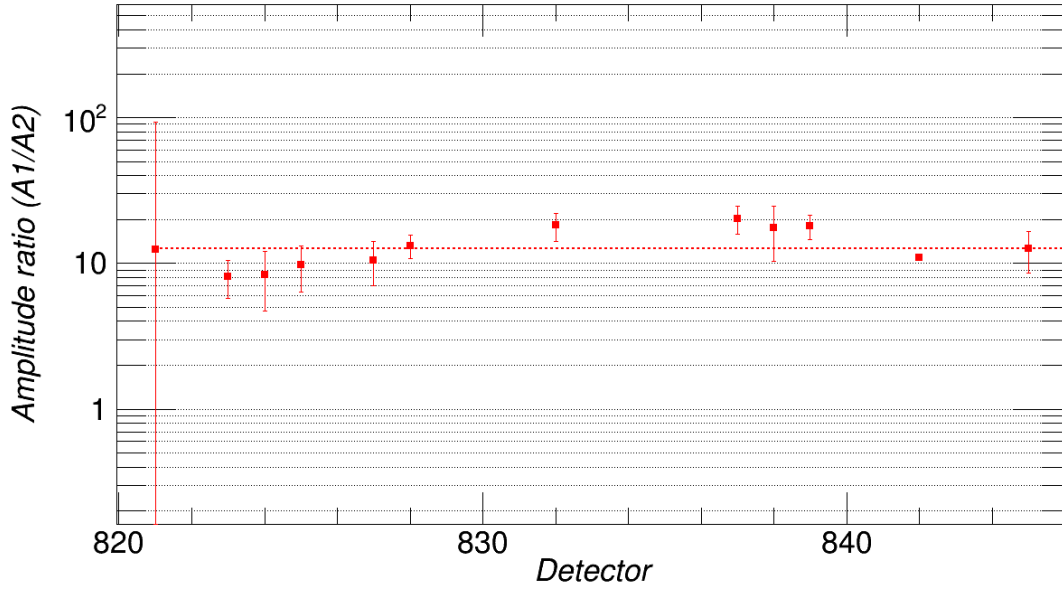


Figure 4.9 – Ratio of the amplitudes A_1 and A_2 of the two exponentials (Eq.4.4) as a function of the detector number, for $E_{\text{phonon}}^{\text{min}} = 10$ keV. The average value of the amplitude is shown in red dashed line.

have the same behavior. The discontinuity of the rate at day 65 is correlated with the rate observed at much later time. The first exponential following day 65 has a time constant of $8 < \tau_1 < 15$ days, and the second exponential has a time constant of $150 < \tau_2 < 350$ days. However, the absolute rates vary from detector to detector.

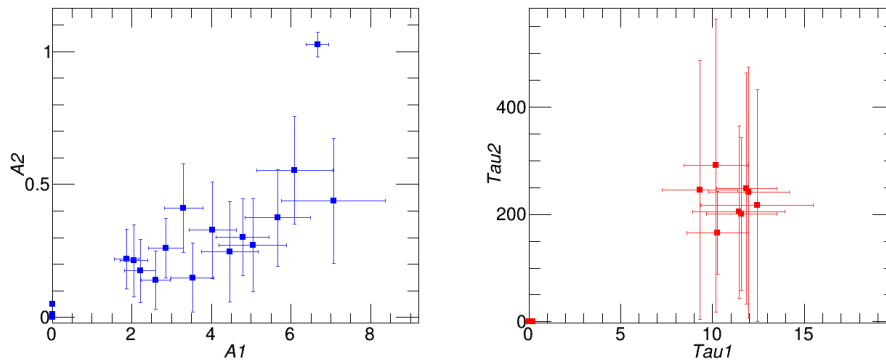


Figure 4.10 – Amplitude A_1 versus amplitude A_2 (left) and time constant τ_1 versus time constant τ_2 (right) for $E_{\text{phonon}}^{\text{min}} = 10$ keV, obtained from fit results as presented in previous figures. A strong correlation is observed between the two exponentials.

III Heat-only energy spectrum

The goal of the study presented in this chapter is to characterize the heat-only events, even if the origin of this background remains unknown. For that, an analysis using HO energy spectrum is made using the Kolmogorov-Smirnov test [97]. To characterize this heat-only energy spectrum, some assumptions have to be verified, such as:

- Does the shape of HO event spectra change when the voltage bias applied to the electrodes vary?
- Does the shape of the HO spectra change as a function of time?
- Does the shape vary from detector to detector?

A modelization of heat-only energy spectrum for each detector can be achieved if the answer to the first two questions allows to define there is no variation. The answer to the last question will allow to determine if a model common to all detectors can be developed.

III.1 Kolmogorov-Smirnov test

To evaluate if the shape of the energy spectra of HO events depends on the detectors, the voltage bias or the time, either a study of these parameters with a parametric test can be achieved, or a non parametric test can be used. The latter method has the advantage of not being biased by any choice of parametric function. Here the non parametric goodness-of-fit test which is performed is the Kolmogorov-Smirnov (KS) test [97]. It is more powerful than a simple binned χ^2 test and it can be applied on smaller datasets. Moreover, it is independent on the binning choice and it takes into account statistical fluctuations.

Considering a sample of N data (X_1, \dots, X_N) , one can define $F_n(X)$ its Empirical Cumulative Distribution Function (ECDF) as:

$$F_n(X) = \frac{\int_0^X f(X)dX}{\int_0^N f(X)dX} \quad (4.5)$$

In the discrete case, the equation becomes:

$$F_n(X) = \frac{1}{N} \sum_{n=1}^N \mathbb{1}_{]-\infty; X]}(X_n) \quad (4.6)$$

where $\mathbb{1}$ is the indicator function, defined as 1 if the event occurs in the range $]-\infty; X]$ and 0 if not:

$$\mathbb{1}_{]-\infty; X]} = \begin{cases} 1 & \text{when } X_n \leq X \\ 0 & \text{when } X_n > X \end{cases} \quad (4.7)$$

In other words, the value of $F_n(X)$ is equal to the number of counts less than or equal to X divided by the total number of events in the sample. Thus, $F_n(X)$ represents the proportion of the sample values that are less than or equal to a given value of x .

Comparing now the two samples (X_1, \dots, X_N) and (Y_1, \dots, Y_M) , the distribution estimator $D_{n,m}$, defined as:

$$D_{n,m} = F_n - F_m \quad (4.8)$$

Chapter 4: Heat-only event characterization

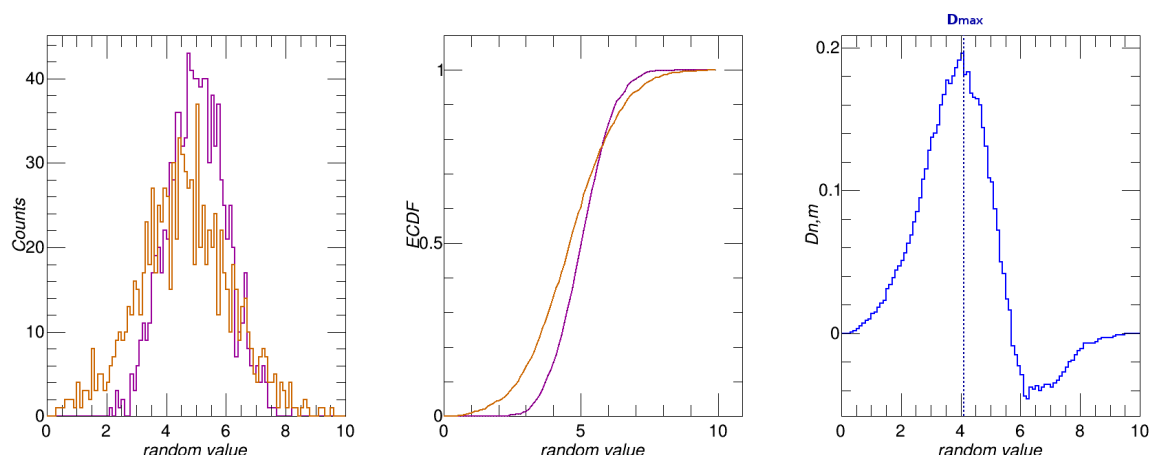


Figure 4.11 – Left: the first simulated distribution (in magenta) comes from a gaussian centered in 5 (with $\sigma = 1$). The second simulated distribution (in orange) derives from a gaussian centered in 4.5 (with $\sigma = 1.5$). Middle: the two ECDF of left samples (with same colors). Right: $D_{n,m}$ distribution associated to these two samples. The dashed dark blue vertical line represents the maximum deviation $D_{n,m}^{max}$ between the two samples, also called maximum deviation estimator of $D_{n,m}$.

α	0.10	0.05	0.025	0.01	0.005	0.001
$c(\alpha)$	1.22	1.36	1.48	1.63	1.73	1.95

Table 4.1 – $c(\alpha)$ values of the Kolmogorov-Smirnov test for different confidence levels α [98].

corresponds to the difference between the ECDF of the two samples ($F_n(X)$ and $F_m(Y)$). Fig.4.11 represents an example of two different simulated distributions (left plot) and their associated ECDF (middle plot). The $D_{n,m}$ distribution for these two samples is also represented (right plot) and is used to determine the maximum deviation estimator $D_{n,m}^{max} = \sup_{X,Y \in \mathbb{R}} |D_{n,m}|$

between the two samples.

The hypothesis H_0 is defined as: the two tested samples follow the same distribution. The Kolmogorov-Smirnov test of H_0 compares the obtained maximum deviation estimator $D_{n,m}^{max}$ to $D_\alpha(n, m)$, which is the critical value of the test, as published by Smirnov [98]. The null H_0 hypothesis is rejected with a confidence level $(1 - \alpha)$ if $D_{n,m}^{max} > D_\alpha(n, m)$ where $D_\alpha(n, m)$ is defined as:

$$D_\alpha(n, m) = c(\alpha) \sqrt{\frac{n+m}{nm}} \quad (4.9)$$

The $c(\alpha)$ coefficients are given in table 4.1 for confidence levels greater than 90%.

The goodness-of-fit test, i.e the KS test, is constructed by using the critical value $D_{n,m}^{max}$. The probability of the Kolmogorov-Smirnov test is defined as:

$$P_{KS}(z) = 2 \sum_{k=1}^{\infty} (-1)^{k-1} \exp(-2k^2 z^2) \quad (4.10)$$

where z corresponds to the distance between the ECDF of the two samples ($F_n(X)$ and $F_m(Y)$),

Chapter 4: Heat-only event characterization

weighted by their sizes n and m :

$$z = D_{n,m}^{max} \times \sqrt{\frac{nm}{n+m}} \quad (4.11)$$

The returned value $P_{KS}(z)$, which is called p-value in the following, gives the statistical test for compatibility between the two samples. The KS probability test results have to be uniformly

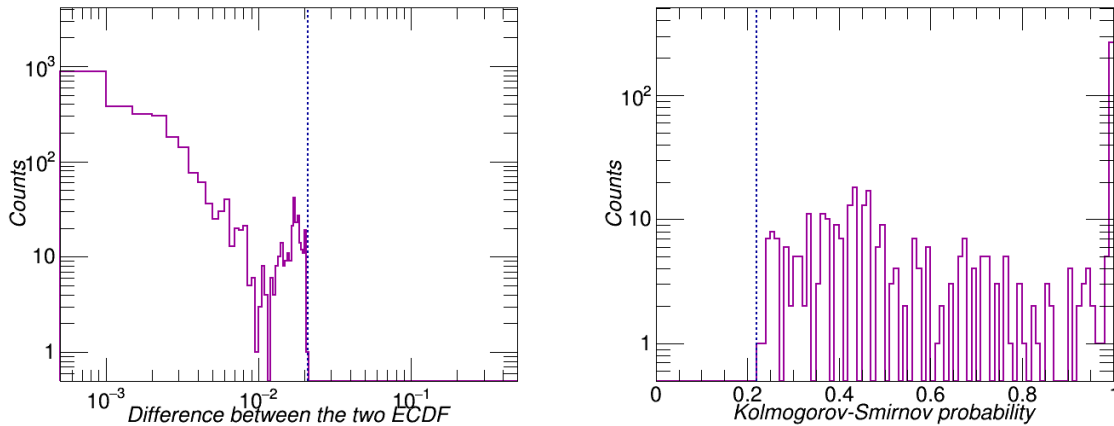


Figure 4.12 – Left: $D_{n,m}$ distribution of the two samples which are random values issue from gaussians with means at 5 (with $\sigma = 1$). The dashed dark blue verticale line corresponds to the $D_{n,m}^{max}$ value, i.e the maximum deviation between the two ECDF of this distribution. Right: Kolmogorov-Smirnov probability (p-value) associated to each $D_{n,m}$ distribution. The dashed dark blue verticale line corresponds to the p-value obtained for $D_{n,m}^{max}$.

distributed between 0 and 1 if the two samples come from the same distribution. If not, the obtained p-values are close to zero. In the first case, the associated ECDF follows a linear behavior whereas it does not in the second case. Values close to 0 are taken as indicating a small probability of compatibility. The calculation of the KS test for 10000 simulations comparing the two distributions illustrated in Fig.4.11 is shown in Fig.4.12. The left plot presents the $D_{n,m}$ distribution and the right is the $P_{KS}(z)$ distribution associated to each value of the left distribution.

To illustrate the result of the Kolmogorov-Smirnov test, three distributions are generated. Two of the distributions contain each 1000 random events generated from a gaussian function with a mean of 5 and $\sigma = 1$. The third distribution contains 1000 random events generated from a gaussian function with a mean of 4.5 and $\sigma = 1$. Two different comparison tests are made: one between the two first distributions, and the other one comparing the first distribution with the third one. The p-values resulting from the thousand Kolmogorov-Smirnov tests verify the expected behavior, as illustrated in Fig.4.13. The distribution is uniformly distributed between 0 and 1 (left top), corresponding to the fact that its ECDF follows the function $f(x) = x$ when the two sample are comparable (top right). Instead of the bottom plots whose samples come from different parent distributions.

To demonstrate how the confidence level obtained with the KS test varies with statistics, two cases have been simulated, with gradually increasing statistics (n):

- in the first, the same two gaussian functions as in the previous example are compared.

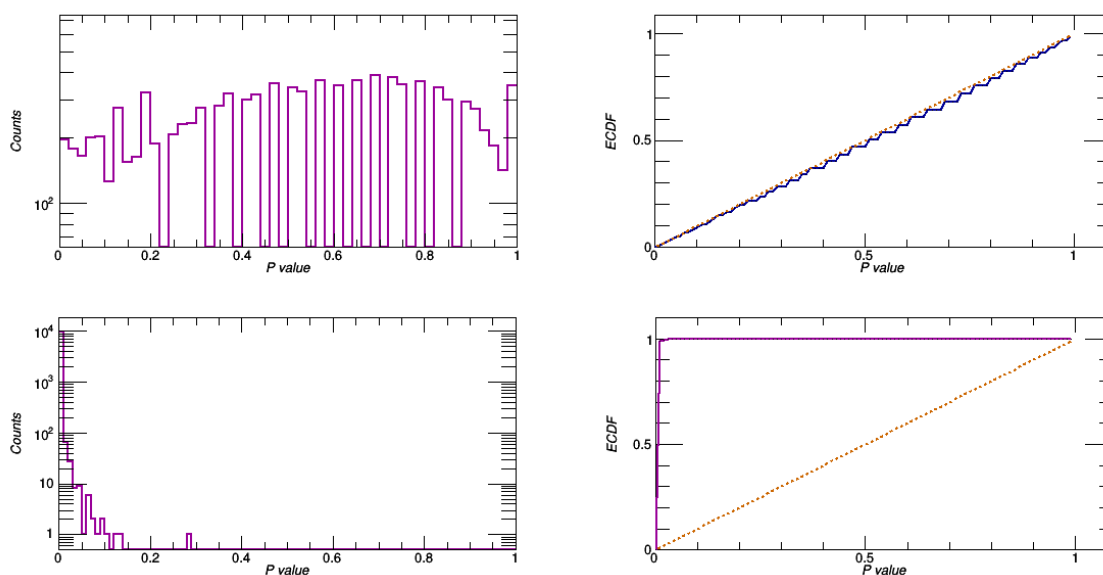


Figure 4.13 – Top, left: distribution of the KS test results (p -values) for the comparison between two random samples issue from the same gaussian functions. As expected, the distribution is uniformly distributed between 0 and 1. Top, right: ECDF of the left results. If the ECDF follows the dashed orange line, corresponding to $f(x) = x$, the two samples are comparable, as it is the case here. Bottom, left: distribution of the p -values for the comparison between two random samples issue from two different gaussian functions. The distribution is mostly around 0. Bottom, right: ECDF of the left results. The ECDF doesn't follow the dashed orange line corresponding to $f(x) = x$, i.e the probabilities are not uniformly distributed between 0 and 1: the two samples are different.

- in the second, the gaussian with mean of 5 and $\sigma = 1$ is compared with another gaussian with mean of 4.95 and $\sigma = 1$.

The two parent distributions in the second case are very similar. Thus the KS test requires a sizeable value of n in order to be sensitive to their difference. As shown in Fig.4.14 (bottom), for such small difference between the two populations, the KS test needs a large sample to be sensitive, with at least $n > 1000$. In contrast, the KS test never declares different two samples coming from the same parent distribution even at low statistics (top plots of the figure), it can thus be used to conclude on the uniformity of the heat-only distributions.

III.2 Study of heat-only spectra dependence

III.2.1 Voltage dependence of heat-only spectra

In run309 and the following runs, the detectors were operated at different voltage biases, ranging from 8 V to 110 V. The question of whether this voltage bias might influence the heat-only rate is of interest in a complete investigation of the possible source of HO events. This question is also highly relevant for the WIMP searches described in chapter 5. The minimum energy at which heat-only events can be discriminated from events with ionization increases with the applied voltage bias. If the heat-only spectrum and the HO rate do not depend on the voltage bias, the 8 V data can provide precise and independent sideband data for the modeling of the

Chapter 4: Heat-only event characterization

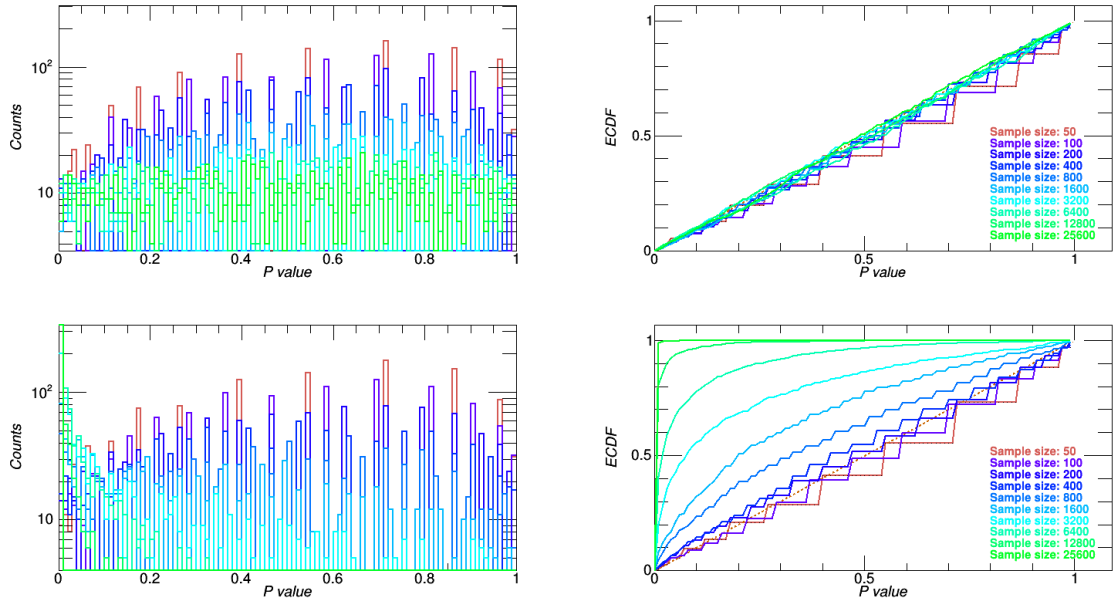


Figure 4.14 – Top, left: distribution of the p-values for the comparison between two random samples issue from the same gaussian functions. The colors represent different size samples. As expected, the distribution are uniformly distributed between 0 and 1. Top, right: ECDF of left results. Each ECDF follows the dashed orange line, corresponding to $f(x) = x$ even in case of low statistics. Bottom, left: distribution of the p-values for the comparison between two random samples coming from two different gaussian functions (see text). Each color represents a size samples. Bottom, right: ECDF of left results. For low statistics ($n < 1000$), the test cannot detect the small difference between the two compared functions.

HO spectrum at 100 V. The detectors that have been tested for high voltage, with the voltage bias values are:

- FID803 operated at 8 V, 20 V, 40 V, 45 V, 50 V, 85 V, 90 V and 100 V;
- FID804 operated at 8 V, 20 V and 70 V;
- FID824 operated at 8 V, 20 V, 25 V, 30 V and 35 V;
- FID829 operated at 8 V, 20 V, 40 V and 45 V.

Heat-only energy spectra have been extracted for each of these detectors and applied voltage biases. For each detector, the Kolmogorov-Smirnov test has been used to compare the data at different voltage biases, as shown in Fig.4.15 (top) for FID803 detector.

Fig.4.15 (bottom, left) shows the resulting ECDF distributions for different values of the minimum phonon energy (5 keV in red, 10 keV in blue and 15 keV in green) for FID803 detector. These results are considered as following the linear function drawn ($f(x) = x$), because there is low statistics (corresponding to almost thirty voltage tests for this detector). Furthermore, some of the studied voltage bias values have low statistics due to very short time periods of data taking. The bottom right plot indicates that results are not biased by low voltage or high voltage values, since blue shades are homogeneously distributed as a function of voltage pairs.

Chapter 4: Heat-only event characterization

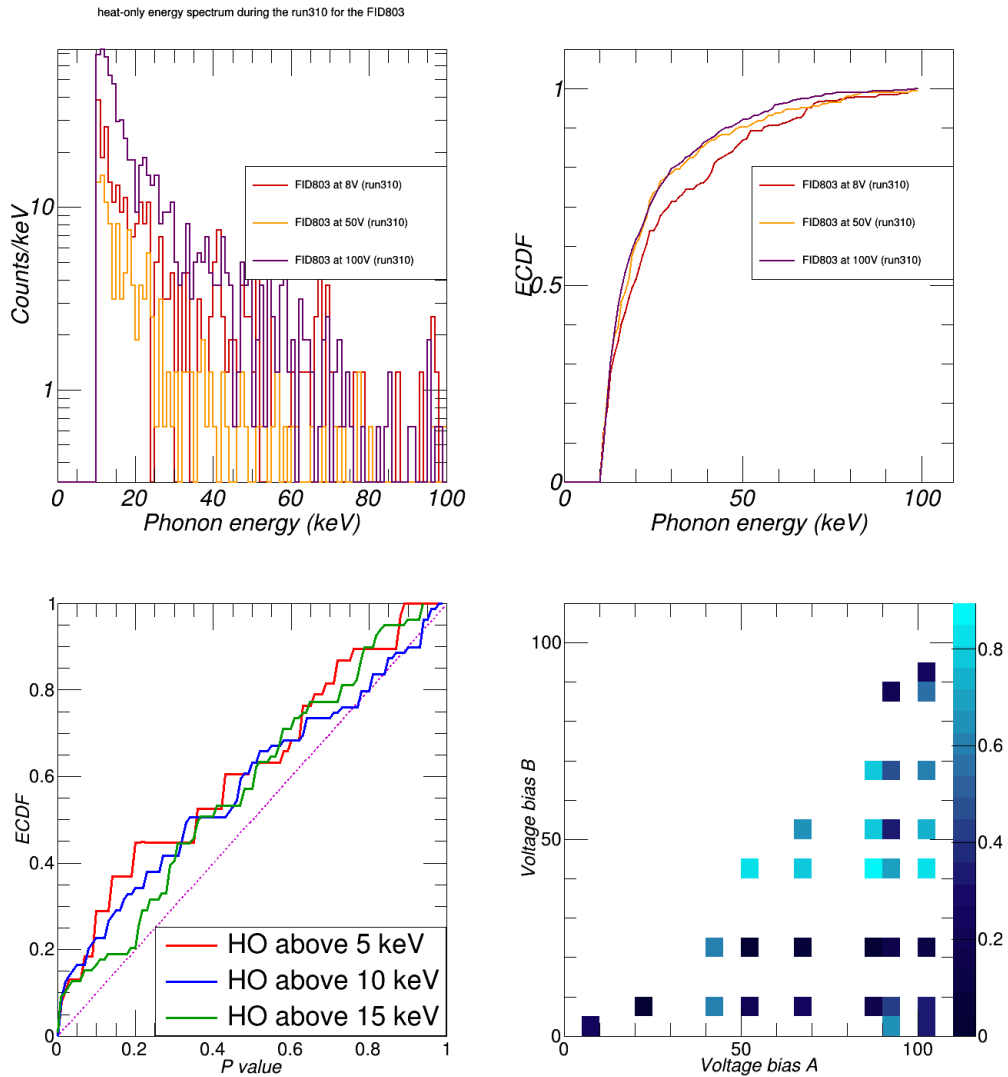


Figure 4.15 – Top, left: heat-only energy spectrum for FID803 detector at 8V (in red), 50V (in orange) and 100V (in magenta). Top, right: ECDF of these three datasets with the same color code. Bottom, left: ECDF as a function of the p-values for an analysis with a minimum phonon energy at 5 keV (in blue), 10 keV (in red) and 15 keV (in green) for the different voltage biases used for FID803 detector. The linear function ($f(x) = x$) is drawn in dashed violet. 1.26% of the results have a p-value less than 0.01 for $E_{\text{phonon}}^{\text{min}} = 10$ keV. Bottom, right: p-values in the space of parameters ($\text{Voltage}_A, \text{Voltage}_B$), using $E_{\text{phonon}}^{\text{min}} = 10$ keV. The blue shades correspond to the obtained p-values (between 0 and 1). It allows to verify that results are also homogeneously distributed in the voltage ranges.

It can be concluded that the heat-only energy spectrum is not modified by the applied voltage bias. Another conclusion is that heat-only events seem to be independent of the charge event collection. If it was the case, a gradient of color would appear on the right plot.

Chapter 4: Heat-only event characterization

III.2.2 Detector dependence

The second question is whether the shape of heat-only spectra depends on the detector. If it was the case, an universal model could represent all spectra. If not, one model per detector will be required. For this analysis, all the detectors in use since run308 are considered. The 70 associated heat-only energy spectra have been compared with the KS test in order to study this assumption for all pairs of detectors, as illustrated in Fig.4.16 (top) for three detectors in run308. Fig.4.16 (bottom) represents the results for all pairs of detectors and runs, for three different minimum phonon energy of 5 keV, 10 keV and 15 keV. ECDF as a function of the p-values (bottom left plot) indicate that heat-only events are different from one detector to another. The disagreement is strongest at low energy (with a E_{phonon}^{min} equal to 5 keV).

Although all detectors have a spectrum that behaves as a double exponential (see Fig.4.1), the exact parameters of the function seem to differ for each of them. This is why a modelization for each detector is required (see section III.3).

III.2.3 Time dependence

During run308 and run311, two strong variations of the heat-only count rate have been observed simultaneously by all detectors (Fig.4.5 and 4.6). The possibility that these sudden increases in rate are associated with a change of the spectra need to be investigated. The time variation of the spectra for run308 has been studied in detail, because it is the longest run available (almost 300 days) and it offers the largest number of detectors for the tests. For the analysis, this run is separated in time periods of one week and the heat-only spectra associated to each time period are compared using the Kolmogorov-Smirnov test (see Fig.4.17, top for FID824 detector). As shown in Fig.4.17 (bottom, left), the ECDF of the Kolmogorov-Smirnov results follow the linear function $f(x) = x$, indicating that the different heat-only spectra are comparable. The results of the KS test in the space of parameters ($Time_A, Time_B$), using $E_{phonon}^{min} = 10$ keV are also plotted (bottom, right). The blue shades corresponds to the p-values (between 0 and 1) and are uniformly distributed in this parameter space. In this way, it can be concluded that heat-only energy spectra don't vary as a function of time. Thus it is possible to modelize them for a given detector. Furthermore, the day corresponding to the sudden variation of the heat-only count rate (day= 65) doesn't affect this result.

III.3 Modelization of the heat-only background

All tests so far did not assume any mathematical form of the energy spectra. However, for the WIMP search, a modelization of this background is needed. Firstly, a model with two exponential function will be tested. Secondly, a Kernel Density Function will be considered.

III.3.1 Two-exponential spectrum model

In this section, a test to determine how well the spectrum can indeed be modeled with two exponentials is presented. All tests so far conclude that, for a given detector, a single spectrum shape is able to describe all data. Thus this study will be applied to the summed data on all runs and voltage biases, for a given detector. Each spectrum is fitted with the following function:

$$f(E_{phonon}) = A_1 \cdot e^{-\frac{E_{phonon}}{E_1}} + A_2 \cdot e^{-\frac{E_{phonon}}{E_2}} + B \quad (4.12)$$

Each energy constant E_i is in keV^{-1} and the amplitudes A_i are in counts, B is a constant background (inspired by the observed spectrum due to lead recoils [92]). An example of the fit

Chapter 4: Heat-only event characterization

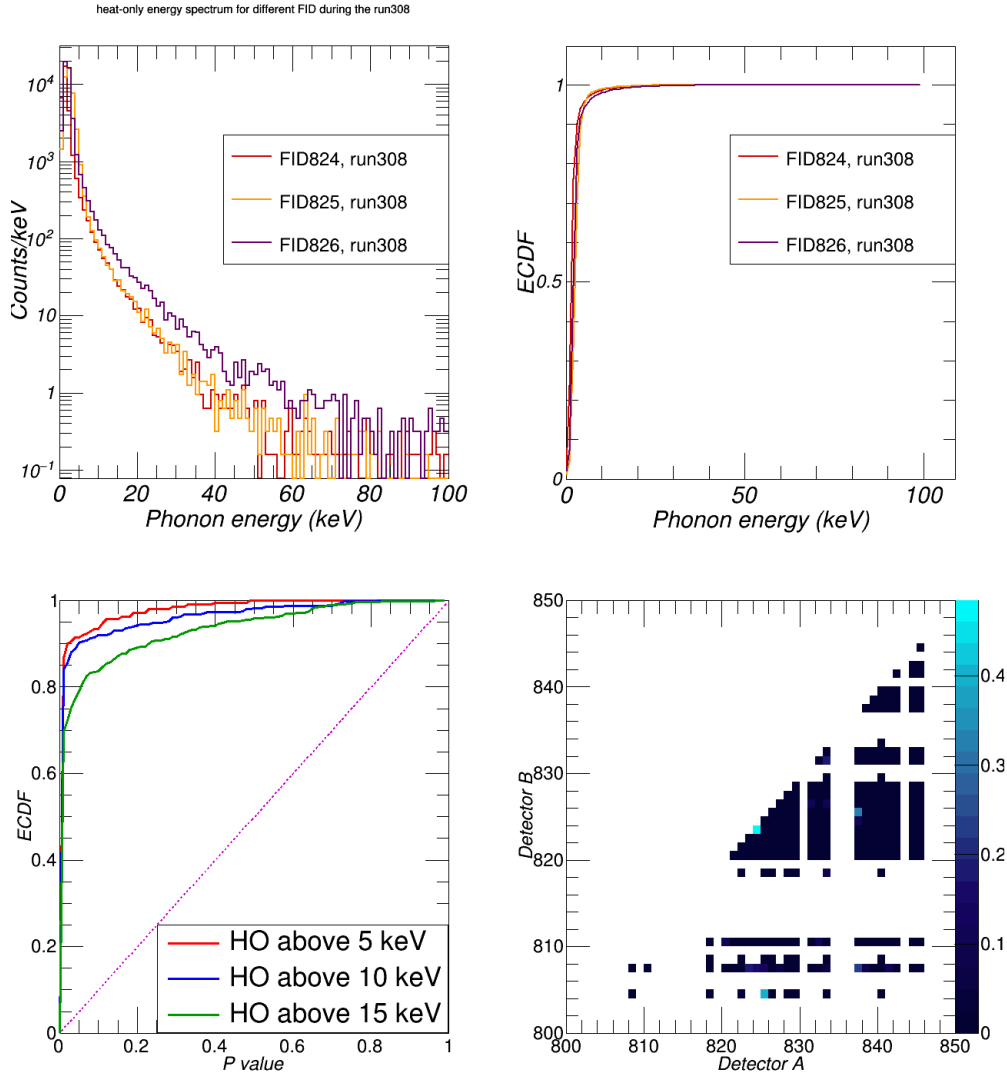


Figure 4.16 – Top, left: heat-only energy spectra of FID824 (red), FID825 (orange) and FID826 (magenta) detectors in run308. Top, right: ECDF of these three distributions. The main difference between these distributions corresponds to the phonon energy range $E_{\text{phonon}} \in [0; 20]$ keV. Bottom, left: ECDF as a function of the p -values between different detectors with $E_{\text{phonon}}^{\text{min}}$ equal to 5 keV (in blue), 10 keV (in red) and 15 keV (in green). The dashed violet line is the linear function ($f(x) = x$). It allows to conclude that the heat-only energy spectra are different whatever the detector independently of the $E_{\text{phonon}}^{\text{min}}$ value. Bottom, right: p -values in the space of parameters ($\text{Detector}_A, \text{Detector}_B$), using $E_{\text{phonon}}^{\text{min}} = 10$ keV. The blue shades correspond to the obtained p -values (between 0 and 1). It is used to verify if a group of detectors show the same heat-only model.

can be seen in Fig.4.18 for FID824 detector and the parameters obtained for the 20 detectors in this study are shown in Fig.4.19.

From the KS test described in section III.2.2, it is expected different parameters for each detector. Indeed, all plots in Fig.4.19 indicate that the parameters vary from detector to another, although some trends can be suspected.

Chapter 4: Heat-only event characterization

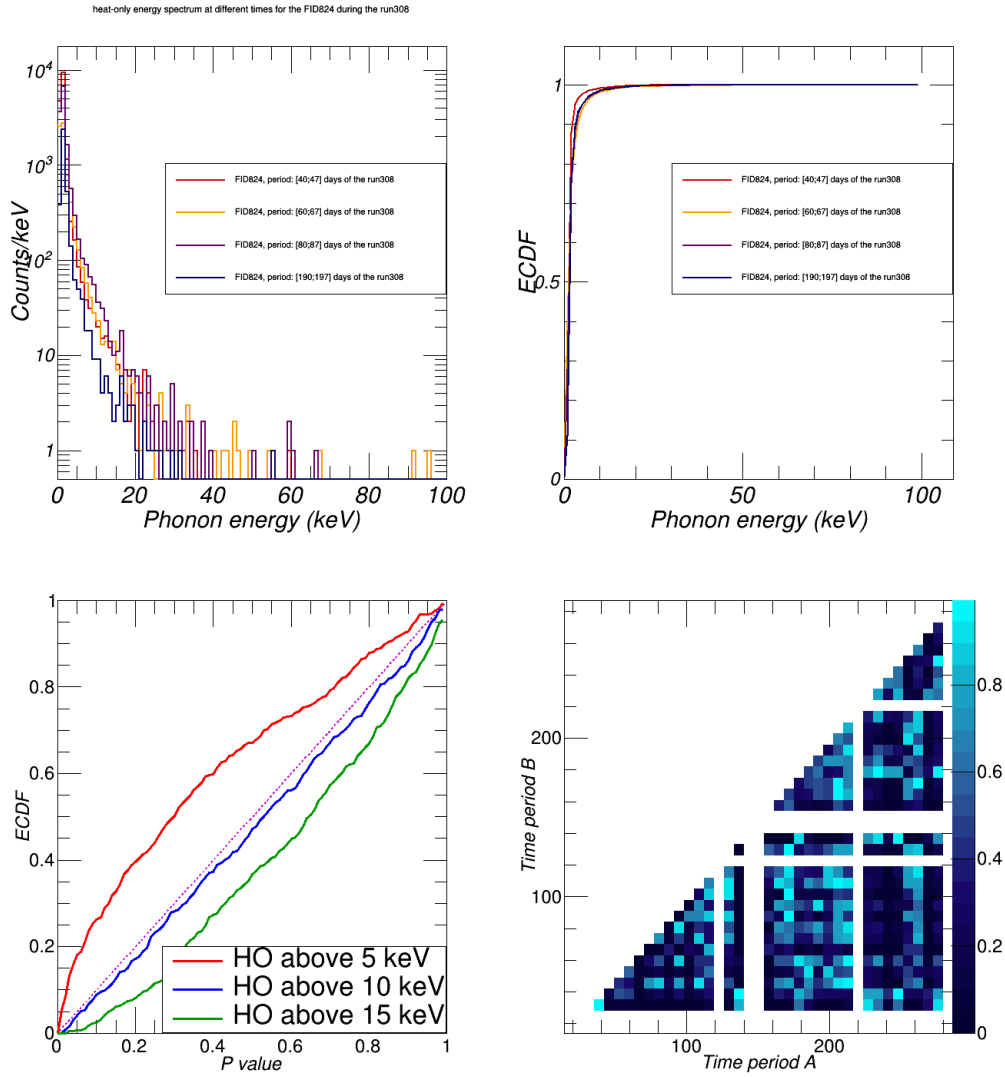


Figure 4.17 – Top, left: heat-only energy spectra of different time periods (of 7 days) for FID824 detector during run308. Top, right: associated ECDF. Bottom, left: cumulatives of p -values for $E_{\text{phonon}}^{\text{min}}$ equal to 5 keV (in blue), 10 keV (in red) and 15 keV (in green). The linear function ($f(x) = x$) is drawn in dashed violet. Bottom, right: p -values for the paired time period (with $E_{\text{phonon}}^{\text{min}} = 10$ keV) in the space of parameters ($\text{Time}_A, \text{Time}_B$). Blue shades represent the obtained p -values between 0 and 1 which are uniformly distributed.

These trends are studied by looking at correlations between the fitted parameters. The top panel of Fig.4.20 shows the ratio of the amplitudes A_1/A_2 and the bottom panel the ratio E_1/E_2 . So far, no clear correlations between the two amplitudes are visible. Contrarily, the ratio of the two energy constants seems to show there is a link between these two parameters.

These correlations are presented in Fig.4.21. Indeed, the energy constant E_2 as a function of the energy constant E_1 (bottom right plot) allows to conclude that the energy constants seem to be correlated. The top right plot showing the amplitude A_1 as a function of the amplitude A_2 can fix the fact there is no correlation between these two parameters. The two left plots show that none of the two exponential functions are similar from detector to detector.

Chapter 4: Heat-only event characterization

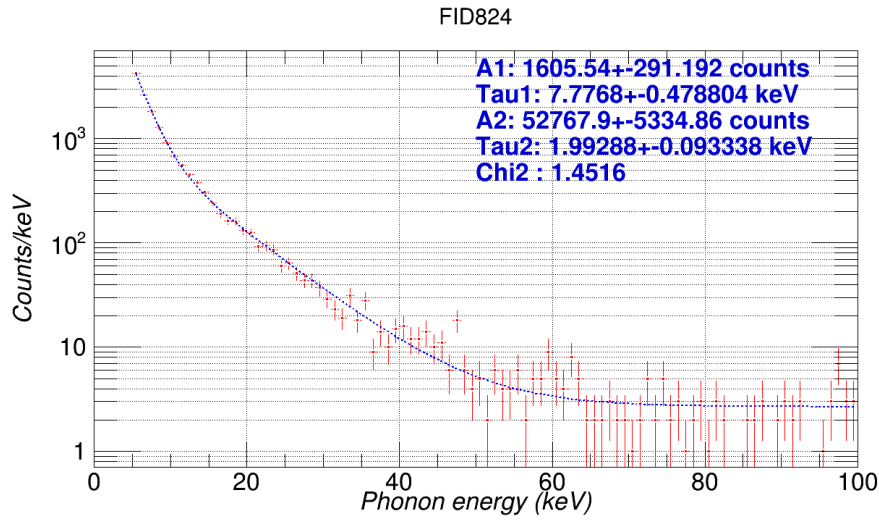


Figure 4.18 – Example of double exponential fit of the combined heat-only energy spectrum (run308, run309 and run310) for FID824 detector.

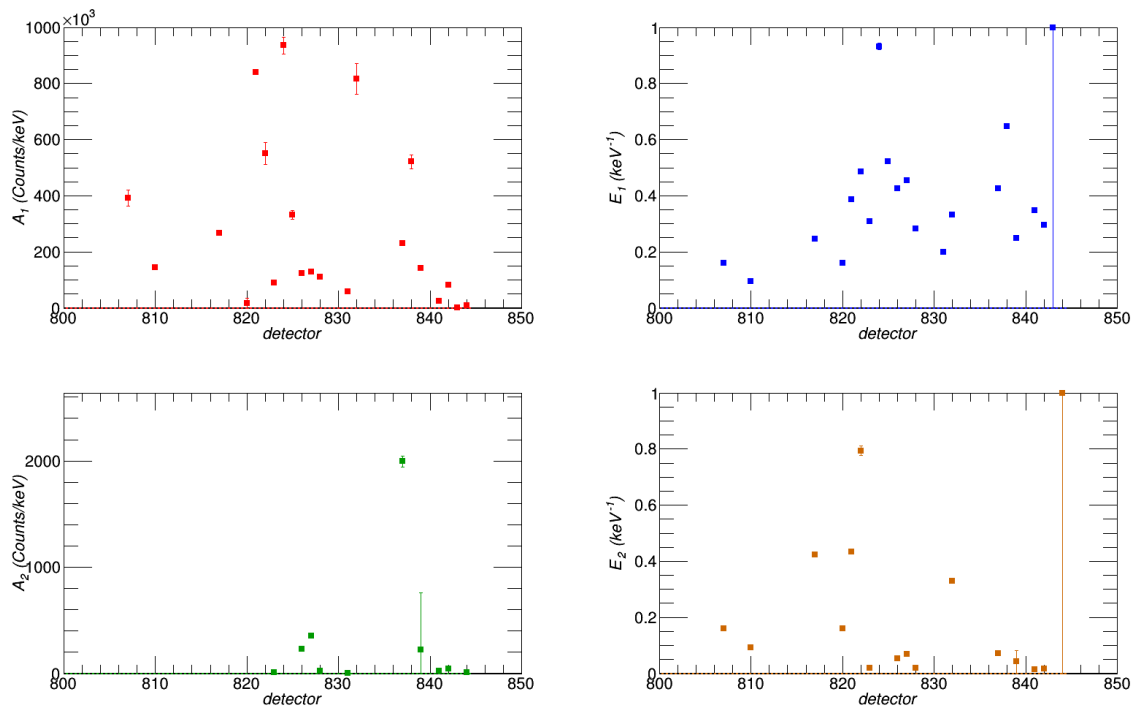


Figure 4.19 – Left: amplitudes A_i as a function of detector number (for the first exponential at the top, and the second exponential at the bottom). Right: energy constant E_i as a function of detector number (for the first exponential at the top, and the second exponential at the bottom).

This study allows to corroborate the results presented in section III.2.2. Moreover, the modelization with two exponential function seems to be sufficiently accurate for a Likelihood analysis. Nevertheless, a Kernel Density Estimation (KDE), as used in [92] has also been tested during this study to modelize the heat-only spectrum (see section III.3.2).

Chapter 4: Heat-only event characterization

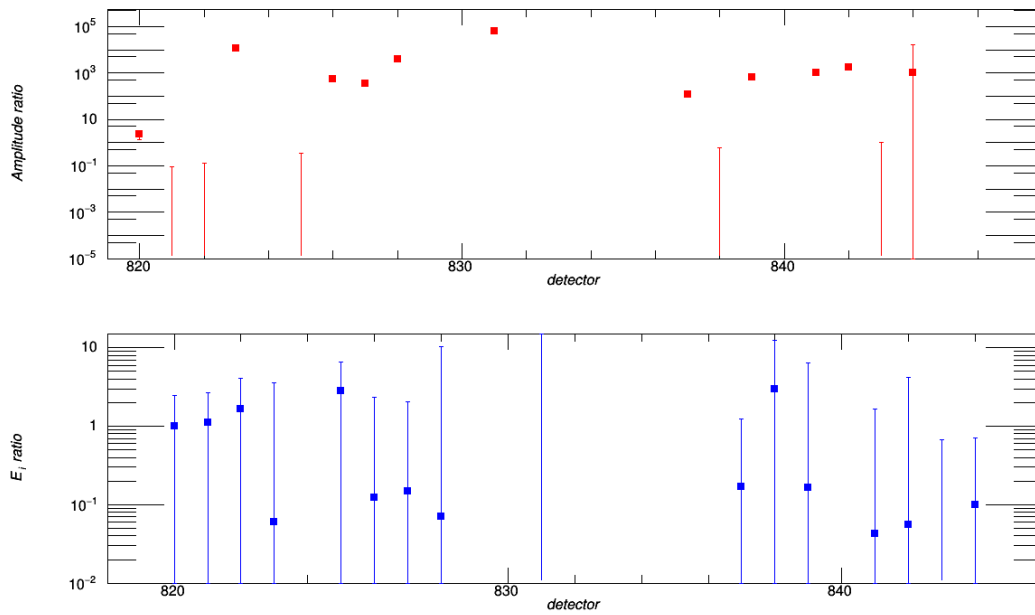


Figure 4.20 – Top: ratio of the amplitudes of the two exponentials as a function of detector number. Bottom: ratio of energy constants of the two exponentials as a function of detector number. The plots are drawn in log scale.

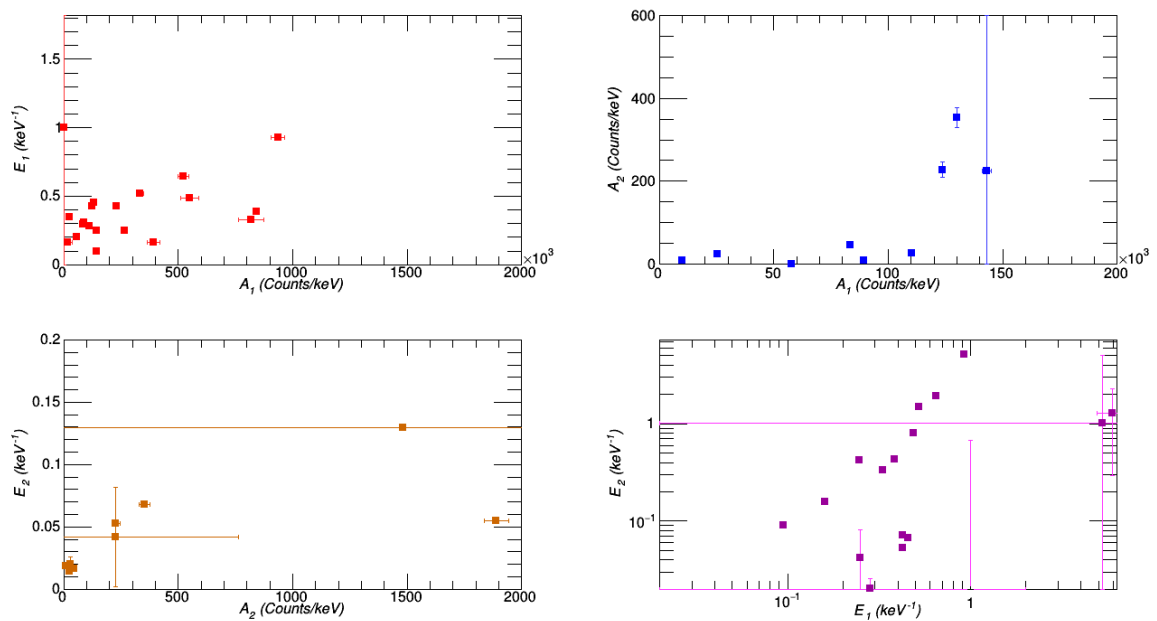


Figure 4.21 – Top, left: energy constant E_1 as a function of the amplitude A_1 . Bottom, left: energy constant E_2 as a function of the amplitude A_2 . Top, right: amplitude A_2 as a function of the amplitude A_1 . Bottom, right: energy constant E_2 as a function of the energy constant E_1 . A correlation is visible between these two parameters.

III.3.2 Kernel Density Function principle

A statistical method allowing to determine the probability density function of an unknown background based on the data is the Kernel Density Estimator (KDE). This method can be used to smoothen experimental data.

The goal of this method is to determine the probability density function PDF of a data sample $X = (X_1, \dots, X_n)$ by:

$$f(X) = \frac{1}{nh} \sum_{i=1}^n K\left(\frac{X - X_i}{h}\right) \quad (4.13)$$

where K is a gaussian function normalized to unity called the Kernel function, and h is the smoothing parameter ($h > 0$) that controls the amount of smoothing. This method is thus bin-independent. The KDE method spreads out each data point into a bump. The Kernel function K can be expressed as:

$$K(z) = \frac{1}{\sqrt{2\pi}} e^{-z^2/2} \quad (4.14)$$

with $z = (X - X_i)/h$. The smoothing parameter h corresponds to the bandwidth of the test. It is constant for each value of i in the case of a fixed Kernel estimator when the X values are uniformly distributed. It is defined as:

$$h = \left(\frac{4}{3}\right)^{1/5} \sigma n^{-1/5} \quad (4.15)$$

corresponding to the value when the mean integrated squared error of f is minimized, and $\sigma = 1$. Note that this parameter is specific to the data sample. For an adaptative Kernel estimation, the bandwidth parameter becomes:

$$h_i = \frac{h}{\sqrt{f(x_i)}} \quad (4.16)$$

It allows to adapt the estimator as a function of density regions. For region with high density, the estimation is more accurate, and for low statistics, the smoothing is wide to take into account statistical fluctuations.

III.3.3 Conclusion: selection of the model

To estimate the shape of heat-only events, the recoil spectrum used is the combination of all runs during which the analyzed detector was in the cryostat. For FID824 detector, it was for run308, run309 and run310. Because heat-only spectrum doesn't vary as a function of the voltage bias (as studied in section III.2.1), all data can be used. As shown in the left panel of Fig.4.22 in magenta, the Kernel estimator allows to smooth the recoil energy spectrum but at low statistics, it includes oscillations instead of estimate a flat background. To check if the KDE model is sufficiently accurate, a Kolmogorov-Smirnov test is applied. For that, a thousand tests comparing randoms issue from the KDE with the heat-only energy spectrum are made. The ECDF as a function of the p-values are shown in Fig.4.22 (right, magenta curve). The same tests have been achieved with the double exponential model (orange curves in both plots).

It allows to conclude that a modelization by a two exponential function is more appropriate than a Kernel estimator. Indeed, the low heat-only event rate at high energy ($E_R > 40$ keV) strongly impacts the Kernel method. A modelization with a two exponential function will be used in the future analyses (see chapter 5).

Chapter 4: Heat-only event characterization

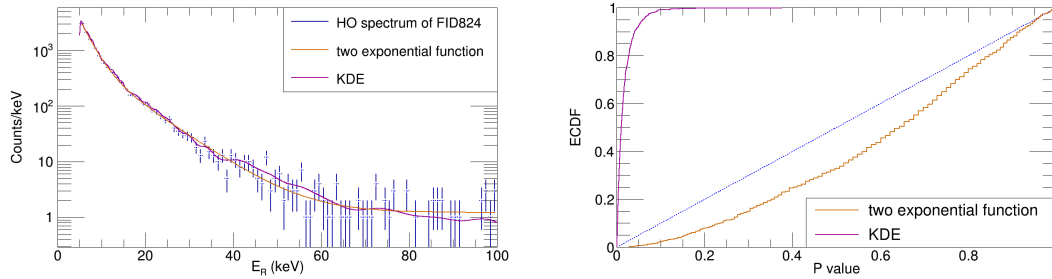


Figure 4.22 – Left: energy spectrum of FID824 detector for all heat-only events (run308, 309 and 310). Blue dots are data. In orange, the fit with two exponentials. In magenta, the Kernel function estimator. Right: comparison between the heat-only energy spectrum and its modelization with two exponentials (in orange), comparison between the heat-only energy spectrum and its Kernel estimator (in magenta). Both comparisons are realized using the Kolmogorov-Smirnov test.

IV Discussion about the possible origin of heat-only events

Finding the origin of the heat-only events has been an intense topic of studies in the EDELWEISS collaboration, with the objectif of reducing or removing them for future detectors. Different hypotheses that have been tested are summarized in table 4.2. The different detectors and support elements reviewed in this section are shown in Fig.4.23. The Ge crystal is illustrated in gray, surrounded by an amorphous layer of Ge (light gray). The surface treatment corresponds to the green dashed block and the Ge NTD sensor to the small gray rectangle, attached with glue in violet. The gold pad is the block in yellow, linked to the bath (Kapton[®], in brown) by a thermal link (orange arrow). The red box represents the vibrations from the environment and the cryostat impacting detectors.

IV.1 Evaporation of ⁴He

To accelerate the cool-down of the detectors and their supports, a gaz exchange of ⁴He is injected in the cryostat during the cooling-down process. At 4 K, this gas becomes superfluid and can deposit a film on the bolometers. To avoid this, the bolometer plate is warmed up as not to be the coldest point of the cryostat, and the exchange gas is cryopumped by active charcoals at the latest step of the cool-down period. Once the exchange gas is pumped, the cooling-down is slower (several days).

One hypothesis was that a ⁴He film remains deposited on detectors. Then it can condensate or evaporate. This sudden phenomenon can provide signals during the data taking. To test and validate this hypothesis, the exchange gas in the run309 cool-down was replaced by ³He, which can't form a superfluid film. Furthermore, during the same cryorun two FID detectors were equipped with strong heater to warm them up and see if that affected the heat-only rate.

Fig.4.24 shows the heat-only rate of FID824 detector for all runs. No clear variation has been detected before or after run309. A ⁴He film cannot explain the observed heat-only event rates.

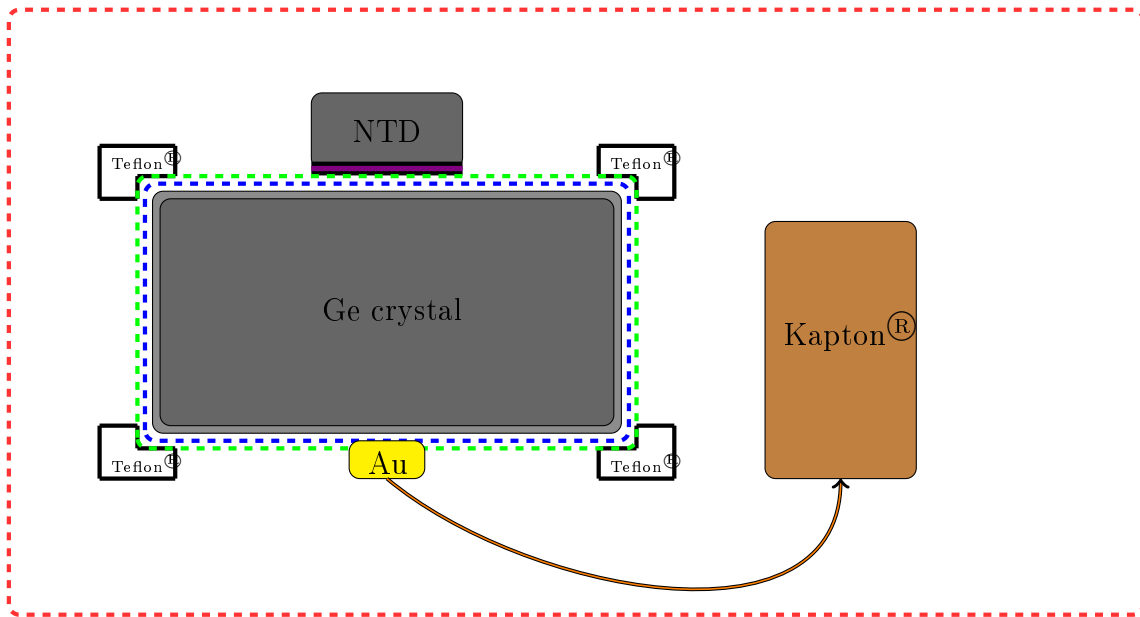


Figure 4.23 – Presentation of the different hypothetical sources of heat-only events on a FID detector. In gray, the Ge crystal surrounded by an amorphous layer of Ge. Electrodes in Al are represented in dashed blue lines. The surface treatment is illustrated by the green dashed block. The Ge NTD sensor corresponds to the small gray rectangle, attached with glue in violet. The gold pad is the block in yellow, linked to the bath (Kapton[®], in brown) by a thermal link (orange arrow). The white box represent the Teflon[®] holders. The red box represents the vibrations from the environment and the cryostat impacting detectors.

Chapter 4: Heat-only event characterization

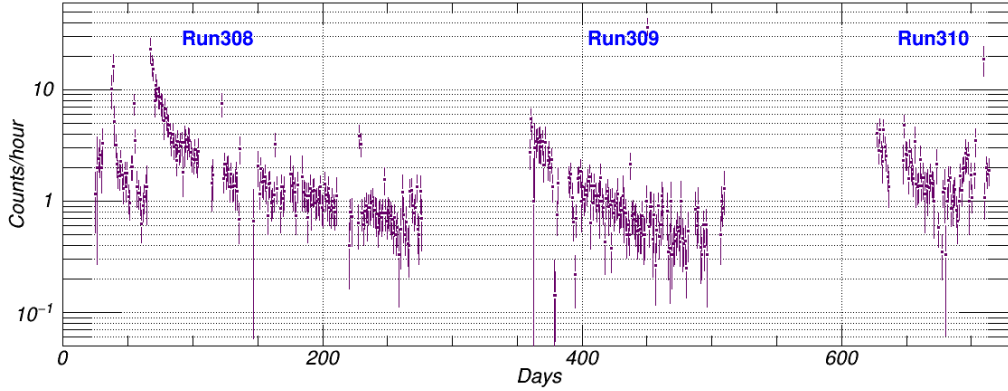


Figure 4.24 – Heat-only count rate since the beginning of the data taking for FID824 detector (which is in the cryostat since 2014, i.e run308) with phonon energy above $E_{\text{phonon}}^{\text{min}} = 5 \text{ keV}$.

IV.2 Stress in germanium induced by vibrations

The EDELWEISS-III cryostat is isolated from vibrations in the laboratory by being supported by four pressured-air suspension. However, the cryostat is not entirely protected against the vibrations of the Gifford-MacMahon thermal machines used to reliquefy the evaporated ^4He and to cool the ^4He vapor used to control the temperature of the 100 K stage. These vibrations are transmitted through the tube where the cryogenic fluids circulate between the machine and the cryostat (the so-called caloduc, see chapter 2). The machines work continuously during the cryorun, inducing noise and vibrations.

One hypothesis was that heat-only events are induced by those vibrations. However, the noise in the detector signal induced by those vibrations fluctuates greatly from day to day, while the measured rate, in contrast, follow quite smooth trends, as shown in Fig.4.24 for FID824 detector. The heat-only rates are systematically better in the last month of each cryorun, while this observation is not true for the vibration-induced noise on the heat signal. A more appealing theory is that vibrations accumulate stress inside the Ge crystals, and that these stress is released gradually over time, thus smoothing up the time dependence of the heat-only rate. To study this hypothesis, a special 200 g FID detector (FID211) has been installed in the suspended tower of the LUMINEU experiment [99], inside the cryostat, during run310. A significant reduction of vibration-induced noise was observed in the LUMINEU detectors, resulting in improved baseline resolution on their heat signal compared to detectors mounted on the same plate support used by EDELWEISS. However no reduction of the heat-only rate of FID211 detector has been noticed.

IV.3 Stress induced from the contact between the Ge crystal and the Teflon[®] holders

Copper being a thermal conductor, the detector cannot touch directly the support plate. Instead, the Ge crystal are maintained by plastic holders, in Teflon[®].

An assumption is that heat-only events may come from the friction between the Ge and the Teflon[®], inducing a stress that can be accumulated and be released at a smooth varying rate. The stress relaxation can lead to an energy release in plastic in contact with the crystal or in the crystal itself. It has to be very fast to mimic a real signal pulse (which have a time rise of a

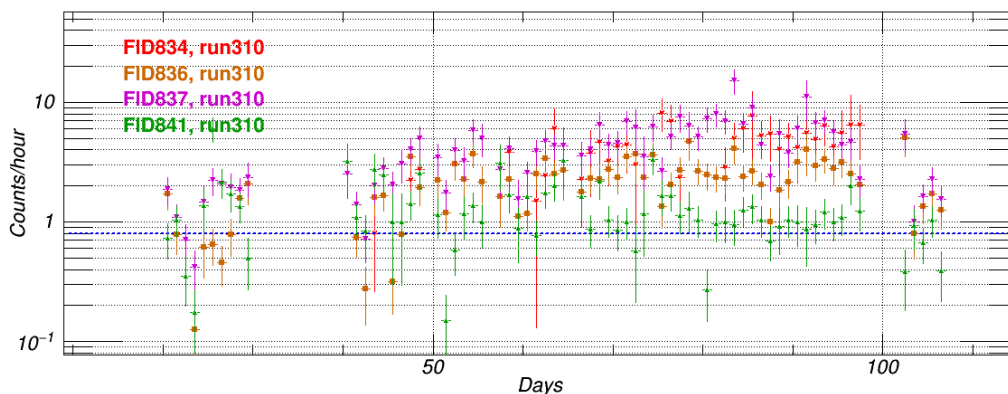


Figure 4.25 – Heat-only count rate for detectors installed in the cryostat to test if heat-only events could be originated from the stress induced by the contact between the Ge and the Teflon[®] holders: FID834 (in red), FID836 (in orange), FID837 (in purple) and FID841 (in green) during run310 with phonon energy above $E_{\text{phonon}}^{\text{min}} = 15 \text{ keV}$.

few ms). To test this, the Teflon[®] holders have been replaced by an other material on several detectors:

- FID834 detector was held by brass springs, insulated from the Ge by a glued sapphire plate.
- FID836 detector was insulated by sapphire (Ge side) on the top and KLF[®] rings (holder side of the slab) on the bottom. There was no glue. This led to an important noise level that degraded the resolution at a point where the heat-only rate could not be measured.
- FID841 detector was also held by brass springs, but isolated using Kapton[®] polyimide adhesive tape.
- FID837 and FID842 detectors in run310 had their Teflon[®] holders replaced with VESPEL[®], which is a polyimide resin, able to resist to extreme temperatures.

Springs are not necessary to compensate the difference in thermal contraction between Cu and Ge if Teflon[®] is used. However the crystal must be firmly tighten to avoid microphonic noise.

Removing the Teflon[®] holders by any other component doesn't change the heat-only event rate, as shown in Fig.4.25, allowing to conclude that they are not responsible for their production.

IV.4 Stress in germanium induced by gluing

Glue is used to ensure a thermal contact at the interface between the NTD and the Ge crystal in FID detectors. At cryogenic temperatures, this glue could induce a stress leading to cracks in the Ge crystal, which could cause heat-only events. To test this hypothesis, detectors with deported NTD have been developed. In this case, the NTD are glued onto a sapphire slab that is thermally connected to the crystal by Au wires. Thus, no glue is in direct contact with the germanium. If a stress was induced in the sapphire slab, the pulse shape observed on the NTD would be faster, as it doesn't transit through the Ge crystal. During run310, two detectors with this design (DEP202 and DEP203) have been installed in the cryostat. Each recorded heat-only events as shown in Fig.4.26. Removing the stress induced by the glue does

Chapter 4: Heat-only event characterization

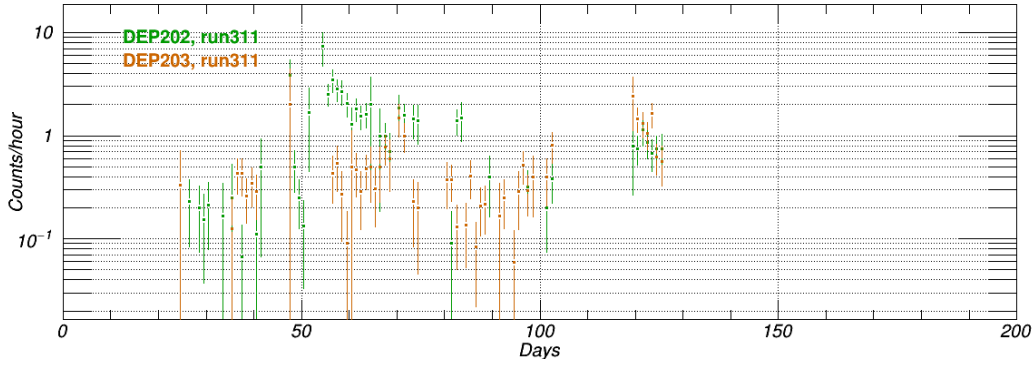


Figure 4.26 – HO rate for DEP detectors which have their NTD deported onto a sapphire slab: DEP202 in green and DEP203 in orange with phonon energy above $E_{\text{phonon}}^{\text{min}} = 15 \text{ keV}$.

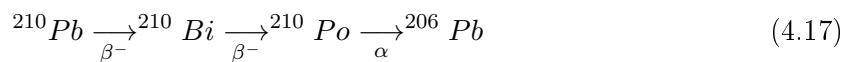
not eliminate heat-only events. Another type of detector that is not using glue for holding the thermal sensor has been used in run310. It was the detector NbSi202, where the heat sensor is a high-impedance Transistor Edge Sensor (TES) made by a thin (50 nm) NbSi film lithographed directly on the surface of the detector. This type of detector had a heat-only rate that was a factor five less than the other detectors. However the remaining rate shows that eliminating the glue cannot remove all heat-only events. Moreover, a key aspect of this type of sensor is that it is not very sensitive to thermal phonons, only to athermal ones, and this may be an indicator that heat-only events are not efficient at producing athermal phonons.

IV.5 Stress induced by surface treatment of FID

The maximum voltage bias that a detector can sustain is limited by leakage currents occurring between the electrodes. To reduce these currents, a surface treatment has been developed [100]. A post-process dry-etching using xenon difluoride (XeF_2) is applied on the detector surface, allowing to reduce leakage currents below 1 pA, for an applied voltage bias of 20 V between the 2 mm-spaced adjacent FID electrodes. A hypothesis was that this chemical process can induce the stress leading to heat-only events. Nevertheless the detectors that did not receive this treatment have also heat-only events. It is the case in particular for FID803 detector, shown in Fig.4.27.

IV.6 Surface events in Al and in the amorphous layer of Ge

An event which interacts directly in the Al electrodes doesn't induce an ionization signal. However, the electrodes are very thin ($< 100 \text{ nm}$) and therefore the particle giving rise to such signal should have a penetration length smaller than this thickness. The only possible candidates compatible with a rate exceeding a few events per day are ^{206}Pb recoils from the α decay of ^{210}Po , daughter of ^{210}Pb :



However, for each observed ^{206}Pb recoil, there is a corresponding rate of α particles. The penetration depth of α particles is 10 to 30 μm , and thus α particles should be observable outside the Al electrodes. The rate of ^{206}Pb recoils interacting in Al electrodes cannot be

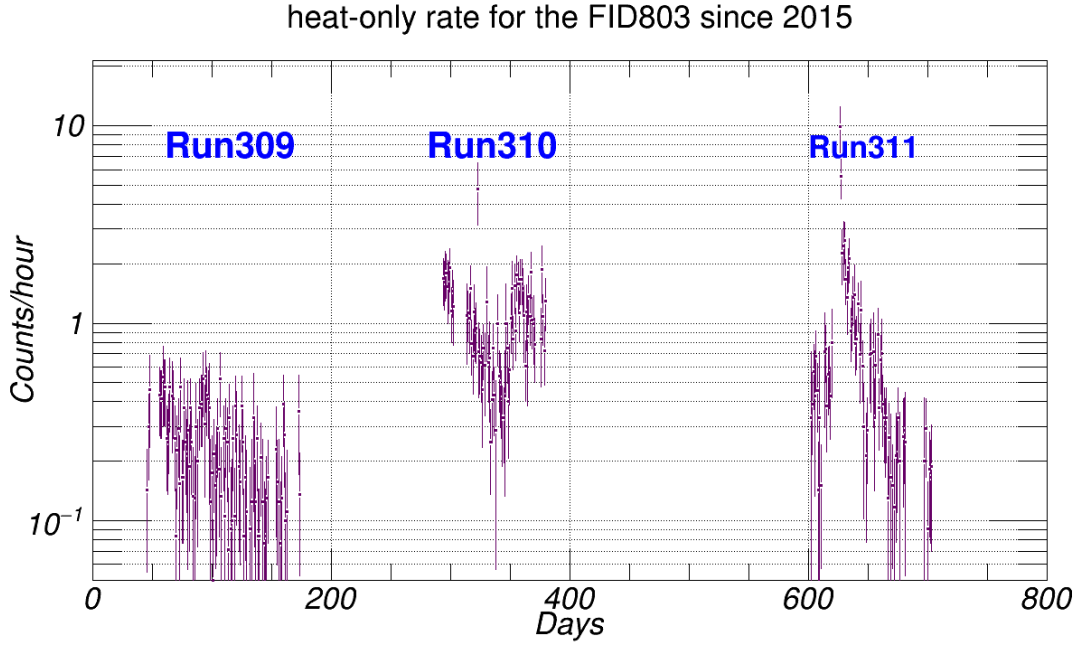


Figure 4.27 – Heat-only count rate of FID803 detector during run309, run310 and run311, for heat-only events with phonon energy above $E_{\text{phonon}}^{\text{min}} = 15 \text{ keV}$.

greater than the observed rate of α . However, this α rate in detectors is at the order of 2 to 10 per day, and much of this rate is matched by the observed rate of ^{206}Pb recoils. These ones interact in the Ge surface not covered by the narrow ($< 150 \mu\text{m}$) Al electrodes and in the amorphous layer of hydrogenated Ge deposited only under the electrodes (the surface between electrodes being left unprocessed), called αGe .

The rate of unaccounted ^{206}Pb recoils in Al electrodes is less than one per day, and thus cannot account for the observed HO rate, at the order of a few per day. Moreover, the decay of ^{210}Pb toward ^{206}Pb ($T_{1/2} = 134 \text{ d}$) matches the τ_2 constant derived in section II.3, but it is completely incompatible with the much faster $\tau_1 \approx 10 \text{ day}$ component.

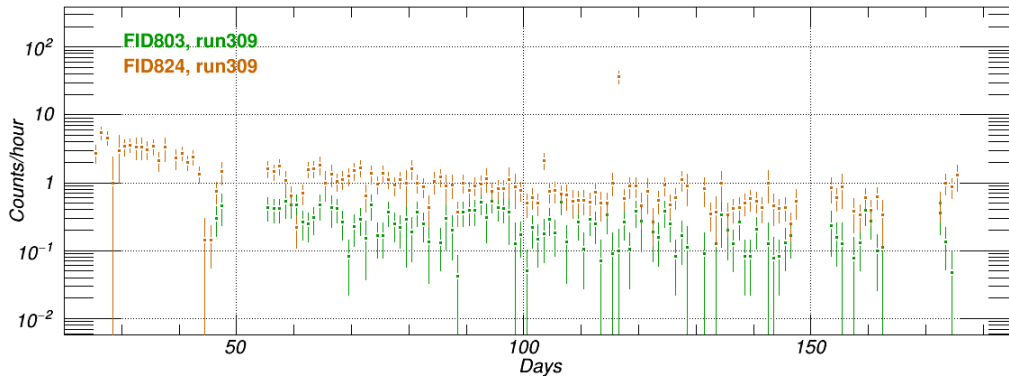


Figure 4.28 – HO rate for FID803 (in green) and FID824 (in orange) detectors in run309: FID824 has an amorphous layer of hydrogenated Ge (αGe) under its electrodes greater than FID803 but a lower HO count rate (with $E_{\text{phonon}}^{\text{min}} = 10 \text{ keV}$).

This is also the case for ^{206}Pb recoils interacting in the αGe layer. For FID803 detector, this

Chapter 4: Heat-only event characterization

layer is 35 nm deep. An incident particle interacting in this thin volume will not produce electron/hole pairs and could correspond to an event without ionization signal. In this case, the FID detectors which have different thickness of α Ge should have different heat-only rates. It is not the case: for example, FID824 detector in run309 has a 60 nm layer of amorphous Ge and have a lower heat-only rate than FID803 detector, as shown in Fig.4.28.

Moreover, the proportion of lead events occurring in the heat-only spectrum can be evaluated as shown in Fig.4.29 which presents three possible lead rates (corresponding respectively to 100%, 50% and 10% of the expected rate obtained from sideband data, as described in chapter 5) compared to the HO spectrum for FID803 detector during run309. Integrating the total number of lead events and HO events in the energy range $E_{\text{phonon}} \in [E_{\text{phonon}}^{\text{min}}, 100]$ keV shows that the proportion of lead events occurring in the heat-only spectrum of this detector can not exceed 5.4%.

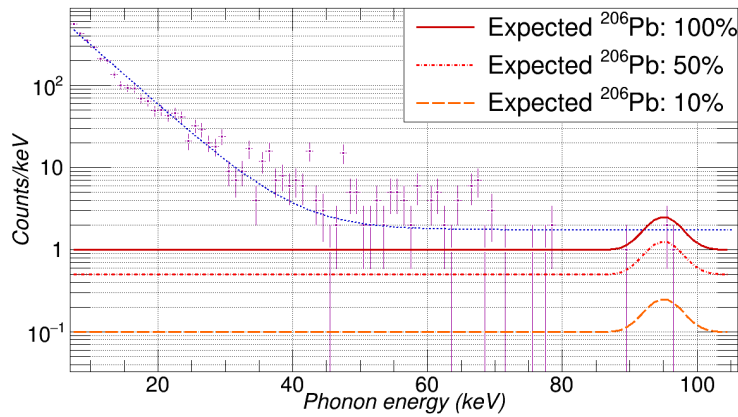


Figure 4.29 – Heat-only energy spectrum (in magenta) for FID803 detector during run309, fitted with a two exponential function (in blue). A function corresponding to a gaussian with a constant term associated to the lead recoil rate as described in chapter 5 is illustrated in dark red. The two other curves correspond to a scale applied on the lead rate (50% for light red dot curve and 10% for orange dashed curve).

IV.7 Nuclear property of the glue at the NTD-absorber interface

Another hypothesis was that the glue used to ensure a contact between NTD and crystal would be radioactive. A measurement of its radioactivity has been made and doesn't corroborate this assumption. Furthermore, the observed rate in the DEP detectors (see section IV.4) do not corroborate this hypothesis.

IV.8 Properties of NTD

NTD sensors are Neutron Transmutation Doped, i.e they are doped by neutron activation. Their radioactivity could be a source of heat-only events. This is why, in run311, a NbSi detector has been installed in the cryostat. It is a germanium crystal of 32 g, equipped with a NbSi Transition-Edge Sensor (TES) as thermal sensor. This sensor is evaporated in the form of an amorphous thin NbSi layer of 50 nm by e-beam onto the Ge crystal. A TES is a

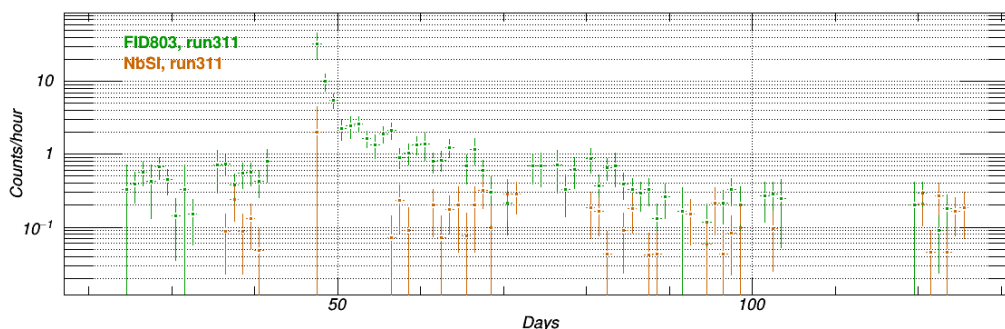


Figure 4.30 – HO rate for FID803 (in green) and NbSI (in orange) detectors in run311 with $E_{\text{phonon}}^{\text{min}} = 10 \text{ keV}$. A significant decrease of the heat-only rate is observed with the used TES.

superconductor which is sensitive mostly to athermal phonons. This NbSi detector has shown a heat-only event rate reduced by a factor 5 with respect to FID detectors, but HO events are still present (see Fig.4.30). It has been concluded that NTD sensors themselves could be a heat-only source. Nevertheless, if NTD radioactivity engendrated NTD events (i.e an event recorded by one NTD), it could have been rejected by a quality cut (as explained in chapter 3), which is not the case in the observed measurements.

Note that heat-only events of the NbSi and FID detectors have the same behavior as shown in Fig.4.31.

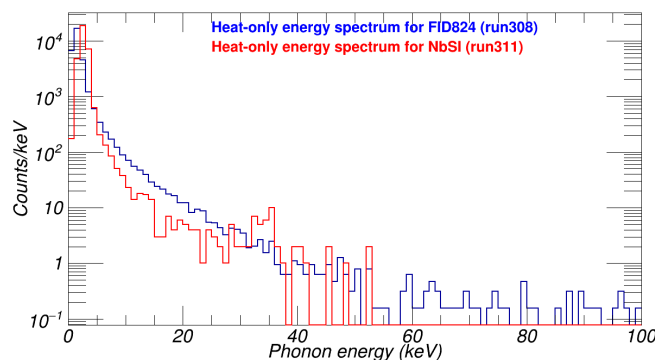


Figure 4.31 – Heat-only energy spectra recorded on FID824 detector during run308 (in blue) and NbSi detector during run311 (in red). NbSi spectrum is scaled with the exposure wrt the FID824 one.

IV.9 Gold pads

Gold pads are put on the NTD to ensure a thermal link between it and the crystal (via Au wires). The assumption was that the pad could be radioactive and in this way, induces HO events. This is not compatible with the measurement of its radioactivity made with HPGe detector at LSM. Furthermore, in run310 FID840 and FID844 have their thermal link realized directly via the NTD and hence no heat pulse could come through that way. However their heat-only rates were observed to be the same as for other detectors and the HO event shape doesn't change anyway.

Chapter 4: Heat-only event characterization

IV.10 Heat pulses coming through the thermal link

The Au wires ensuring the thermal link are connected to the copper casing via a Kapton[®] film, glued onto it. A hypothesis was that heat-only events could come from stress in Kapton[®] releasing energy in the absorber (Ge crystal) via the Au wire bonds. Events in Kapton[®] could also be due to radioactivity. A heat signal would thus be transmitted via the thermal link. To verify this assumption, the thermal link has been put directly on the NTD of FID840 and FID844 detectors during run310. Furthermore, DEP202 and DEP203 detectors, used in the same run, had their thermal links on the two sapphire chips. Kapton[®] cracks should produce NTD-like events as a result of the difference between the heat conductivity of the NTD and the absorber. No difference has been noticed neither for the two FID detectors during run310, as shown in Fig.4.32, nor for DEP detectors (see Fig.4.26) and this hypothesis has been excluded.

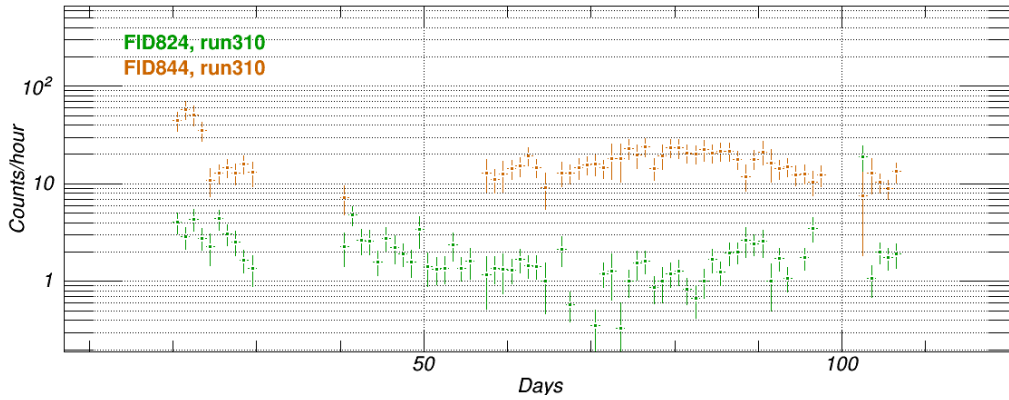


Figure 4.32 – HO rate for FID824 (in green) and FID844 (in orange) detectors in run310. The latter had its thermal links directly on NTD sensors with $E_{\text{phonon}}^{\text{min}} = 5 \text{ keV}$.

IV.11 Electronic noise

Heat-only events may come from electronic noise but it doesn't explain why this type of events is present at high energy and is not rejected by a χ^2 quality cut. Furthermore, an assumption was they could have a different proportion of both thermal and athermal components in pulses [84] compared to non-HO events. An analysis has demonstrated that there is no significant difference between the shapes of non-HO and heat-only events [101].

Hypothetic source	induced by	Tests	Cryorun period	time
Stress in Ge	vibration pressure from holder gluing	GM ON/OFF + FID211 Removed Cu holder NbSi + DEP detectors	run309, run310 run310 run311	
^4He	condensation/evaporation	^3He as exchange gas	run309	
^{206}Pb , α , β	in Al in αGe	Study of surface event rate and ratio Study of surface event rate and ratio	all runs all runs	
Glue	radioactivity	HPGe measurements + NbSi + DEP detectors	run311	
NTD	radioactivity	Event shape + NbSi TES	run311	
Gold pad	radioactivity	HPGe measurements	run310	
Thermal link (Kapton [®])	radioactivity \rightarrow injection of a heat pulse via the thermal link	Thermal link directly on NTD FID840 and FID844	run311	
Teflon [®]	radioactivity and stress	Replaced by VESPEL [®] (FID837) + Cu holders (FID841)	run310	
XeF ₂ etching	chemical treatment of detector surface	Difference between detectors	all runs	
Radiogenic source	^{222}Rn , ...	Study of heat-only event rate	all runs	

Table 4.2 – Summary of the different tested hypotheses concerning the origin of heat-only events. Expected characteristics and tests realized to remove them are presented.

Chapter 4: Heat-only event characterization

V Conclusion

A description of the heat-only event selection has been presented as well as the study of the HO properties. From these studies, one can conclude that the heat-only energy spectra don't vary as a function of the voltage bias or the time despite an observed abrupt variation of the heat-only count rate during run308 or run311. Each detector has an energy spectrum with a different shape, which led to build a different model for each one, using a double exponential function to modelize this background in a Likelihood analysis in the next chapter.

Different hypotheses were postulated to understand HO event origins. Several tests have been carried out in order to determine if they were correct. No single origin can simultaneously account for all observations. Sudden variations in the heat-only rate can not have the same origin as heat-only events from the plateau. The conclusion of this study is there are more than one source of heat-only events, and unfortunately no origin has been clearly isolated so far.

Chapter 4: High-voltage data analysis

WIMP search results with EDELWEISS-III detectors operated at high voltage bias

This chapter describes the first results obtained by operating EDELWEISS FID800 detectors at high voltage bias. First, a study of each observed background using sideband data has been made in order to include it in a Likelihood analysis. The different event rates extracted with this study will be compared with the rates obtained from previous EDELWEISS analyses. Second, the general features of the different analysis methods used to extract a limit on spin-independent WIMP-nucleon scattering cross-sections will be exposed. An analysis with the Poisson statistical method will be then presented as well as the associated results using the dataset of the first cryorun at high voltage bias. A study of the background limitation on a possible improvement by the exposure will be also described. All these results will drive the Likelihood analyses presented at last. The complete description of the Likelihood method used for the high-voltage data analysis will be developed. A test performed on run309 data will be compared with the optimal range method. Finally, the run310 dataset will be used to determine the first EDELWEISS limit on the spin-independent WIMP-nucleon cross-section below $5 \text{ GeV}/c^2$. A comparison with the other experiments in this region of interest will be eventually discussed.

I Characterization of the different EDELWEISS backgrounds

The main goal of this thesis is to obtain the best possible limits on the spin-independent WIMP-nucleon cross-section using the first samples of high-voltage data recorded with the EDELWEISS FID800 detectors. The study presented in [91] has shown that a Likelihood approach is the most adapted method to reach the best results for low-mass WIMP. This strategy requires a maximum of information on the experimental backgrounds that will affect this search to avoid any bias in the results. This is why the first part of this chapter is dedicated to the study of all observed backgrounds in EDELWEISS, by using sideband data of FID803

detector¹. This analysis has been performed with data taking at 8 V voltage bias during run309 and run310. In the first cryorun the detector was in FID mode whereas in the latter one it was in planar mode, at the considered voltage bias.

I.1 Compton background

The natural radioactivity of materials around the detectors and the cosmic-ray interactions produce γ -rays that will predominantly interact in detectors via compton interactions. This results in electronic recoils with an expected quenching factor of one. In [76], the shape of the compton background below 50 keV was studied using Monte-Carlo simulations, coincidence events and ¹³³Ba calibration events. The conclusion was that it can be considered as a flat background within statistical uncertainties.

I.1.1 Fiducial compton events

If the shape of the compton plateau below 50 keV is well defined, its overall normalization needs to be determined for each individual detector and cryorun. The rate of fiducial γ -events is determined as following. The selection of well-reconstructed events by using the quality cuts on the χ^2 of the different ionization and heat channels is applied as well as the NTD event rejection described in section III.3 of 3. Lastly, the fiducial events are selected by applying the procedure detailed in section III.5 of chapter 3. The rate is calculated from the number

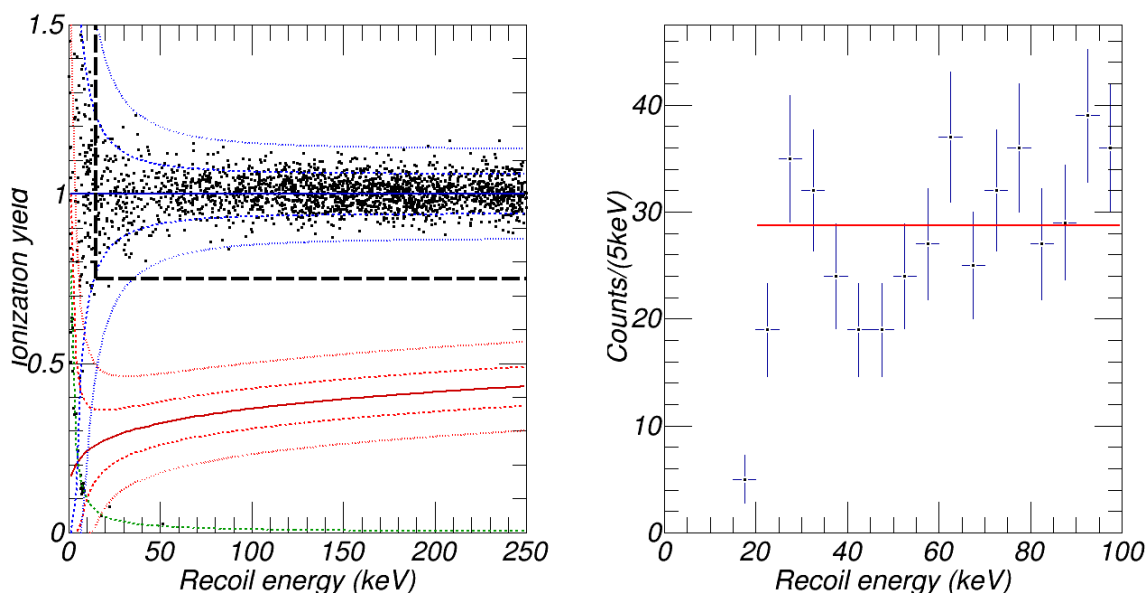


Figure 5.1 – Left: ionization yield as a function of the recoil energy (in keV) for fiducial events in FID803 detector during run309. In blue, the electronic recoil bands at 90% and 99.9% C.L. In red, the nuclear recoil bands at 90% and 99.9% C.L. The fiducial selection is illustrated with the dashed black lines. Right: recoil energy distribution (in keV) for fiducial gamma events and the corresponding fit with a constant term in red.

¹This detector has reached the best performance during the considered cryoruns. This is why only this detector is used for the limit calculation.

Chapter 5: High-voltage data analysis

of events with a quenching factor $Q > 0.75$ and a recoil energy higher than $E_R > 15$ keV, as shown in left panel of Fig.5.1. The recoil energy spectrum, shown in right panel of Fig.5.1, is fitted by a constant term to determine the number of γ -events per keV and per kg.days. The rate of fiducial compton events $\Gamma_{\gamma, fid}$ for FID803 detector in run309 is:

$$\Gamma_{\gamma, fid} = 0.33 \pm 0.01 \text{ dru} \quad (5.1)$$

where the dru unit is defined as $1 \text{ dru} = 1 \text{ event}/(\text{keV.kg.day})$. This result, determined using γ -rays above 15 keV and thus above the search domain for WIMP, is extrapolated down to low energies. It corresponds to the expected $\Gamma_{\gamma, fid}$ rate, used in the last analyses of the EDELWEISS experiment [92, 91].

I.1.2 Surface compton events

The surface γ -background (γ -events in the non-fiducial volume) has a similar signature than the fiducial γ one. In planar mode, the compton interaction outside the fiducial volume must be taken into account. The same quality cuts as for fiducial events are applied, except that here the events rejected by the fiducial cut are considered. To avoid β -events and ^{210}Pb recoils in the recoil energy spectrum, only events with $Q > 0.75$ and $E_R > 20$ keV are accepted, as shown in Fig.5.2 (left). Thus the extracted surface γ -rate $\Gamma_{\gamma, surf}$ is:

$$\Gamma_{\gamma, surf} = 0.22 \pm 0.01 \text{ dru} \quad (5.2)$$

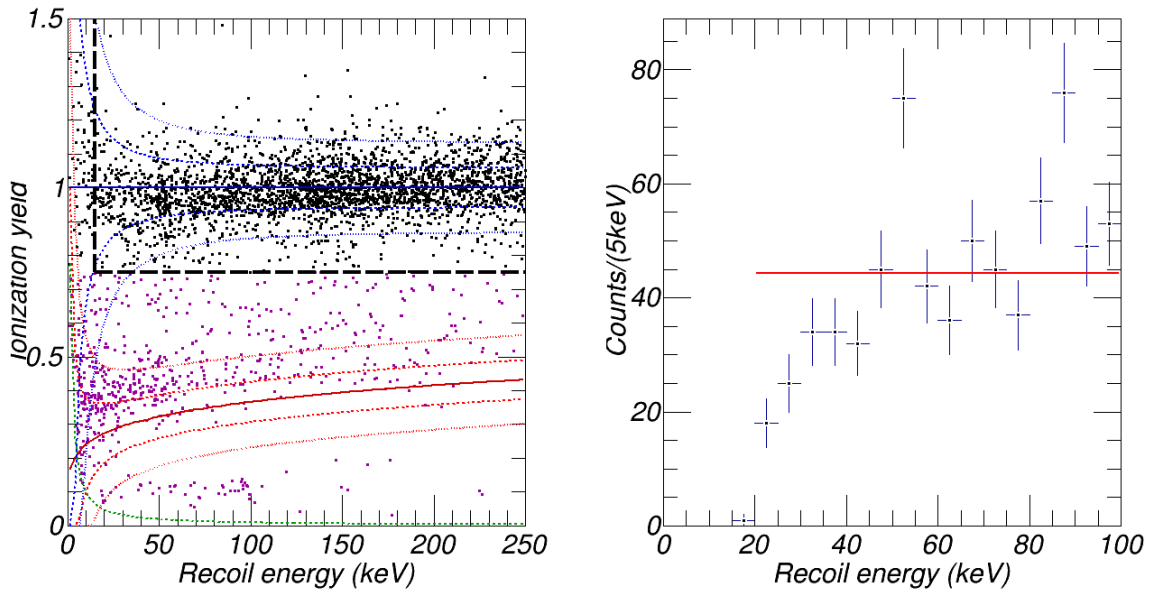


Figure 5.2 – Left: ionization yield as a function of the recoil energy (in keV) for surface events with a quenching factor superior to 0.75 for FID803 detector in run309. In blue, the electronic recoil bands at 90% and 99.9% C.L. In red, the nuclear recoil bands at 90% and 99.9% C.L. The quenching selection is illustrated with the dashed black lines. Right: recoil energy distribution (in keV) for surface gamma events and the corresponding fit with a constant term in red.

It can be noticed that the compton rate per kg.days is larger in the surface volume (non-fiducial volume), as this part of the detectors does not benefit from self-shielding effects. Also, compton

Chapter 5: High-voltage data analysis

scatters leaving energy deposit in both parts of the detector will be considered as surface events. In the same way as realized for fiducial γ -background, an extrapolation at low energy is made to obtain the number of expected events in the energy range interesting for this analysis.

I.1.3 Total compton rate

Using exposure values presented in section III.2 of chapter 3 for fiducial and surface volumes, the total rate of γ -rays due to compton interactions in run309 is:

$$\Gamma_{\gamma}(\text{run309}) = 0.52 \pm 0.09 \text{ dru} \quad (5.3)$$

This rate can be used for the run309 dataset but not for run310. Indeed, this second dataset has been recorded in planar mode. It includes 8 V voltage bias data which are used as sideband for evaluating the gamma rate of run310. No fiducial selection can be applied on the dataset and the total rate is directly extracted using the same quality cuts and imposing a quenching factor $Q > 0.75$:

$$\Gamma_{\gamma}(\text{run310}) = 0.60 \pm 0.03 \text{ dru} \quad (5.4)$$

This 15% variation of the total rate is within the range of fluctuations observed from detector to detector due to efficiency for coincidences. Moreover, FID803 detector had a different position in the cryostat during the two cryoruns, also explaining the rate variations. As a consequence, the two γ counting rates in Eq.5.3 and Eq.5.4 will be used for analyses of run309 and run310 respectively.

I.2 Cosmogenic background

The production of FID800 detectors occurred above ground, exposing Ge crystals to activation by cosmic-rays and associated hadronic showers, and producing daughter isotopes that can generate cosmogenic background. Once the detectors are stored sufficiently deep to suppress the hadronic component of the cosmic-rays, only the daughter isotopes with a lifetime larger than a few months can still be present in the Ge crystal. The study of this cosmogenic background has been performed in [76]. The isotopes of interest at low energy are those that decay via electron-capture, followed by a K- or L-shell X-ray emission. Table 5.1 lists all the isotopes decaying via electron-capture with a half-life $T_{1/2} > 10$ days for $21 \leq Z \leq 33$.

A study of the different event rates associated to these cosmogenic isotopes has been carried out in this work. To follow the methodology of [76], the energy estimator E_{opt} used for this study is the average of the heat and ionization energies weighted by the inverse of the square of their associated baseline resolutions σ_{heat} and σ_{ion} , as measured hour by hour:

$$E_{opt} = \frac{\frac{E_{ion}}{\sigma_{ion}^2} + \frac{E_{heat}}{\sigma_{heat}^2}}{\left(\frac{1}{\sigma_{ion}}\right)^2 + \left(\frac{1}{\sigma_{heat}}\right)^2} \quad (5.5)$$

I.2.1 Peaks background

Each expected cosmogenic peak has a gaussian structure such as:

$$f(E_R) = \frac{1}{\sigma(E_R)\sqrt{2\pi}} e^{-\frac{(E_R - E_X)^2}{2\sigma^2}} \quad (5.6)$$

Chapter 5: High-voltage data analysis

	daughter isotope	E_K (keV)	E_L (keV)	half-life $T_{1/2}$	EC B.R (%)	coincidences with γ rays and internal conversion
^{74}As	^{74}Ge	11.10		17.8 d	66	
^{73}As	^{73}Ge	11.10		80.3 d	100	
^{71}Ge	^{71}Ga	10.37	1.30	11.4 d	100	
^{68}Ge	^{68}Ga	10.37	1.30	271.0 d	100	
^{68}Ga	^{68}Zn	9.66	1.19	67.7 min	11.12	
^{65}Zn	^{65}Cu	8.98	1.10	243.9 d	100	50.0% (1115.5 keV)
^{58}Co	^{58}Fe	7.11		70.9 d	100	99.5% (810.8 keV)
^{57}Co	^{57}Fe	7.11		271.7 d	100	99.8% (122.1 or 136.5 keV)
^{56}Co	^{56}Fe	7.11		77.2 d	100	100% (846.8 keV and others)
^{55}Fe	^{55}Mn	6.54		2.74 y	100	
^{54}Mn	^{54}Cr	5.99		312.1 d	100	100% (834.9 keV)
^{51}Cr	^{51}V	5.46		27.7 d	100	9.9% (320.1 keV)
^{49}V	^{49}Ti	4.97		330 d	100	
^{44}Ti	^{44}Sc	4.49		60.0 y	100	100% (78.3 + 67.9 keV)
^{44}Sc	^{44}Ca	4.04		4.0 h	100	99.9% (1157.0 keV)

Table 5.1 – Isotopes decaying by electron-capture with a period $T_{1/2} > 10$ days, for $21 \leq Z \leq 33$, taken from [76].

where E_X is the energy of the K or L-shell X-ray and:

$$\sigma(E_R) = \sqrt{\sigma_0^2 + (\alpha E_R)^2} \quad (5.7)$$

corresponding to the width of a peak, with α a free parameter and $\sigma_0 = 1/\sqrt{\sigma_{ion}^{-2} + \sigma_{heat}^{-2}}$ fixed to the value derived from the measured average baseline resolutions σ_{heat} and σ_{ion} . From the study in [76], it is expected that the main peaks from cosmogenic activation will be at 8.98 and 10.37 keV. By using data at 8 V voltage bias as sideband, the associated event rate can be determined. The peaks are more clearly identifiable in the fiducial volume, so that selection is applied to the run309 dataset, resulting in the spectrum shown in Fig.5.3 (right). The

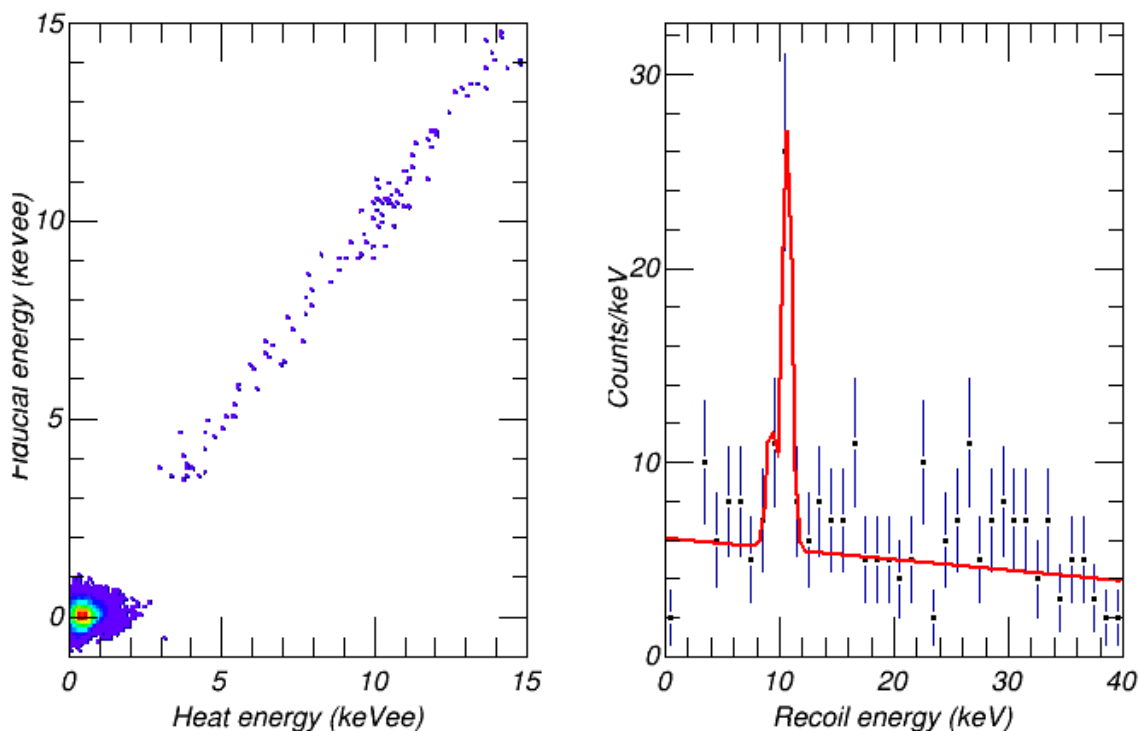


Figure 5.3 – Left: fiducial ionization energy (keV_{ee}) as a function of heat energy (keV_{ee}) for FID803 detector during run309. Events well-reconstructed (selection on the χ^2 of the different channels) and occurring in the fiducial volume of the detector are used. Right: recoil energy spectrum for these events. A double-gaussian function is fitted on these data to determine the amplitude of the two peaks at 8.98 keV and 10.37 keV.

amplitude of the two main peaks are determined from a gaussian fit. The left plot of Fig.5.3 is the associated event distribution on $(E_{fid}, E_{heat})^2$. The sum Γ_{peak} of the rates of the 8.98 and 10.37 keV peaks for FID803 detector in run309 is thus:

$$\Gamma_{peak}(\text{run309}) = 0.66 \pm 0.17 \text{ events}/(\text{kg}\cdot\text{day}) \quad (5.8)$$

It is consistent with the fact that the detector has been installed at the LSM since 2014.

At the beginning of run310, an activation with a neutron source has been performed. Consequently, the Γ_{peak} has to be re-evaluated for this cryorun. Fig.5.4 illustrates the same fit result

² E_{fid} is the average energy measured by the two fiducial electrodes.

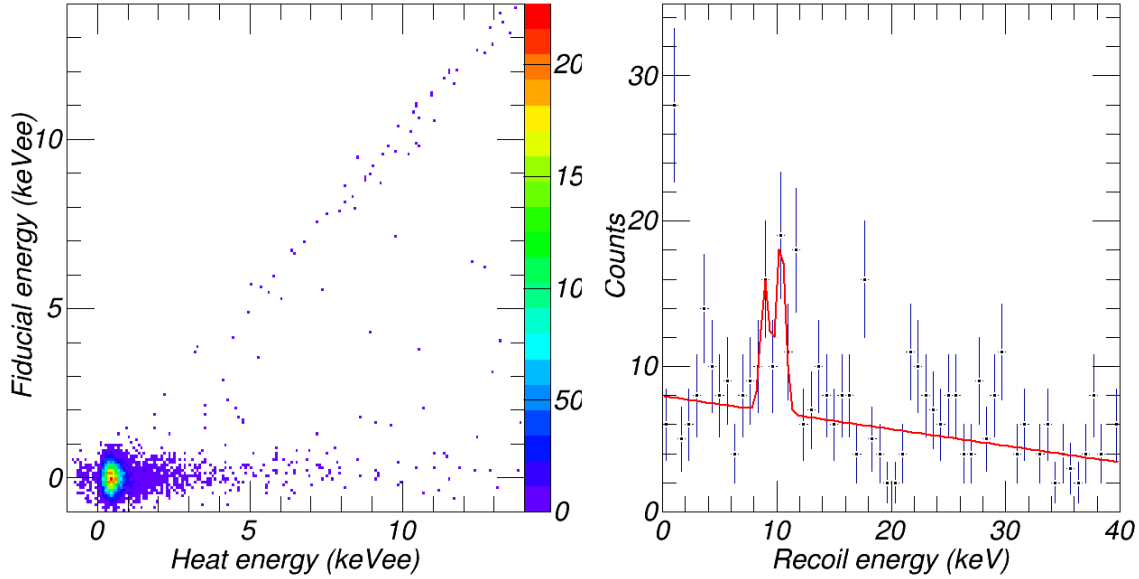


Figure 5.4 – Left: fiducial ionization energy (keV_{ee}) as a function of the heat energy (keV_{ee}) for FID803 detector during run310. Events well-reconstructed (selection on the χ^2 of the different channels) have been used. Heat-only events have been rejected. Right: recoil energy spectrum for these events. A double-gaussian function is fitted on these data to determine the amplitude of the peaks at 8.98 keV and 10.37 keV.

on the 8 V planar data (right plot) as well as the associated event distribution in (E_{fid}, E_{heat}) (left plot). Taking into account the respective exposures (64 days for run309 and 11 days for run310), the amplitude of the peak for run310 is clearly higher than for run309. The evaluation of this rate for run310 gives:

$$\Gamma_{peak}(\text{run310}) = 2.35 \pm 0.83 \text{ events}/(\text{kg}\cdot\text{day}) \quad (5.9)$$

These results will be used in further analyses as a function of the run.

I.2.2 Tritium background

As discussed in [76], a significant portion of the smooth background lying below the cosmogenic peaks comes from events resulting from the beta decay of tritium (${}^3\text{H}$). This tritium originates from nuclear reactions induced by the interaction of the hadronic component of cosmic-rays with atoms in the germanium. The half-life of ${}^3\text{H}$ is 12.32 years, so this background remains longer than any of the cosmogenic isotopes presented in the previous section. The events have a quenching factor $Q = 1$ and the associated electron recoil energy spectrum has an end-point Q_β at 18.6 keV. The rate in a given detector depends on the exposure of the crystal at the surface (between the time it is grown and its installation underground). This background is produced uniformly in the entire detector volume. It is however easier to identify it when applying the fiducial selection. These electronic recoils in the bulk are selected by requesting $Q > 0.75$. The expected shape of the energy spectrum is described by:

$$\frac{dN}{dT} = \sqrt{T^2 + 2mc^2T(T + mc^2)}(Q_\beta - T)^2 F(T, Z = 2) \quad (5.10)$$

where T is the kinetic energy of the electron, m is the electron mass, c is the speed of light and $F(T, Z = 2)$ is the Fermi function for tritium decay. This function can be approximated in the non relativistic limit as $\frac{x}{(1-e^{-x})}$, where $x = \frac{4\pi\alpha c}{\nu}$, with α the fine structure constant and ν the electron velocity. Using this Fermi function, and T in keV, the equation becomes:

$$\frac{dN}{dT} \propto (T^2 + mc^2)(Q_\beta - T)^2 \left(1 - e^{-\frac{1.466}{\sqrt{T}}}\right)^{-1} \quad (5.11)$$

The total tritium rate is given by the integral of this function in the interval $T = [0; 18.6]$ keV. The spectrum shown in Fig.5.5 (right) is adjusted with this function in order to extract the

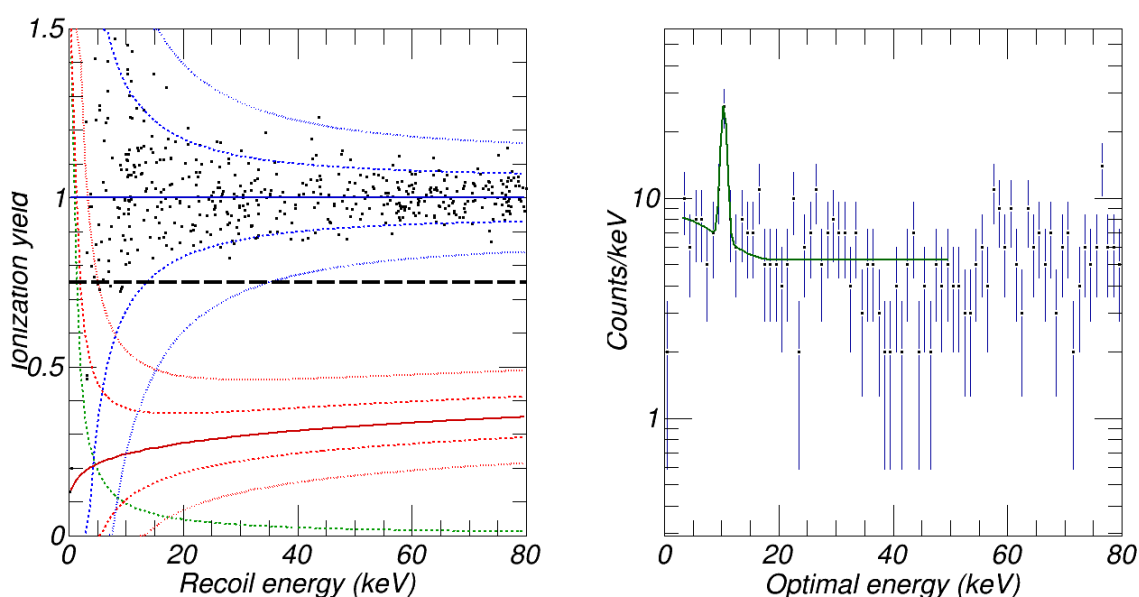


Figure 5.5 – Left: ionization yield as a function of the recoil energy (in keV) for fiducial events having an electronic recoil for FID803 detector in run309. The nuclear and electronic recoil bands are also drawn (in red and blue respectively). Right: spectrum of the optimal energy E_{opt} (in keV) as described by Eq.5.5. The tritium function described by Eq.5.11 is fitted on these data to determine the rate of this background for FID803 detector.

tritium rate. For FID803 detector in run309, the total rate $\Gamma_{tritium}$ is:

$$\Gamma_{tritium}(\text{FID803}) = 0.62 \pm 0.27 \text{ events}/(\text{kg}\cdot\text{day}) \quad (5.12)$$

This result is within the range of the different rates measured in 19 detectors of run308 in [76]. FID824 detector, studied in [76] as well as in this work, was measured in run308 to have a total ${}^3\text{H}$ rate of 0.67 ± 0.34 events/(kg.day) whereas this analysis applied to run309 data (see Fig.5.6) gives a tritium rate of 0.92 ± 0.26 events/(kg.day). Even before considering the systematic uncertainties on the run309 result, the two rates are compatible at the 1σ -level. Thus the $\Gamma_{tritium}(\text{FID803})$ rate of Eq.5.12 will be used in the Likelihood analysis, in section III.

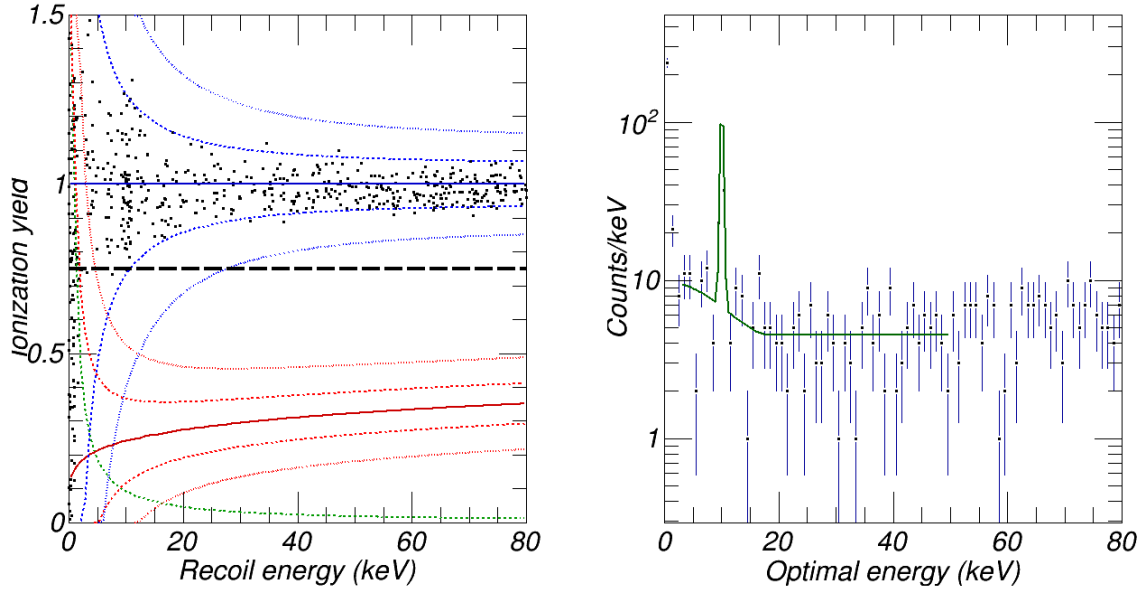


Figure 5.6 – Left: ionization yield as a function of the recoil energy (in keV) for fiducial events having an electronic recoil for FID824 detector in run309. The nuclear and electronic recoil bands are also drawn (in red and blue respectively). Right: spectrum of the optimal energy E_{opt} (in keV) as described by Eq.5.5. The tritium function described by Eq.5.11 is fitted on this data to determine the rate of this background for FID824 detector.

I.3 Beta background

As discussed in section I.5 of chapter 2, the most important source of radioactive surface contaminations is the decay of ^{210}Pb . The decay proceeds via two successive β -decays followed by one α -decay. The decay to ^{210}Bi produces low energy β : in 20% of the cases, a β with an end-point energy at 63.5 keV is produced, and in the remaining cases, a β with an end-point energy at 17.0 keV occurs, followed by X-rays, conversion and Auger electrons. The second β -decay, toward ^{210}Po , has a higher end-point energy (1162.1 keV), and is less important for the study of the low-energy spectrum.

The β -background has been studied with Monte-Carlo simulations as well as measured using ^{210}Pb source at the beginning of the EDELWEISS-III experiment. Unfortunately, there are large uncertainties in the simulations associated to the exact deposition depth of the ^{210}Pb contamination in either the germanium or copper surfaces. This is why this background has been studied for the detectors used in this analysis. The associated model is thus data-driven.

I.3.1 Spectral shape

In [92], it was found that the shape of the β -background recoil energy spectrum could be described as:

$$f_{\beta}(E_R) = a_{\beta} \cdot e^{b_{\beta} E_R} + c_{\beta} \cdot e^{\frac{(E_R - d_{\beta})^2}{2 \times e_{\beta}^2}} \quad (5.13)$$

with a_{β} , b_{β} , c_{β} , d_{β} and e_{β} parameters resulting from the fit. The same parametrization is adopted in this analysis. A selection on surface events has been realized as well as the different

χ^2 quality cut selections to obtain Fig.5.7. The distribution of events in the range $0.2 < Q < 0.6$ on the left panel corresponds to β -events according to [92]. The recoil energy spectrum of this population (right panel) is fitted by the function 5.13 to determine the different parameters. Furthermore, the rate of this background can be extracted with this procedure and for FID803

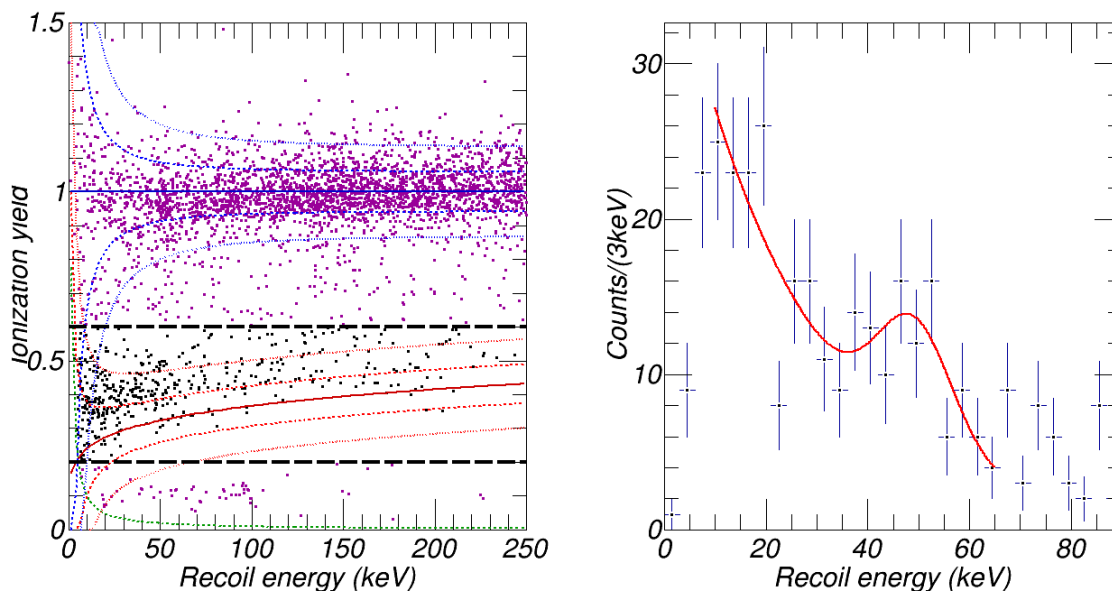


Figure 5.7 – Left: ionization yield as a function of the recoil energy (in keV) for surface events for FID803 detector in run309. In blue, the electronic recoil bands at 90% and 99.9% C.L. In red, the nuclear recoil bands at 90% and 99.9% C.L. The quenching selection $Q \in [0.2; 0.6]$ is illustrated with the dashed black lines: rejected events are the magenta dots. Right: recoil energy distribution (in keV) for these events with the resulting fit of the beta function of Eq.5.13 in red.

detector in run309 is:

$$\Gamma_{\beta}(\text{FID803}) = 6.80 \pm 4.23 \text{ events}/(\text{kg}\cdot\text{day}) \quad (5.14)$$

which is compatible with what was used in [92, 91]. In these studies, a quenching factor of $Q \simeq 0.4$ is defined but it is not evident that this value doesn't vary with the voltage bias (i.e in FID or planar mode). This is why a dedicated study has been realized in this work.

I.3.2 Quenching factor of β -events

In high-voltage runs, the detectors are operated in planar mode, i.e the veto and fiducial electrodes are at the same voltage bias, leading to an impossibility to reject surface events (see section IV.2 of chapter 2). This is why the β -rate has been extracted from the data recorded in FID mode at 8 V voltage bias. However the quenching factor for these events seems to change from the planar to the FID mode. The ionization yield distributions for the datasets recorded at 8 V in both FID³ and planar⁴ modes are shown in Fig.5.8 (top). The quenching distribution for the dataset in FID mode presents a bump at $Q \approx 0.4$ (see also bottom left plot), in accordance

³(+4/-4) V for fiducial electrodes and (+1.5/-1.5) V for veto electrodes in FID mode in run309.

⁴(+4/+4) V for top electrodes and (-4/-4) V for bottom electrodes in planar mode in run310.

Chapter 5: High-voltage data analysis

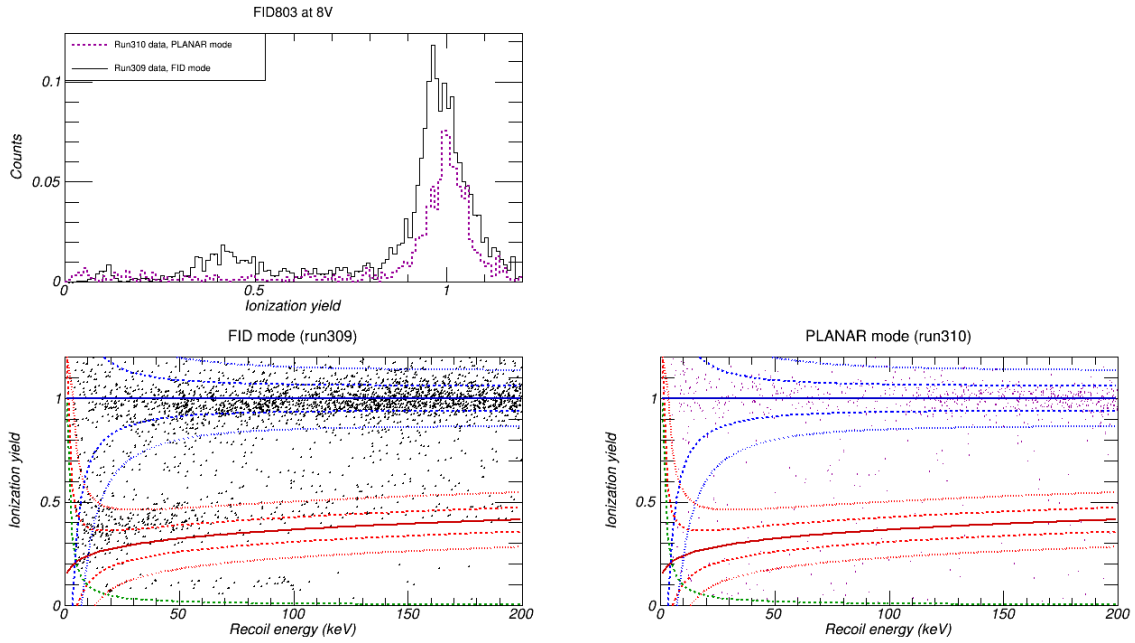


Figure 5.8 – Top, left: quenching factor distribution of FID803 detector at 8 V during run309 (in FID mode, black) and run310 (in planar mode, in magenta) for recoil energies $E_R \in [0; 200]$ keV. Bottom, left: ionization yield as a function of the recoil energy for FID803 detector during run309, operating in FID mode. Bottom, right: ionization yield as a function of the recoil energy for FID803 detector during run310, operating in planar mode.

with what was observed for the detectors in the same mode in [92]. In contrast, the 8 V dataset of run310 doesn't show any excess in this region. Moreover, there is no significant excess in the tail regions below $Q = 0$ and above $Q = 1$. This is consistent with the observation in [102] that the ionization yield for low-energy β -events in EDELWEISS detectors with planar electrodes is very close to 1 (right plot). Thus the approximation that Q_β quenching is equal to 1 when detectors operate in planar mode is used in this work. Nevertheless, a systematic error associated to this assumption will be considered in section IV.3.

I.4 Lead background

After the two successive β -decays of ^{210}Pb , the resulting ^{210}Po decays by emitting a 5.3 MeV α -particle and a stable ^{206}Pb nucleus (see Fig.2.5), which has a recoil energy of 103 keV. Since they are emitted back-to-back, from either the Ge or Cu surfaces, the measured rates for both the α -particle and the recoiling nucleus should be equal, a fact that can be used to verify the measured rate of each of them. The ^{206}Pb rate is extracted from the same data as in Fig.5.7, but selecting events with $0.01 < Q < 0.2$ (see Fig.5.9 top left). In [92], it was observed that the average quenching for ^{206}Pb recoils was 0.08. The same is observed in the non-fiducial events of FID803 detector recorded in FID mode at 8 V in run309 (see Fig.5.9). As in [92], the expected spectral shape is described with the function:

$$f_{Pb}(E_R) = d_{Pb} + a_{Pb} \cdot e^{\left(-0.5 \times \frac{(E_R - b_{Pb})}{c_{Pb}}\right)^2} \quad (5.15)$$

where d_{Pb} corresponds to a flat background at low energy. The b_{Pb} parameter must be around 100, because of the expected recoil energy of the lead at 103 keV. The fit applied in data

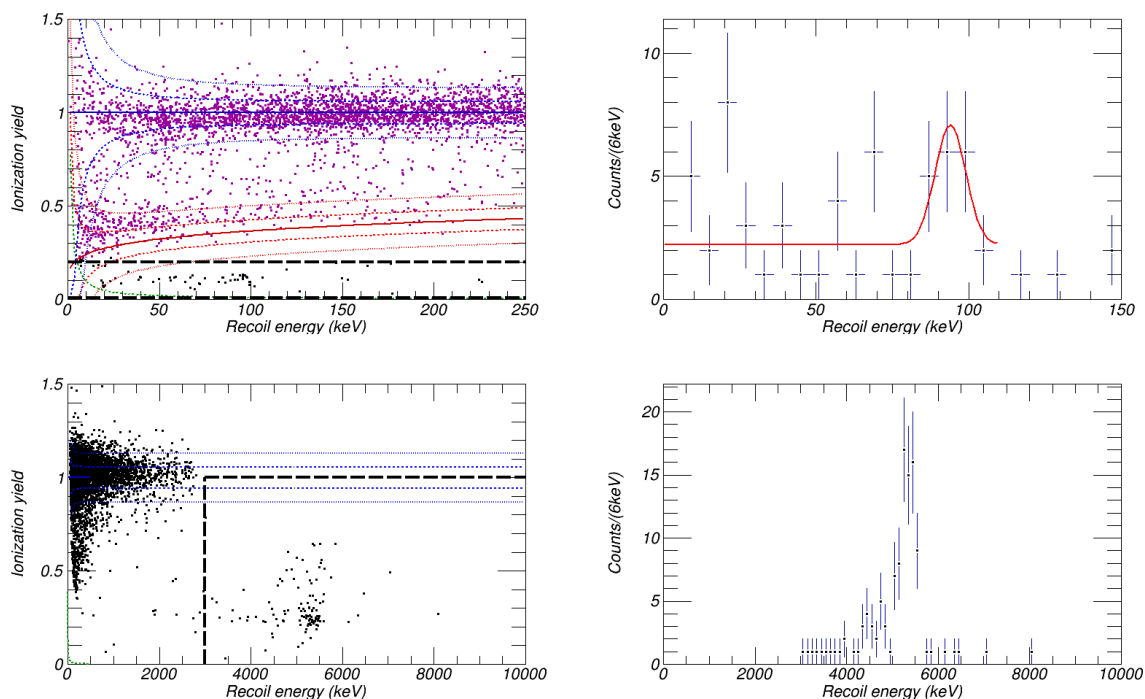


Figure 5.9 – Top, left: ionization yield as a function of the recoil energy (in keV) for surface events for FID803 detector in run309. In blue, the electronic recoil bands at 90% and 99.9% C.L. In red, the nuclear recoil bands at 90% and 99.9% C.L. The Pb-quenching selection (a quenching factor below 0.2) is illustrated with the dashed black lines: rejected events are the magenta dots. Top, right: recoil energy distribution (in keV) for the same events adjusted with the lead function (Eq.5.15) in red. Bottom, left: ionization yield as a function of the recoil energy (in keV). The α -quenching selection (recoil energy higher than 3000 keV and a quenching factor less than 1) is illustrated with the dashed black lines: accepted events are in the bottom right corner. Bottom, right: recoil energy spectrum for α -decays (in keV).

presented in Fig.5.9 (top right) results in a Γ_{Pb} rate:

$$\Gamma_{Pb} = 0.97 \pm 0.25 \text{ events}/(\text{kg.day}) \quad (5.16)$$

The study of the high-energy α -decays requires to relax the selection cuts. The heat χ^2 cuts must be removed, as the energy dependence is difficult to estimate reliably at these high energies. The resulting distribution of Q versus E_R is shown in Fig.5.9. Relax the selection can be done without degrading significantly the purity of the data sample, as the signal-to-noise ratio of high-energy events is significantly better than those of low-energy events. An event is considered to be an α -particle if $E_R > 3000$ keV and $Q < 1$ (see Fig.5.9 bottom).

The rate of the α -background is obtained from counting the number of events in this selection:

$$\Gamma_{\alpha} = 1.77 \pm 0.36 \text{ events}/(\text{kg.day}) \quad (5.17)$$

The difference between Γ_{Pb} and Γ_{α} is: 0.70 ± 0.61 which is compatible with zero as expected.

Chapter 5: High-voltage data analysis

I.5 Neutron background

Single-detector neutron scattering is an irreducible background of nuclear recoils. However from the measured rate of multiple scatter nuclear recoil events and the predicted single-to-multiple ratio derived from Geant4 Monte-Carlo simulations, it was estimated in [92] that the rate of single-detector nuclear recoils from neutron scattering is:

$$\Gamma_{neutron} = (5.18 \pm 0.52) \times 10^{-3} \text{ events}/(\text{kg}\cdot\text{day}) \quad (5.18)$$

This rate being smaller than all other sources of background, this value is adopted in the subsequent analyses, and the same function for the energy spectra is used:

$$f(E_R) = A_1 \cdot e^{-\tau_1 E_R} + A_2 \cdot e^{-\tau_2 E_R} \quad (5.19)$$

With A_i and τ_i the amplitude and energy parameters respectively. This spectral shape is a decreasing two-exponential function giving a recoil energy spectrum similar to that calculated for higher WIMP masses.

A simulation made by Monte-Carlo with Geant4 in 2014, using a detailed model of the EDELWEISS-III set-up and the installed detectors, allowed to determine the recoil energy spectrum associated to this background. Because coincidences between detectors can remove multiple-neutron events, only single-neutron events will be considered for the Likelihood analysis. Their interactions in the crystals produce nuclear recoils with the same ionization yield Q_{nr} expected from WIMP-nucleon scattering:

$$Q_{nr}(E_R) = 0.16 E_R^{0.18} \quad (5.20)$$

I.6 Heat-only background

The study of HO events in chapter 4 allowed to determine that a modelization with two exponentials is possible. The expected HO event number is determined by taking the event rate for each studied cryorun and fitting it with a decreasing slope. The integral of this fitted function in the time range corresponding to the data taking at high voltage bias is the number Γ_{HO} of expected heat-only events. For run309, it corresponds to:

$$\Gamma_{HO}(\text{Run309}) = 92 \pm 10 \text{ events for } E_R \in [0; 100] \text{ keV} \quad (5.21)$$

For run310, the same analysis leads to:

$$\Gamma_{HO}(\text{Run310}) = 512 \pm 50 \text{ events for } E_R \in [0; 100] \text{ keV} \quad (5.22)$$

II WIMP rate limit obtained from Poisson fluctuations within an optimized range

Before developing a full Likelihood analysis to derive limits on the spin-independent cross-section on the scattering of WIMP on nucleons, it is interesting to first perform a relevant analysis using a much simplified method, for the first sample used (100 V voltage bias data of FID803 detector in run309). A 90% C.L. upper limit on a count rate in a defined energy range can be derived in a straightforward way from Poisson statistics, taking the very conservative assumption that there is no background and all counts being potential WIMP scattering event candidates. The limit derived with this Poisson statistical method will then be compared with

the one obtained from a full Likelihood analysis (section III), which is expected to give better limit results than using all counts as potential signal candidates. Even if using the Poisson distribution is a straightforward operation, the actual number of counts will of course depend on the chosen energy interval. And this choice should not be in any way biased by the statistical fluctuations of the data used for the search. The method used to select an optimized energy range without bias is described hereafter.

II.1 Methodology of WIMP limit calculations

To obtain the spin-independent WIMP-nucleon cross-section, an approach based on the Poisson statistics has been first considered.

II.1.1 Poisson method

The easiest method to calculate an exclusion limit in a rare event search experiment is the Poisson method. It is based on the Poisson statistics and depends only on the total number of events N_{obs} observed in the experiment. It is the most conservative approach as it does not use any information about the expected backgrounds. Each observed event is considered as a potential WIMP event. If N_{obs} is the number of events accepted by the quality cuts (in the region of interest, ROI), the excluded cross-section σ_{exc} corresponding to a number of excluded events μ_{exc} at a confidence level $1 - \alpha(\mu_{exc})$ is defined by:

$$\alpha(\mu_{exc}) = e^{-\mu_{exc}} \sum_{k=1}^{N_{obs}} \frac{\mu_{exc}^k}{k!} \quad (5.23)$$

A cross-section $\sigma_{exc}(\mu_{exc})$ excluded at 90% C.L. (the conventional confidence level used to set exclusion limits in direct dark matter detection) corresponds to:

$$1 - \alpha(\mu_{exc}) = 90\% \quad (5.24)$$

In this way, if an experiment observes no event in the signal region ($N_{obs} = 0$), it excludes at 90 % C.L. a cross-section $\sigma(\mu_{exc})$ that would produce in average $\mu_{exc} = 2.3$ events. For $N_{obs} = 1$, the corresponding value of μ_{exc} at 90% C.L. is 3.9, and as N_{obs} becomes larger, μ_{exc} tends toward N_{obs} . The most sensitive aspect of this method is the choice of the interval for N_{obs} counting. The choice of the interval can not be made on observed data to avoid introducing any bias in the analysis. However, this choice can be based on any information on the relative size of the different backgrounds compared to the intensity of the expected signal in samples that are statistically independent on the observed events in the ROI (a so-called sideband sample).

II.1.2 Optimization of the counting interval

The following subsection will present the results obtained with a Poisson limit, where the interval used to count N_{obs} from the final heat energy spectrum $f_{exp}(E_{heat})$ is systematically optimized, using the expected WIMP distribution and a background model derived from a sideband sample.

The main lines of the optimization procedure are described first. The optimization is performed for each WIMP mass. First of all, the recoil energy distribution for a given WIMP mass and a given cross-section σ_{WIMP} is computed (as described in chapter 1). This distribution is then smeared by the experimental resolution and convoluted by the trigger efficiency to match

Chapter 5: High-voltage data analysis

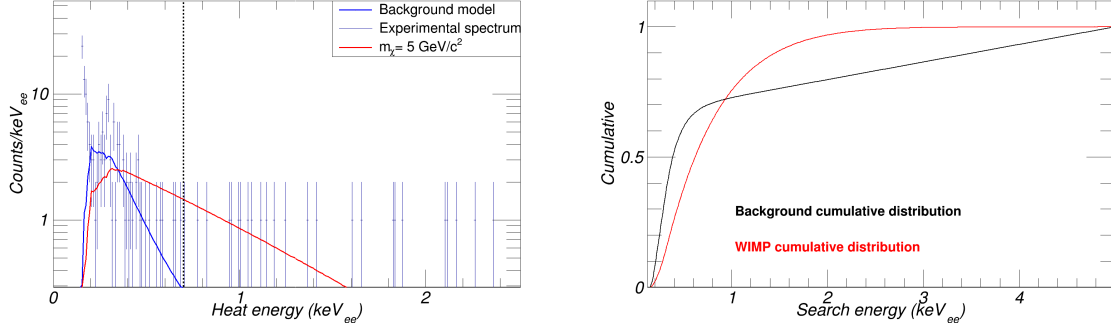


Figure 5.10 – Left: the red curve represents the WIMP spectrum for a WIMP mass of $5 \text{ GeV}/c^2$ convoluted with the trigger efficiency, and the blue curve is the background model. The final heat energy spectrum $f_{\text{exp}}(E_{\text{heat}})$ for FID803 detector during run309 is also shown in light blue. Right: cumulatives ϵ_{bkg} and ϵ_{signal} of the background experimental distribution convoluted with the trigger efficiency (in black) and of the WIMP function convoluted with the trigger efficiency (in red), respectively.

the expected WIMP signal distribution measured by the detector ($f_{\text{signal}}(E_{\text{heat}})$), as shown in Fig.5.10 (left).

The background model $f_{\text{bkg}}(E_{\text{heat}})$ is obtained from sideband data (the population of the dominant background, i.e. heat-only events at 8 V voltage bias). The cumulative $\epsilon_{\text{signal}}(E)$ and $\epsilon_{\text{bkg}}(E)$ of the two distributions $f_{\text{signal}}(E_{\text{heat}})$ and $f_{\text{bkg}}(E_{\text{heat}})$, respectively, are determined to obtain the fraction of observed events at a given heat energy E value:

$$\epsilon_{\text{signal}}(E) = \frac{\int_0^E f_{\text{signal}}(E_{\text{heat}}) dE_{\text{heat}}}{\int_0^\infty f_{\text{signal}}(E_{\text{heat}}) dE_{\text{heat}}} \quad (5.25)$$

$$\epsilon_{\text{bkg}}(E) = \frac{\int_0^E f_{\text{bkg}}(E_{\text{heat}}) dE_{\text{heat}}}{\int_0^\infty f_{\text{bkg}}(E_{\text{heat}}) dE_{\text{heat}}} \quad (5.26)$$

Using these two cumulatives, shown in Fig.5.10 (right), the heat energy range $[E_{\text{min}}; E_{\text{max}}]$ for which the limit calculation is optimal can be determined as following.

For each heat energy range, the Poisson sum S_p is calculated as:

$$S_p = \sum_{i=1}^{N_{\text{bkg}}} e^{-\mu_{\text{bkg}}} \times \frac{\mu_{\text{bkg}}^i}{i!} \times \mu_{\text{bkg}} \quad (5.27)$$

with μ_{bkg} the number of events contained in a chosen energy range $[E_{\text{inf}}; E_{\text{sup}}]$, defined from the corresponding values of the cumulative $[\epsilon_{\text{bkg}}^{\text{inf}}; \epsilon_{\text{bkg}}^{\text{sup}}]$ and $[\epsilon_{\text{signal}}^{\text{inf}}; \epsilon_{\text{signal}}^{\text{sup}}]$, for the background model and the signal spectrum, respectively. Thus μ_{bkg} is given as:

$$\mu_{\text{bkg}} = (\epsilon_{\text{bkg}}^{\text{sup}} - \epsilon_{\text{bkg}}^{\text{inf}}) \times N_{\text{obs}} \quad (5.28)$$

The optimal energy range $[E_{\text{min}}; E_{\text{max}}]$, which contains N_{signal} events such as:

$$N_{\text{signal}} = \int_{E_{\text{min}}}^{E_{\text{max}}} f_{\text{signal}}(E) dE \quad (5.29)$$

Chapter 5: High-voltage data analysis

is finally defined as the one that minimizes the Γ variable:

$$\Gamma = \frac{S_p}{(\epsilon_{signal}^{sup} - \epsilon_{signal}^{inf})} \quad (5.30)$$

In this way, the number N_{bkg} of events contained in the background model distribution f_{bkg} in this optimal energy range is:

$$N_{bkg} = \int_{E_{min}}^{E_{max}} f_{bkg}(E) dE \quad (5.31)$$

whereas the number N_{obs} of events contained in the final experimental heat energy distribution f_{exp} is:

$$N_{obs} = \int_{E_{min}}^{E_{max}} f_{exp}(E) dE \quad (5.32)$$

They are used respectively to determine the associated projection of the cross-section:

$$\sigma_{proj} = \frac{\sigma_{WIMP} \times N_{bkg}}{N_{signal}} \quad (5.33)$$

and the corresponding limit on the cross-section:

$$\sigma_{lim} = \frac{\sigma_{WIMP} \times N_{obs}}{N_{signal}} \quad (5.34)$$

where N_{signal} is the number of events in the optimal energy range in the WIMP energy spectrum.

II.2 WIMP rate limits

II.2.1 Expected signal used

Since the expected signal has a different nuclear recoil spectrum as a function of the WIMP mass, a Probability Density Function (PDF) is built for each WIMP mass, based on Eq.1.42. This spectrum of WIMP-nucleon interactions is calculated using a cross-section of $\sigma_\chi = 10^{-40} \text{ cm}^2$ as an input as well as the exposure⁵ (in run309, there is 5.76 kg.day of exposure and 25.42 kg.day for run310). The astrophysical parameters are chosen in agreement with those used in the literature [92]:

$$\rho_{DM} = 0.3 \text{ GeV}/c^2/\text{cm}^3 \quad (5.35)$$

$$v_{esc} = 544 \text{ km/s} \quad (5.36)$$

$$v_0 = 220 \text{ km/s} \quad (5.37)$$

$$v_{Earth} = 230 \text{ km/s} \quad (5.38)$$

Moreover, the target nucleus used by EDELWEISS being germanium, an atomic mass of $A = 72.63$ is used, taking into account the isotope fraction in the natural germanium:

- ^{70}Ge : 20.57%
- ^{72}Ge : 27.45%

⁵The method used to calculate the exposure is presented in chapter 3.

Chapter 5: High-voltage data analysis

- ^{73}Ge : 7.75%
- ^{74}Ge : 36.50%
- ^{76}Ge : 7.73%

The quenching factor for nuclear recoils used in this analysis is:

$$Q_{nr}(E_R) = 0.16E_R^{0.18} \quad (5.39)$$

as this parametrization corresponds to the one usually used by germanium target experiments [51]. It describes well the observation in the different datasets of neutron calibration in EDELWEISS. The impact of a possible variation of this parametrization will be discussed at the end of this chapter (see section IV.3).

II.2.2 Optimization of the energy range

The method described in section II.1 to optimize the energy range used to determine the excluded cross-section σ_{exc} has been applied to the WIMP search with high-voltage data of FID803 detector. The range has been optimized as a function of the WIMP mass using the theoretical spectrum smeared with the experimental heat resolution and applying the threshold model associated to the corresponding cryorun, together with the heat-only spectrum measured with the independent datasets recorded at 8 V voltage bias (Fig.5.10 right). Fig.5.11 (left)

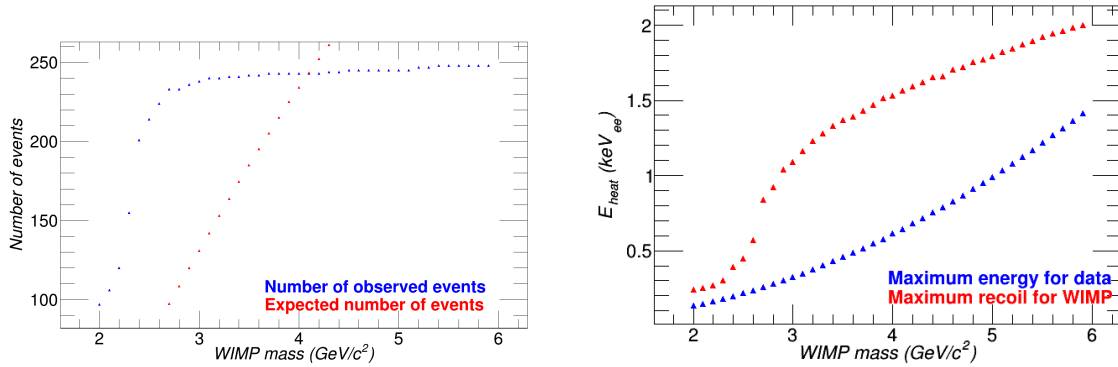


Figure 5.11 – Left: number of events in the energy range found by the algorithm (in blue) and expected number of WIMP events for $\sigma = 10^{-40} \text{ cm}^2$ (in red) as a function of the studied WIMP mass. Right: maximum heat energy E_{heat}^{max} found by the algorithm (in blue) and expected for the WIMP signal (in red) as a function of the studied WIMP mass.

illustrates the number of observed events in the optimized range as a function of the WIMP mass (in blue). The main part of the final spectrum used to determine the number N_{obs} is below 2 keV_{ee} which corresponds to the maximum recoil energy for the WIMP spectrum, as shown in Fig.5.11 (right). At these energies, the background model presented in the previous section predicts a rate dominated by HO events.

II.2.3 Limit associated to the first run at high voltage

The final heat energy spectrum used to determine the spin-independent WIMP-nucleon cross-section is shown in Fig.5.12 (bottom) as well as the trigger efficiency (top), which corresponds

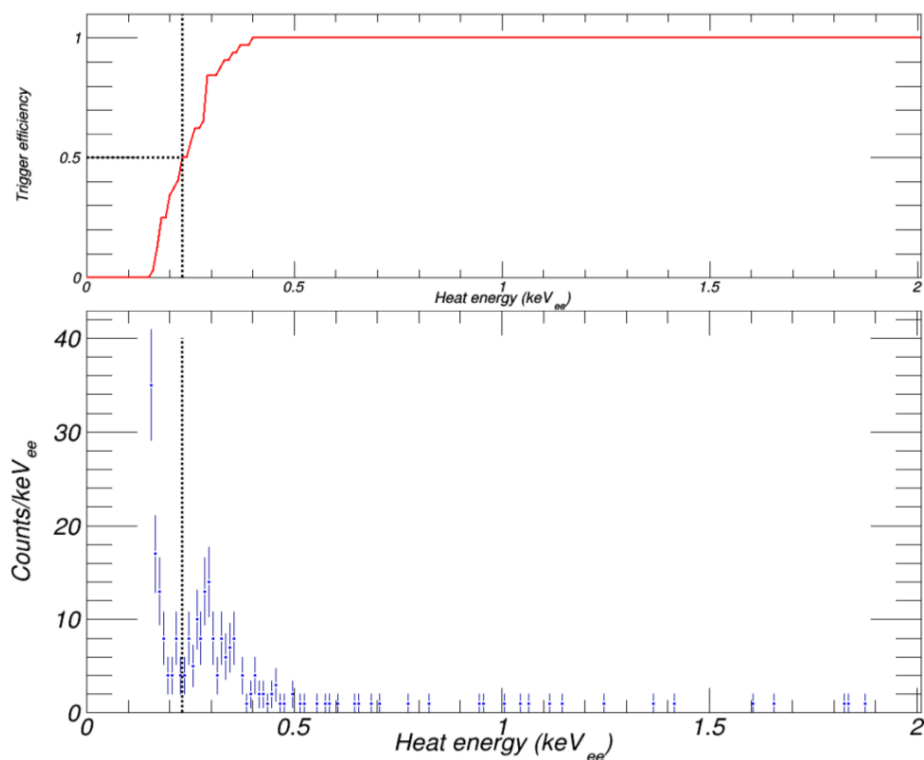


Figure 5.12 – Trigger efficiency (top) in red and final heat energy spectrum (bottom), in blue, for FID803 detector during run309. In both plots, the vertical dashed black line shows the 230 eV_{ee} heat energy threshold obtained for a trigger efficiency of 50%.

to a 230 eV_{ee} heat energy threshold for a 50% trigger efficiency. It has been determined with the same cut procedure as described in section III of chapter 3. The exposure of this dataset corresponds to 5.76 kg.day. By applying the optimal range method, the WIMP-nucleon cross-section excluded at 90% C.L. has been calculated for each WIMP mass, as illustrated in Fig.5.13. This limit can be compared to a projection of the sensitivity using the method based on the expected shape of the WIMP signal and the energy spectrum and rate of HO events recorded at 8 V with FID803 detector. A simulation of fake dataset based on this assumption has been performed. The limit obtained with the data is compatible with the projections calculated from Eq.5.33. It improves the previous low-mass WIMP-nucleon cross-section limit of the EDELWEISS experiment below 4.5 GeV/c² [92], which is drawn in dark red in Fig.5.13. Other limits on the plot are the ones by CRESST [54] (magenta) and CDMSlite Run2 [51] (blue), which are two other cryogenic experiments discussed in chapter 1. This first result using high-voltage data is higher than the CRESST limit mainly because of the heat-only background strongly impacting the low-energy part of the heat energy spectrum. At this point of the study, one question remains unanswered: which exposure has to be reached before being limited by the backgrounds?

II.2.4 Study of the exposure limitation on WIMP-nucleon cross-section for low-mass WIMP

The run309 being the first cryorun using the threshold improvement by Luke-Neganov effect, a crucial question was how the limit would be improved by increasing the statistics, i.e how long should the run last before the backgrounds limit the dark matter search. To answer this

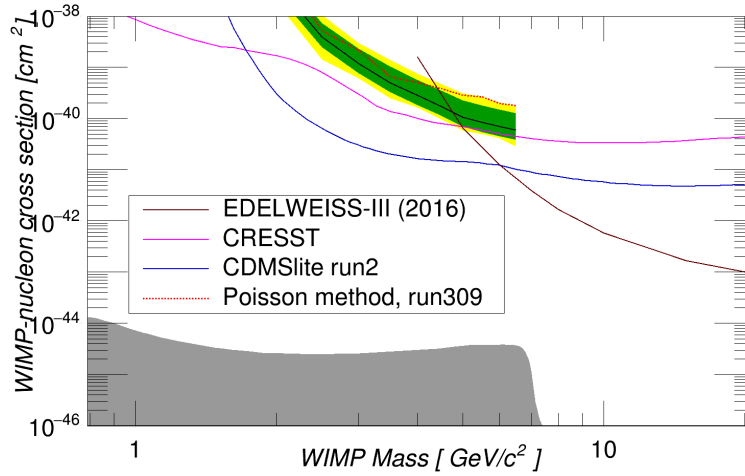


Figure 5.13 – Excluded spin-independent WIMP-nucleon cross-section (in cm^2) as a function of the WIMP mass (in GeV/c^2). The projection sensitivity calculated with the FID803 detector data of run309 corresponds to the black curve for $m_\chi \in [2.5; 7] \text{ GeV}/c^2$, with the error bands at 1σ and 2σ in green and yellow respectively. The limit obtained in this work with the Poisson statistical method is the red curve. The magenta curve corresponds to the CRESST results [54], the blue curve to CDMSlite Run2 [51] and the dark red curve to the previous EDELWEISS-III limit [92].

question, the projections described above have been repeated for different increasing exposures. These fake experiments were simulated from the hypothesis that heat-only events are the main background, a hypothesis well supported by the fact that the limit shown in Fig.5.13 is compatible with the projections obtained under this assumption.

The result is shown in Fig.5.14 for four different WIMP masses. To improve significantly the sensitivity, the exposure would have to be increased by more than a factor 2 ($> 10 \text{ kg}\cdot\text{day}$). Even then, the improvement would be modest at low mass, and negligible at $5 \text{ GeV}/c^2$. This motivated the choice to test a Likelihood approach for the FID803 detector dataset in run309, based on the work done in [71].

III Likelihood analysis

To fully exploit all information on the different backgrounds obtained in the study of the different sideband data, it was decided to perform a maximum Likelihood analysis that takes them into account. The information about the backgrounds is contained in the Probability Density Functions (PDF) that describe each of them as well as the signal expected from a WIMP-nucleon scattering. Nuisance parameters for each background are defined to describe the uncertainty on their normalisation.

The next subsection presents how these PDF have been built for the different backgrounds. The maximum likelihood as well as the profile likelihood allowing to extract the excluded WIMP-nucleon cross-sections are detailed then. Different tests have been implemented to verify that the algorithm works without analysis bias. Finally, the results associated to this method will be presented.

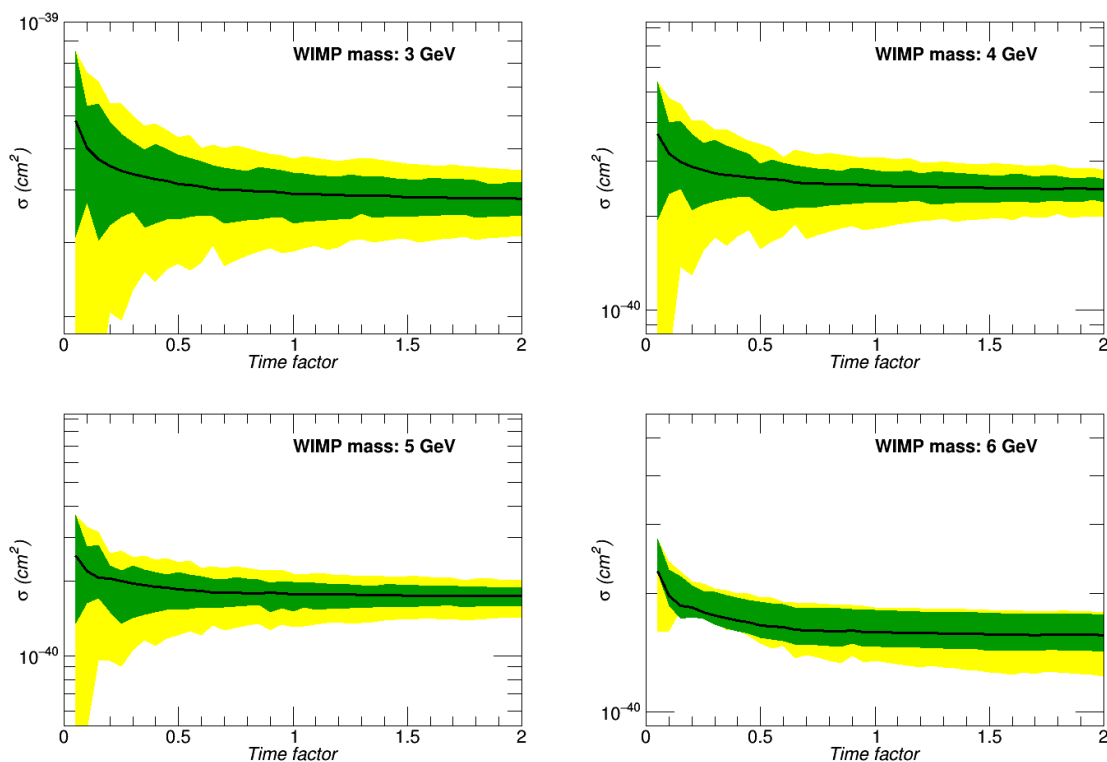


Figure 5.14 – Projection sensitivity (black line) of the WIMP-nucleon cross-section as a function of the time factor for a WIMP mass of $3 \text{ GeV}/c^2$ (top, left), $4 \text{ GeV}/c^2$ (top, right), $5 \text{ GeV}/c^2$ (bottom, left) and $6 \text{ GeV}/c^2$ (bottom, right). A time factor of 1 corresponds to the current exposure of FID803 detector in run309, i.e. 5.76 kg.days . As shown on all plots, with a factor 2 on the exposure, no significant gain is expected with respect to the value at 1. The error bands at 1σ and 2σ are shown in green and yellow respectively.

III.1 Modelization of the different types of events

The Probability Density Functions (PDF) describe the different event populations of the EDELWEISS experiment as well as the expected signal. They are a function of two variables: the average sum of the signals on the two NTD sensors E_{heat} and the ionization energy given by the mean of the planar electrodes E_{ion} . In principle, it is possible to use the 6 variables corresponding to the 6 readout channels (two heats and four ionizations). However this approach is not considered in this thesis because of the required CPU time: the numerical integration, used for the normalization of the PDF, is not suited for high dimensionality, and some of the information is redundant. Thus the two chosen variables are a combination of the different readout channels. Each of the variables has a corresponding resolution σ_{heat} (for E_{heat}) and σ_{ion} (for E_{ion}). No selection on fiducial events will be applied on this analysis because of the planar mode used when applying high voltage bias on detectors. The variables are described by:

$$E_{ion} = I(E_R) = Q(E_R) \times E_r \text{ in keV}_{ee} \quad (5.40)$$

$$E_{heat} = H(E_R) = E_R \frac{1 + Q(E_R) \frac{V}{3}}{1 + \frac{V_{fid}}{3}} \text{ in keV}_{ee} \quad (5.41)$$

Chapter 5: High-voltage data analysis

where E_R is the recoil energy, V is the difference of potential applied to the considered electrodes (either fiducial or surface electrodes) and V_{fid} is the difference of potential applied to fiducial electrodes in FID mode (in planar mode there is no specific fiducial electrodes so V_{fid} as to be replaced by V in Eq.5.41). The quantity $Q(E_R)$ corresponds to the ionization yield of the event. Eq.5.41 shows how the heat energy is affected by the Luke-Neganov effect as described in section VI of chapter 2. It characterizes the shifting to lower values of the heat energy for events with an ionization yield lower than one. The function $I(E_R)$ is used to compute the ionization energy of events.

III.1.1 Probability Density Functions

Constructing a Probability Density Function with the two observables E_{heat} and E_{ion} requires to start with the recoil energy spectrum $\rho(E_R)$ of the expected signal and the different backgrounds, defined as:

$$\rho(E_R) = \frac{dN}{dE_R}(E_R) \quad (5.42)$$

The event density as a function of E_R , E_{heat} and E_{ion} is:

$$\rho(E_R, E_{heat}, E_{ion}) = \frac{d^3N(E_R, E_{heat}, E_{ion})}{dE_R dE_{heat} dE_{ion}} \quad (5.43)$$

By neglecting any resolution effects and using the detector response described by Eq.5.40 and Eq.5.41, the event density can be rewritten:

$$\rho(E_R, E_{heat}, E_{ion}) = \rho(E_R) \times \delta(E_R - H^{-1}(E_{heat})) \times \delta(E_R - I^{-1}(E_{ion})) \quad (5.44)$$

where δ is the delta function. To compute the recoil energy corresponding to given energy values of E_{heat} and E_{ion} , the inverse of the functions H and I are used. For neutrons and WIMP, the quenching factor Q is dependent on E_R . To inverse the functions, an interpolator is necessary to connect the recoil energy to the ionization and heat energies. For the other backgrounds, the quenching factor is defined as independent of the recoil energy, leading to an analytical function for $H^{-1}(E_{heat})$ and $I^{-1}(E_{ion})$.

The resolutions σ_{ion} and σ_{heat} have to be taken into account, as several couples of (E_{heat}, E_{ion}) can give the same value of E_R . Thus Eq.5.44 is convolved with two gaussian functions:

$$\rho(E_R, E_{heat}, E_{ion}) = \frac{1}{2\pi\sigma_{heat}\sigma_{ion}} \rho(E_R) \times e^{-\left(\frac{E_{heat}-H(E_R)}{\sqrt{2}\sigma_{heat}}\right)^2} \times e^{-\left(\frac{E_{ion}-I(E_R)}{\sqrt{2}\sigma_{ion}}\right)^2} \quad (5.45)$$

By integrating over the input recoil energy spectrum, the event density in the two observables can be determined as:

$$\rho(E_{heat}, E_{ion}) = \frac{d^2N}{dE_{heat}dE_{ion}}(E_{heat}, E_{ion}) \quad (5.46)$$

$$= \frac{1}{2\pi\sigma_{heat}\sigma_{ion}} \int_0^\infty \rho(E_R) e^{-\frac{(E_{heat}-H(E_R))^2}{2\sigma_{heat}^2}} e^{-\frac{(E_{ion}-I(E_R))^2}{2\sigma_{ion}^2}} dE_R \quad (5.47)$$

To take into account the impact of the online trigger on the heat channel, the trigger efficiency $\epsilon_{th}(E_{heat})$ will be used. It is defined in section III.4 of chapter 3 as:

$$\epsilon_{th}(E_{heat}) = \frac{1}{2} \left(\operatorname{erf} \left(\frac{E_{offline} - E_{online}}{\sqrt{2}\sigma_{offline-online}} \right) + 1 \right) \quad (5.48)$$

Chapter 5: High-voltage data analysis

with E_{online} , $E_{offline}$ and $\sigma_{offline-online}$ defined in section III.4 of chapter 3. By applying this function as a correction on the event density, Eq.5.47 becomes:

$$\rho(E_{heat}, E_{ion}) = \frac{\epsilon_{th}(E_{heat})}{2\pi\sigma_{heat}\sigma_{ion}} \int_0^\infty \rho(E_R) e^{-\frac{(E_{heat}-H(E_R))^2}{2\sigma_{heat}^2}} e^{-\frac{(E_{ion}-I(E_R))^2}{2\sigma_{ion}^2}} dE_R \quad (5.49)$$

The expected number of background events N_i for a given recoil energy spectrum $\rho(E_R)$ is obtained by integrating the event density distribution over the two variables within the range of interest:

$$N_i = \int_{E_{ion}^{min}}^{E_{ion}^{max}} \int_{E_{heat}^{min}}^{E_{heat}^{max}} \rho(E_{heat}, E_{ion}) dE_{heat} dE_{ion} \quad (5.50)$$

with i the considered background. The normalization of each PDF f_B^i is made by using this number as:

$$f_B^i(E_{heat}, E_{ion}) = \frac{\rho(E_{heat}, E_{ion})}{N_i} \quad (5.51)$$

Integrations of each PDF (signal and backgrounds) are performed numerically.

While the backgrounds have to be determined once for a detector, the signal PDF depends on the nuclear recoil spectrum of WIMP in germanium, which varies as a function of the WIMP mass (see Fig.1.13). Consequently, a normalized signal PDF f_S will be constructed for each WIMP mass m_χ of this analysis:

$$f_S(E_{heat}, E_{ion}) = \frac{\rho(E_{heat}, E_{ion})}{N_\chi} \quad (5.52)$$

The expected number of signal events N_χ is defined for each WIMP mass as a function of the parameter of interest, i.e the WIMP-nucleon scattering cross-section σ_χ . N_χ can be calculated by integrating the WIMP PDF in the region of interest in the same way as for background N_i , but using a starting cross-section value⁶.

III.1.2 Generating fake experiments

A simulation of fake experiments is necessary to determine the projections associated to each dataset. From the PDF of each event populations, fake experiments can be generated by repeating the following procedure:

- the numbers of expected events for each background are determined with Eq.5.50,
- a gaussian fluctuation is applied on these numbers to describe the systematic uncertainties in their modelization,
- then a Poissonian fluctuation is applied to obtain a random number for each background simulation.

Then, fake data are simulated by:

- extracting a random value of E_R from the $\rho(E_R)$ distribution,
- then calculating the associated values of E_{heat} and E_{ion} , determined with Eq.5.40 and Eq.5.41, respectively. These values are smeared with gaussian fluctuations based on the corresponding resolutions (σ_{heat} and σ_{ion}).

⁶The value chosen to generate the WIMP recoil energy spectrum is $\sigma_\chi^0 = 10^{-40} \text{ cm}^2$.

Chapter 5: High-voltage data analysis

Simulated events are kept only if they are in the energy range of the analysis. The verification of these simulated experiments is described for each background as well as for the signal in appendix A. The different components needed to perform a Likelihood analysis are determined: the models for signal and backgrounds and their PDF, the detector response model (i.e the trigger efficiency) and the fake data simulation method. The maximum likelihood function can now be determined.

III.2 Maximum likelihood function

From the spectral shape of the backgrounds and the signal, the maximum likelihood function is built to determine the number of events of a signal μ_S and backgrounds μ_B that best describe the dataset. The number of events corresponding to the best approximation of the dataset are the estimators $\hat{\mu}_S$ and $\hat{\mu}_B$. In this work, the μ_S parameter is the one which allows to constrain the WIMP-nucleon cross-section: this is the parameter of interest. This analysis can be made by binning or not the data. The second allows to extract more information about the spectral shape, this is why it is used here.

First of all, the Bayes theorem states that the probability that a dataset D contains the true values μ_S and μ_B is:

$$P(\mu_S, \mu_B|D) = \frac{P(D|\mu_S, \mu_B) \times P(\mu_S, \mu_B)}{P(D)} \quad (5.53)$$

$P(\mu_S, \mu_B|D)$ is the probability that μ_B and μ_S are the correct parameters knowing the data D . $P(\mu_S, \mu_B)$ is the probability that μ_B and μ_S are the correct parameters, $P(D)$ the probability to observe the data, $P(D|\mu_S, \mu_B)$ the probability to observe the data knowing the μ_B and μ_S parameters. This last one is the likelihood function $\mathcal{L}(\mu_S, \mu_B)$. The Bayes theorem can thus be written as:

$$P(\mu_S, \mu_B|D) \propto \mathcal{L}(\mu_S, \mu_B) \quad (5.54)$$

In this way, the estimators which maximize the probability $P(\mu_S, \mu_B|D)$ also maximize $\mathcal{L}(\mu_S, \mu_B)$.

For a given dataset, the likelihood function is defined as the product of the individual probabilities for all N events:

$$\mathcal{L}_{ind} = \prod_{e=1}^N (\mu_S f_S(E_{heat}^e, E_{ion}^e) + \sum_j \mu_B^j f_B^j(E_{heat}^e, E_{ion}^e)) \quad (5.55)$$

where $f_S(E_{heat}, E_{ion})$ and $f_B^j(E_{heat}, E_{ion})$ are the 2-dimension PDF of the signal and backgrounds normalized on the energy range of the analysis (Eq.5.51 and Eq.5.52). j corresponds to the type of background. The number of measured events N is related to the total rate μ for all backgrounds and signal.

An additional Poisson term $Pois(N|\nu) = \exp(-(\mu_S + \sum_j \mu_B^j))$ can then be added to the likelihood function \mathcal{L} . It corresponds to the probability to observe N_i events whose the expected value is μ_i and allows to take into account that the number of measured events N is a statistical realization of the expected event rate. The resulting function is called extended likelihood function and is expressed as:

$$\mathcal{L}(\sigma, \mu_B) = \exp(-(\mu_S + \sum_j \mu_B^j)) \times \prod_{e=1}^N (\mu_S f_S(E_{heat}^e, E_{ion}^e) + \sum_j \mu_B^j f_B^j(E_{heat}^e, E_{ion}^e)) \quad (5.56)$$

Furthermore, the likelihood function can incorporate an additional information about the degree of belief of the different background models, in order to properly estimate their systematic

uncertainties $\vec{\sigma}_{\mu_B}$. For that, the $\vec{\mu}_B$ parameters are determined from the sideband measurement and called nuisance parameters. The term associated to the likelihood function is a gaussian term defined as:

$$\mathcal{L}_{sys}(\vec{\mu}_B, \vec{\sigma}_{\mu_B}) = \prod_j \mathcal{L}_{sys}^j(\mu_B^j, \sigma_{\mu_B}^j) = \prod_j \frac{1}{\sqrt{2\pi}\sigma_{\mu_B}^j} \exp\left(-\frac{1}{2}\left(\frac{\mu_B^j - N_j}{\sigma_{\mu_B}^j}\right)^2\right) \quad (5.57)$$

where N_j is the expected number of events obtained with Eq.5.50 for each background j and $\sigma_{\mu_B}^j$ is the uncertainty on background j multiply by N_j .

By considering these different terms, the maximum likelihood function can be written in two dimensions:

$$\begin{aligned} \mathcal{L}(\sigma, \mu_B) = \exp(-(\mu_S + \sum \mu_B^j)) &\times \prod_{e=1}^N (\mu_S f_S(E_{heat}^e, E_{ion}^e) + \sum_j \mu_B^j f_B^j(E_{heat}^e, E_{ion}^e)) \\ &\times \prod_j \frac{1}{\sqrt{2\pi}\sigma_{\mu_B}^j} \exp(-\frac{1}{2}(\frac{\mu_B^j - N_j}{\sigma_{\mu_B}^j})^2) \end{aligned} \quad (5.58)$$

A typical application for a likelihood function is to consider the logarithm of this equation⁷: $\ln(\mathcal{L}(\sigma, \mu_B))$. To estimate the parameters, one defines the set of parameters $\hat{\theta}_i$ that properly takes into account systematic uncertainties in a frequentist approach. The value $\hat{\theta}_i$ which maximizes the likelihood $\mathcal{L}(\hat{\theta}_i)$ is called Maximum Likelihood Estimator (MLE). Likelihood functions are frequently used in parameter estimation, as the MLE is consistent (i.e converge to the true value) and is unbiased and normally distributed for a sufficiently large number of events N . For a model with several parameters it is possible to define a conditional MLE, corresponding to fix one parameter at a given value during the minimization of the likelihood. This procedure is called a profile Likelihood.

III.3 Profile Likelihood

The parameter estimation, i.e the way to find the estimator θ_i that minimizes $\ln(\mathcal{L}(\sigma, \mu_B))$, is not sufficient to constrain the WIMP-nucleon cross-section. A hypothesis test has to be built to obtain a statistical significance of the calculated results, i.e to extract the excluded WIMP-nucleon cross-section. In this thesis, the test used is a profile Likelihood, described in [103].

In a hypothesis test, the agreement between a hypothesis and the measured data is quantified. If the so-called p-value, i.e the fraction of theoretical experiments which are less compatible with the hypothesis than the measured data, is below a given value, the hypothesis is excluded. The null hypothesis H_0 is defined as there is no signal events in the dataset and the hypothesis H_σ assumes that WIMP have a cross-section value σ . To set a limit, the hypothesis to reject is H_σ . To calculate the p-value, the statistical test is defined as well as its value for the data measured with the \mathcal{L} distribution under a given hypothesis. Thus the associated profile Likelihood ratio is:

$$\lambda(\sigma) = \frac{\mathcal{L}(\sigma, \hat{\theta})}{\mathcal{L}(\hat{\sigma}, \hat{\theta})} \quad (5.59)$$

where the parameters $\hat{\sigma}$ and $\hat{\theta}$ correspond to the MLE of the signal and of the nuisance parameters ($\theta \equiv \vec{\mu}_B$). The conditional estimator $\hat{\theta}$, which is a function of σ , is the value of θ which maximizes the likelihood \mathcal{L} for a fixed value of σ . By definition, $0 \leq \lambda(\sigma) \leq 1$, where a good agreement between the hypothesis and data is given for $\lambda(\sigma) \simeq 1$.

⁷ $\mathcal{L}(\sigma, \mu_B)$ having typically weak values.

Chapter 5: High-voltage data analysis

To reject the H_σ hypothesis and thus set an exclusion limit on the parameter of interest, one defines q_σ as:

$$\begin{aligned} q_\sigma &= -2 \ln(\lambda(\sigma)) \text{ for } \hat{\sigma} \leq \sigma \\ &= 0 \text{ for } \hat{\sigma} > \sigma \end{aligned} \quad (5.60)$$

It permits to reduce the data to one variable. Only positive values of q_σ are allowed ($q_\sigma \geq 0$) and increasing the q_σ value corresponds also to increase the incompatibility between the hypothesis and the data, i.e. to reject the hypothesis H_σ .

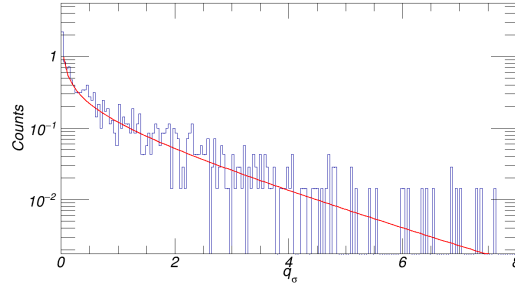


Figure 5.15 – Comparison between the $f(q_\sigma|H_\sigma)$ distribution (Eq.5.62) obtained by Monte-Carlo simulations, in blue, and the q_σ distribution obtained by the asymptotic formula (Eq.5.60), in red. The $f(q_\sigma|H_\sigma)$ distribution follows the expected q_σ behavior, allowing to ensure a correct implementation of this method.

The p_s p-value used to reject the signal hypothesis H_σ , with $p_s \leq 1 - \alpha$, corresponds to the fact that the result associated to a random experiment excludes a cross-section inferior to σ_{exc} (where σ_{exc} is the cross-section corresponding to the hypothesis H_σ). p_s can thus be calculated as:

$$p_s = \int_{q_\sigma^{obs}}^{+\infty} f(q_\sigma|H_\sigma) dq_\sigma \quad (5.61)$$

where q_σ^{obs} is the value of the statistical test observed from data and $f(q_\sigma|H_\sigma)$ is the probability density function, which describes how q_σ is distributed for a given σ value. It can be derived with Monte-Carlo toy data or parametrized using an asymptotic approximation. In the case of a large data sample N the $f(q_\sigma|H_\sigma)$ distribution also follows a half chi-square distribution, which simplifies the p_s value calculation, according to the Wilks theorem [103]:

$$f(q_\sigma|H_\sigma) = \frac{1}{2} \delta(q_\sigma) + \frac{1}{2} \frac{1}{\sqrt{2\pi}} \frac{1}{\sqrt{q_\sigma}} e^{-\frac{q_\sigma}{2}} \quad (5.62)$$

In this way, $f(q_\sigma|H_\sigma)$ is independent of σ and the p_s value can be evaluated without generating Monte-Carlo simulations. The upper limit on the cross-section is the largest value of σ for which $p_s = \alpha$. In this case, the cross-section value is excluded with a confidence level $1 - \alpha$. Thus, from the dataset, the excluded cross-section at 90% C.L. is the σ_{exc} value obtained for $q_\sigma^{obs} = 1.64$.

To illustrate the agreement between the q_σ value from Eq.5.60 and the $f(q_\sigma|H_\sigma)$ probability density function from Eq.5.62, the q_σ distribution is generated by Monte-Carlo simulations as shown in Fig.5.15. At high statistics, the match is correct but at too low statistics, the q_σ value doesn't follow the $f(q_\sigma|H_\sigma)$ distribution.

The next step is to verify the behavior of the λ and q_σ distributions as a function of the σ cross-section value, as shown in Fig.5.16. A simulation by Monte-Carlo simulation is realized

and the values of these two variables are extracted for each test. It is expected that q_σ vary as a function of σ to reach a minimum corresponding to the μ_S parameter of interest (the input value of the cross-section), which is illustrated by the red dashed line on the right plot. The violet dashed line corresponds to the μ_S value for the excluded cross-section σ_{exc} , given here for $q_\sigma = 1.64$ (90% C.L.). For values too far from μ_S , the q_σ are too high, decreasing the probability to obtain the corresponding values of σ as excluded cross-section. Concerning the λ parameter, it is expected that its distribution increases as a function of σ to reach a maximum corresponding to the μ_S input value, as shown in Fig.5.16 (left). It is illustrated in this plot by the red dashed line. Also the violet dashed line illustrates the μ_S value associated to the σ_{exc} excluded cross-section.

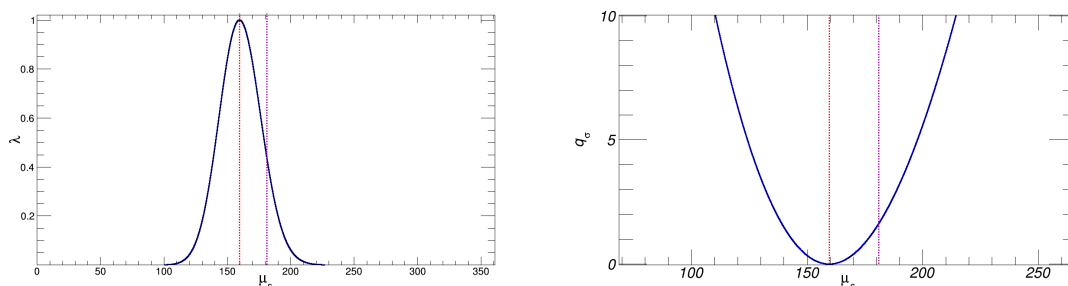


Figure 5.16 – Left: λ distribution as a function of the μ_S value. Right: q_σ distribution as a function of the μ_S value. In both plots, the red dashed line corresponds to the μ_S input value of the cross-section, and the violet dashed line to the μ_S value of the excluded cross-section σ_{exc} .

III.3.1 Experimental sensitivity

The exclusion limit calculated using the procedure described above can be confronted to the projected sensitivity of the experiment. This sensitivity is defined by the median significance, assuming that the data follow the hypothesis H_0 , for which a non-zero value for σ can be rejected. To evaluate it, N_{exp} experiments are simulated by Monte-Carlo simulation under this hypothesis, considering q_σ as the observed value q_σ^{obs} . The median of the σ_{exc} excluded cross-section distribution obtained with this simulation gives the experiment projection of the cross-section.

As an example of this method, $N = 2500$ experiments are generated, with an input cross-section signal of $\sigma = 10^{-40}$ cm² injected in the dataset. The distribution of the σ_{exc} excluded cross-section obtained with this simulation is shown in Fig.5.17, with the median value given by the pink vertical line. The σ_{exc} values associated to the 1σ and 2σ error bands are obtained using the 15.9% and 84.1 quantiles (vertical green full lines) and the 2.5% and 97.5% quantiles (vertical green dashed lines), respectively. It has also been verified that the 10% quantile (vertical dashed orange line) corresponds exactly to the input value of σ_{exc} injected in the simulation (violet dashed line), i.e in 90% of the cases, the method excludes a cross-section value higher than the input value. It confirms that the result of the test corresponds to the chosen 90% confidence level.

To check the validity of the used algorithm, a generation of fake data under the hypothesis H_σ is carried out using Monte-Carlo simulations, as the same way as to obtain the sensitivity of the experiment. The maximum of the likelihood function has to be reached for a number of signal and background events corresponding to those in input of the simulation. Fig.5.18 shows the

Chapter 5: High-voltage data analysis

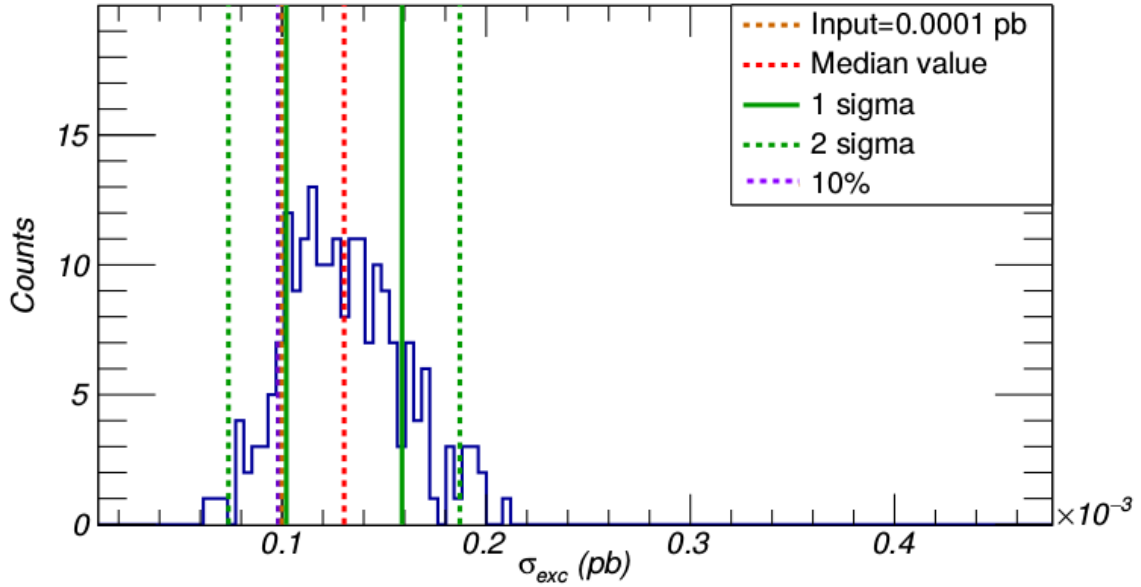


Figure 5.17 – Distribution of the σ_{exc} excluded cross-section for a Monte-Carlo simulations of 2500 experiments with a WIMP-nucleon cross-section of 10^{-40} cm^2 at 90% C.L. The orange vertical dashed line corresponds to the input value of σ_{exc} and the violet one is the value reconstructed after minization of the likelihood function, associated here to the 10% quantile. It allows to verify that in 90% of the case, the method excludes a σ_{exc} value higher than the input one. The magenta dashed line corresponds to the median of the distribution. The vertical green full lines and dashed lines correspond to the 15.9%- and 84.1-quantiles and to the 2.5% and 97.5% quantiles, respectively, as used to obtain the σ_{exc} values associated to the 1σ and 2σ error bands.

result of this simulation for $N = 5000$ experiments, whose the rightest plot of each serie is the distribution of the reconstructed events, for the signal on the 1st line and for each considered background on the other lines. The dashed red line on each rightest plot corresponds to the respective input value, which is first smeared via a gaussian fluctuation, then via a poissonian fluctuation for each Monte-Carlo simulation. The dashed blue line corresponds to the median value of each distribution. The superposition of the two lines ensures that the statistical test reconstructs correctly the backgrounds, which is the case here considering the excellent agreement. In case of no bias, the maximum likelihood function as well as the implemented Monte-Carlo simulation are correctly defined.

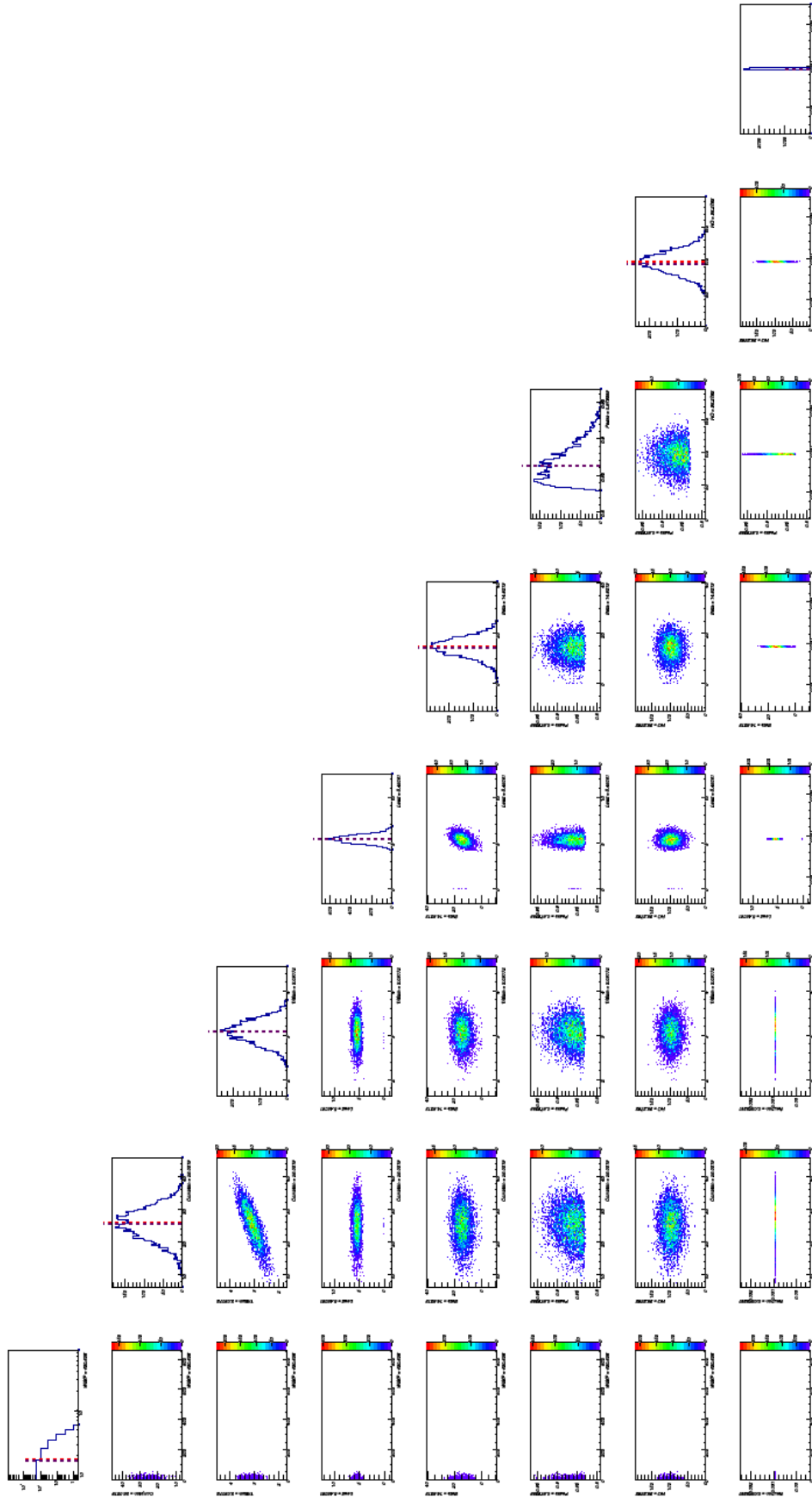


Figure 5.18 – Distributions of the μ_s (signal) and μ_B (background) values for a simulation of 5000 fake experiments. The first line is associated to the WIMP signal, other lines are for backgrounds with the order: compton, tritium, lead, beta, cosmogenics, heat-only and neutron. The input value of each rightest plot is shown by the vertical red line, and the value obtained by the minimization corresponds to the violet one. The lines are very near in each plot, ensuring that both values are in excellent agreement. Other plots are associated to the correlations between the parameters (the signal and the different considered backgrounds).

IV Extraction of the exclusion limits

After the study of the expected signal and different backgrounds, giving all the associated PDF, the likelihood model has been implemented following the determination presented in section III. Due to the relatively small exposures of 5.76 kg.day (for run309) and 25.42 kg.day (for run310), the Likelihood analysis has to focus on low-mass WIMP. Indeed, no improvement can be expected at high mass with respect to the 496 kg.day of the previous EDELWEISS analysis [92]. Nevertheless, the decreasing of the energy threshold thanks to the Luke-Neganov effect is an important upgrade for the experiment and would improve significantly the results at low WIMP masses, i.e below 5 GeV/c². First, a limit will be extracted from the small exposure dataset of FID803 detector in run309 and compared with results from the Poisson analysis shown in section II.2.3 with the same data. Second, the dataset of FID803 detector in run310, with a higher exposure, will be used to extract the WIMP-nucleon cross-section as the result of the EDELWEISS-III experiment for low-mass WIMP. It will be compared with those of other cryogenic experiments. Finally, a discussion about the different uncertainties will be presented.

IV.1 Dataset of the FID803 detector in run309

The signal PDF has been obtained for each WIMP mass m_χ between [3; 6] GeV/c² with a step of 0.5 GeV/c² as well as for $m_\chi = 10$ and 20 GeV/c², and the likelihood function has been calculated. Furthermore, each parameter has been determined for the run309 dataset as:

- the different count rates N_i for the signal and the different backgrounds, as well as their uncertainties (all defined in section I),
- the average heat energy resolution for the 100 V voltage bias dataset,
- the average ionization energy resolution for the 100 V voltage bias dataset,
- the periods of the run at 100 V voltage bias, corresponding to an exposure of 5.76 kg.day,
- the trigger efficiency model as described in section III.4 of chapter 3.

The analysis has been restricted to WIMP masses above 3 GeV/c² corresponding to a heat energy associated to a recoil of 0.30 keV_{ee}, which is close to the heat energy threshold of 0.23 keV_{ee} for a 50% trigger efficiency, as shown in Fig.5.12. The results associated to the dataset of run309 for FID803 detector are presented in Fig.5.19. The associated sensitivity calculated with the Likelihood method is the black curve and the error bands at 1 σ and 2 σ are drawn in green and yellow respectively. The limit obtained by this method is the red dashed curve, which is in good agreement with the projections. As expected from the statistical method described in section II.2.3, associated to the dotted red curve in Fig.5.19, this run309 limit obtained with the Likelihood method improves the previous low-mass WIMP-nucleon cross-section limit of the EDELWEISS experiment [92] below 4.5 GeV/c² (dark red curve) but not for $m_\chi > 5$ GeV/c², due to the small exposure. Nevertheless, the run309 limit obtained with the Likelihood method reaches the CRESST limit [54] (in magenta), for a WIMP mass of $m_\chi = 5$ GeV/c², which is a better result than the one obtained with the statistical method for the same dataset.

There is no σ_{exc} value below $m_\chi = 3$ GeV/c², due not only to the analysis threshold imposed at 0.26 keV_{ee} in this analysis, but also to the poor exposure of the run309 dataset, which limits the sensitivity as explained in section II.2.4.

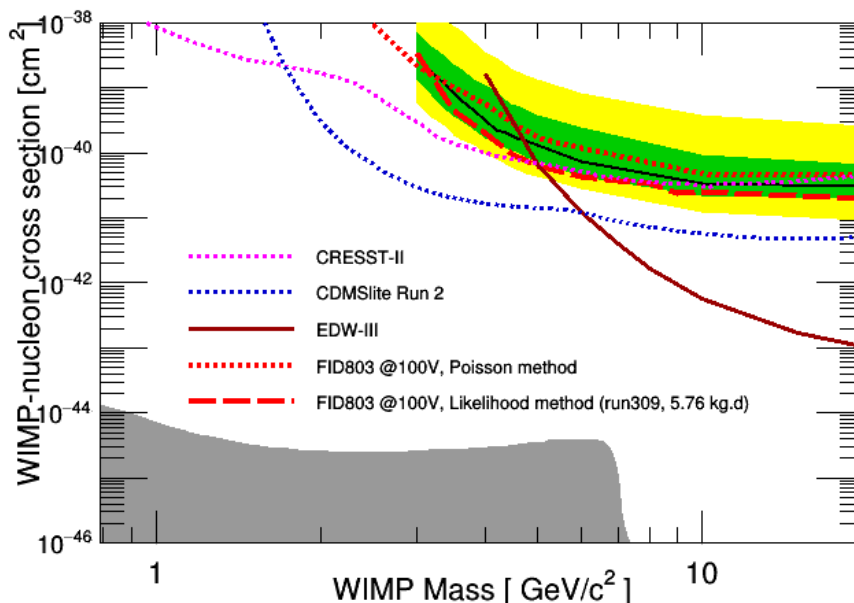


Figure 5.19 – WIMP-nucleon cross-section as a function of the WIMP mass. The black curve represents the sensitivity of the experiment for run309 for $m_\chi \in [3; 20] \text{ GeV}/c^2$, with the error bands at 1σ and 2σ in green and yellow, respectively. The red dashed curve is the limit associated to the dataset of the run309. The previous limit obtained with the statistical method (section II.2.3) is also drawn as the dotted red line for comparison. The magenta curve corresponds to the CRESST results [54], the blue curve to CDMSlite Run2 [51] and the dark red curve to the previous EDELWEISS-III limit [92].

In conclusion, these results allowed to verify that the Likelihood method is correctly implemented and provide a better cross-section limit than the Poisson statistical method presented in section II.2.3. Moreover, the improvement of the threshold by applying the Luke-Neganov effect strongly impacts the limit below $5 \text{ GeV}/c^2$ with respect to the 2016 EDELWEISS results, motivating a WIMP search with a larger exposure in this high-voltage mode.

IV.2 Dataset of the FID803 detector in run310

The run310 dataset of FID803 detector has an exposure of 25.42 kg.day in high-voltage mode, i.e five times more than for run309. Because of this increase of the exposure, an improvement on the limit with the Likelihood method is expected. The same parameters as for the run309 Likelihood analysis are implemented (section IV.1). Note that the rise of the trigger efficiency at low energy in run310 is quite smooth with respect to the one of run309. It allows to have a lower heat energy threshold (200 eV_{ee}) in run310, for a 50% trigger efficiency, than in run309 (230 eV_{ee}), as illustrated in Fig.5.20. Due to this lower heat energy threshold of 200 eV_{ee} , it has been possible to search for a less strict minimal WIMP mass of $2.7 \text{ GeV}/c^2$, which has a 260 eV_{ee} heat energy associated to the recoil, but not below, to avoid conflict between the expected signal spectrum and the analysis threshold. Indeed, small imperfections in the efficiency model can lead to large relative change in its apparent value and a possible overestimation of the sensitivity of the experiment. This effect is avoided by restricting the analysis in the region where the efficiency is at least 50%.

Chapter 5: High-voltage data analysis

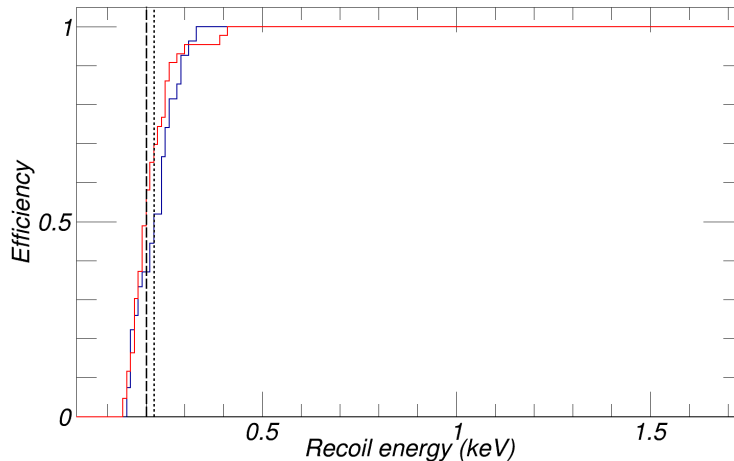


Figure 5.20 – Trigger efficiency obtained by applying the method described in section III.4 of chapter 3 for FID803 detector during run309 (in blue) and run310 (in red). The two vertical black dashed lines corresponds to the 50% trigger efficiency value and give the heat energy thresholds which are 230 eV_{ee} and 200 eV_{ee} , for run309 and run310 respectively.

The significant improvement of the WIMP-cross section limit as a function of the WIMP mass ($m_\chi \in [2.7; 20] \text{ GeV}/c^2$) obtained in run310 for the FID803 detector by the EDELWEISS experiment is presented in Fig.5.21. The sensitivity associated to the dataset parameters is shown in black and the error bands at 1σ and 2σ are drawn in green and yellow respectively. The red curve is the limit obtained from this work with the Likelihood analysis, and is in good agreement with the projections. Below $8 \text{ GeV}/c^2$, the limit is one sigma below the average sensitivity. This can be explained by a HO event rate that is approximately one sigma below the model value.

The comparison is better shown in Fig.5.22, which presents the different experimental spin-independent WIMP-nucleon scattering cross-section as a function of the WIMP mass without the projected sensitivity. The red curve is the limit obtained with an exposure of $25.42 \text{ kg}\cdot\text{day}$ for the detector FID803 at 100 V (run310). It is the central result of this work. It improves the limits obtained with the same FID803 detector but a smaller exposure in run309, either with the statistical method (dotted red curve) or the Likelihood method (dashed red curve). The conclusion doesn't change concerning the comparison with the previous low-mass WIMP-nucleon cross-section limit of the EDELWEISS experiment [92]. The run310 limit is below the one reported by the CRESST experiment⁸ from [54] for WIMP masses $m_\chi > 4 \text{ GeV}/c^2$.

Above $m_\chi = 5 \text{ GeV}/c^2$, this work results is approximately a factor two above the one of CDMSlite [51]. This is due to their lower analysis threshold of 56 eV_{ee} compared to the 200 eV_{ee} threshold used in this work. The combination of the two datasets of the FID803 detector (in both run309 and run310) has not been realized since it would unfortunately not improve significantly neither the threshold nor the limit due to the main heat-only background.

⁸More recent preliminary CRESST limits have been presented at the IDM2018 conference [104], just as this document had been completed. They significantly improve their constraints below $0.8 \text{ GeV}/c^2$, and reach the CDMSlite limits near $8 \text{ GeV}/c^2$.

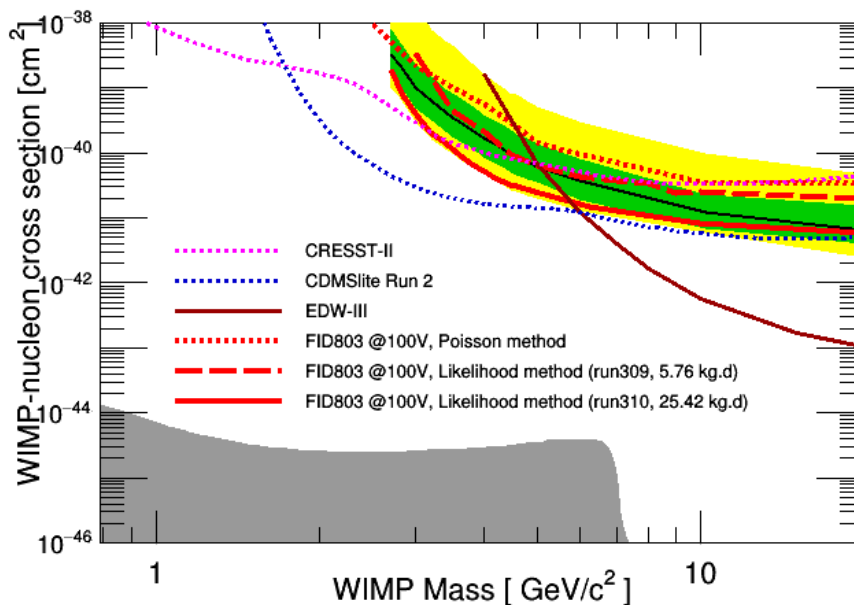


Figure 5.21 – WIMP-nucleon cross-section as a function of the WIMP mass. The black curve represents the sensitivity of the experiment for run310 for $m_\chi \in [2.7; 20] \text{ GeV}/c^2$, with the error bands at 1σ and 2σ in green and yellow, respectively. The red curve is the limit associated to the dataset of the run310. The previous limits obtained for the same FID803 detector in run309 with the statistical method and the Likelihood analysis are also shown (red dotted curve and red dashed curve respectively) for comparison. The magenta curve corresponds to the CRESST results [54], the blue curve to CDMSlite run2 [51] and the dark red curve to the previous EDELWEISS-III limit [92].

IV.3 Discussion

Some assumptions have been made in this work and have to be discussed. These hypotheses are:

- the beta quenching factor Q_β has been considered equal to 1 in planar mode since this is the value most compatible with observations (see section I.3),
- the nuclear recoil parametrization is given by $Q_{nr}(E_R) = \alpha E_R^\beta$ where $\alpha = 0.16$ and $\beta = 0.18$ for E_R in keV,
- the relative uncertainty on the heat-only population has been considered to be 20% (i.e. the nuisance parameter associated to this background equal to 0.2).

A simulation of $N_{exp} = 5000$ experiments has been carried out under these assumptions for a WIMP mass of $m_\chi = 5 \text{ GeV}/c^2$ and the Likelihood method has been applied. The associated σ_{exc} distribution is shown in Fig.5.23.

Three other simulations have been carried out changing one parameter each time, for $Q_\beta = 0.4$ instead of 1, for $Q_{nr}(E_R) = 0.17E_R^{0.19}$ instead of $Q_{nr}(E_R) = 0.16E_R^{0.18}$ (as proposed in [92]), and using a heat-only nuisance parameter of 0.4 instead of 0.2, respectively. The associated σ_{exc} distributions are also drawn in Fig.5.23 for comparison.

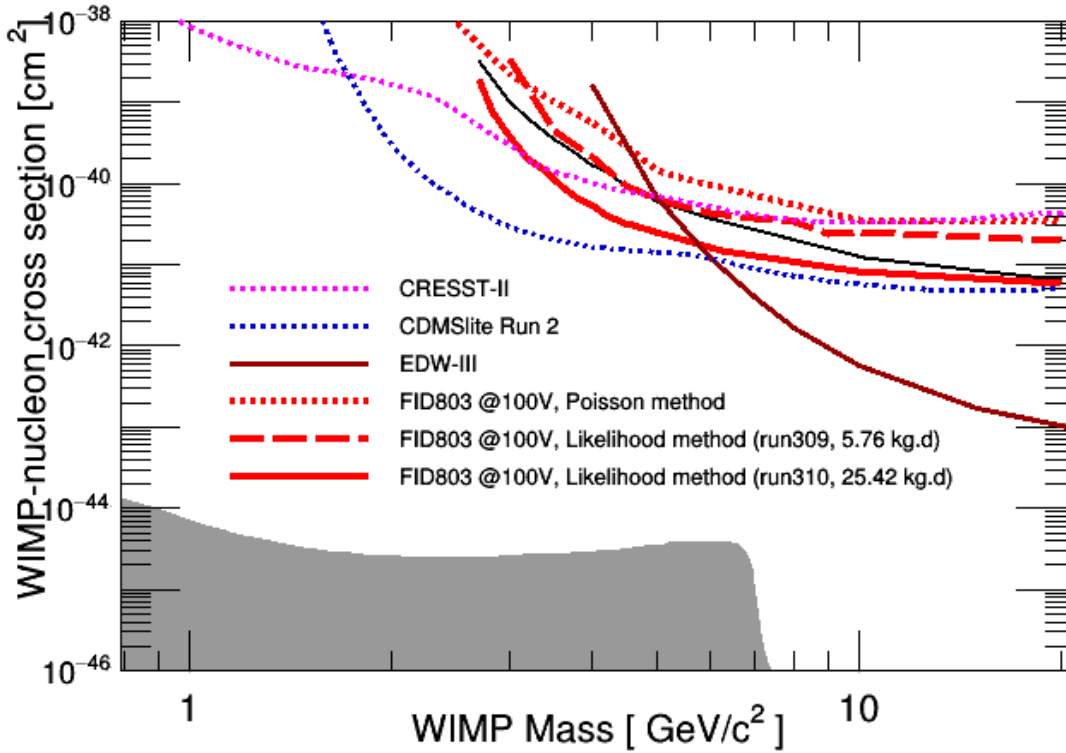


Figure 5.22 – WIMP-nucleon cross-section as a function of the WIMP mass. The red curve is the final limit obtained from this work and corresponds to the dataset of the FID803 detector in run310, with an exposure of 25.42 kg.day in high-voltage mode. The previous limits obtained for the same detector in run309 with the statistical method and the Likelihood analysis are also shown (red dotted curve and red dashed curve respectively) for comparison. The magenta curve corresponds to the CRESST results [54], the blue curve to CDMSlite Run2 [51] and the dark red curve to the previous EDELWEISS-III limit [92].

Hypothesis	σ_{exc} (cm ²) for $m_\chi = 4$ GeV/c ²	σ_{exc} (cm ²) for $m_\chi = 5$ GeV/c ²
Standard parameter set	6.92×10^{-41}	3.21×10^{-41}
$Q_\beta = 0.4$	5.69×10^{-41}	2.53×10^{-41}
$Q_{nr}(E_R) = 0.17E_R^{0.19}$	7.90×10^{-41}	3.46×10^{-41}
$\theta_{HO} = 0.4$	4.28×10^{-41}	3.05×10^{-41}

Table 5.2 – σ_{exc} value for a WIMP mass of $m_\chi = 4$ GeV/c² and a WIMP mass of $m_\chi = 5$ GeV/c², for this work parameter set, and changing one parameter each time. See text for details.

The four distributions are distributed in a same way, allowing to conclude that the used assumptions don't affect the excluded WIMP-nucleon cross-section calculated before. Furthermore, the limit can be calculated under each hypothesis to compare their σ_{exc} value. It has been done for different values m_χ of the WIMP mass. As an example, the σ_{exc} values calculated for

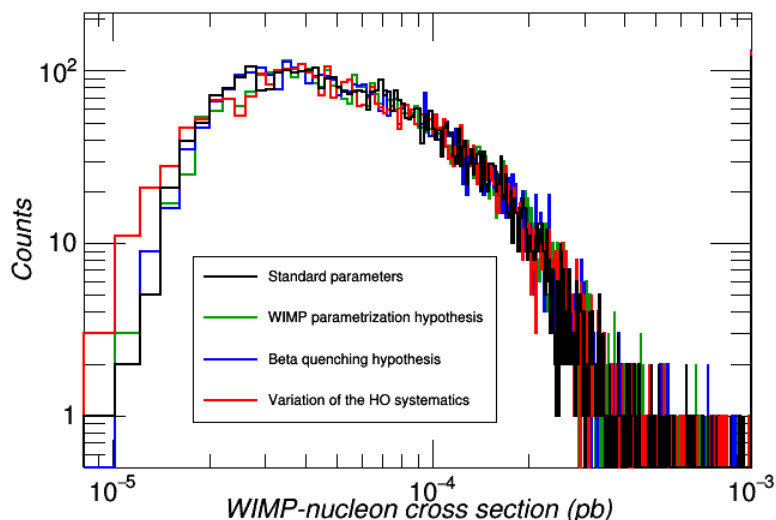


Figure 5.23 – Excluded WIMP-nucleon cross-section distribution for a WIMP mass $m_\chi = 5 \text{ GeV}/c^2$ for different input parameters. The black histogram is the sensitivity for the standard parameters used in this work. The blue histogram is the sensitivity if changing for $Q_\beta=0.4$, the red histogram corresponds to the sensitivity for a nuisance parameter of 0.4 for heat-only events and the green histogram represents the excluded cross-section with a different parametrisation of nuclear recoils ($Q_{nr}(E_R) = 0.17E_R^{0.19}$).

$m_\chi = 4 \text{ GeV}/c^2$ and $m_\chi = 5 \text{ GeV}/c^2$ are shown in table 5.2. The variations do not exceed 40%. The modifications of Q_β and of the HO event model tend to increase the sensitivity of the experiment, while the change in quenching of the nuclear recoils deteriorates the sensitivity by 12%.

No strong variation is observed for each tested mass. Moreover, the results associated to the different hypotheses vary in the error bands of Fig.5.21. Thus the systematic errors associated to these assumption do not affect significantly the results.

V Conclusion

This section presented the study of each the background expected in the first dataset EDELWEISS obtained with FID800 detectors operated at high voltage, as well as the Likelihood method used to determine from this dataset limits on the spin-independent cross-section of low-mass WIMPs. The dominating background contributions from heat-only events has been modeled based on the finding of chapter 4. The limits obtained with the Likelihood method are shown to be more sensitive to those obtained from the Poisson fluctuations of count rates observed in optimized energy ranges. The constraints obtained in the present work are better than those obtained previously by EDELWEISS [92] for WIMP masses below $5 \text{ GeV}/c^2$, and those obtained by CRESST [54] for WIMP masses above $4 \text{ GeV}/c^2$. The most important systematic uncertainties on these limits are discussed, and do not affect strongly those conclusions.

Conclusion and outlook

The main goal of this thesis was to analyse the first dataset of the EDELWEISS experiment collected at high voltage in order to improve the experimental energy threshold of the experiment. It was demonstrated that the Luke-Neganov effect does improve the resolution on heat channels of the FID800 detectors by the expected factor of $(1 + \frac{V}{3})$. This improvement in experimental resolution and threshold is achieved at the cost of reducing significantly the ability to reject the backgrounds from electron recoils, from surface events and heat-only events. This is why these backgrounds are studied systematically using sideband data, in order to produce reliable models to be used in a Likelihood analysis of the data.

The dominant background at low energy is from heat-only events. The different hypotheses about their origin were considered and tested experimentally. No single cause can explain all the observations, despite the fact that all detectors are affected in the same manner and at rates that vary simultaneously, although no events occur in coincidence between detectors. The heat-only event energy spectrum has been extracted for each detector and experimental conditions since 2014. A statistical comparison has determined that their spectrum shape does not vary as a function of the voltage bias and of the time, even at the moment of a count rate anomaly observed in run308. Nevertheless, the observed shapes of the heat-only energy spectra are sufficiently different for each detector, that a modelization for each one is needed. A model with two exponential functions has been studied.

This ability to modelize the dominant background at low energy led to use it in a maximum Likelihood analysis to determine constraints of the cross-section for the spin-independent scattering of low-mass WIMP on nucleons from the experimental data of EDELWEISS. This statistical analysis uses information about the shape of the energy spectra of each background as well as the expected signal to their relative rate as a function of WIMP mass.

The final result of this work, obtained with an exposure of 25.42 kgd recorded with the detector FID803 operated at 100V during the run310 cool-down, provides for the first time in the EDELWEISS experiment constraints on WIMP with masses below 5 GeV/c². The obtained limit, in the range from 2.7 to 10 GeV/c², has been improved by a factor 1000 at 4 GeV/c² wrt the previous EDELWEISS-III limit⁹ [92]. Above 6 GeV/c², the previous limit is better because it is based on a larger exposure of 496 kg.days. Compared to other cryogenic experiments, the limits obtained in this work are a factor 2 above the one from CDMSlite Run2 at 5 GeV/c². They are below those from CRESST from [54] for WIMP masses above 4 GeV/c². The region

⁹This result used an analysis threshold of 0.9 keV_{ee}.

Conclusion and outlook

around $5 \text{ GeV}/c^2$ has recently been covered with non-cryogenic experiments with better sensitivities at that mass¹⁰, such as DarkSide [62], PandaX-II [61], PICO [66] and, very recently, LUX. This leads the cryogenic experiments like EDELWEISS, CDMS and CRESST to develop new detector and sensor designs able to extend their sensitivities to WIMP masses below $1 \text{ GeV}/c^2$, thus fully exploiting the superior energy resolution of these devices. The present work is an important step in understanding the behavior of the EDELWEISS detectors in the regime of increasingly lower thresholds.

This work has also demonstrated the advantage of the EDELWEISS detectors to be operated indiscriminately in planar mode at either 8 or 100 V voltage bias, or in FID mode. In this way, all the backgrounds on each detector can be studied thoroughly, resulting in background models that can be reliably used in a maximum Likelihood analysis. Despite these successes, it is clear that it is important to improve the heat resolution (as well as the number of detectors that can reach high voltage bias). Faster progress in sensitivity could be obtained by finally understanding the origin of all sources of heat-only events, and eliminating them. Some progress have been achieved with the used of NbSi TES sensors.

Finally, it can be noted that while extending the experimental constraints on low-mass WIMP depends crucially on progress in the experimental resolution of the heat signal¹¹, the goal of reaching the neutrino floor will likely be achieved only via similar progress on the ionization channel, in order to reinstate the background rejection capability.

¹⁰See e.g. the recent presentations by these experiments at the conference IDM2018 [104].

¹¹A 32 g germanium detector with 18 eV_{ee} heat energy resolution has been operated by the EDELWEISS collaboration and the first above-ground limit for germanium below $1 \text{ GeV}/c^2$ has been obtained.

To check the behavior of the Probability Density Functions (PDF) for each background and the expected signal as described in chapter 5, each one has been plotted in the parameter space (E_{ion}, E_{heat}) . Moreover, the projections on the x- and y-axis have been also achieved. Then, the generation of fake data has been verified as evoked in section III.1.2 of chapter 5.

I Expected signal

Based on the expected signal presented in section II.2.1 of chapter 5, a simulation of 10000 events of this population has been realized. Each of these events has to follow the PDF from which they are issued. The comparison between events generated by Monte-Carlo (red) and the PDF (blue) allows to confirm the agreement between the two distributions (see Fig.24). In the parameter space (E_{ion}, E_{heat}) (left top plot and bottom right plot for the PDF and simulation, respectively), there is a good agreement allowing to verify that the PDF as well as the simulations are correctly defined. Moreover, the projections along the x- and y-axis (top right plot and bottom left plot, respectively) for the two distributions are exactly determined. A deviation of one bin is visible, corresponding to the way the histograms have been filled.

II Compton background

The PDF associated to the compton background provides from the description made in section I.1 of chapter 5. It is expected that the behavior of the γ -background follows the electronic recoil band (i.e a linear behavior in the parameter space (E_{ion}, E_{heat})). The Monte-Carlo simulations of these events as well as the associated PDF are shown in Fig.25 (bottom right plot and top left plot, respectively). They are in excellent agreement. Moreover, the projections along the x- and y-axis (top right and bottom left plots) are also correctly defined.

At 100 V voltage bias, the surface γ -events are merged with the fiducial ones in this parameter space because the detectors operate in planar mode and no selection on a fiducial volume is possible. Hence the simulation of this background takes into account the total rate Γ_γ (Eq.5.3 for run309 and Eq.5.4 for run310) instead of the $\Gamma_{\gamma, fid}$ and $\Gamma_{\gamma, surf}$ separately. The PDF is also generated with Γ_γ for the same reason.

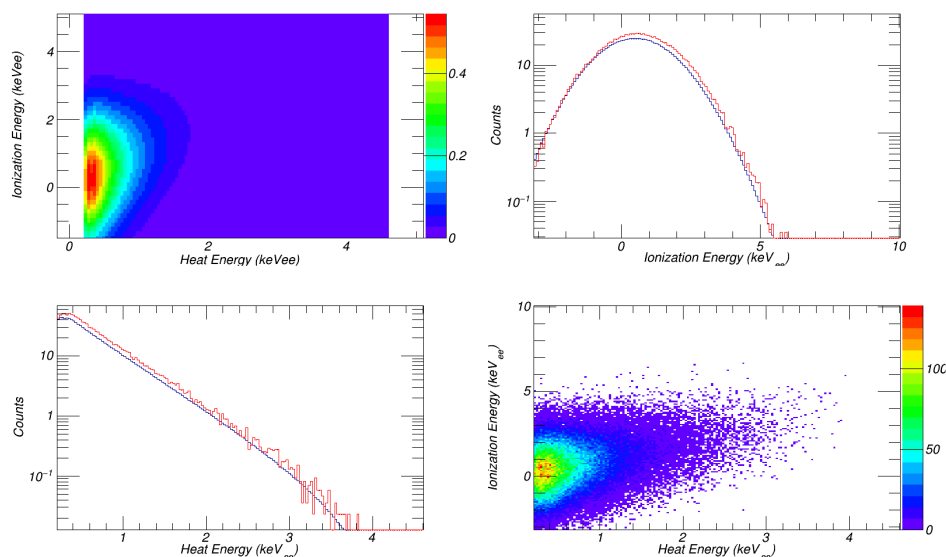


Figure 24 – Top, left: Probability Density Function for the expected signal of a WIMP in a FID800. It is expressed as a function of the two chosen variables of the analysis: E_{ion} and E_{heat} . Bottom, right: simulation of WIMP signals in the same parameter space. This figure allows to confirm that simulated data are in good agreement with the PDF. Top, right: ionization energy spectrum for fake data (in red) and providing from the PDF (in blue). Bottom, left: heat energy spectrum for fake data (in red) and from the PDF definition (in blue). The both are in excellent agreement, modulo one bin corresponding to the way they are filled.

III Tritium background

The simulation of this background and its PDF are made from the description in section I.2.2. It is expected that it has an electronic recoil, as the γ -background. This is what is observed in Fig.26 (top left and bottom right for the PDF and simulated events respectively). Moreover, the projections along the x- and y-axes (top right and bottom left) are also fully compatible. The rate used in this analysis corresponds to: $\Gamma_{tritium}$ for FID803 detector.

IV Cosmogenic peaks background

The cosmogenic events have discrete energies, with an input recoil energy spectrum corresponding to a delta function $\delta(E_R)$. The PDF for the associated peaks is thus:

$$\rho(E_{heat}, E_{ion}) = \frac{\epsilon_{th}(E_{heat})}{2\pi\sigma_{heat}\sigma_{ion}} \rho(E_R) e^{-\frac{(E_{heat}-f^{-1}(E_R))^2}{2\sigma_{heat}^2}} e^{-\frac{(E_{ion}-g^{-1}(E_R))^2}{2\sigma_{ion}^2}} \quad (63)$$

The building PDF for each peak is shown in Fig.27 (top left). As expected, it corresponds to gaussians around their true value, spread with the resolution as illustrated by their projections along the x- and y-axes (top right and bottom left). An excellent agreement is observed between these distributions.

Appendix A

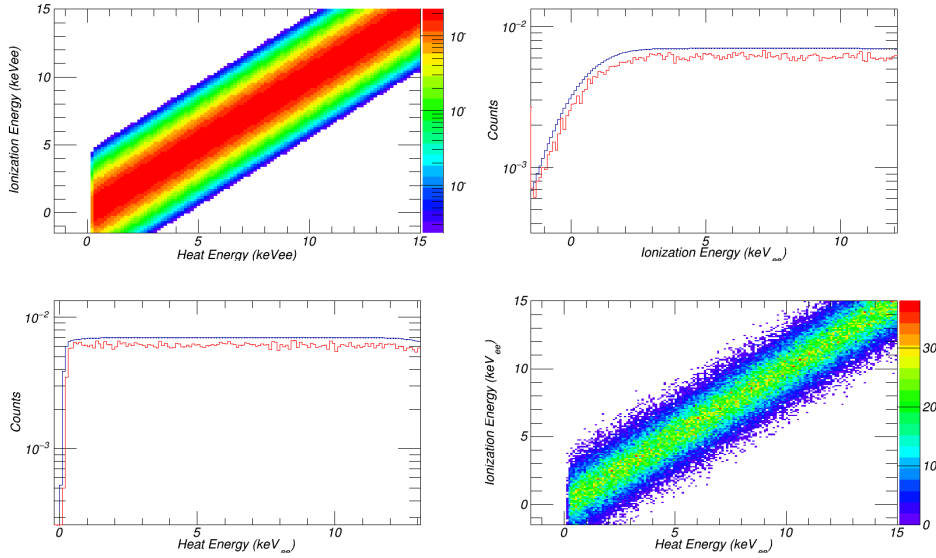


Figure 25 – Top, left: Probability Density Function corresponding to the γ -background in the parameter space (E_{ion}, E_{heat}). Bottom, right: simulation of γ -events in the same parameter space. This figure allows to confirm that simulated data are in good agreement with the PDF. Top, right: ionization energy spectrum for fake data (in red) and providing from the PDF (in blue). Both are in excellent agreement. Bottom, left: heat energy spectrum for fake data (in red) and from the PDF definition (in blue). The same agreement is observed.

V Beta background

The β -background is defined with Eq.5.13 described in section I.3 of chapter 5. Moreover, the quenching of this background is considered as 1 in high-voltage mode, because of the study defined in this section. The PDF calculated for this background with this information is illustrated in Fig.28 (top left) as well as the simulation based on it (bottom right). The projections along the x- and y-axis are also represented (top right and bottom left plots). These results allows to confirm that there is no difference between PDF and simulations. In section IV.3 of chapter 5, the β -quenching factor and its impact on the calculated limit will be discussed.

VI Lead background

The ^{206}Pb recoil background is defined as a gaussian around 100 keV with a flat function below it. The corresponding PDF is illustrated in Fig.29 as well as the associated simulated events. As expected, the gaussian function is shifted at $\sim 10 \text{ keV}_{ee}$ corresponding to the Luke-Neganov boost at high voltage bias. It is also recorded on the projections along x- and y-axis in this figure (top right and bottom left plots).

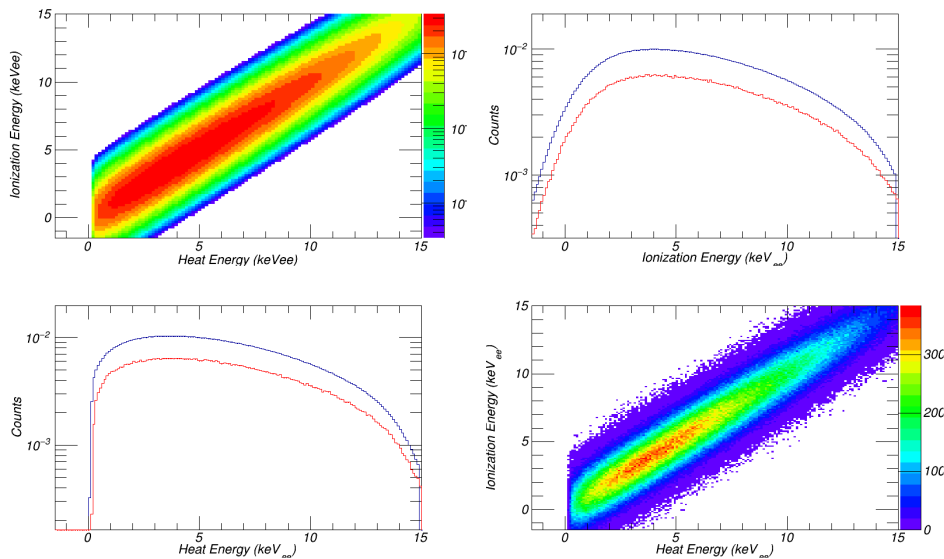


Figure 26 – Top, left: Probability Density Function corresponding to the tritium background in the parameter space (E_{ion}, E_{heat}) . Bottom, right: simulation of tritium events in the same parameter space. This figure allows to confirm that simulated data are in good agreement with the PDF. Top, right: ionization energy spectrum for fake data (in red) and providing from the PDF (in blue). Both are in excellent agreement. Bottom, left: heat energy spectrum for fake data (in red) and from the PDF definition (in blue), showing the same agreement.

VII Neutron background

The neutron background is similar to a WIMP signal. Their interactions produce the same ionization yield ($Q_{nr}(E_R) = 0.16E_R^{0.18}$) and their recoil energy spectrum is expected to be an exponential decreasing. Dedicated simulations carried out in the EDELWEISS collaboration allowed to determine the number of neutrons expected in the final recoil energy spectrum. As shown in Fig.30, the PDF (top left) is very similar to one of a WIMP signal. The simulated events follow this result (bottom right) as well as the projection along x- and y-axis (top right and bottom left plots). The expected rate for this background is around 0.03 events for the exposure of the high-voltage mode of run309. In section IV.3 of chapter 5, a discussion about the nuclear recoil parametrization is made and a test with a different $Q_{nr}(E_R)$ is achieved.

VIII Heat-only background

The parametrization of HO background is based on the model defined in chapter 4. The PDF and the simulations associated to this background are shown in Fig.31 (top left plot and bottom right plot, respectively). No difference is observed between these two distributions as well as between the projections along x- and y-axis where the blue curves correspond to the PDF and the red ones to simulations (top right and bottom left plots). A discussion about the uncertainties of this background is achieved in section IV.3 of chapter 5.

Appendix A

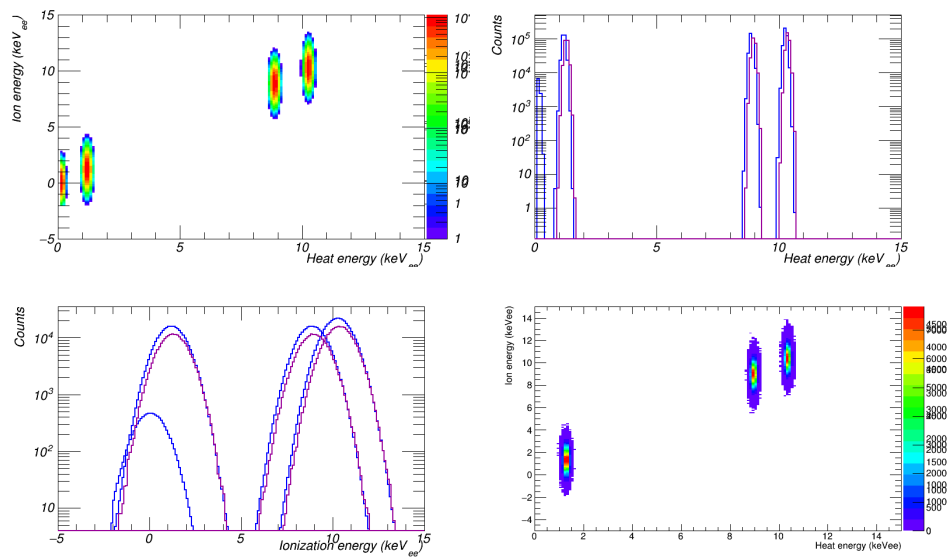


Figure 27 – Top, left: Probability Density Function corresponding to the cosmogenic peak background in the parameter space (E_{ion}, E_{heat}). Bottom, right: simulation of cosmogenic peak events in the same parameter space. This figure allows to confirm that simulated data are in good agreement with the PDF. Bottom, left: ionization energy spectrum for fake data (in magenta) and providing from the PDF (in blue). Both are in excellent agreement. Top, right: heat energy spectrum for fake data (in magenta) and from the PDF definition (in blue).

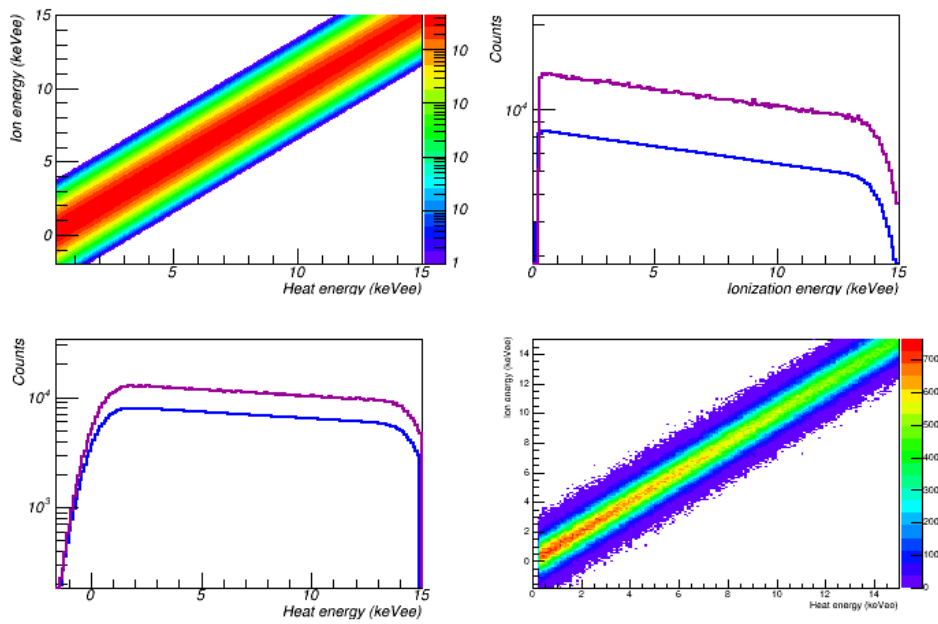


Figure 28 – Top, left: Probability Density Function corresponding to the β -background in the parameter space (E_{ion}, E_{heat}). Bottom, right: simulation of β -events in the same parameter space. This figure allows to confirm that simulated data are in good agreement with the PDF. Top, right: ionization energy spectrum for fake data (in magenta) and providing from the PDF (in blue). Both are in excellent agreement. Bottom, left: heat energy spectrum for fake data (in magenta) and from the PDF definition (in blue), showing the same excellent agreement.

Appendix A

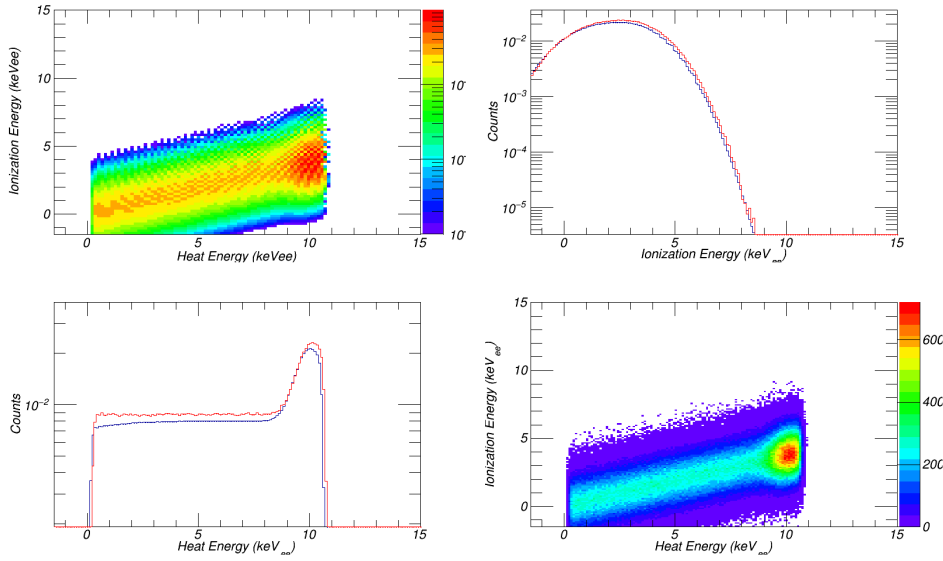


Figure 29 – Top, left: Probability Density Function corresponding to the ^{206}Pb background in the parameter space (E_{ion}, E_{heat}) . Bottom, right: simulation of ^{206}Pb events in the same parameter space. This figure allows to confirm that simulated data are in good agreement with the PDF. Top, right: ionization energy spectrum for fake data (in red) and providing from the PDF (in blue). Both are in excellent agreement. Bottom, left: heat energy spectrum for fake data (in red) and from the PDF definition (in blue), showing the same excellent agreement.

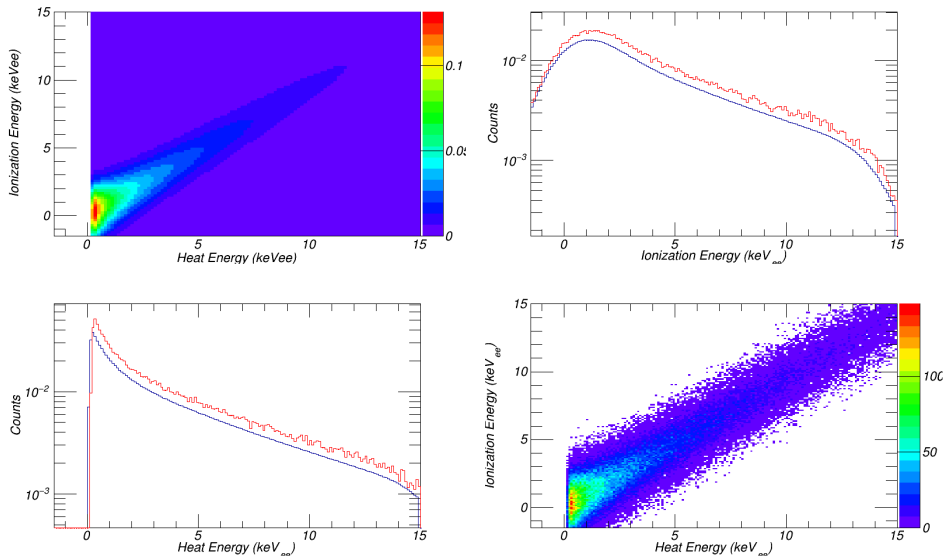


Figure 30 – Top, left: Probability Density Function corresponding to the neutron background in the parameter space (E_{ion}, E_{heat}) . Bottom, right: simulation of neutron events in the same parameter space. This figure allows to confirm that simulated data are in good agreement with the PDF. Top, right: ionization energy spectrum for fake data (in red) and providing from the PDF (in blue). Both are in excellent agreement. Bottom, left: heat energy spectrum for fake data (in red) and from the PDF definition (in blue), showing the same excellent agreement.

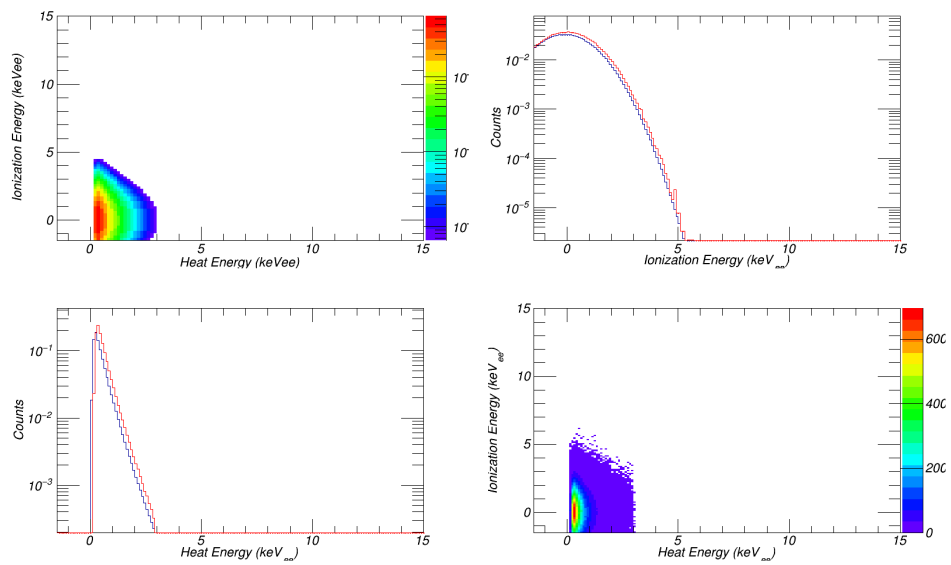


Figure 31 – Top, left: Probability Density Function corresponding to the heat-only background, expressed as a function of E_{ion} and E_{heat} . Bottom, right: simulation of heat-only events. This figure allows to confirm that simulated data are in good agreement with the PDF. Top, right: ionization energy spectrum for fake data (in red) and providing from the PDF (in blue). The both are in excellent agreement. Bottom, left: heat energy spectrum for fake data (in red) and from the PDF definition (in blue).

Appendix A

Bibliography

- [1] Einstein A. Relativity: The special and general theory, *Translation 1920*. 1916.
- [2] Hubble E. A relation between distance and radial velocity among extra-galactic nebulae. *Proceedings of the National Academy of Sciences of the United States of America*, 15:168–173, 03 1929.
- [3] P. A. R. Ade et al. planck 2015 results. xiii. cosmological parameters. *Astron. Astrophys.*, 594:A13, 2016.
- [4] C. Patrignani et al. (Particle Data Group). The review of particle physics (2017). *Chin. Phys. C*, 40, 2017.
- [5] Fermilab. Fermilab 1986: Annual report of the fermi national accelerator laboratory. *The Astrophysical J.*, 1986.
- [6] V. C. Rubin and W. K. Ford, Jr. Rotation of the Andromeda Nebula from a Spectroscopic Survey of Emission Regions. *The Astrophysical J.*, 159:379, February 1970.
- [7] Louis E. Strigari, James S. Bullock, Manoj Kaplinghat, Joshua D. Simon, Marla Geha, Beth Willman, and Matthew G. Walker. A common mass scale for satellite galaxies of the Milky Way. *Nature*, 454:1096–1097, 2008.
- [8] F. Zwicky. Die rotverschiebung von extragalaktischen nebeln. *Helvetica Physica Acta*, 6:110–127, 00 1933.
- [9] Gary A. Lokas, Ewa L.; Mamon. Dark matter distribution in the coma cluster from galaxy kinematics: breaking the mass-anisotropy degeneracy. *Monthly Notice of the Royal Astronomical Society*, 343:401–412, 08 2003.
- [10] Eddington A. & Davidson C. Dyson F. *Phil. Trans. Roy. Soc*, 220:290, 1919.
- [11] Hubble collaboration. <http://hubblesite.org/image/1930/category/15-galaxy-clusters>.
- [12] D. J. Fixsen. The temperature of the cosmic microwave background. *The Astrophysical Journal*, 707(2):916, 2009.
- [13] Daniel J. Eisenstein. An analytic expression for the growth function in a flat universe with a cosmological constant. *Astrophys. J.*, 1997.
- [14] York et al. SDSS Collaboration. The Sloan Digital Sky Survey: Technical Summary. *Astrophysical J.*, 120:1579–1587, September 2000.
- [15] G. Gamow. The origin of elements and the separation of galaxies. *Phys. Rev.*, 74:505–506, Aug 1948.
- [16] Masahiro Kawasaki et al. Revisiting big-bang nucleosynthesis constraints on dark-matter annihilation. *Phys. Lett. B*, 751:246–251, 2015.
- [17] Dragan Huterer and Daniel L Shafer. Dark energy two decades after: Observables, probes, consistency tests. *Rept. Prog. Phys.*, 81(1):016901, 2018.
- [18] Martin Kunz, Savvas Nesseris, and Ignacy Sawicki. Constraints on dark-matter properties from large-scale structure. *Phys. Rev.*, D94(2):023510, 2016.

- [19] Efstathiou G. Frenk C. S. & White S. D. M. Davis, M. The evolution of large-scale structure in a universe dominated by cold dark matter. *Astrophysical Journal, Part 1*, 292(1):371–394, 1985.
- [20] P. Tisserand et al. Limits on the Macho Content of the Galactic Halo from the EROS-2 Survey of the Magellanic Clouds. *Astron. Astrophys.*, 469:387–404, 2007.
- [21] A. de Rújula, S. L. Glashow, and U. Sarid. Charged dark matter. *Nuclear Physics B*, 333:173–194, March 1990.
- [22] S. R. Chivukula, A. G. Cohen, S. Dimopoulos, and T. P. Walker. Bounds on halo-particle interactions from interstellar calorimetry. *Physical Review Letters*, 65:957–959, August 1990.
- [23] J. L. Basdevant, R. Mochkovitch, J. Rich, M. Spiro, and A. Vidal-Madjar. Is there room for charged dark matter? *Physics Letters B*, 234:395–398, January 1990.
- [24] E. Gabrielli, L. Marzola, M. Raidal, and H. Veermäe. Dark matter and spin-1 milli-charged particles. *ArXiv e-prints*, July 2015.
- [25] Scott W. Randall, Maxim Markevitch, Douglas Clowe, Anthony H. Gonzalez, and Marusa Bradac. Constraints on the Self-Interaction Cross-Section of Dark Matter from Numerical Simulations of the Merging Galaxy Cluster 1E 0657-56. *Astrophys. J.*, 679:1173–1180, 2008.
- [26] Douglas Clowe, Marusa Bradac, Anthony H. Gonzalez, Maxim Markevitch, Scott W. Randall, Christine Jones, and Dennis Zaritsky. A direct empirical proof of the existence of dark matter. *Astrophys. J.*, 648:L109–L113, 2006.
- [27] Benjamin Audren, Julien Lesgourgues, Gianpiero Mangano, Pasquale Dario Serpico, and Thomas Tram. Strongest model-independent bound on the lifetime of Dark Matter. *JCAP*, 1412(12):028, 2014.
- [28] C. Boehm, P. Fayet, and R. Schaeffer. Constraining dark matter candidates from structure formation. *Physics Letters B*, 518:8–14, October 2001.
- [29] J. R. Primack and M. A. K. Gross. *Hot dark matter in cosmology*, pages 287–308. 2001.
- [30] V. S. Berezinsky, V. I. Dokuchaev, and Y. N. Eroshenko. Small-scale clumps of dark matter. *Physics Uspekhi*, 57:1–36, January 2014.
- [31] D. J. Croton, V. Springel, S. D. M. White, G. De Lucia, C. S. Frenk, L. Gao, A. Jenkins, G. Kauffmann, J. F. Navarro, and N. Yoshida. The many lives of active galactic nuclei: cooling flows, black holes and the luminosities and colours of galaxies. *MNRAS*, 365:11–28, January 2006.
- [32] M. Colless, G. Dalton, S. Maddox, W. Sutherland, P. Norberg, S. Cole, J. Bland-Hawthorn, T. Bridges, R. Cannon, C. Collins, W. Couch, N. Cross, K. Deeley, R. De Propris, S. P. Driver, G. Efstathiou, R. S. Ellis, C. S. Frenk, K. Glazebrook, C. Jackson, O. Lahav, I. Lewis, S. Lumsden, D. Madgwick, J. A. Peacock, B. A. Peterson, I. Price, M. Seaborne, and K. Taylor. The 2dF Galaxy Redshift Survey: spectra and redshifts. *MNRAS*, 328:1039–1063, December 2001.
- [33] Jonathan L. Feng. Dark Matter Candidates from Particle Physics and Methods of Detection. *Ann. Rev. Astron. Astrophys.*, 48:495–545, 2010.

Appendix A

- [34] C. Alcock et al. The MACHO project: Microlensing results from 5.7 years of LMC observations. *Astrophys. J.*, 542:281–307, 2000.
- [35] Andreas Ringwald. Alternative dark matter candidates: Axions. *PoS*, NOW2016:081, 2016.
- [36] G. Jungman, M. Kamionkowski, and K. Griest. Supersymmetric dark matter. *Phys. ReV.*, 267:195–373, March 1996.
- [37] Nicolas Deutschmann, Thomas Flacke, and Jong Soo Kim. Current LHC Constraints on Minimal Universal Extra Dimensions. *Phys. Lett.*, B771:515–520, 2017.
- [38] Shigeki Matsumoto, Satyanarayan Mukhopadhyay, and Yue-Lin Sming Tsai. Effective Theory of WIMP Dark Matter supplemented by Simplified Models: Singlet-like Majorana fermion case. *Phys. Rev.*, D94(6):065034, 2016.
- [39] Albert M Sirunyan et al. Search for dark matter in events with energetic, hadronically decaying top quarks and missing transverse momentum at $\sqrt{s} = 13$ TeV. 2018.
- [40] Vardan Khachatryan et al. Searches for invisible decays of the Higgs boson in pp collisions at $\sqrt{s} = 7, 8,$ and 13 TeV. *JHEP*, 02:135, 2017.
- [41] Ming-Yang Cui, Xu Pan, Qiang Yuan, Yi-Zhong Fan, and Hong-Shi Zong. Revisit of cosmic ray antiprotons from dark matter annihilation with updated constraints on the background model from AMS-02 and collider data. 2018.
- [42] Dan Hooper, Pasquale Blasi, and Pasquale Dario Serpico. Pulsars as the Sources of High Energy Cosmic Ray Positrons. *JCAP*, 0901:025, 2009.
- [43] Ams-02 collaboration.
- [44] H. Abdalla et al. H.E.S.S. discovery of very high energy γ -ray emission from PKS 0625-354. *Mon. Not. Roy. Astron. Soc.*, 2018.
- [45] G. A. Caliandro et al. The missing GeV γ -ray binary: Searching for HESS J0632+057 with Fermi-LAT. *Mon. Not. Roy. Astron. Soc.*, 436:740, 2013.
- [46] H. Abdalla et al. H.E.S.S. Limits on Linelike Dark Matter Signatures in the 100 GeV to 2 TeV Energy Range Close to the Galactic Center. *Phys. Rev. Lett.*, 117(15):151302, 2016.
- [47] S. Bhandari et al. The SURvey for Pulsars and Extragalactic Radio Bursts II: New FRB discoveries and their follow-up. *Mon. Not. Roy. Astron. Soc.*, 475(2):1427–1446, 2018.
- [48] M. G. Aartsen et al. Search for Neutrinos from Dark Matter Self-Annihilations in the center of the Milky Way with 3 years of IceCube/DeepCore. *Eur. Phys. J.*, C77(9):627, 2017.
- [49] J. D. Lewin and P. F. Smith. Review of mathematics, numerical factors, and corrections for dark matter experiments based on elastic nuclear recoil. *Astropart. Phys.*, 6:87–112, 1996.
- [50] David G. Cerdeno and Anne M. Green. Direct detection of wimps. *Particle dark matter*, pages 347–369, 2010.

- [51] R. Agnese et al. Low-mass dark matter search with CDMSlite. *Phys. Rev.*, D97(2):022002, 2018.
- [52] A. Fieguth, M. Hoferichter, P. Klos, J. Menéndez, A. Schwenk, and C. Weinheimer. Discriminating WIMP-nucleus response functions in present and future XENON-like direct detection experiments. *Physic Review D.*, 2018.
- [53] P. Agnes et al. Low-Mass Dark Matter Search with the DarkSide-50 Experiment. 2018.
- [54] F. Petricca et al. First results on low-mass dark matter from the CRESST-III experiment. 2017.
- [55] Paolo Gondolo and Graciela Gelmini. Compatibility of DAMA dark matter detection with other searches. *Phys. Rev.*, D71:123520, 2005.
- [56] Richard W. Schnee. Introduction to dark matter experiments. In *Physics of the large and the small, TASI 09, proceedings of the Theoretical Advanced Study Institute in Elementary Particle Physics, Boulder, Colorado, USA, 1-26 June 2009*, pages 775–829, 2011.
- [57] J. Billard. Lecture 2, Ecole de GIF. 2016.
- [58] K. Abe et al. A measurement of the scintillation decay time constant of nuclear recoils in liquid xenon with the XMASS-I detector. *JINST*, 13(12):P12032, 2018.
- [59] B. Lehnert. DEAP-3600 Recent Dark Matter Results. In *53rd Rencontres de Moriond on Cosmology La Thuile, Italy, March 17-24, 2018*, 2018.
- [60] D. S. Akerib et al. Projected WIMP sensitivity of the LUX-ZEPLIN (LZ) dark matter experiment. 2018.
- [61] Xiangyi Cui et al. Dark Matter Results From 54-Ton-Day Exposure of PandaX-II Experiment. *Phys. Rev. Lett.*, 119(18):181302, 2017.
- [62] P. Agnes et al. DarkSide-50 532-day Dark Matter Search with Low-Radioactivity Argon. 2018.
- [63] P.N. Luke. Voltage assisted calorimetric ionization detector. *J. Appl. Phys.*, 64:6858, 1988.
- [64] B. Neganov and V. Trofimov. Voltage assisted calorimetric ionization detector. *Otkrytia i izobretenia*, 146:215, 1985.
- [65] R. Agnese et al. Results from the Super Cryogenic Dark Matter Search (SuperCDMS) experiment at Soudan. *Phys. Rev. Lett.*, 120:061802, 2018.
- [66] C. Amole et al. Dark Matter Search Results from the PICO-60 C₃F₈ Bubble Chamber. *Phys. Rev. Lett.*, 118(25):251301, 2017.
- [67] Frederick Seitz. On the theory of the bubble chamber. *Physics of Fluids - PHYS FLUIDS*, 1:2–13, 01 1958.
- [68] The PICASSO Collaboration. On the theory of the bubble chamber. *Nucl. Instrum. Meth.*, A55:184–204, 2005.
- [69] B. Schmidt et al. Muon-induced background in the EDELWEISS dark matter search. *Astropart. Phys.*, 44:28–39, 2013.

Appendix A

- [70] C.Kefelian. Search for dark matter with edelweiss-iii excluding background from muon-induced neutrons. *thesis*, 2016.
- [71] Quentin Arnaud. *Détection directe de matière noire avec l'expérience EDELWEISS-III : étude des signaux induits par le piégeage de charges, analyse de données et caractérisation de la sensibilité des détecteurs cryogéniques aux WIMPs de basse masse*. PhD thesis, 2015. Thèse de doctorat dirigée par Gascon, Jules Physique des particules Lyon 1 2015.
- [72] V. Chazal et al. Neutron background measurements in the underground laboratory of modane. *Astropart. Phys.*, 9:163–172, 1998.
- [73] R. Lemrani and the EDELWEISS Collaboratio. Update of neutron studies in edelweiss. *Phys. Conf. Ser.*, 39:145–147, 2006.
- [74] Thibault Main de Boissière. *Low mass WIMP and axion searches with the EDELWEISS experiment*. Theses, Université Paris Sud - Paris XI, July 2015.
- [75] E. Armengaud et al. Performance of the EDELWEISS-III experiment for direct dark matter searches. *JINST*, 12(08):P08010, 2017.
- [76] E. Armengaud et al. Measurement of the cosmogenic activation of germanium detectors in EDELWEISS-III. *Astropart. Phys.*, 91:51–64, 2017.
- [77] Gamma interaction in the germanium. <https://www.nuclear-power.net/nuclear-power/reactor-physics/interaction-radiation-matter/interaction-gamma-radiation-matter/gamma-ray-attenuation/linear-attenuation-coefficient/>.
- [78] H.Bethe. Zur theorie des durchgangs schneller korpuskularstrahlen durch materie. *Annalen der Physik*, 397:325–400, 1930.
- [79] Radon level in the lsm. [LaboratoireSouterraindeModane, ModaneUndergroundLaboratory,Website,http://www-lsm.in2p3.fr/](http://www-lsm.in2p3.fr/).
- [80] G.T.Ewan and A.J.Tavendale. A High Resolution Lithium-Drift Germanium Gamma-Ray Spectrometer. *Nucl.Instr.Methods*, 25:185, 1963.
- [81] O. Martineau et al. Calibration of the EDELWEISS Cryogenic Heat-and-ionisation Germanium Detectors for Dark Matter Search. *NIM Phys. Res.*, A(530):426–439, 2004.
- [82] A. Broniatowski. Intervalley Scattering of Hot Electrons in Germanium at Millikelvin Temperatures. *JLTP*, 176:860–869, 2014.
- [83] A.Efros and B.Shklovskii. C8,L49, 1975.
- [84] Billard J. et al. Characterization and optimization of EDELWEISS-III FID800 heat sensors. In *Proceedings, 16th Low Temperature Detectors Conference*, 2015.
- [85] E. Haller et al. Instrumentation in astronomy viii. *SPIE*, 2198:630, 1994.
- [86] A. Broniatowski et al. A new high-background-rejection dark matter ge cryogenic detector. *Phys. Lett. B*, 681:305–309, 2009.
- [87] Q. Arnaud et al. Signals induced by charge-trapping in edelweiss fid detectors: analytical modeling and applications. *JINST*, 11, 2016.

- [88] M. Scharff J. Lindhard, V. Nielsen and P. Thomsen. Integral equations governing radiation effects. *Mat. Fys. Medd.*, 33:10, 1963.
- [89] B. J. Scholz, A. E. Chavarria, J. I. Collar, P. Privitera, and A. E. Robinson. Measurement of the low-energy quenching factor in germanium using an $^{88}\text{Y}/\text{Be}$ photoneutron source. *Phys. Rev.*, D94(12):122003, 2016.
- [90] R. Agnese et al. First Dark Matter Constraints from SuperCDMS Single-Charge Sensitive Detectors. *Submitted to: Phys. Rev. Lett.*, 2018.
- [91] Q. Arnaud et al. Optimizing EDELWEISS detectors for low-mass WIMP searches. *Phys. Rev.*, D97(2):022003, 2018.
- [92] L. Hehn and All. Improved edelweiss-iii sensitivity for low-mass wimps using a profile likelihood approach. *The European Physical Journal C*, 76(10):548, 2016.
- [93] Xavier Defay. *Recherche de matière noire au sein de l'expérience EDELWEISS avec des bolomètres germanium à double composante ionisation/chaueur : Rejet des évènements de surface avec la voie ionisation*. PhD thesis, 2008. Thèse de doctorat dirigée par Jacholkowska, Agnieszka et Broniatowski, Alexandre Astronomie. Astrophysique Montpellier 2 2008.
- [94] Q. Arnaud et al. Signals induced by charge-trapping in EDELWEISS FID detectors: analytical modeling and applications. *JINST*, 11(10):P10008, 2016.
- [95] Rene Brun and Fons Rademakers. ROOT - An Object Oriented Data Analysis Framework. In *AIHENP 96 Workshop, Lausanne, Sep. 1996, Nucl. Inst. & Meth. in Phys. Res.*, pages 81–86, 1997.
- [96] J. Astrom et al. Fracture processes studied in CRESST. *NIM*, 2006.
- [97] Laha Chakravarti and Roy. Handbook of Methods of Applied Statistics. *John Wiley and Sons*, I:392–394, 1967.
- [98] Kolmogorov-smirnov table. <http://www.real-statistics.com/statistics-tables/kolmogorov-smirnov-table/>.
- [99] D. V. Poda. ^{100}Mo -enriched Li_2MoO_4 scintillating bolometers for $0\nu 2\beta$ decay search: From LUMINEU to CUPID-0/Mo projects. *AIP Conf. Proc.*, 1894(1):020017, 2017.
- [100] S. Marnieros et al. Controlling the Leakage-Current of Low Temperature Germanium Detectors Using XeF_2 Dry Etching. In *Proceedings, 15th Low Temperature Detectors Conference*, 2013.
- [101] J. Billard. Private Communication, 2017.
- [102] Silvia Scorza. *EDELWEISS-II, direct Dark Matter search experiment : first data analysis and results*. PhD thesis, 2009. Thèse de doctorat dirigée par Gascon, Jules Physique des Particules Lyon 1 2009.
- [103] Glen Cowan, Kyle Cranmer, Eilam Gross, and Ofer Vitells. Asymptotic formulae for likelihood-based tests of new physics. *Eur. Phys. J.*, C71:1554, 2011. [Erratum: *Eur. Phys. J.* C73,2501(2013)].
- [104] Idm 2018. <https://www.brown.edu/conference/IDM2018/home>.